

**Structural, Magnetic and Thermal Studies of
 $\text{Ce}_{1-x}\text{Eu}_x\text{CrO}_3$ Nano-Powders**

by

Maryam Taheri

A THESIS SUBMITTED IN PARTIAL FULFILLMENT OF THE
REQUIREMENTS FOR THE DEGREE OF
DOCTOR OF PHILOSOPHY

in

The Faculty of Mathematics and Sciences

Department of Physics

BROCK UNIVERSITY

September 28, 2015

2015 ©Maryam Taheri

In presenting this thesis in partial fulfillment of the requirements for advanced degree at Brock University, I agree that the Library shall make it freely available for reference and study. I further agree that permission for extensive copying of this thesis for scholarly purposes may be granted by the head of my department or by his or her representatives. It is understood that copying or publication of this thesis for financial gain shall not be allowed without my written permission.

.....

(Signature)

Department of Physics

Brock University

St. Catharines, Canada

Date

Abstract

A new series of nano-sized $\text{Ce}_{1-x}\text{Eu}_x\text{CrO}_3$ ($x = 0.0$ to 1.0) with an average particle size of 50 - 80 nm were synthesized using a solution combustion method. Nano-powders $\text{Ce}_{1-x}\text{Eu}_x\text{CrO}_3$ with the canted antiferromagnetic property exhibited interesting magnetic behaviors including the reversal magnetization and the exchange bias effect. The effect of europium doping as the ion with the smaller radius size and different electron configuration on structural, magnetic and thermal properties of $\text{Ce}_{1-x}\text{Eu}_x\text{CrO}_3$ were investigated using various experimental techniques, i.e. DC/AC magnetic susceptibility, heat capacity, thermal expansion, Raman scattering, X-ray photoemission spectroscopy, transmission/scanning electron microscopy, X-ray powder diffraction and neutron scattering.

An exchange bias effect, magnetization irreversibility and AC susceptibility dispersion in these samples confirmed the existence of the spin disorder magnetic phase in $\text{Ce}_{1-x}\text{Eu}_x\text{CrO}_3$ compounds. The exchange bias phenomenon, which is assigned to the exchange coupling between glassy-like shell and canted antiferromagnetic core, showed the opposite sign in CeCrO_3 and EuCrO_3 at low temperatures, suggesting different exchange interactions at the interfaces in these compounds. The energy level excitation of samples were examined by an inelastic neutron

scattering which was in good agreement with the heat capacity data.

Neutron scattering analysis of EuCrO_3 was challenging due to the large neutron absorption cross-section of europium. All diffraction patterns of $\text{Ce}_{1-x}\text{Eu}_x\text{CrO}_3$ showed the magnetic peak attributed to the antiferromagnetic Cr^{3+} spins while none of the diffraction patterns could detect the magnetic ordering of the rare-earth ions in these samples.

Dedication

This dissertation is dedicated to my husband, Alireza, who has been a constant source of support and encouragement during the challenges of graduate school and life. I give my deepest expression of love and appreciation for all sacrifices he made.

Declaration

I hereby certify that the dissertation entitled “The Structural, Magnetic and Thermal Studies of $\text{Ce}_{1-x}\text{Eu}_x\text{CrO}_3$ Nano-Powders” is entirely my original research work except where otherwise indicated clearly with reference to the literature or acknowledgment of collaborative research and discussions.

Name : Maryam Taheri

Signed:

Date:

Acknowledgments

First and foremost I would like to express my gratitude to my research supervisor Prof. Fereidoon S. Razavi for all the opportunities and guidance he gave me. This work would not have been possible without his mentorship and support. I wish to thank Prof. David A. Crandles and Prof. Kirill Samokhin for the valuable feedback and support throughout my graduate work as my advisory committee. I truly appreciate all scientific collaborations which I had with Prof. R. K. Kremer, especially for his valuable discussion, helpful comments and all his help for diffraction pattern refinements. Special thanks to Dr. Simon Trudel for giving me the opportunity of working in his lab at the University of Calgary. My warm thank to Dr. Zahra Yamani and Dr. Roxana Flacau for the neutron scattering measurements. I am grateful to Dr. Tobias Fürstenhaupt for the electron microscopy training he has given me. I would like to thank Dr. M. Konuma for performing X-ray photoemission spectroscopy and Dr. Patrick G. Reuvekamp for performing thermal expansion measurement in Max Plank Institute. I thank technical staffs at the machine and electronic shop, and glassblower for their constant help in troubleshooting and fabricating the required components in my research.

It is a pleasure to thank whole Faculty members and staff of Physics Department for their kindness and friendship. Many thanks to all my friends and colleagues, in particular Biljana Indovski and Laila Obied, for their advice, help, friendship and fun time throughout these five years.

Most importantly, none of this would have been possible without the love and support of my family. I would like to express my heart-felt gratitude to my parents who have been encouraging, supportive and shown belief in me and my work. I would like to thank my husband, Alireza, for his understanding, love and patience throughout this endeavor. His faithful support and encouragement made this dissertation possible. I will be forever indebted to him.

Contents

1	Introduction	1
1.1	Rare Earth Chromites	1
1.2	Outline	8
2	Magnetism	16
2.1	Early History of Magnetism	16
2.2	The Magnetic Phenomenon	17
2.2.1	Curie's Law and Curie-Weiss Law	20
2.2.2	Magnetic Hysteresis Loop	23
2.2.3	Pauli Exclusion Principle	24
2.2.4	Hund's Rules	25
2.2.5	Orbital Angular Momentum Quenching	26
2.2.6	Spin-Orbit Coupling	28
2.2.7	Rare Earth Elements	29
2.2.8	Exchange Interaction	32
2.3	Disordered Magnetic Systems	41
2.3.1	Magnetic Frustration	41

2.3.2	Spin Glasses	42
2.3.3	Exchange Bias	44
3	Synthesis of Samples	54
3.1	Combustion Method	54
3.2	Sample Preparation	55
4	Sample Characterization and Morphology	62
4.1	Crystallography	62
4.1.1	Direct Lattice	62
4.1.2	Reciprocal Lattice	66
4.1.3	Perovskite Structure	66
4.2	X-Ray Diffraction	68
4.2.1	X-Rays	68
4.2.2	X-ray Diffraction	75
4.2.3	X-ray Powder Diffraction Methods	80
4.2.4	Crystallite Size	82
4.2.5	Experiment	84
4.3	X-Ray Photoelectron Spectroscopy	106
4.3.1	XPS Results	109
4.4	Electron microscopy	125
4.4.1	Transmission Electron microscopy	125
4.4.2	Scanning Electron Microscopy coupled with Energy Dispersive X-ray Spectroscopy	130

5	Magnetic and Thermal Measurements	141
5.1	Magnetic Properties Measurement System	141
5.1.1	DC Magnetization Results	144
5.1.2	Exchange bias Effect	161
5.2	Physical Property Measurement System	169
5.2.1	AC Measurement System	170
5.2.2	Heat Capacity Measurement	176
5.3	Thermal Expansion	192
5.3.1	Thermal Expansion Results	193
5.4	Raman Spectroscopy	195
5.5	Dielectric Properties	203
5.5.1	Dielectric Results	204
6	Neutron Scattering	212
6.1	Why Neutrons?	212
6.2	Neutron Scattering Sources	214
6.3	Theory of Neutron Scattering	216
6.3.1	Elastic Neutron Scattering	216
6.3.2	Inelastic Neutron Scattering	222
6.3.3	Magnetic Neutron Scattering	225
7	Conclusion and Future Work	251
7.1	Conclusion	251
7.2	Recommendation for Future Work	254

List of Figures

1.1	(a) Spin configurations in the FM, G-type antiferromagnet, C-type antiferromagnet and A-type antiferromagnet structures. (b) Spin configurations of Cr ions in Γ_1 , Γ_2 and Γ_4 in ErCrO_3 with $Pbnm$ space group. The yellow balls are represented as Er ion without spins, reprinted from Ref. [15].	4
1.2	Paramagnetic to antiferromagnetic transition temperature (T_N) of rare earth chromites (RCrO_3) versus rare-earth ionic radius, showing the Néel temperature reduction while decreasing in ionic radius [22].	5
1.3	(a) Temperature dependence of the dielectric constant in different frequencies, (b) a polarization loop of YCrO_3 , reprinted from Ref. [4, 28].	8
2.1	Schematic of the magnetic dipole moments ordering in the different types of magnetic materials, reprinted from Ref. [5].	19
2.2	(a) Temperature dependence of inverse susceptibility for paramagnets ($\theta_c = 0$), ferromagnets ($T_c = \theta_c > 0$), and antiferromagnets ($\theta_c < 0$). (b) Magnetization versus magnetic field for ferro-, para- and diamagnetic materials, reprinted from Ref. [5].	21

2.3	Magnetic hysteresis loop of a ferromagnet, where M_r and H_c are the remanent magnetization and the coercivity field, respectively.	24
2.4	Representation of the electron energy levels of the octahedral d shell splitting, where Δ_0 is the value of the energy level splitting, reprinted from Ref. [9].	28
2.5	(a) The energy levels of Eu^{3+} ion in the absence of an external magnetic field, (b) The observed and calculated magnetic susceptibility of Eu^{3+} in EuCoO_3 compound [19]. Inset shows the effective magnetic moment of free Eu^{3+} ion, reprinted from Ref. [18].	33
2.6	Schematic exchange interactions of (a) antiferromagnet and ferromagnetic ordering in direct interaction, (b) the indirect interactions through conduction electrons, (c) antiferromagnetism and ferromagnetism orientation in super-exchange interactions, depending on the bonding angle, (d) ferromagnetic ordering in double exchange interactions, Reprinted from Ref. [22].	37
2.7	The antisymmetric DM vector D_{ij} is proportional to the position of the oxygen ion (green ball) between two magnetic ions (red balls). Weak ferromagnetism (FM) in antiferromagnet LaCu_2O_4 as well as weak ferroelectricity (FE) in RMnO_3 where polarization is $\mathbf{P} \propto \mathbf{Q} \times (\mathbf{S}_i \times \mathbf{S}_j)$ [23].	40
2.8	Ferromagnetic (FM) and antiferromagnetic (AFM) alignments of magnetic spins on a 2-D triangle lattice.	41

2.9	Schematic exchange bias phenomenon which is observed by the horizontal as well as the vertical shift in M-H loop after field cooling measurements.	45
2.10	Schematic drawing of the spin configuration of FM-AFM couple at the different points of M-H loop measurements when (a) AFM anisotropy is large, (b) AFM anisotropy is small. Reprinted from Ref. [30].	48
3.1	The images of (a) starting materials solution, (b) fluffy ash of EuCrO_3 after auto-ignition process, (c) CeCrO_3 and (d) EuCrO_3 calcined powders at 500°C , (e) CeCrO_3 and (f) EuCrO_3 sintered pellets at 950°C	58
3.2	Schematic drawing of the horizontal tubular furnace used for preparation of $\text{Ce}_{1-x}\text{Eu}_x\text{CrO}_3$ powders. This was achieved by sintering the samples placed inside an alumina tube in a reducing ambient, namely Ar and H_2	59
3.3	The flow chart of the preparation method of $\text{Ce}_{1-x}\text{Eu}_x\text{CrO}_3$ nano-powders, using the combustion method.	60
4.1	(a) Lattice parameters and angles in the cubic crystal structure, (b) planes and directions in the cubic system.	64
4.2	Bravais lattice types in the three dimensions. P, I, F and C are referred to as simple, body, face and base centers, respectively [2].	65

4.3	The structure of a perovskite, ABO_3 , in the ideal cubic (centrosymmetric) and BO_6 tilted (the ferroelectric phase), reprinted from Ref. [6]. . .	67
4.4	The schematic X-ray tube using for X-ray generating, reprinted from Ref [8].	71
4.5	The atomic levels and allowed transitions in copper. K_α and K_β are the characteristic X-ray wavelengths.	72
4.6	The schematic structure of a synchrotron using for X-ray generating, reprinted from Ref. [13].	74
4.7	The schematic Bragg diffraction. Two beams with an identical wavelength and the same phase approach a crystalline solid and are then scattered off.	79
4.8	The schematic diagram of the Debye-Scherrer powder diffraction method and the opened film represented the diffracted lines [15]. . .	82
4.9	The vertical geometric arrangement of the Bragg-Brentano diffractometer, reprinted from Ref [16].	83
4.10	Scattering width peaks comparison in the scattering from samples with the small particles and the large particles, reprinted from Ref. [19].	85
4.11	(a) The Rigaku Multiflex X-ray diffractometer, (b) a horizontal sample holder, (c) the Stoe Stadi P diffractometer and (d) a vertical capillary sample holder.	87
4.12	XRD patterns of $CeCrO_3$, sintered at $950^\circ C$ for 12 h in oxygen, argon and air, using $Cu K_\alpha$ radiation.	89

4.13	XRD pattern of CeCrO_3 , sintered at 950°C for 12 h in the mixture of argon and hydrogen, using Cu K_α radiation. The red lines show the CeCrO_3 data base, obtained from Ref. [20].	89
4.14	The database XRD patterns of CeO_2 , Cr_2O_3 and CeCrO_3 as the references, using Cu K_α wavelength [21, 22, 20].	90
4.15	Refined XRD pattern of CeCrO_3 , sintered at 950°C for 12 h, using $\text{Mo K}_{\alpha 1}$ radiation. Red, black and blue lines refer to the observed, fitted and the difference between experimental and fitted X-ray diffraction patterns. The bars show the position of the Bragg's reflections.	91
4.16	The orthorhombic crystal structure of the CeCrO_3 powder. Cr^{3+} (yellow atoms) are located at the center and O^{2-} (red atoms) are at the corners of the octahedral. The purple balls are Ce^{3+} cations. . .	93
4.17	(a) Two distorted CrO_6 octahedral that each chromium atom surrounded by two apical oxygen atoms (O_1) and four equatorial oxygen atoms (O_2), (b) and (c) cerium atom placed between four O_1 and eight O_2 with the different Ce-O_1 and Ce-O_2 bond lengths in the CeCrO_3 crystal structure. Ce^{3+} , Cr^{3+} and O^{2-} atoms are shown using purple, yellow and red balls, respectively.	94
4.18	XRD patterns of samples $\text{Ce}_{1-x}\text{Eu}_x\text{CrO}_3$, sintered at 950°C for 12 h, using Cu K_α radiation which indicate a small shift in the peaks. .	95
4.19	Refined XRD patterns of $\text{Ce}_{1-x}\text{Eu}_x\text{CrO}_3$, where $x = 0.1, 0.3, 0.5$ and 0.6 , sintered at 950°C for 12 h, using $\text{Mo K}_{\alpha 1}$ wavelength. . . .	96

4.20	Refined XRD pattern of EuCrO_3 , using $\text{Mo K}_{\alpha 1}$ radiation, sintered at $950\text{ }^\circ\text{C}$ for 12 h. The upper image shows the crystal structure of EuCrO_3 , visualized by VESTA crystallographic program.	97
4.21	Average shape and size of the EuCrO_3 nano-particles, determined from X-ray diffraction by modeling the broadening of the Bragg reflections with spherical harmonics (<i>FullProf</i> program, model-size = 18).	98
4.22	(a) Tolerance factor, (b) and (c) lattice parameters and (d) volume unit cell of $\text{Ce}_{1-x}\text{Eu}_x\text{CrO}_3$ versus europium concentration (X).	104
4.23	(a) Value of $\frac{c}{(a+b)/2}$ versus b/a , (b) the ratio of the $ 2(a-b)/(a+b) $ versus europium concentration, (c) and (d) the x and y atomic positions of Ce/Eu versus europium concentration (X).	105
4.24	The schematic diagram of a core-level-photoelectron emission process, where E_F , E_V , E_K and E_B are the Fermi energy level, vacuum energy level, kinetic energy and binding energy, respectively.	107
4.25	The schematic diagram of the basic elements in XPS experiment [34].	109
4.26	The Ce 3d XPS spectra of Ce^{4+} and Ce^{3+} compounds, reprinted from Ref. [36].	110
4.27	The XPS survey spectrum of CeCrO_3 before surface cleaning.	111
4.28	Ce 3d core level XPS spectra of CeCrO_3 nano-powders (a) before surface sputtering and (b) after surface sputtering.	112

4.29	Ce 4d core level XPS spectra of CeCrO ₃ nano-powders (a) before surface sputtering and (b) after surface sputtering.	113
4.30	Cr 2p core level XPS spectra of CeCrO ₃ nano-powders (a) before surface sputtering and (b) after surface sputtering.	114
4.31	(a) O 1s XPS spectra and (b) valence-band level (vb) XPS spectra of the core level for CeCrO ₃ nano-powders before surface sputtering (blue line) and after surface sputtering (red line).	115
4.32	(a) Ce 3d, (b) Eu 3d, (c) Ce/Eu 4d and (d) Cr 2p spectra of samples Ce _{1-x} Eu _x CrO ₃ , before Ar ion sputtering.	116
4.33	(a) Ce 3d, (b) Eu 3d, (c) Ce/Eu 4d and (d) Cr 2p spectra of samples Ce _{1-x} Eu _x CrO ₃ after Ar ion sputtering.	117
4.34	The XPS survey spectrum of EuCrO ₃ before surface cleaning.	118
4.35	Eu 3d core level XPS spectra of EuCrO ₃ nano-powders (a) before surface sputtering and (b) after surface sputtering.	119
4.36	Eu 4d core level XPS spectra of EuCrO ₃ nano-powders (a) before surface sputtering and (b) after surface sputtering.	120
4.37	Cr 2p core level XPS spectra of EuCrO ₃ nano-powders (a) before surface sputtering and (b) after surface sputtering.	121
4.38	(a) O 1s XPS spectra and (b) valence-band level (vb) XPS spectra of EuCrO ₃ nano-powders before surface sputtering (blue line) and after surface sputtering (red line).	121
4.39	Transmission electron microscopy (TEM) system, reprinted from Ref. [51].	126

4.40	TEM image of nano-powder CeCrO_3 with corresponding size distribution histogram.	127
4.41	HR-TEM micrographs of the nano-powder CeCrO_3	128
4.42	TEM image with corresponding size distribution histogram of nano-powders $\text{Ce}_{0.9}\text{Eu}_{0.1}\text{CrO}_3$	129
4.43	(a) TEM image with corresponding size distribution histogram, (b) and (c) HR-TEM images of nano-powder EuCrO_3	130
4.44	SEM micrograph with corresponding EDX spectrum of the nano-powder CeCrO_3	132
4.45	SEM images with corresponding EDX results of nano-powders $\text{Ce}_{1-x}\text{Eu}_x\text{CrO}_3$, where $x = 0.1, 0.3$ and 0.5 , respectively.	133
4.46	SEM micrograph with corresponding EDX result of the nano-powder EuCrO_3	134
5.1	Schematic drawing of MPMS probe and dewar cabinet in MPMS system, reprinted from Ref. [1].	142
5.2	Schematic drawings of (a) the SQUID system in the MPMS, (b) a sample mounted in the plastic drinking straw and attached to the sample rod used for the magnetization measurement in the MPMS, reprinted from Ref. [4].	143
5.3	(a) ZFC (blue line)/FC (red line) susceptibilities versus temperature measurements of CeCrO_3 under an applied magnetic field of 0.5 kOe. (b) Inverse magnetic susceptibilities of CeCrO_3 under different magnetic field.	145

5.4	(a) FC susceptibility measurements of CeCrO_3 in different magnetic fields, (b) ZFC/FC susceptibility measurements of CeCrO_3 in $H = 5$ kOe (blue line) and $H = 30$ kOe (red line). The inset shows the existence of the divergence in the ZFC and FC susceptibilities even in $H = 30$ kOe.	149
5.5	The magnetization hysteresis loops of CeCrO_3 at (a) $T = 5$ K, (b) higher temperatures.	149
5.6	(a) ZFC (blue line)/FC (red line) susceptibilities versus temperature measurements under an applied field of 0.5 kOe, (b), (c) and (d) the magnetic hysteresis loops at the different temperatures of the sample $\text{Ce}_{0.8}\text{Eu}_{0.2}\text{CrO}_3$	150
5.7	(a) ZFC and (b) FC susceptibilities measurements under an applied magnetic field of 0.5 kOe of samples $\text{Ce}_{1-x}\text{Eu}_x\text{CrO}_3$, where $x = 0.1, 0.5, 0.9, 0.95$	151
5.8	(a) ZFC (blue line)/ FC (red line) susceptibilities measurements under an applied magnetic field of 0.5 kOe, (b), (c) and (d) the magnetic hysteresis loops at the different temperatures of $\text{Ce}_{0.02}\text{Eu}_{0.98}\text{CrO}_3$	152
5.9	ZFC (blue line)/FC (red line) susceptibilities versus temperature of EuCrO_3 under an applied magnetic field of 0.5 kOe, (Lower inset shows the $\chi(\text{FC})$ below 50 K and the upper inset presents $\chi(\text{ZFC})$ around the transition temperature).	153

5.10	Inverse magnetic susceptibility of EuCrO_3 (a) under different magnetic field, (b) measured with a field of 10 kOe. The solid red line represents fit of a Curie-Weiss law.	153
5.11	(a) ZFC and (b) FC susceptibility measurements of EuCrO_3 in the different magnetic fields.	156
5.12	(a) ZFC/FC susceptibility measurements of EuCrO_3 in $H=5$ kOe (blue line) and $H=30$ kOe (red line), (b) the irreversible temperature versus an applied magnetic field of EuCrO_3	157
5.13	The magnetic hysteresis loops of EuCrO_3 at (a) $T = 5$ K and (b) $T = 15, 55, 150$ and 200 K.	158
5.14	(a) Total hysteresis loop (black line), background (red line) and FM component (green line) of EuCrO_3 at 100 K. (b) The temperature dependence of the saturated magnetic field (H_s). (c) Magnetic hysteresis loops of EuCrO_3 at 135 K (blue line) and 175 K (red line).	158
5.15	The experimental effective magnetic moments of $\text{Ce}_{1-x}\text{Eu}_x\text{CrO}_3$ versus europium dopant (X).	160
5.16	ZFC (blue line)/FC (red line) magnetic hysteresis loops of CeCrO_3 after cooling in 50 kOe at 5 K.	162
5.17	The temperature dependence of (a) the exchange bias magnetic field and (b) the exchange bias magnetization of CeCrO_3	164

5.18	The cooling magnetic field dependence of exchange bias magnetic field (blue line) and the exchange bias magnetization (red line) in CeCrO_3 at (a) $T = 5$ K and (b) $T = 150$ K.	164
5.19	ZFC (blue line)/FC (red line) magnetic hysteresis loops of EuCrO_3 after cooling in 50 kOe at 5K.	165
5.20	(a) and (b) Temperature dependence of the exchange bias magnetic field and exchange bias magnetization under 50 kOe cooling field, (c) and (d) the cooling magnetic field dependence of the exchange bias field and exchange bias magnetization at $T = 5$ K in EuCrO_3	166
5.21	IRM and TRM versus magnetic field of the (a) typical spin glass system $\text{AuFe}(0.5\%)$, (b) typical DAFF system $\text{Fe}_{0.48}\text{Zn}_{0.52}\text{Fe}$ and (c) DAFF Co_3O_4 nanowires and (d) core-shell 2D DAFF, reprinted from Ref. [26, 23]	167
5.22	IRM (blue line) and TRM (red line) versus magnetic field at $T = 5$ K of the samples (a) CeCrO_3 and (b) EuCrO_3	168
5.23	The schematic drawing of the core-shell structure of CeCrO_3 in the magnetic field H	169
5.24	The schematic drawings of the ACMS insert and coil sets as well as the sample rod used for the AC magnetization measurement in PPMS, reprinted from Ref. [30].	171
5.25	(a) Real and (b) imaginary AC susceptibilities versus temperature of CeCrO_3 in different frequencies in 10 Oe AC magnetic field and the zero DC magnetic field.	173

5.26	(a) Real and (b) imaginary AC susceptibilities versus temperature of CeCrO ₃ in different AC magnetic fields under 500 Hz frequency and the zero DC magnetic field.	174
5.27	Real AC susceptibility versus temperature in different frequencies, 10 Oe AC magnetic field and the zero DC magnetic field of the samples (a) Ce ₅₀ Eu ₅₀ CrO ₃ and (b) Ce ₁₀ Eu ₉₀ CrO ₃	174
5.28	(a) Real and (b) imaginary AC susceptibilities versus temperature of EuCrO ₃ in different frequencies in 10 Oe AC magnetic field and the zero DC magnetic field.	176
5.29	$\ln\tau$ versus freezing temperature T_m for (a) CeCrO ₃ and (b) EuCrO ₃ . The figure shows the best fitting data corresponding to the Vogel-Fulcher and power laws.	177
5.30	(a) Real and (b) imaginary AC susceptibilities versus temperature of EuCrO ₃ in different AC magnetic fields, the zero DC magnetic field and the frequency of 500 Hz.	177
5.31	The schematic drawing of thermal connections to the sample and the sample platform in the PPMS heat capacity measurements, reprinted from Ref. [35].	185
5.32	(a) Total heat capacity of CeCrO ₃ which shows λ -like transition at $T = 256$ K and Schottky anomaly at low temperatures (inset), (b) total heat capacity of CeCrO ₃ (blue line) with the heat capacity of LaGaO ₃ (red line) and the magnetic heat capacity of CeCrO ₃ (green line) at the zero magnetic field.	188

5.33	(a) Temperature dependence of the magnetic heat capacity and (b) temperature dependence of the magnetic entropy of CeCrO ₃ at the zero magnetic field.	188
5.34	(a) Schottky heat capacity anomaly of CeCrO ₃ (blue line) with the cubic back ground (green) and fitting with two-level Schottky model at the zero magnetic field, (b) Schottky heat capacity anomaly of CeCrO ₃ with two-level model fitting at H=9 T, (c) the energy splitting versus an applied magnetic field obtained using the two-level Schottky model.	190
5.35	Magnetic field dependence of (a) the magnetic ordering transition temperature and (b) the magnetic entropy in CeCrO ₃	190
5.36	(a) Total heat capacity of EuCrO ₃ (blue line) with the heat capacity of LaGaO ₃ (red line) and the magnetic heat capacity of EuCrO ₃ (green line) at the zero magnetic field, (b) the magnetic entropy of EuCrO ₃	191
5.37	(a) The schematic drawing of the thermal expansion dilatometer cell and (b) the dilatometer cell which was mounted in PPMS probe, reprinted from Ref. [43, 44].	194
5.38	The temperature dependence of (a) the length change ($\frac{\Delta L}{L}$) relative to 300 K and (b) the coefficient of the linear thermal expansion (α) for sample CeCrO ₃ . (α) derived from the length change displayed in (a)	195

5.39	The temperature dependence of (a) the length change ($\frac{\Delta L}{L}$) relative to 300 K and (b) the coefficient of the linear thermal expansion (α) for sample EuCrO_3	196
5.40	Raman spectra of EuCrO_3 at different temperatures. The mode assignment is given above the topmost (300 K) spectrum.	199
5.41	(a) linewidth, (b) Raman shift and (c) the difference $\omega(T) - \omega_{anh}$ of B_{2g} at $\approx 160 \text{ cm}^{-1}$. The red line is the Lorentzian fitting.	200
5.42	Raman shifts of $A_g - B_{1g}$ doublet observed near 380 cm^{-1}	202
5.43	The common Lorentzian linewidth of $A_g - B_{1g}$ doublet observed near 380 cm^{-1}	203
5.44	Temperature dependence of (a) the relative permittivity and (b) the conductance of EuCrO_3 at different frequencies, (c) Arrhenius Plot of the maximum peak versus frequency. The best fit line is shown in red.	205
6.1	Producing neutrons by (a) fission process and (b) spallation reaction, printed from Ref. [5].	214
6.2	National Research Universal (NRU) Reactor (Plan View), printed from Ref. [5].	215
6.3	Incident plane waves are scattered by a nucleus at $r = 0$ and produced circular scattered waves [8].	217

6.4	(a) Incident and scattered beams produce the scattering vector, Q . (b) Incident neutrons along z -direction are scattered into a scattering angle θ with the azimuthal angle ϕ in a solid angle $d\Omega$. dS is an scattering area on a detector [8].	218
6.5	(a) The vanadium cylindrical sample holder and (b) an aluminum flat sample holder.	223
6.6	The schematic diagram of three-axis spectrometer using in the inelastic scattering, reprinted from Ref. [11].	226
6.7	Neutron diffraction patterns of CeCrO_3 with 2.37 \AA wavelength at (a) $T = 3.5 \text{ K}$ and (b) $T = 280 \text{ K}$	229
6.8	(a) Neutron diffraction patterns of CeCrO_3 with $\lambda = 2.37 \text{ \AA}$ at different temperatures and (b) the magnetic phase transition diagram of CeCrO_3	231
6.9	Neutron diffraction patterns of CeCrO_3 with $\lambda = 2.37 \text{ \AA}$ zoomed around (a) $2\theta = 31^\circ$ and (b) $2\theta = 44^\circ$ with high statistics.	232
6.10	Temperature dependence of nuclear lattice parameters of CeCrO_3	233
6.11	Neutron diffraction patterns of $\text{Ce}_{1-x}\text{Eu}_x\text{CrO}_3$ at $T = 3.5 \text{ K}$ (red line) and 280 K (blue line) with $\lambda = 2.37 \text{ \AA}$ where (a) $x = 0.1$, (b) $x = 0.5$ and (c) $x = 0.9$	235
6.12	Temperature dependence of the magnetic peak, indicating the magnetic phase transition temperature of $\text{Ce}_{1-x}\text{Eu}_x\text{CrO}_3$ where (a) $x = 0.1$, (b) $x = 0.5$ and (c) $x = 0.9$	236

6.13	Neutron diffraction patterns of EuCrO_3 with 1.3282 \AA wavelength at (a) $T = 3.5 \text{ K}$ and (b) $T = 280 \text{ K}$	238
6.14	(a) Neutron diffraction patterns of EuCrO_3 with 2.37 \AA wavelength at different temperatures and (b) magnetic phase transition diagram of EuCrO_3	238
6.15	(a) Neutron diffraction patterns of EuCrO_3 at $T = 3 \text{ K}$ (red line) and 290 K (blue line) with $E_f = 30 \text{ meV}$. (Inset is the neutron diffraction pattern with $E_f = 14.5 \text{ meV}$ at 3 K) and (b) neutron diffraction patterns of EuCrO_3 with very high statistics at $T = 3 \text{ K}$ (red line) and 290 K (blue line) with $\lambda = 1.638 \text{ \AA}$ zoomed in expected rare earth magnetic peak region.	239
6.16	Temperature dependence of the nuclear volume cell of EuCrO_3 with 2.37 \AA wavelength. The dash red line is a guide to the eye.	240
6.17	Inelastic neutron scattering of CeCrO_3 at (a) $T = 3 \text{ K}$ (red line) and 290 K (blue line) with $Q = 1 \text{ \AA}^{-1}$, (b) $T = 3 \text{ K}$ with $Q = 1 \text{ \AA}^{-1}$ (red line) and $Q = 1.4 \text{ \AA}^{-1}$ (green line).	241
6.18	Q-E color map of CeCrO_3 at $T = 3 \text{ K}$	243
6.19	(a) Momentum transfer dependence of the magnetic form factor of CeCrO_3 with the energy transfer of 4.57 meV , $E_f = 14.5 \text{ meV}$ (blue line) and $E_f = 30 \text{ meV}$ (green line), (b) T-dependence of the peak at 4.57 meV	243
6.20	Energy scan of CeCrO_3 to the higher energies at $T = 3 \text{ K}$ (red line) and 290 K (blue line) with (a) $Q = 2.8 \text{ \AA}^{-1}$ and (b) $Q = 1.4 \text{ \AA}^{-1}$	245

6.21	(a) Temperature dependence of the magnetic peak intensity of CeCrO_3 with 1.4104 \AA^{-1} . (b) Zoomed in temperature dependence of the magnetic peak around the transition temperature.	245
6.22	Inelastic neutron scattering of $\text{Ce}_{1-x}\text{Eu}_x\text{CrO}_3$ at $T = 3 \text{ K}$ (red line) and $T = 290 \text{ K}$ (blue line) (a) $x = 0.1$, (b) $x = 0.5$, (c) $x = 0.9$ and (d) the magnetic phase transition of $\text{Ce}_{1-x}\text{Eu}_x\text{CrO}_3$	246
6.23	(a) Temperature dependence of the Cr^{3+} magnetic peak with the fixed momentum transfer $Q = 1.4164 \text{ \AA}$ (Inset shows the T-dependence of the Eu^{3+} magnetic peak). (b) Inelastic neutron scattering of EuCrO_3 at $T = 3 \text{ K}$ (blue and red lines) and 290 K (green line) with final energy of $E_f = 30 \text{ meV}$ and 14.5 meV	248
6.24	Néel transition temperature (T_N) versus europium concentration (x) in $\text{Ce}_{1-x}\text{Eu}_x\text{CrO}_3$, obtained from different experiments in this work.	248

List of Tables

2.1	Effective magneton numbers μ_{eff} for transition metal ions [4].	27
2.2	Ionic radius and effective magneton moment of cerium and europium ions [4, 11].	33
3.1	Raw materials properties used in the experiment [4].	56
4.1	Tolerance factor (t) in the different perovskite structures with the examples [3].	69
4.2	Characteristic wavelengths and energies of some common target materials used in the X-ray tubes [9].	73
4.3	Geometric relations for the plane spacing (d), Miller indices (h k l) and the lattice parameters (a, b, c) in the different crystal structures [9].	80
4.4	The lattice parameters (a, b, c) and unit cell volume (V) of CeCrO ₃ at 300 K.	91
4.5	Wyckoff positions of group 62 (<i>Pbnm</i>).	92
4.6	The lattice parameters and unit cell volume of EuCrO ₃ at 300 K.	97

4.7	Structural parameters and conventional reliability indices obtained from the Rietveld refinement of the X-ray diffraction patterns of CeCrO ₃ and EuCrO ₃ with the space group of <i>Pbnm</i> at room temperature. An absorption corrections for the XPD of CeCrO ₃ and EuCrO ₃ were performed assuming $\mu R \sim 0.85$ cm and 1 cm, respectively [24]	99
4.8	The interatomic distances (d), average distances (<d>), distortion parameter (Δ) and angles at 300 K obtained from the Rietveld refinement of the XRD patterns of CeCrO ₃ and EuCrO ₃	101
4.9	Average interatomic distances (<d>) and angles at 300 K of Ce _{1-x} Eu _x CrO ₃ obtained from the Rietveld refinement of the XRD patterns.	102
4.10	Binding energy values (E_B) of the 3d and 4d level peaks in CeCrO ₃ (before Ar ion sputtering) and CeCrO ₃ -as (after Ar ion sputtering).	115
4.11	Binding energy values (E_B) of 3d and 4d level peaks in EuCrO ₃ (before Ar ion sputtering) and EuCrO ₃ - as (after Ar ion sputtering).	122
4.12	Binding energy values (E_B) of Cr (2p) and O (1s) peaks in CeCrO ₃ and EuCrO ₃ (before Ar ion sputtering) and CeCrO ₃ -as and EuCrO ₃ -as (after Ar ion sputtering).	123
4.13	Typical binding energies (E_B) of Eu, Ce, Cr ions in the different compounds, reported in literature.	124
4.14	Atomic% of Ce _{1-x} Eu _x CrO ₃ , obtained from EDX results.	134
5.1	The transition temperatures (T_1 and T_{N2}), the temperature at which χ (ZFC) and χ (FC) cross each other (T_{cross}) and temperature at which χ (FC) is maximum (T_b) in Ce _{1-x} Eu _x CrO ₃	159

- 6.1 Structural parameters and conventional reliability indices obtained from the Rietveld refinement of the neutron diffraction patterns of CeCrO_3 with the space group of $Pbnm$ at $T = 3.5 \text{ K}$ and $T = 280 \text{ K}$. 230
- 6.2 Structural parameters and conventional reliability indices obtained from the Rietveld refinement of the neutron diffraction patterns of EuCrO_3 with the space group of $Pbnm$ at $T = 3.5 \text{ K}$ and $T = 280 \text{ K}$. 237

Chapter 1

Introduction

1.1 Rare Earth Chromites

Perovskite rare earth chromium oxides, with the RCrO_3 chemical formula, where R is a rare earth or yttrium element, have attracted much attention due to their high chemical stability at high temperatures and physical properties, which make them a good candidate in the applications such as catalysts [1], electrolytes, fuel cells [1, 2], spin valves, refractory ceramics [3], thermoelectric materials [4] as well as gas-sensor application [5]. Interest in these compounds was first begun in the 1960s when they were considered as an excellent electrode materials in the magneto-hydrodynamic power generating devices [6].

RCrO_3 compounds with 4 formulas per unit cells have a GdFeO_3 distorted orthorhombic structure with the space group of $Pbnm(62)$ [7, 8, 9, 10]. In the ideal cubic RCrO_3 perovskite, each Cr^{3+} cation is surrounded by 6 oxygen ions and located at the center of the cubic, while R^{3+} ions are placed at the corners. The energy level of 3d orbitals in Cr^{3+} splits into two states (t_{2g} and e_g). According to Hund's rule, these 3 electrons of octahedral CrO_6 are located in the t_{2g} state

with parallel spins. The ideal Cr-O-Cr bond angle is 180° and their magnetic moments should be antiparallel, however, the difference in Cr^{3+} and R^{3+} radius size forms a distortion and thus Cr-O-Cr is tilted from the ideal structure. Varying the rare earth ions with the different radius size and electronic configuration has a significant role in the magnitude of Cr-O-Cr tilting which strongly affects the physical properties of chromites [7, 8].

Most members of the RCrO_3 family have two antiferromagnetic sublattices consisting of Cr^{3+} ($3d^3$, $\mu_{eff} = 3.87 \mu_B$, spin only value) and R^{3+} ($4f^n$) moments [11], while the canting of the Cr^{3+} moments results in a canted antiferromagnetism with a weak ferromagnetism in these compounds [7, 12, 13]. The Cr^{3+} ions usually order at Néel temperatures of 112 - 282 K [7, 8], while the R^{3+} ions order magnetically below a transition temperature much lower than the Néel temperature of Cr^{3+} . Above this transition temperature, R^{3+} ions are paramagnetic, but are partially magnetized by the induced molecular field of Cr^{3+} ions. The net magnetic moment of R^{3+} sublattice is oriented parallel or antiparallel to the Cr^{3+} subsystem, depending on the Cr^{3+} - R^{3+} interaction.

There are four types of magnetic configurations for Cr^{3+} ions in RCrO_3 , according to the Bertaut notation [14]: $\Gamma_1(A_x, G_y, C_z)$, $\Gamma_2(F_x, C_y, G_z)$, $\Gamma_3(C_x, F_y, A_z)$ and $\Gamma_4(G_x, A_y, F_z)$. In his assumption, the magnetic and crystalline unit cells are identical. Figure 1.1(a) shows the spin configurations of ferromagnet (F), G-type antiferromagnet, C-type antiferromagnet and A-type antiferromagnet for a cubic structure. For example, $\Gamma_4(G_x, A_y, F_z)$ show the G-type antiferromagnetic spin arrangement in x direction while the magnetic configuration along y direction

is the A-type antiferromagnet. The ferromagnetic component is oriented in z direction.

In the orthorhombic compounds with non-magnetic R^{3+} , weak ferromagnetism has been reported below the Néel temperature with Γ_4 configuration while it can be converted to Γ_2 or Γ_3 configuration in chromites with the magnetic R^{3+} ion. Γ_1 configuration reported in some members such as ErCrO_3 at low temperatures when no ferromagnetism is observed [15, 16].

Three spin configurations in ErCrO_3 are plotted in Figure 1.1(b) where the blue spins are attributed to the Cr^{3+} spins.

The competition between Cr^{3+} - Cr^{3+} , Cr^{3+} - R^{3+} and R^{3+} - R^{3+} interactions in different temperature regions creates interesting magnetic behaviors such as a reversal of magnetization in some members of this family. This appealing phenomenon has been recently reported in some compounds such as manganites, orthovanadate and orthochromites [17, 18, 19, 20]. A reversal of magnetization at low temperatures in HoCrO_3 [8], CeCrO_3 [11], GdCrO_3 [21] and YbCrO_3 [19] are the examples of this behavior in the orthochromite family, due to the spin reorientation of the R^{3+} ion. This phenomenon can be explained by different factors such as the competition between the Cr^{3+} moment and the R^{3+} moment at different temperatures [8, 18]. In general, the super-exchange interaction of Cr^{3+} - Cr^{3+} is the strongest interaction at high temperatures while R^{3+} magnetization starts ordering at lower temperatures.

Decrease in the ionic radius of R^{3+} cation enhances the distortion, and thus decreases the antiferromagnetic ordering transition of Cr^{3+} monotonically from 282

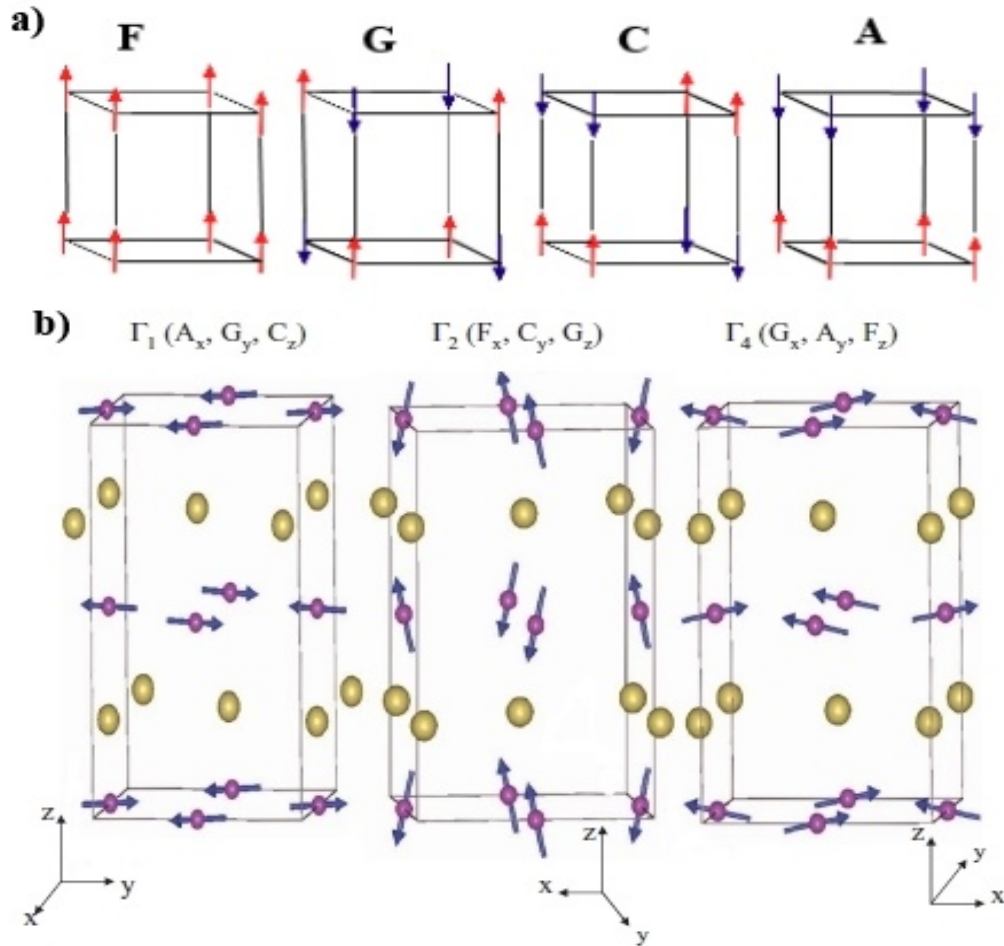


Figure 1.1: (a) Spin configurations in the FM, G-type antiferromagnet, C-type antiferromagnet and A-type antiferromagnet structures. (b) Spin configurations of Cr ions in Γ_1 , Γ_2 and Γ_4 in ErCrO_3 with $Pbnm$ space group. The yellow balls are represented as Er ion without spins, reprinted from Ref. [15].

K in LaCrO_3 to 112 K in LuCrO_3 [2]. Figure 1.2 shows the rare earth ionic radius size dependence of the Néel temperature $T_N(\text{Cr}^{3+})$ in RCrO_3 compounds.

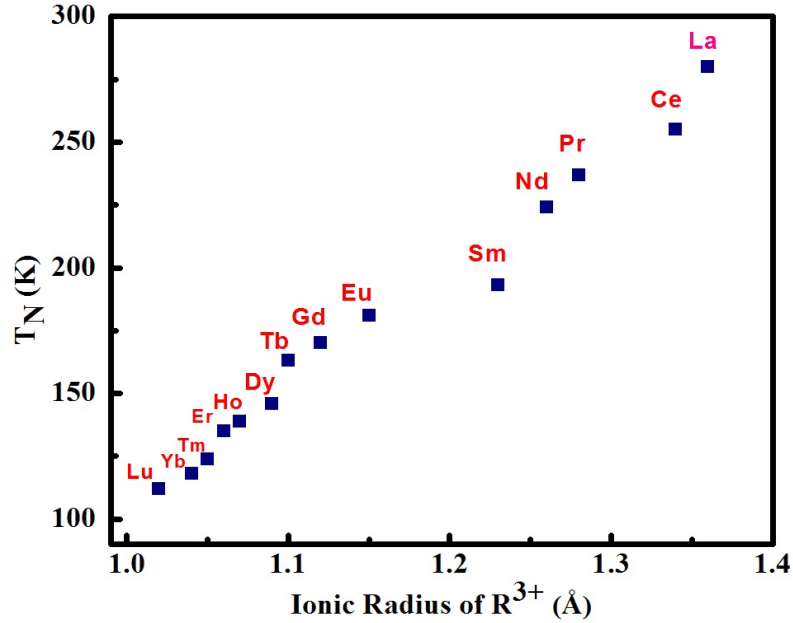


Figure 1.2: Paramagnetic to antiferromagnetic transition temperature (T_N) of rare earth chromites (RCrO_3) versus rare-earth ionic radius, showing the Néel temperature reduction while decreasing in ionic radius [22].

The co-existence of ferroelectricity and ferromagnetism (multi-ferroic) has been recently observed in several chromites [23, 24, 11]. Ferroelectricity can be created in the crystal by a distortion in the structure. This distortion can happen for different reasons. The common distortion in the perovskites comes from the overlapping of the empty d orbital of transition metal ions and p orbital of oxygen atoms. The ferroelectricity can happen due to the existence of lone pair activity. In BiFeO_3 and PbVO_3 compounds, $6s^2$ lone-pair electrons of Bi^{3+} and Pb^{2+} reduces their ideal symmetry. The other example of broken symmetry is rotating of MnO_5 in the hexagonal YMnO_3 . Furthermore, in some materials,

ferroelectricity is induced by the magnetic ordering [25].

Multiferroicity has been detected in BiCrO_3 with the T_E of 440 K and T_N of 114 K, although this compound is not a member of rare earth chromites [26].

RCrO_3 compounds with half filled t_{2g} and empty e_g energy levels, have $Pbnm$ centrosymmetric space group which excludes the required distortion to cause the ferroelectricity. However, it has been reported that these materials can be locally non-centrosymmetric [24]. Not all members of rare earth chromites can be ferroelectric, as LaCrO_3 is paraelectric while LuCrO_3 is ferroelectric [24]. There are different suggestions about the reason of the ferroelectricity, especially in the heavy rare earth chromites. Khomskii proposed that an off-centering distortion may happen by the hybridization of the e_g levels of chromium ions and p orbitals of oxygen ions [27]. Serrao et al. suggested two structural instabilities which cause ferroelectricity in the YCrO_3 crystal: the oxygen octahedra motion and Y^{3+} displacement with respect to the oxygen cage [28] while Ramesha et al. believed in the Cr off-centering [29]. Widatallah et al. reported the stronger distortion of Eu^{3+} ion than that of Cr^{3+} ions in EuCrO_3 which can form ferroelectricity [1].

The interaction of two magnetic ions in the materials with two magnetic sublattices has an influence on their electrical properties. Hornreich suggested that the antisymmetric coupling of Er^{3+} - Cr^{3+} in ErCrO_3 crystal, called Dzyaloshinski - Moria (DM) exchange interaction, causes ferroelectricity, which is the same explanation for GdCrO_3 , HoCrO_3 and YbCrO_3 compounds [19, 30, 31]. This antisymmetric exchange interaction between Cr^{3+} and R^{3+} in RCrO_3 especially in the heavier rare earth compounds can lead to the ferroelectricity and thus they

can be considered biferroic materials [1, 28, 15].

RCrO_3 compounds have shown the ferroelectric transition temperature T_E around 430 - 500 K with electric polarization of 0.2 - 0.8 $\mu\text{C}/\text{cm}^2$, considering them as weak ferroelectric materials while Lal et al reported the maximum polarization of 0.72 $\mu\text{C}/\text{cm}^2$ around 340 K for GdCrO_3 . Their dielectric constants show a large frequency dispersion below T_E and frequency independent above T_E , which is the typical behavior of the relaxor ferroelectric materials. Furthermore, relaxor ferroelectrics show a larger and broader dielectric dispersion with no crystal structure transition while classic ferroelectrics display sharp and narrow peaks at the transition temperature. A decrease in the size of the rare earth element in RCrO_3 compounds enhances the dielectric constant and the ferroelectric transition temperature [4, 6, 15, 24, 28]. Some experimental examples of ferroelectricity reported about YCrO_3 are shown in Figure 1.3.

As far as the electronic properties are concerned, RCrO_3 oxides can be considered as insulators although some of their members such as SmCrO_3 , YCrO_3 , LaCrO_3 and NdCrO_3 have been reported as the p-type semiconductors. The electric conductivity of RCrO_3 oxides can be enhanced by the partial replacement of rare earth ions with an alkaline-earth metals (Mg, Ca, or Sr) [32].

The observation of exchange bias effect in the magnetic measurements is the challenging property of RCrO_3 compounds. The physical origin of the exchange bias phenomenon in the typical ferromagnet-antiferromagnet combination is an anisotropy induced in a ferromagnetic material from an antiferromagnetic material, depending on the strength of the antiferromagnetic anisotropy [33, 35]. The

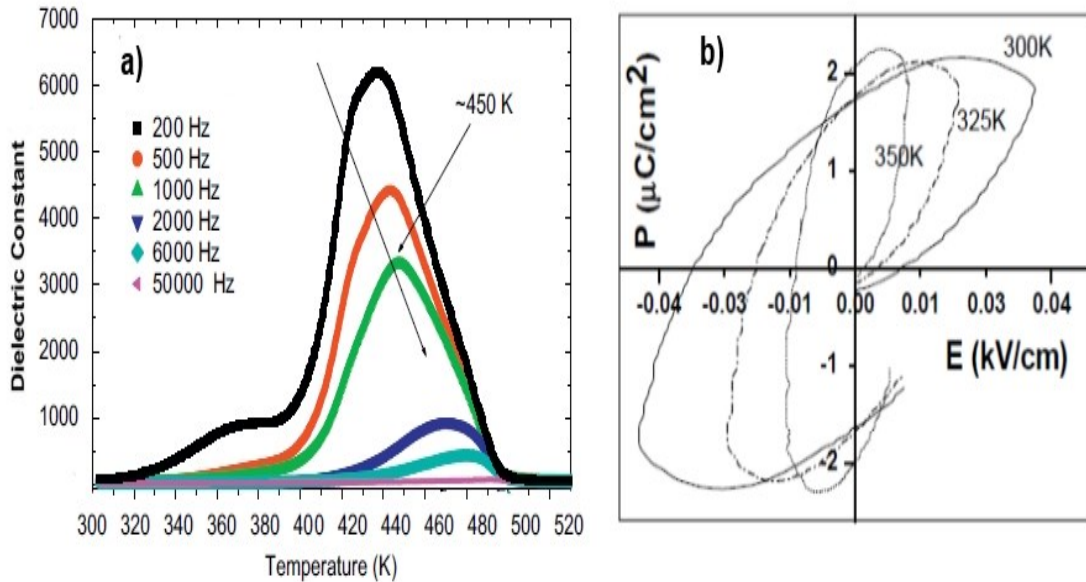


Figure 1.3: (a) Temperature dependence of the dielectric constant in different frequencies, (b) a polarization loop of YCrO_3 , reprinted from Ref. [4, 28].

exchange bias effect has been discovered in antiferromagnet and ferrimagnet oxides, in particular, in the nano-size powders and layers, they can be used in the different magnetic devices including spin-valve devices and magnetic recording materials [33]. The sign reversal of the exchange bias effect has been observed in some materials which can be utilized in thermally assisted magnetic random access memory [34, 21]. Out of the perovskite RCrO_3 family, only $\text{La}_{0.2}\text{Ce}_{0.8}\text{CrO}_3$ [34] and $\text{La}_{1-x}\text{Pr}_x\text{CrO}_3$ [21] have been studied from the point of the exchange bias phenomenon.

1.2 Outline

Among all rare earth chromites, there is some literature describing the physical properties of CeCrO_3 [11, 36] and EuCrO_3 [3, 37, 38], however, further information

about the structure and magnetic properties of these compounds is needed. Furthermore, minimal work has been done on the substitution of these compounds.

As has already been described, CeCrO_3 [11] and EuCrO_3 [37, 38] show magnetic ordering below $T \approx 257$ K and 178 K, respectively. Shukla et al [11] reported the relaxor-like dielectric behavior of CeCrO_3 with an optical band gap around 3.04 eV which makes it a good potential in multifunctional applications. CeCrO_3 has the highest Néel temperature in RCrO_3 after LaCrO_3 which is desirable for applications near room temperature. It was reported that how the physical properties of LaCrO_3 change by Ce^{3+} doping, including an increase in the magnetization as well as a reduction in the Néel temperature and band gap [39]. The reported optical band gap shows that CeCrO_3 is suitable for visible light-driven photocatalyst. Lal et al [6] measured the maximum value of spontaneous polarization ($P_s = 0.42 \text{ } \mu\text{C}/\text{cm}^2$ at $T \approx 375$ K) for EuCrO_3 and claimed the existence of ferroelectricity in this compound although the value of polarization was small compared with the values observed in other perovskite ferroelectrics. Furthermore, the exchange bias effect and the sign reversal of exchange bias make these compounds applicable in different magnetic devices including spin-valve devices, magnetic recording materials and thermally assisted magnetic random access memory. Therefore, all these applications as well as the possibility of the multiferroic properties in these compounds encouraged us to choose them for our investigation.

In this work, we aim to study the CeCrO_3 oxides substituted by the Eu ion through investigating the structural, thermal and magnetic properties. Cerium(III) ion with ionic radius size of 1.34 Å [22] and odd electron configuration ($4f^1$) has

a magnetic ground state, while europium(III) ion with 1.12 Å [22] ionic radius size and even electron configuration ($4f^6$) is a singlet. However, it is worth mentioning that Eu^{3+} ions usually act as a Van Vleck paramagnetic element, due to the small energy spacing between the ground and excited states. Thus, CeCrO_3 and EuCrO_3 will show interesting physical properties especially through doping. Thus far, no research has been reported on the preparation and characterization of $\text{Ce}_{1-x}\text{Eu}_x\text{CrO}_3$ nano-powders.

The conventional method of the rare earth chromite preparation is the solid state reaction which needs a high calcination temperature and sometimes mechanical milling. The desired phase formation happens through the reaction between rare earth oxide and chromium oxide powders. In this study, the orthorhombic $\text{Ce}_{1-x}\text{Eu}_x\text{CrO}_3$ nano-powders were synthesized using the solution combustion method where the desired single phase can be formed at a much lower temperature, compared to the conventional method; furthermore, it is faster and a simpler method. The possibility of the contamination is lower as no milling is needed.

Furthermore, there is little research on neutron scattering measurement of RCrO_3 compounds, especially inelastic neutron scattering [40]. The study of neutron scattering of europium compounds is challenging due to the large neutron absorption cross-section of Eu^{3+} , thus no research has been reported on the neutron scattering analysis of EuCrO_3 nano-powders.

The history and some theoretical parts in magnetism which are used in this thesis have been reported in Chapter 2. The preparation method and the optimum condition to obtain the desired single phase will be discussed in detail in

Chapter 3. Afterwards, we shall carry out the characterization and morphology of the $\text{Ce}_{1-x}\text{Eu}_x\text{CrO}_3$ polycrystallites, using X-ray diffraction, transmission electron microscopy, scanning electron microscopy and X-ray photoemission spectroscopy measurements in Chapter 4. We will discuss in Chapter 5 the magnetic and thermal properties of the $\text{Ce}_{1-x}\text{Eu}_x\text{CrO}_3$ nano-powders by studying the DC/AC magnetic susceptibilities, magnetic hysteresis loops, specific heat measurements, thermal expansion, Raman spectroscopy and dielectric properties in the temperature, magnetic field and frequency variation. In Chapter 6, we discuss the elastic neutron scattering measurements in order to clarify the structural and the magnetic behavior of $\text{Ce}_{1-x}\text{Eu}_x\text{CrO}_3$ compounds, while inelastic neutron scattering will determine the crystal field splitting energy levels. At the end, we present the conclusions of this work in Chapter 7.

Bibliography

- [1] H. M. Widatallah, T. M. Al-Shahumi, Z. Klencsar, M. Pekala, A. M. Gismelseed, I. A. Al-Omari, A. D. Al-Rawas, D. Seifu, J. Acta Mater., 61, 4461-4473, (2013)
- [2] P. S. Devi, J. Mater. Chem. 3(4), 373-379, (1993)
- [3] H. M. Widatallah, S. H. Al-Harhi, C. Johnson, Z. Klencsar, A. M. Gismelseed, E. A. Moore, A. D. Al-Rawas, C. I. Wynter and D. E. Brown, J. Phys. D: Appl. Phys. 44, 265403, (2011)
- [4] A. Duran, A. M. Arevalo-Lopez, E. Castillo-Martinez, M. Garci-Guaderrama, E. Moran, M. P. Cruz, F. Fernandez, M. A. Alario-Franco, J. Solid State Chem., 183, 18631871, (2010)
- [5] M. Siemons, A. Leifert, and U. Simon, Adv. Funct. Mater., 17, 21892197, (2007)
- [6] H. B. Lal, R. D. Dwivedi, K. Gaur, J. Mater. Sci. - Mater. Electron., 1, 204-208, (1990)

-
- [7] A. Jaiswal, R. Das, S. Adyanthaya, P. Poddar, *J. Nanopart. Res.*, 13, 1019-1027, (2011)
- [8] Y. Su, J. Zhang, Z. Feng, Z. Li, Y. Shen, S. Cao, *J. Rare Earths.*, 29, 1060, (2011)
- [9] T. Arakawa, S. Tsuchi-ya, J. Shiokawa, *J. Mater. Res. Bull.*, 16, 97, (1981)
- [10] I. Bhati, P. B. Punjabi, S. C. Ameta, *J. Chem. Chem Eng.*, 29, 195-202, (2010)
- [11] R. Shukla, A. K. Bera, S. M. Yusuf, S. K. Deshpande, A. K. Tyagi, W. Hermes, M. Eul, R. Pottgen, *J. Phys. Chem. C*, 113, 12663-12668, (2009)
- [12] E. I. Golovenchits, V. A. Sanina, T. A. Shaplygina, *Sov. Phys. JETP*, 53(5), (1981)
- [13] E. T. Lacheisserie, D. Gignoux, M. Schlenker, "Magnetism: Materials and Applications", Springer New York, (2005)
- [14] E. F. Bertaut, *Acta Crystallogr, A*, 24(1), 217 -231, (1968)
- [15] B. Rajeswaran, D. I. Khomskii, A. K. Zvezdin, C. N. R. Rao, A. Sundaresan, *Phys. Rev. B.*, 86, 214409, (2012)
- [16] B. Tiwari, M. K. Surendra, M. S. R. Rao, *Mater. Res. Express*, (2014)
- [17] Y. Ma, M. Guilloux-Viry, P. Barahona, O. Pena, C. Moure, *Appl. Phys. Lett.*, 86, (2005)
- [18] F. Bartolom, J. Bartolom, J. Campo, *Physica. B*, 312, 769-771, (2002)

-
- [19] Y. Su, J. Zhang, Z. Feng, L. Li, B. Li, Y. Zhou, Z. Chen, S. Cao, *J. Appl. Phys.*, 108, (2010)
- [20] L. D. Tung, M. R. Lees, G. Balakrishnan, D. M. Paul, *Physica. Rev. B*, 75, (2007)
- [21] K. Yoshii, *Appl. Phys. Lett.*, 99, 142501, (2011)
- [22] R. D. Shannon, *Acta Crystallogr.*, 32, 751, (1976)
- [23] S. Picozzi, C. Ederer, *J. Phys. Condens. Matter.*, 21, 303201, (2009)
- [24] J. R. Sahu, C. R. Serrao, N. Ray, U. V. Waghmare, C. N. R. Rao, *J. Mater. Chem.*, 17, 42-44, (2007)
- [25] D. Khomskii, *J. Phys. 2*, 20, (2009)
- [26] S. Niitaka, M. Azuma, M. Takano, E. Nishibori, M. Takata and M. Sakata, *Solid State Ionics*, 172, 557, (2004)
- [27] D. I. Khomskii, *J. Magn. Magn. Mater.*, 306, 18, (2006)
- [28] C. R. Serrao, A. K. Kundu, S. B. Krupanidhi, U. V. Waghmare, C. N. R. Rao, *Phys. Rev. B*, 72, 220101(R), (2005)
- [29] K. Ramesha, A. Llobet, T. Proffen, C. R. Serrao, C. N. R. Rao, *J. Phys: Condens. Matter*, 19, 102202, (2007)
- [30] R. M. Hornreich, *J. Magn. Magn. Mater.*, 7, 280-285, (1978)

-
- [31] J. Prado-Gonjal, R. Schmidt, D. Avila, U. Amador, E. Moran, *J. Eur. Ceram. Soc.*, 32, 611618, (2012)
- [32] K. Hirota, H. Hatta, M. Io, M. Yoshinaka, O. Yamaguchi, *J. Mater. Sci.*, 38, 34313435, (2003)
- [33] J. Nogués, J. Sort, V. Langlais, V. Skumryev, S. Surinach, J.S. Munoz, M.D. Baro, *Phys. Rep.*, 22, 65117, (2005).
- [34] P. K. Manna, S. M. Yusuf, R. Shukla, A. K. Tyagi, *Appl. Phys. Lett.*, 96, 242508, (2010)
- [35] J. Nogués, I. K. Schuller, *Magn. Magn. Matter.*, 192, 203-232, (1999)
- [36] Y. Cao, S. Cao, W. Ren, Z. Feng, S. Yuan, B. Kang, B. Lu and J. Zhang, *Appl. Phys. Lett.*, 104, 232405, (2014)
- [37] K. Tsushima, I. Takemura, S. Osaka, *Solid State Commun.* 7, 71, (1969)
- [38] J. Prado-Gonjal, R. Schmidt, J. J. Romero, D. Ávila, U. Amador, E. Morán, *Inorg. Chem.* 52 313, (2013)
- [39] R. Shukla, J. Manjanna, A. K. Bera, S. M. Yusuf, S. K. Deshpande. A. K. Tyagi, *J. Inorg. Chem. C*, 48, 11691-11696, (2009)
- [40] N. Shamir, M. Melamud, H. Shaked, S. Shtrikman, *Physica* 90B, 217-222 (1977)

Chapter 2

Magnetism

2.1 Early History of Magnetism

Magnetism was first discovered through the mineral magnetite (Fe_3O_4), when it attracted other iron materials. It was named magnesian stone about 600 B.C., a reference to Magnesia which is today a place in Western Turkey. Later, people found that magnetite can change direction while it is suspended; this observation led to the invention of the first magnetic compass, leading magnetite to become known as lodestone, or “leading stone”. In the 16th century, William Gilbert first proposed that the Earth was actually a giant magnet and all materials had electrical effects, denoting him as the “father of electricity and magnetism”. The discovery of two magnetic poles was made by Petrus Peregrinus de Maricourt about 1269 A.D. and later accomplished by Charles Augustin de Coulomb. In 1819, Hans Christian Oersted demonstrated the strong connection between electricity and magnetism by showing that electric currents generate magnetic fields, an important aspect of electromagnetism.

After this demonstration, different studies in this field occurred, such as

Faraday's law of electromagnetic induction in 1831. His law predicts the interaction between a magnetic field and an electric circuit which produces an electromotive force (EMF).

The materials were classified in two classes, namely diamagnetic and paramagnetic, depending on the direction of magnetic force exerted by the magnetic field. The experiments were done by using magnetic balances invented by Louis George Gouy and Michael Faraday. Diamagnetic materials are expelled by the magnetic field, however, paramagnetic materials are attracted by the magnetic field. Pierre Curie's contribution was in the analysis of magnetic properties of materials, which resulted in Curie's law in 1895. Further, the magnetic concept was extended with the work of Weiss, leading to two other classes of materials; antiferromagnetic and ferromagnetic. These aspects of materials are involved in the Curie-Weiss law which will be discussed in detail in the following sections [1, 2, 3].

2.2 The Magnetic Phenomenon

Magnetism is a physical phenomenon, associated with the interactions between unpaired electron spins in the materials which determine what type of magnetic properties a substance will have. On the atomic scale, the spin angular momentum and the orbital angular momentum are the foundation of intrinsic magnetic moments (μ), which is the elementary quantity in solid-state magnetism. A magnetic moment per unit volume is defined as the magnetization, represented by \mathbf{M} . The response of an isotropic homogeneous material to an applied magnetic field, \mathbf{H} , can be measured quantitatively in terms of the magnetic susceptibility, χ :

$$\chi = \frac{M}{H}, \quad (2.1)$$

χ is a dimensionless quantity in SI and $\frac{emu}{cm^3 Oe}$ in cgs units. The magnetic induction, B , is a response of the material when it is placed in a magnetic field, H . The general relationship between B and H in CGS units is given by:

$$\mathbf{B} = \mathbf{H} + 4\pi\mathbf{M}. \quad (2.2)$$

The effect of the interaction of an external magnetic field on the orbital motion of electrons in an atom is defined as diamagnetism. When a material is exposed to an applied magnetic field, a magnetization in the opposite direction of an applied field is produced, according to Lenz's law. Diamagnetism is a fundamental property of all matter, although it is usually weak. Diamagnetic materials are composed of atoms with completely filled electron shells which have no net magnetic moments. Their response to the magnetic field is negative [4].

On the other hand, materials with unpaired electrons can be classified into four different categories: paramagnetic (PM), ferromagnetic (FM), antiferromagnetic (AFM), and ferrimagnetic (FIM), due to their magnetic moments ordering. The magnetic moment alignments for these four types of magnetic materials are depicted in Figure 2.1.

Paramagnetic materials have a small, positive susceptibility to the magnetic fields. These materials are slightly attracted by a magnetic field, due to the realignment of unpaired electrons. When these materials are removed from the

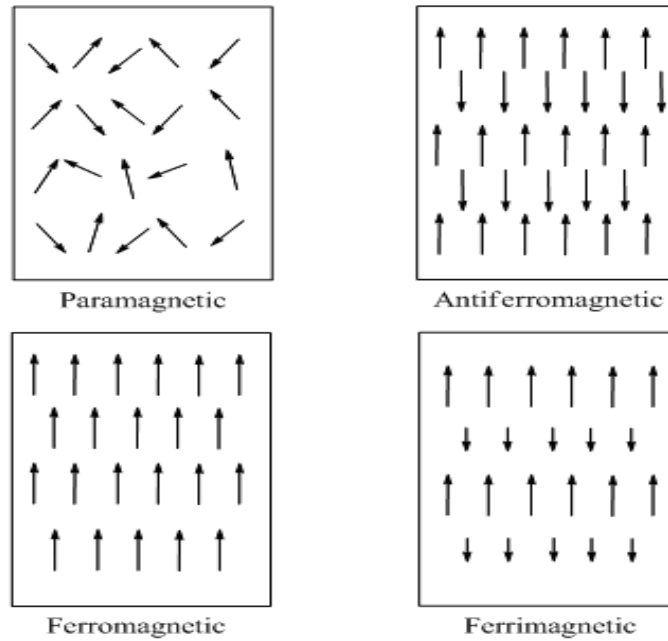


Figure 2.1: Schematic of the magnetic dipole moments ordering in the different types of magnetic materials, reprinted from Ref. [5].

magnetic field, moments return to their random ordering, losing their temporary magnetic properties. In contrast to the paramagnetic materials, the ferromagnetic materials display a strong attraction to the magnetic field and retain their magnetic properties after the external magnetic field is removed. Ferromagnetic materials have parallel alignments of the magnetic moments, leading to a net magnetic moment. However, in an antiferromagnet, the parallel and antiparallel alignments of the magnetic moments are equivalent, leading to a zero net magnetic moment. Ferrimagnetic materials are similar to the antiferromagnetic materials in as far as having an opposite magnetic moment alignment but the net magnetization of ferrimagnets is not zero due to the different magnitudes of the magnetic moments. Total magnetic susceptibility which is measured in the lab consists of the paramagnetic susceptibility (χ_p) and diamagnetic susceptibility (χ_D) [4].

2.2.1 Curie's Law and Curie-Weiss Law

The response of the localized moments of paramagnetic materials to a magnetic field as a function of temperature, is known as Curie's law:

$$\chi_p = \frac{C}{T}, \quad (2.3)$$

where C and T are the Curie constant and the absolute temperature, respectively. Although this theory has foundational merit, it is barely accurate to describe the susceptibility of most materials with the internal interaction between magnetic moments. This interaction is called exchange field or molecular field (H_E) which makes the magnetic moments orient parallel in the ferromagnetic materials.

The magnetic susceptibility of a ferromagnet in the paramagnetic region can be described using the Curie-Weiss law:

$$\chi_p = \frac{\mathbf{M}}{\mathbf{H}_a + \mathbf{H}_E} = \frac{C}{T - \theta_c}, \quad (2.4)$$

where \mathbf{H}_a is the applied magnetic field and \mathbf{H}_E and θ_c are given by:

$$\mathbf{H}_E = \lambda \mathbf{M}; \quad (2.5a)$$

$$\theta_c = C\lambda, \quad (2.5b)$$

λ is the Weiss molecular field constant and θ_c is the Curie-Weiss temperature. Figure 2.2(a) shows the temperature variation of inverse magnetic susceptibility (χ^{-1}) for para, ferro, and antiferromagnetic materials. It is linear for a paramagnetic,

which passes through the origin (Curie behavior) or intercept the temperature axis at $T = \theta_c$ (Curie-Weiss behavior). When the alignment of spins are parallel, χ is increased, that is, $\theta_c > 0$ and when spins align antiparallel, χ is decreased, that is, $\theta_c < 0$. The transition from paramagnetic to ferromagnet occurs at the “Curie temperature”, T_c . The transition between paramagnet to antiferromagnet appears at the Néel temperature (T_N) [4]. Figure 2.2(b) represents the magnetic field variation of magnetization in dia-, para- and ferromagnetic materials which is linear for dia- and paramagnetism.

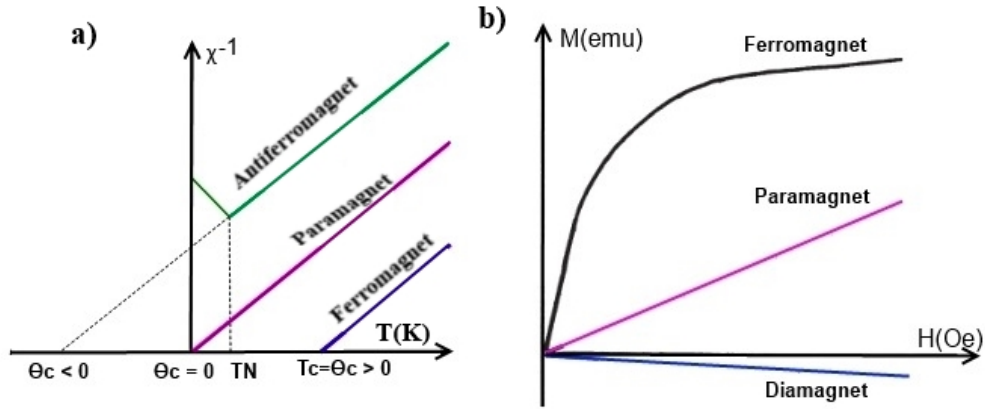


Figure 2.2: (a) Temperature dependence of inverse susceptibility for paramagnets ($\theta_c = 0$), ferromagnets ($T_c = \theta_c > 0$), and antiferromagnets ($\theta_c < 0$). (b) Magnetization versus magnetic field for ferro-, para- and diamagnetic materials, reprinted from Ref. [5].

The magnetic moment of an atom in the free space is calculated by:

$$\boldsymbol{\mu} = -g\mu_B\mathbf{J}, \quad (2.6)$$

where $\mathbf{J} = \mathbf{S} + \mathbf{L}$ is the total angular momentum. $\mu_B = 9.27 \times 10^{-21} \text{ erg/G}$ is the Bohr magneton constant. The quantity g in electronic systems, called g -factor

or the spectroscopic splitting factor, is given by:

$$g = 1 + \frac{J(J+1) + S(S+1) - L(L+1)}{2J(J+1)}, \quad (2.7)$$

where S and L are spin and orbital angular momentum quantum numbers, respectively. For an electron spin, $g = 2.0023$, usually chosen as 2.00. When the external magnetic field H is applied to the magnetic dipole moments, the atomic energy levels will be split, which means that the interaction energy of the magnetic moments with an applied field is quantized. This energy splitting of an atom in an applied magnetic field H is known as the “Zeeman effect” and is defined by:

$$U = -\boldsymbol{\mu} \cdot \mathbf{H} = m_j g \mu_B H, \quad (2.8)$$

where $m_j = J, J-1, \dots, -J$ is the azimuthal quantum number. The single dipole partition function $Q_1(\beta)$ with $\beta = \frac{1}{k_B T}$ is given by:

$$Q_1(\beta) = \sum_j e^{\beta U_j} = \sum_{m_j=-J}^J e^{\beta m_j g \mu_B H}. \quad (2.9)$$

By introducing $x = \beta g \mu_B J H$, the Equation (2.9) becomes:

$$\begin{aligned} Q_1(\beta) &= \sum_{m_j=-J}^J e^{\frac{m_j x}{J}} = \frac{e^{(2J+1)x/2J} - e^{-(2J+1)x/2J}}{e^{x/2J} - e^{-x/2J}} \\ &= \frac{\sinh\{(1 + \frac{1}{2J})x\}}{\sinh\{(\frac{1}{2J})x\}}. \end{aligned} \quad (2.10)$$

The magnetic moment in the direction of the magnetic field is then obtained by:

$$\begin{aligned}
 \mathbf{M} &= \frac{N}{\beta} \frac{\partial}{\partial H} \ln Q_1(\beta) \\
 &= N(g\mu_B J) \left[\left(1 + \frac{1}{2J}\right) \coth\left\{\left(1 + \frac{1}{2J}\right)x\right\} - \frac{1}{2J} \coth\left\{\frac{1}{2J}x\right\} \right] \\
 &= N(g\mu_B J) B_J(x), \tag{2.11}
 \end{aligned}$$

where $B_J(x)$ is the Brillouin function and N is the total number of atoms. For high fields and low temperatures ($x \gg 1$), the Brillouin function goes to 1 and thus magnetization reaches its magnetic saturation state. For high temperatures, $x = \frac{g\mu_B JH}{k_B T} \ll 1$, and using the expansion of $\coth x = \frac{1}{x} + \frac{x}{3} - \frac{x^3}{45} + \dots$, magnetic susceptibility can be written as:

$$\chi = \frac{NJ(J+1)g^2\mu_B^2}{3k_B T} = \frac{N\mu_{eff}^2\mu_B^2}{3k_B T} = \frac{C}{T}, \tag{2.12}$$

while $\mu_{eff} = g\sqrt{J(J+1)}$ is named the effective number of Bohr magneton [6].

2.2.2 Magnetic Hysteresis Loop

When a ferromagnet is placed in the magnetic field, its magnetic moments will align themselves with respect to the magnetic field and it will not be demagnetized completely if the field is removed. By applying a magnetic field in the opposite direction or applying heat, it may be demagnetized. A loop is generated by measuring the magnetization of a ferromagnetic material while the magnetic field is

changed. The lack of retraceability of the magnetization curve is a specific property in the ferromagnetic materials called hysteresis which is related to the existence of magnetic domains in these materials. It takes some energy to turn back the magnetic moments in the domains. This is the effect that makes ferromagnetic materials useful as a magnetic memory. The magnitude of the magnetization at zero magnetic field is called the remanent magnetization, M_r , and the strength of the magnetic field while magnetization disappears, is named the coercivity, H_c (Figure 2.3).

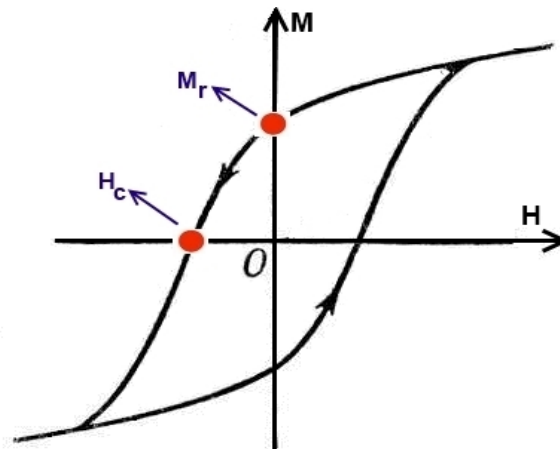


Figure 2.3: Magnetic hysteresis loop of a ferromagnet, where M_r and H_c are the remanent magnetization and the coercivity field, respectively.

2.2.3 Pauli Exclusion Principle

There are four quantum numbers to completely describe electrons in the atom, which are as follows:

- The principal quantum number ($n = 1, 2, \dots$) to describe the electron shell, or energy level of an atom.

- The azimuthal quantum number ($l = 0, 1, \dots, n-1$) (known as orbital quantum number) to describe the subshells called orbitals.
- The magnetic quantum number ($m_l = -l, \dots, l$) to describe the specific orbital within that subshell.
- The spin projection quantum number ($m_s = -s, \dots, s$, where s is the spin quantum number) to describe the spin of the electron within that orbital.

Due to the Pauli exclusion principle, two electrons cannot share the same set of quantum numbers within the same system simultaneously; for two electrons in an orbital with the same quantum numbers n, l and m_l , the spin quantum number m_s must be different, thus in that situation, the electrons have opposite spins and order antiparallel [7].

2.2.4 Hund's Rules

In atomic physics, we know that electrons will fill the lowest energy orbitals first, and then move up to higher energy orbitals. However, there are a set of rules governing the occupancy of energy level of each orbital known as Hund's rules [4]:

- For a given electron configuration, the electrons maximize their total spin "S", within the limits set by the Pauli exclusion principle.
- The electron configuration for the lowest energy with a given spin arrangement results in the largest value of the total orbital angular momentum "L".

- For incompletely filled shells, the total angular momentum J is given by:

$J = L-S$ for a shell less than half occupied

$J = L+S$ for a shell more than half occupied

2.2.5 Orbital Angular Momentum Quenching

In 3d transition metals, no outer electrons exist to shield the electrons in 3d shells as the outermost orbital and the 3d wave function are spatially more extended compared to 4f electron wave functions. Thus, the effect of the inhomogeneous crystal electric field (CEF), produced by neighboring ions in the crystal, on 3d shell is much stronger than the spin-orbit coupling. The CEF acts on orbitals with the total orbital angular momentum L and lifts $2L+1$ degeneracy of the orbital angular momentums, therefore, the energy splitting will happen. In these elements, orbital moments have been quenched and the magnetism can be attributed to the electron spin alone [4]. Table 2.1 shows the experimental and the theoretical magneton numbers for transition metal ions which proves the good agreement of the orbital quenching in this group.

Energy Level Splitting in an Octahedral Field

In d band, there are five d orbitals, referred to as d_{xy} , d_{xz} , d_{yz} , d_{z^2} and $d_{x^2-y^2}$. An octahedral structure where a transition metal cation is at the center and where it is surrounded by six anions, the crystal field produced by these anions, creates the orbital splitting of the d bands. The $3d_{xy}$, $3d_{xz}$, $3d_{yz}$ orbitals (t_{2g} states) lie between the anions and experience less of Coulomb repulsion, thus their energy is

Table 2.1: Effective magneton numbers μ_{eff} for transition metal ions [4].

Ion	Configuration	Basic Level	$\mu_{eff} = g\sqrt{J(J+1)}$	$\mu_{eff} = g\sqrt{S(S+1)}$	$\mu_{eff}(exp)$
Ti^{3+}, V^{4+}	$3d^1$	${}^2D_{3/2}$	1.55	1.73	1.8
V^{3+}	$3d^2$	3F_2	1.63	2.58	2.8
Cr^{3+}, V^{2+}	$3d^3$	${}^4F_{3/2}$	0.77	3.87	3.8
Mn^{3+}, Cr^{2+}	$3d^4$	5D_0	0	4.90	4.9
Fe^{3+}, Mn^{2+}	$3d^5$	${}^6D_{5/2}$	5.92	5.92	5.9
Fe^{2+}	$3d^6$	5D_4	6.70	4.90	5.4
Co^{2+}	$3d^7$	${}^4D_{9/2}$	6.63	3.87	4.8
Ni^{2+}	$3d^8$	3F_4	5.59	2.83	3.2
Cu^{2+}	$3d^9$	${}^2D_{5/2}$	3.55	1.73	1.9

lowered; however, the Coulomb repulsion between charges on anions and electrons in $3d_{z^2}$ and $d_{x^2-y^2}$ orbitals (e_g states) increases the energy of those orbitals [8]. The splitting energy between t_{2g} and e_g states is shown by Δ_0 , observed in Figure 2.4.

Chromium is the 6th most abundant transition metal with the ground state electronic configuration of $[Ar] 4s^1 3d^5$. It exhibits +2 to +6 oxidation states while most stable oxidation states are +2 (CrO), +3 (Cr₂O₃) and +6 (K₂Cr₂O₇) [10]. By losing one electron of 4s and two electrons of 3d, the Cr(III) ion with the $3d^3$ electron configuration and 0.62 Å ionic radius [11] is formed. Cr³⁺ ions in RCrO₃ are surrounded by 6 oxygen ions and create the CrO₆ octahedral. According to the Hund's rule, these three electrons are located in the t_{2g} state with parallel spins and the configuration is t_{2g}^3 . The energy of these three states is equivalent. If one

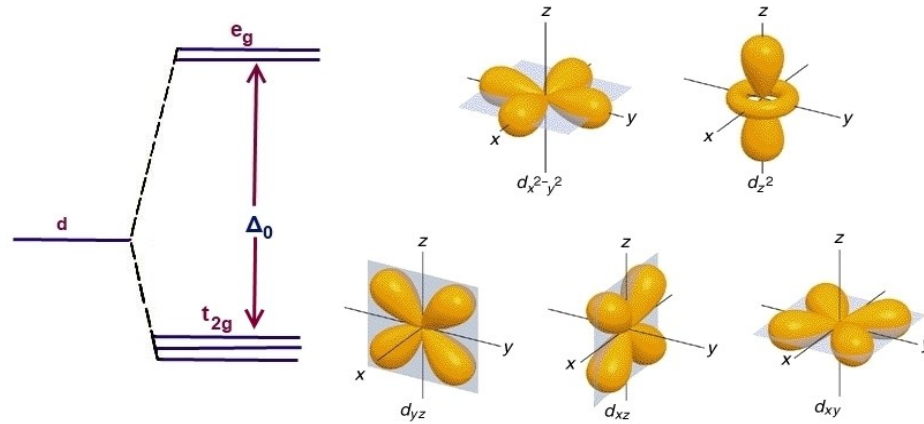


Figure 2.4: Representation of the electron energy levels of the octahedral d shell splitting, where Δ_0 is the value of the energy level splitting, reprinted from Ref. [9].

electron is excited, the configuration will be $t_{2g}^2 e_g^1$.

2.2.6 Spin-Orbit Coupling

The interaction of a particle's spin with its orbital motion is known as the spin-orbit coupling which caused a shift in an electron's atomic energy levels. The Hamiltonian of the interaction (H_{SO}) between an electron's magnetic moment ($\boldsymbol{\mu}_s$) and the magnetic field produced by rotating an electron in its orbit around the nucleus (\mathbf{H}_L) is defined by:

$$H_{SO} = -\boldsymbol{\mu}_s \cdot \mathbf{H}_L. \quad (2.13)$$

In the reference frame of the electron, the proton is rotating around an electron in the orbit with the radius r . This orbital motion can be considered to be a continuous current loop $I = \frac{e}{T}$, which generates a magnetic field H , given by the Biot-Savart law:

$$\mathbf{H} = \frac{\mu_0 I}{2r} \hat{\mathbf{z}}; \quad (2.14a)$$

$$L = rmv = \frac{2\pi mr^2}{T}, \quad (2.14b)$$

where L , m , e , T and v are the orbital angular momentum, electron mass, electron charge, the period of the orbit and the velocity of the electron rotation, respectively.

Thus, the magnetic field which an electron experiences can be written as:

$$\mathbf{H} = \frac{\mu_0}{4\pi\epsilon_0} \frac{e}{mc^2 r^3} \mathbf{L}. \quad (2.15)$$

where $c^2 = \frac{1}{\epsilon_0\mu_0}$. The magnetic moment of an electron spin is $\boldsymbol{\mu}_s = -\frac{g_s\mu_B}{\hbar}\mathbf{S}$, where \mathbf{S} is the spin angular momentum vector. $\mu_B = \frac{e\hbar}{2m_e c}$ and $g_s = 2$ are the Bohr magneton and electron spin g-factor. By adding a factor $\frac{1}{2}$, known as the Thomas precession, the spin-orbit interaction of the atom with Z electrons is given by:

$$H_{SO} = \left(\frac{Ze^2}{8\pi\epsilon_0}\right) \frac{1}{m^2 c^2 r^3} \mathbf{L} \cdot \mathbf{S}, \quad (2.16)$$

where $\mathbf{L} \cdot \mathbf{S}$ can be written as $\frac{1}{2}(\mathbf{J}^2 - \mathbf{L}^2 - \mathbf{S}^2)$. The Equation (2.16) indicates that the strength of the spin-orbit coupling increases with the atomic number [7].

2.2.7 Rare Earth Elements

The rare earth ions are usually paramagnetic and since they follow the Curie-Weiss law, their susceptibility increases by lowering the temperature. Rare earth ions with 4f electrons and (+3) valence are situated well into the interior of

the atom and surrounded by 5s, 5p, 5d electrons, thus the effect of the crystal field on them is negligible. On the other hand, the 4f electrons are close to the nucleus and the spin-orbit coupling becomes strong. However, the crystalline electric fields influence the ionic behavior at low temperatures, especially in the rare earth ions with odd number of the electrons, named Kramer ions [4].

Cerium with electron configuration of [Xe] 4f¹ 5d¹ 6s² is the most abundant of the rare earth elements and the second member in the lanthanide series. It exhibits three oxidation states, +2, +3 and +4 although the +2 state is rare. The most common compounds of cerium is cerium(IV) oxide (CeO₂) and cerium(III) oxide (Ce₂O₃) [12]. Cerium(III) ion with 4f¹ electron configuration has the total angular momentum of $J = L - S = \frac{1}{2} + 3 = \frac{5}{2}$. This ion with an odd number of the electrons follows the Kramer's theorem, i.e. an ion has at least one degenerate energy level. The ground state of Ce³⁺ is ²F_{5/2} while the magnetic field can split the ground state into three doublets with $m_J = \pm\frac{1}{2}, \pm\frac{3}{2}, \pm\frac{5}{2}$ [13].

Van Vleck Susceptibility

A quantum mechanical calculation done by John Hasbrouck Van Vleck [15] shows that a temperature independent term must be added to the Equation 2.12. Thus, the expression for the Van Vleck paramagnetic susceptibility can be written as:

$$\chi_{VV} = \mu_0 \frac{N_A \mu_B^2}{3k_B T} \frac{\sum_{J=|L-S|}^{J=L+S} (2J+1) F_J e^{\left[\frac{-\lambda_{LS}}{2} \frac{J(J+1)}{k_B T}\right]}}{\sum_{J=|L-S|}^{J=L+S} (2J+1) e^{\left[\frac{-\lambda_{LS}}{2} \frac{J(J+1)}{k_B T}\right]}}, \quad (2.17)$$

where $F_J = g_J^2 J(J+1) + 2(g_J - 1)(g_J - 2) \frac{k_B T}{\lambda_{LS}}$ and $\lambda_{LS} = \pm \frac{\zeta}{2S}$ (the energy level difference). ζ is the spin-orbit coupling parameter and the g_J values are calculated by Equation (2.7). λ_{LS} is positive for the ions with less than half subshell.

For most of the rare earth ions, the multiplet widths are much larger than the thermal energy ($E_J - E_{J-1} \gg k_B T$), thus all atoms will be in their ground states. On the other hand, when the energy interval between the ground state and the excited states is of the same order of $k_B T$, not all atoms will be in the ground states and the excited energy levels will contribute to the susceptibility. Sm^{3+} and Eu^{3+} are examples of these systems.

Europium is the most reactive rare earth element with the atomic number of 63 and the electron configuration of $4f^7 6s^2$. It usually assumes the oxidation state of +3 although the oxidation state of +2 is also common [15]. The trivalent Eu ion with $4f^6$ electron configuration has seven singlet energy levels of ${}^7F_0, {}^7F_1, {}^7F_2, {}^7F_3, {}^7F_4, {}^7F_5, {}^7F_6$. Total quantum number of Eu^{3+} is zero ($J = |L - S| = 3 - 3 = 0$); thus, the ground state of 7F_0 is non-magnetic and Curie-Weiss susceptibility of Eu^{3+} is zero. The energy interval between the ground state and the first excited state in Eu^{3+} is not large compared to $k_B T$ and thus the overlapping of 7F_0 and 7F_1 energy states cause the nonzero effective magnetic moment. The susceptibility of this ion follows the Van Vleck paramagnetic susceptibility which is not zero in the vicinity of $T = 0$ and almost temperature independent below $T \approx 100$ K [19, 20].

The susceptibility for Eu^{3+} according to the Equation (2.17) has been calculated by Lueken [18]:

$$\chi_{VV} = \mu_0 \frac{N_A \mu_B^2}{3k_B T} \mu_{eff}^2 \quad (2.18a)$$

$$\begin{aligned} \mu_{eff}^2 = Z^{-1} & \left[144 \frac{k_B T}{\zeta} + \left(\frac{27}{2} - 9 \frac{k_B}{\zeta} \right) e^{\left(-\frac{\zeta}{6k_B T} \right)} + \left(\frac{135}{2} - 15 \frac{k_B}{\zeta} \right) e^{\left(-\frac{\zeta}{2k_B T} \right)} + \right. \\ & \left. \left(189 - 21 \frac{k_B T}{\zeta} \right) e^{\left(-\frac{\zeta}{k_B T} \right)} + \left(405 - 27 \frac{k_B T}{\zeta} \right) e^{\left(-\frac{5\zeta}{3k_B T} \right)} + \right. \\ & \left. \left(\frac{1485}{2} - 33 \frac{k_B T}{\zeta} \right) e^{\left(-\frac{5\zeta}{2k_B T} \right)} + \left(\frac{2457}{2} - 39 \frac{k_B T}{\zeta} \right) e^{\left(-\frac{7\zeta}{2k_B T} \right)} \right] \quad (2.18b) \end{aligned}$$

$$\begin{aligned} Z = & \left[1 + 3e^{-\frac{\zeta}{6k_B T}} + 5e^{-\frac{\zeta}{2k_B T}} + 7e^{-\frac{\zeta}{k_B T}} + 9e^{-\frac{5\zeta}{3k_B T}} + \right. \\ & \left. 11e^{-\frac{5\zeta}{2k_B T}} + 13e^{-\frac{7\zeta}{2k_B T}} \right], \quad (2.18c) \end{aligned}$$

where $g_J = \frac{3}{2}$ for the multiplets $J = 1, 2, 3, 4, 5, 6$ and $g_J = L+2 = 5$ for $J = 0$.

The spin-orbit coupling parameter ζ of Eu^{3+} is 1326 cm^{-1} .

Figure 2.5(a) represents the energy states of the lowest multiplet in Eu^{3+} ion which is caused by the spin-orbit splitting in the absence of an external magnetic field while Figure 2.5(b) shows the temperature dependence of the magnetic susceptibility of Eu^{3+} ion. Inset is the magnetic moment of free Eu^{3+} ion versus temperature.

Table 2.2 shows the theoretical and the experimental effective magneton moment as well as the ionic radius of cerium and europium ions.

2.2.8 Exchange Interaction

The total wave function for two electrons, which are identical fermions, is anti-symmetric. All particles with a half-integer spin are fermions. The wave function of one electron can be written as a product of a spatial wave function

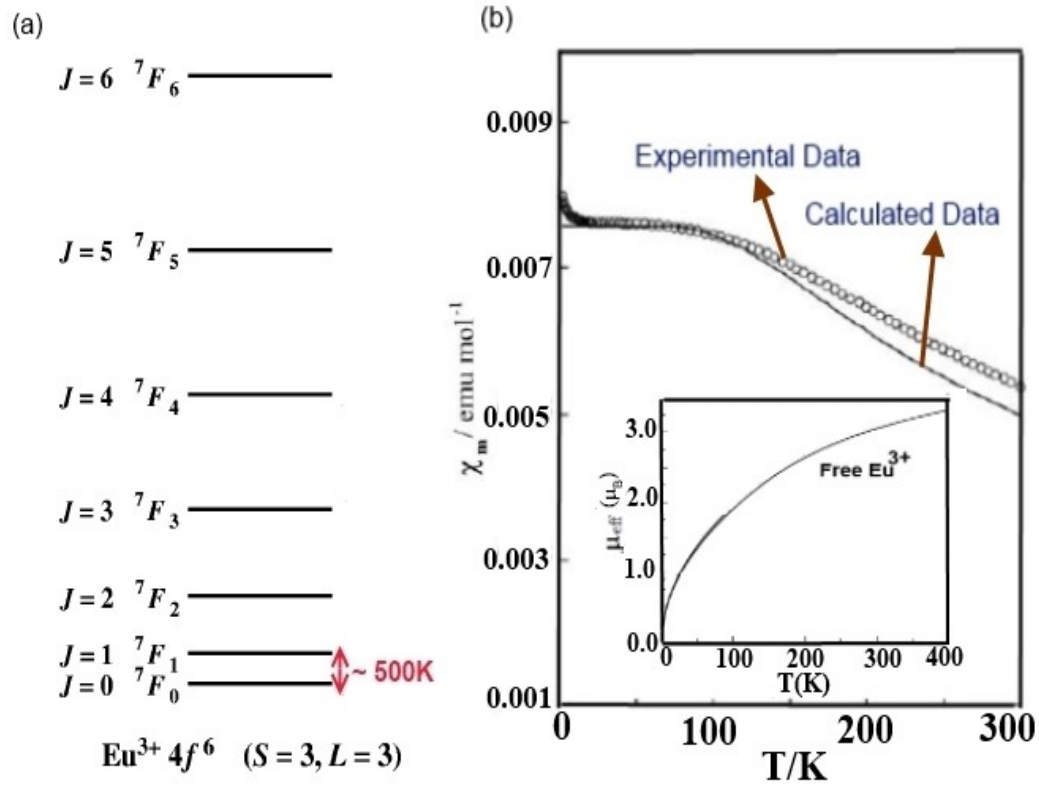


Figure 2.5: (a) The energy levels of Eu^{3+} ion in the absence of an external magnetic field, (b) The observed and calculated magnetic susceptibility of Eu^{3+} in EuCoO_3 compound [19]. Inset shows the effective magnetic moment of free Eu^{3+} ion, reprinted from Ref. [18].

Table 2.2: Ionic radius and effective magneton moment of cerium and europium ions [4, 11].

Ion	Configuration	Basic Level	ionic radius(\AA)	$\mu_{\text{eff}} = g\sqrt{J(J+1)}$	$\mu_{\text{eff}}(\text{exp})$
Ce^{3+}	$5s^2p^64f^1$	${}^2F_{5/2}$	1.20	2.54	2.4
Eu^{3+}	$5s^2p^64f^6$	7F_0	0.940	0	3.5

ψ and a spin-dependent function χ . In order to keep the total wave function of the two-electron system antisymmetric, either the spatial or the spin part must be antisymmetric and the other will be symmetric:

$$\Psi_A(1, 2) = \begin{cases} \psi_S(\mathbf{r}_1, \mathbf{r}_2) \cdot \chi_A(1, 2); \\ \psi_A(\mathbf{r}_1, \mathbf{r}_2) \cdot \chi_S(1, 2), \end{cases}$$

where,

$$\psi_S(\mathbf{r}_1, \mathbf{r}_2) = \frac{1}{\sqrt{2}}[\psi_a(\mathbf{r}_1)\psi_b(\mathbf{r}_2) + \psi_b(\mathbf{r}_1)\psi_a(\mathbf{r}_2)]; \quad (2.19a)$$

$$\psi_A(\mathbf{r}_1, \mathbf{r}_2) = \frac{1}{\sqrt{2}}[\psi_a(\mathbf{r}_1)\psi_b(\mathbf{r}_2) - \psi_b(\mathbf{r}_1)\psi_a(\mathbf{r}_2)];$$

$$\chi_S = \left. \begin{cases} |1, 1\rangle = \uparrow\uparrow & \text{while } m_s = +1 \\ |1, 0\rangle = \frac{1}{2}(\uparrow\downarrow + \downarrow\uparrow) & \text{while } m_s = 0 \\ |1, -1\rangle = \downarrow\downarrow & \text{while } m_s = -1 \end{cases} \right\} \quad S=1, \text{ Triplet State}; \quad (2.19b)$$

$$\chi_A = |0, 0\rangle = \frac{1}{2}(\uparrow\downarrow - \downarrow\uparrow) \quad \text{while } m_s = 0, \quad S = 0, \text{ Singlet State.}$$

A simple example is a molecule with two electrons (a hydrogen molecule) where the electrons behave independently. Assume that $\psi_a(r_1)$ is the spatial wave functions of the first electron and $\psi_b(r_2)$ is the spatial wave function of the second electron. Hamiltonian is given by:

$$H = -\frac{\hbar^2}{2m}(\nabla_1^2 + \nabla_2^2) - \frac{e^2}{r_1} - \frac{e^2}{r_2} + \left(\frac{e^2}{R_{ab}} + \frac{e^2}{r_{12}} - \frac{e^2}{r_{a1}} - \frac{e^2}{r_{b2}}\right), \quad (2.20)$$

where r_{a1} , r_{b2} , R_{ab} and r_{12} are electron-proton distance in first molecule, electron-proton distance in second molecule, proton-proton distance and electron-electron distance, respectively. Two energy eigenvalues are obtained by:

$$E_{\pm} = E_0 + \frac{C \pm J_{ex}}{1 \pm B^2}, \quad (2.21)$$

where E_+ , E_- and E_0 are the spatially symmetric solution, the spatially antisymmetric solution and the energy solution from the first three terms in Equation (2.20), respectively. The Coulomb integral (C), the overlap integral (B) and the exchange integral (J_{ex}) are given by [21]:

$$C = \int \psi_a(\mathbf{r}_1)^2 \left(\frac{1}{R_{ab}} + \frac{1}{r_{12}} - \frac{1}{r_{a1}} - \frac{1}{r_{b2}} \right) \psi_b(\mathbf{r}_2)^2 d^3 r_1 d^3 r_2; \quad (2.22a)$$

$$B = \int \psi_b(\mathbf{r}_2) \psi_a(\mathbf{r}_2) d^3 r_2; \quad (2.22b)$$

$$J_{ex} = \int \psi_a(\mathbf{r}_1) \psi_b(\mathbf{r}_2) \left(\frac{1}{R_{ab}} + \frac{1}{r_{12}} - \frac{1}{r_{a1}} - \frac{1}{r_{b2}} \right) \psi_b(\mathbf{r}_1) \psi_a(\mathbf{r}_2) d^3 r_1 d^3 r_2. \quad (2.22c)$$

It is worth noting that above equations exclude the spin contribution. By considering two electron spins, S_1 and S_2 , the exchange interaction of two spins (called Heisenberg exchange) is defined:

$$H_{Heis} = -2J_{12}\mathbf{S}_1 \cdot \mathbf{S}_2, \quad (2.23)$$

where $J_{12} = \frac{1}{2}(E_+ - E_-)$ is the exchange constant.

$$\mathbf{S}_1 \cdot \mathbf{S}_2 = \frac{1}{2}[(S_1 + S_2)^2 - S_1^2 - S_2^2] = \frac{1}{2}[S_{tot}(S_{tot} + 1) - S_1(S_1 + 1) - S_2(S_2 + 1)].$$

For spin single state ($S_{tot}=0$), thus $\mathbf{S}_1 \cdot \mathbf{S}_2 = \frac{\hbar^2}{2}[0 - \frac{3}{2}] = -\frac{3}{4}\hbar^2$.

For spin triplet state ($S_{tot}=1$), thus $\mathbf{S}_1 \cdot \mathbf{S}_2 = \frac{\hbar^2}{2}[2 - \frac{3}{2}] = \frac{1}{4}\hbar^2$.

The Heisenberg Hamiltonian in the crystal for all ij pairs is given by:

$$H_{Heis} = \frac{1}{2}(-2 \sum_{ij} J_{ij} S_i S_j). \quad (2.24)$$

The exchange interaction between the neighboring magnetic ions forces each moment to order parallel (ferromagnetic) or antiparallel (antiferromagnetic) with their neighbors. There are different types of exchange interactions which include direct exchange, indirect exchange, super-exchange and double exchange, which are shown in Figure 2.6.

Direct Exchange Interaction

A direct exchange is the direct interaction between the magnetic moments, which are close enough to overlap their wavefunctions. It gives a strong but short range coupling which decreases rapidly as the ions are separated. When atoms are very close and the overlapping is strong, spins align in the opposite directions (antiferromagnetism) explained by the Pauli's exclusion principle, however, they will be parallel (ferromagnetism) when the atoms are far enough to minimize the electron-electron repulsion.

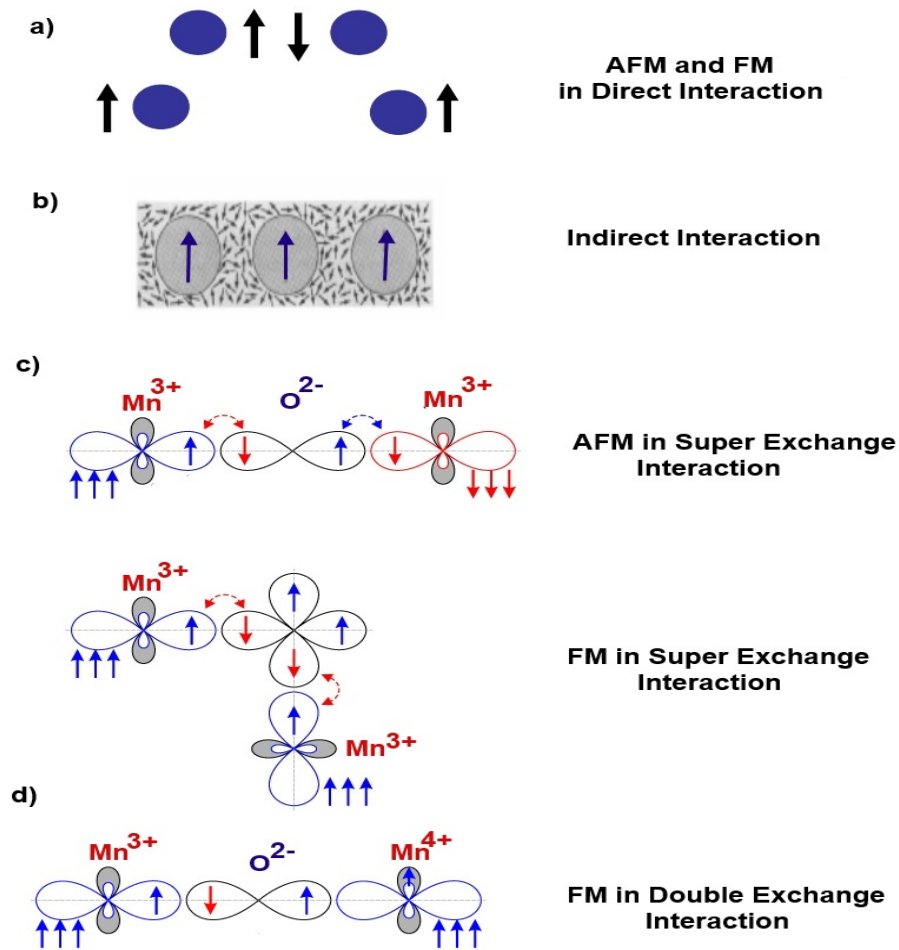


Figure 2.6: Schematic exchange interactions of (a) antiferromagnet and ferromagnetic ordering in direct interaction, (b) the indirect interactions through conduction electrons, (c) antiferromagnetism and ferromagnetism orientation in super-exchange interactions, depending on the bonding angle, (d) ferromagnetic ordering in double exchange interactions, Reprinted from Ref. [22].

Indirect Exchange Interaction

An indirect exchange is the coupling between the magnetic moments over relatively large distances through the conduction electrons. It is the dominant exchange interaction in the metals, where the direct overlapping between neighboring electrons is very small. The magnetic coupling in the indirect interaction can be ferromagnetic or antiferromagnetic, depending on the separation between a pair of ions. For example, magnetic electrons in the 4f shells in the rare earth metals are covered by the 5s and 5p electrons; thus, the overlapping the wave functions of the localized 4f electrons in the rare earth metal atoms are too small. The direct exchange in these atoms is difficult; therefore, the indirect interaction through the conduction electrons causes the magnetic ordering.

Super-Exchange Interaction

Super-exchange interaction describes the interaction between the moments of two nearest neighbor magnetic ions through a non-magnetic ion. The example can be the coupling between the moments of a pair of Mn^{3+} cations separated by O^{2-} anion, leading an antiferromagnetic ordering. If the two cations are connected at 90° through the non-magnetic anion, then the interaction could be a ferromagnetic interaction.

Double Exchange Interaction

The interaction between the magnetic ions with the different oxidation in some oxides creates a ferromagnetic arrangement, such as the interaction between

Fe^{2+} and Fe^{3+} in magnetite (Fe_3O_4).

The Dzyaloshinskii-Moriya Interaction

The crystal symmetry in some magnetic systems favors the canted spin arrangement rather than antiparallel aligned magnetic moments and thus weak ferromagnetism is created in these antiferromagnet systems; this concept was first proposed by Igor Dzyaloshinskii and later by Toru Moriya. This antisymmetric exchange, called Dzyaloshinskii-Moriya (DM) interaction, is expressed by the total magnetic exchange interaction between two neighboring magnetic spins via a ligand:

$$H_{DM} = \mathbf{D}_{ij} \cdot (\mathbf{S}_i \times \mathbf{S}_j), \quad (2.25)$$

where the DM vector ($\mathbf{D}_{ij} \propto \mathbf{r}_i \times \mathbf{r}_j = \mathbf{x} \times \mathbf{r}_{ij}$) is proportional to the spin-orbit coupling constant and depends on the position of the ligand ion between two magnetic transition metal ions. \mathbf{D}_{ij} is perpendicular to the triangle spanned by the involved three ions and will be zero if the three ions are in line. The antisymmetric anisotropy may create an electric polarization by small shifts of the ligand ions induced by spiral spin ordering in the DM model, often due to the magnetic frustration. However, their polarization is usually small [23]. Figure 2.7 shows the antisymmetric DM vector and anion displacement between two magnetic ions as well as the magnetization and the polarization created by this kind of displacement.

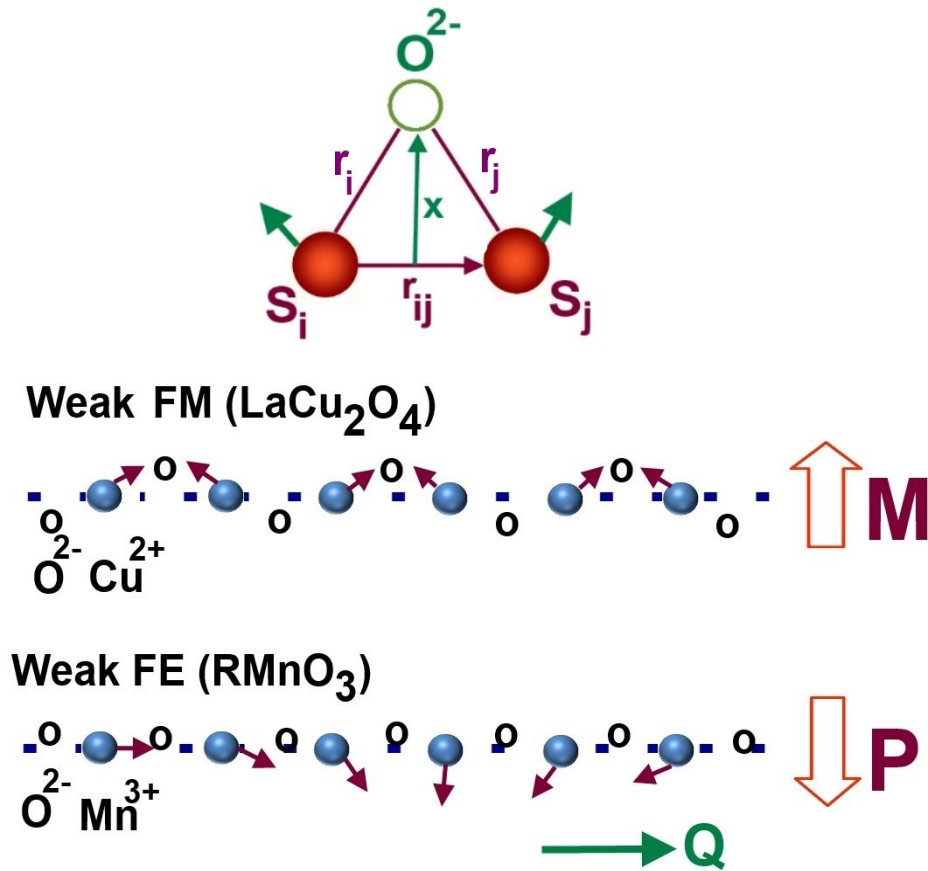


Figure 2.7: The antisymmetric DM vector D_{ij} is proportional to the position of the oxygen ion (green ball) between two magnetic ions (red balls). Weak ferromagnetism (FM) in antiferromagnet LaCu_2O_4 as well as weak ferroelectricity (FE) in RMnO_3 where polarization is $\mathbf{P} \propto \mathbf{Q} \times (\mathbf{S}_i \times \mathbf{S}_j)$ [23].

2.3 Disordered Magnetic Systems

2.3.1 Magnetic Frustration

Magnetic geometrical frustration term refers to a system which is not able to simultaneously satisfy all of its magnetic exchange interactions, due to its geometry. To illustrate this phenomenon, let us have a look at a two dimensional triangular spin lattice (see Figure 2.8) as an example for the geometrical frustration.

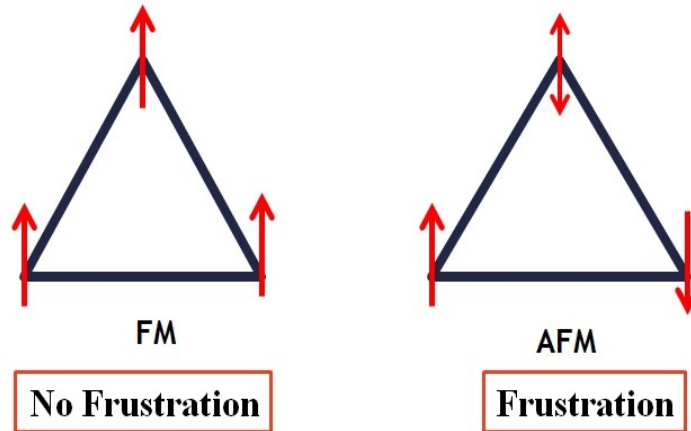


Figure 2.8: Ferromagnetic (FM) and antiferromagnetic (AFM) alignments of magnetic spins on a 2-D triangle lattice.

Three spins are placed at the corners of a triangle with antiferromagnetic interactions between them; the energy is minimized when each spin is ordered opposite to the neighbors. If two Ising spins in a triangle arrangement align anti-parallel, the third spin can only orientate antiferromagnetically to one of the spins but not with the other one. Its two possible orientations, up and down, give the same energy and thus the system is frustrated. However, the ferromagnetic triangle lattice is not frustrated. Similarly in three dimensions, four spins arranged ferromagnetically in a tetrahedron lattice may experience geometric frustration.

The magnetic frustrated systems usually do not exhibit the long-range magnetic order due to the magnetic ground state degeneracy [19].

2.3.2 Spin Glasses

Spin glasses are disordered magnetic systems in which the interactions between the magnetic spins are in conflict with each other. There is no long-range ordering in the spin glassy systems, which is usually observed in materials with ferromagnetic or antiferromagnetic materials. At high temperatures, all the magnetic spins behave independently due to the thermal fluctuations. While it is cooling down, the magnetic spins start slowing down and forming some local units, known as clusters or domains with random magnetic moments orientation. Below the glassy transition temperature, called the freezing temperature, spins are frozen, being aware of their neighbors. Thus, the correlation between the spins will be short range. Randomness and frustration are essential but may not be sufficient to exhibit spin-glass behavior [20].

The experimental research on the spin glasses started in the 1970s after the discovery of a peak in the AC susceptibility of diluted gold-iron alloys by Cannella and Mydosh [24]; the notion was pursued in the mathematical analysis in 1980s and the systematically studied in 1990s. Despite intensive scientific work on disordered and glassy materials over many years, our understanding remains poor [25]. Generally, the spin glass behavior is commonly observed in dilute magnetic alloys and insulators. However, it has been widely reported in antiferromagnetic and ferrimagnetic oxides as well, due to the surface effect. The splitting in field

and zero-field cooling magnetization, the exchange bias effect, aging effect and AC susceptibility dispersion are some important features of glassy state in the fine-particles [26, 27].

If the energy barrier (activation energy), E_a , for a magnetization reversal is comparable to the thermal energy, $k_B T$, the nano-particles will be defined as the superparamagnetic. These small non-interacting magnetic particles behave like paramagnetic atoms although their susceptibility is usually much larger than that of paramagnets. Superparamagnets have sometimes similar behavior as spin glasses. In these systems, the magnetic interactions between the particles are sufficiently small. The relaxation time ($\tau = \frac{1}{f}$) is well described by the Arrhenius law as follows:

$$\tau = \tau_0 e^{\left(\frac{E_a/k_B}{T_m}\right)}, \quad (2.26)$$

where τ_0 , f and k_B are the relaxation time constant, frequency and the Boltzmann constant, respectively. T_m is denoted as the freezing temperature which is the temperature at the maximum peak of the AC susceptibility graph.

However, in the case of spin glass materials with an intermediate interactions between particles, the frequency dependence of freezing temperature T_m is defined by the Vogel-Fulcher law:

$$\tau = \tau_0 e^{\left(\frac{E_a/k_B}{(T_m - T_{VF})}\right)}. \quad (2.27)$$

The Vogel-Fulcher temperature T_{VF} is often interpreted as a measure of the intercluster interaction strength which corresponds to the temperature at which τ

is infinite. The spin glass systems are relaxing slowly to reach an equilibrium but their relaxation time is smaller than that of superparamagnetic materials. The other dynamic scaling law for the spin glass behavior analysis is the frequency dependence power law given as:

$$\tau = \tau_0 \left(\frac{T_m - T_g}{T_g} \right)^{-z\nu}, \quad (2.28)$$

where $z\nu$ and T_g are the dynamic critical exponent and static spin glass temperature, respectively [26, 27, 28].

Surface Effects

The term nano-powders refers to the materials with the 1-100 nm particle size. They will be named magnetic nano-particles if they show a response to an applied magnetic field. As the size of the particle decreases, the ratio of the surface atoms to the bulk atoms increases, thus enhancing the surface contribution to their physical properties. Below a critical size, magnetic particles become a single domain and exhibit different magnetic properties. The different types of defects at the surface such as atomic vacancies, change in the atomic coordination, broken bonds and different oxidation might break the symmetry, creating the frustration and thus forming the spin disorder layer [27].

2.3.3 Exchange Bias

The exchange interactions at the interfaces between the ferromagnetic and antiferromagnetic materials can create a directional anisotropy called the exchange

bias, which is observed as a shift in the magnetic hysteresis loop when the sample is cooled in an external magnetic field. This phenomenon can be observed in other different magnetic combinations such as ferrimagnet and/or spin glass as well [29, 30]. The schematic exchange bias effect is depicted in Figure 2.9, where the horizontal shift and the vertical shift are named the exchange bias magnetic field (H_{EB}) and the exchange bias magnetization (M_{EB}), respectively.

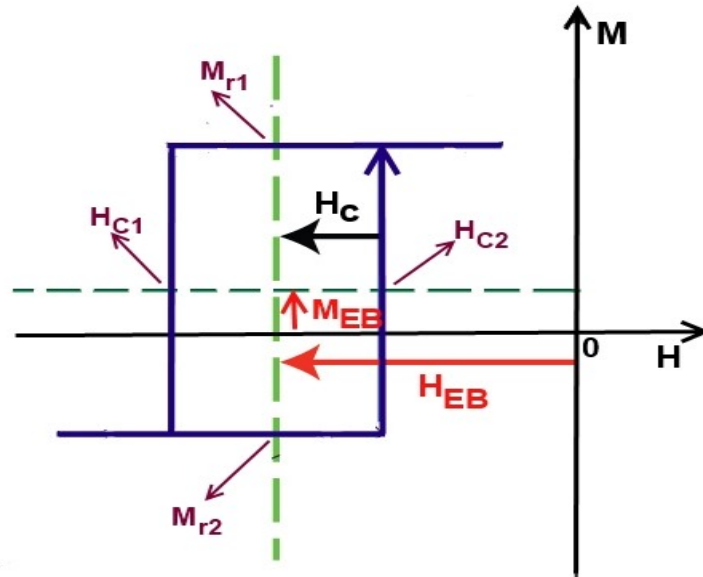


Figure 2.9: Schematic exchange bias phenomenon which is observed by the horizontal as well as the vertical shift in M-H loop after field cooling measurements.

The exchange bias magnetic field, the exchange bias magnetization, the total coercivity field and remanent magnetization are calculated through the following equations, where H_{c1} and H_{c2} are the left and right coercivity fields and M_{r1} and M_{r2} are the up and down remanent magnetizations, respectively.

$$H_{EB} = -\frac{(H_{c1} + H_{c2})}{2}; \quad (2.29a)$$

$$M_{EB} = -\frac{(M_{r1} + M_{r2})}{2}; \quad (2.29b)$$

$$H_c = -\frac{|H_{c1} - H_{c2}|}{2}; \quad (2.29c)$$

$$M_r = -\frac{|M_{r1} - M_{r2}|}{2}. \quad (2.29d)$$

The physical origin of the exchange bias phenomenon in the typical FM-AFM combination is an anisotropy induced in FM from AFM. A torque induced by antiferromagnetic spins on ferromagnetic spins may cause a shift in the M-H loop as well as an increase in the magnetic coersivity. Usually in these systems, the Néel transition temperature of the antiferromagnetic material (T_N) is smaller than the Curie transition temperature of ferromagnetic material (T_c). It is northworthy that the magnetic anisotropy of the AFM in this exchange interaction plays a significant role. If the large magnetic field is applied on the FM-AFM couple at the temperature below T_c , all ferromagnetic spins will align with the magnetic field while antiferromagnetic spins remain random. When the system cools down through T_N , the antiferromagnetic moments starts ordering. The first layer of the antiferromagnetic spins at the interface with ferromagnetic spins align parallel with an applied magnetic field as well as ferromagnetic spins. When the magnetic field is reversed, the ferromagnetic spins start rotating but the situation for magnetic moments in AFM can not always be the same.

If the antiferromagnetic anisotropy is large enough (Figure 2.10(a)), the

antiferromagnetic spins prefer to keep themselves in their original positions as well as ferromagnetic spins. Therefore, the required magnetic field to reverse the ferromagnetic spins completely will be higher than that for uncoupled ferromagnetic material, increasing the coercivity field in the negative branch. Oppositely, when the magnetic field is reversed back to the positive branch, the induced torque from AFM is in the same direction of an applied field and ferromagnetic spins will rotate easily. In summary, the M-H loop is shifted along the magnetic field.

On the other hand, when the antiferromagnetic anisotropy is too small, both the ferromagnetic and antiferromagnetic spins tend to rotate with the magnetic field, enhancing the coercivity in both sides of M-H hysteresis (Figure 2.10(b)). However, in some compounds including nano-particles both M-H shift and coercivity enhancement have been observed due to the different reasons such as the structural defects. Observation of a vertical shift is rare and usually attributed to the uncompensated spins at the FM-AFM interface.

While the temperature increases, the exchange bias phenomenon disappears. The temperature at which the exchange bias effect vanishes, is usually called the blocking temperature (T_B) [30, 31].

The exchange bias was discovered first in the FM-AFM nano-particles of the Co/CoO compound in 1956 [32] and later in many different systems including small particles, inhomogeneous materials and multilayers [33]. The first commercial device to employ the exchange bias was magneto-resistance disk drive recording head in the 1970s and later, the spin valve head in 1990s. The exchange bias can be used in different magnetic devices including magnetic recording media as

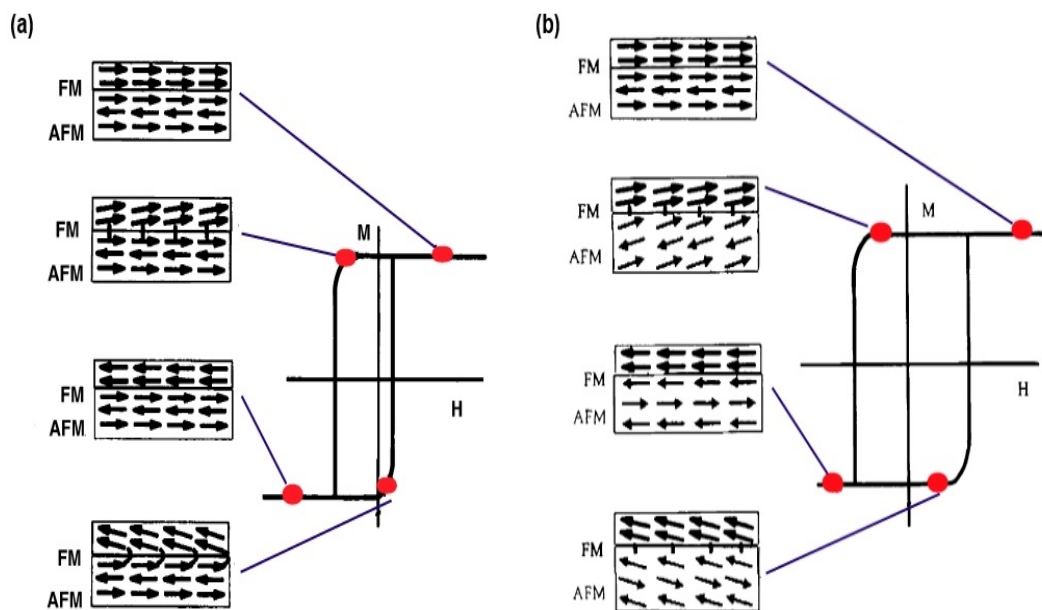


Figure 2.10: Schematic drawing of the spin configuration of FM-AFM couple at the different points of M-H loop measurements when (a) AFM anisotropy is large, (b) AFM anisotropy is small. Reprinted from Ref. [30].

permanent magnet materials [30]. Furthermore, the sign reversal of the exchange bias effect have been observed in a few materials which can be utilized in thermally assisted magnetic random access memory [34, 35].

The exchange bias phenomenon is strongly dependent on the particle morphology, including the AFM-FM thickness, magnetic anisotropy and interface disorder. For example it is reported that in the FM-AFM bilayer, the exchange bias magnetic field is directly proportional to the AFM thickness but inversely proportional to the FM thickness [31].

The exchange bias can be formed by different methods such as the chemical surface modification (e.g., oxidation or nitration) or FM particles embedded in AFM materials. Furthermore, this effect has been extensively reported in antiferromagnetic and ferrimagnetic oxides, in particular, in the nano-size powders where the surface effect is dominant. Some examples of exchange bias effect in the pure materials are NiFe_2O_3 (ferrimagnetic oxide) [36], $\gamma\text{-Fe}_2\text{O}_3$ (FM oxide) [37] and NiO (AFM oxide) [38], which have been described with the core-shell model and surface spin disordering. This spin disorder layer can be considered as an AFM shell around a FM core or also an AFM core surrounded by a FM shell at low temperatures. According to the literature, the exchange bias effect might become more significant while the particle size decreases, due to the surface effect enhancement [27].

Bibliography

- [1] A. F. Orchard, "Magnetochemistry", Oxford University Press, New York, (2003)
- [2] J. Stohr, H. C. Siegmann, "Magnetism: From Fundamentals to Nanoscale Dynamics", Springer Berlin Heidelberg, (2006)
- [3] E. T. Lacheisserie, D. Gignoux, M. Schlenker, "Magnetism: Materials and Applications", Springer New York, (2005)
- [4] C. Kittel, "Introduction to Solid State Physics", 8th ed., John Wiley & Sons Ltd, (2005)
- [5] N. A. Spaldin, "Magnetic Materials Fundamentals and Device Applications", Cambridge University Press, (2006)
- [6] R. K. Pathria, "Statistical Mechanics", Oxford: Pergamon Press, (1972)
- [7] D. J. Griffiths, "Introduction to Quantum Mechanics", 2nd ed., Addison-Wesley, (2005)
- [8] www.chm.davidson.edu/vce/coordchem/splitting
- [9] www.ellesmere-chemistry.wikia.com/wiki/D_orbital

-
- [10] www.en.wikipedia.org/wiki/Chromium
- [11] R. D. Shannon, *Acta Crystallogr.*, **32**, 751, (1976)
- [12] www.en.wikipedia.org/wiki/Cerium
- [13] F. F. Popescu, V. Bercu, J. N. Barascu, M. Martinelli, C. A. Massa, L. A. Pardi, M. Stefan, S. V. Nistor, M. Nikl, *Opt. Mater.*, **32**, 570575, (2010)
- [14] J. H. Van Vleck, "Theory of Electric and Magnetic Susceptibilities", Oxford University Press, (1932)
- [15] www.en.wikipedia.org/wiki/Europium
- [16] Y. Takikawa, S. Ebisu, S. Nagata, *J. Phys. Chem. Sol.* **71**(11), 1592-1598, (2010)
- [17] K. Umemoto, Y. Seto, Y. Masuda, *Thermochimica Acta*, **431**, 117-122, (2005)
- [18] H. Lueken, "Course of Lectures on Magnetism of Lanthanide Ions under Varying Ligand and Magnetic Fields", Institute of Inorganic Chemistry, RWTH Aachen, (2008)
- [19] R. Moessner, A. P. Reimers, *Phys. Today*, 24-29, (2006)
- [20] K. Binder, A. P. Young, *Rev. Mod. Phys.*, **58**(4), (1986)
- [21] A. H. Morrish, "The Physical Principles of Magnetism", Wiley-IEEE Press, (2001)
- [22] M. Opel, *J. Phys. D: Appl. Phys.* **45**, 033001, (2012)

-
- [23] S. W. Cheong, M. Mostovoy, *Nat. Mater.*, 6, 1, 13-20, (2007)
- [24] V. Cannella, J. A. Mydosh, *Phys. Rev. B*, 6, 4220, (1972)
- [25] E. Bolthausen, A. Bovier, "Spin Glasses", Springer, Verlag Berlin Heidelberg, (2007)
- [26] S. Bedanta, W. Kleemann, *J. Phys. D: Appl. Phys.* 42, (2009)
- [27] B. Issa, I. M. Obaidat, B. A. Albiss, Y. Haik, *Int. J. Mol. Sci.*, 14, 21266-21305, (2013)
- [28] K. Vijayanandhini, C. Simon, V. Pralong, V. Caignaert, B. Raveau, *Phys. Rev.* 79, 224407, (2009)
- [29] R. L. Stamps, *J. Phys. D: Appl. Phys.*, 33, 247-268, (2000)
- [30] J. Nogués, J. Sort, V. Langlais, V. Skumryev, S. Surinach, J. S. Munoz, M. D. Baro, *Phys. Rep.*, 22, 65117, (2005)
- [31] J. Nogués, I. K. Schuller, *Magn. Magn. Mater.*, 192, 203-232, (1999)
- [32] W. H. Meiklejohn, C. P. Bean, *Phys. Rev.* 102, 1413, (1956)
- [33] S. Karmakar, S. Taran, E. Bose, K. Chaudhuri, C. P. Sun, C. L. Huang, H. D. Yang, *J. Phys. Rev. B.*, 77, 144409, (2008)
- [34] P. K. Manna, S. M. Yusuf, R. Shukla, A. K. Tyagi, *Appl. Phys. Lett.*, 96, 242508, (2010)
- [35] K. Yoshii, *Appl. Phys. Lett.*, 99, 142501, (2011)

- [36] R. H. Kodama, A. E. Berkowitz, E. J. McNiff, S. Foner, Phys. Rev. Lett., 77, 394, (1996)

- [37] B. Martinez, X. Obradors, L. Balcells, A. Rouanet, C. Monty, Phys. Rev. Lett., 80, 1, (1998)

- [38] R. H. Kodama, Phys. Rev. Lett., 79, 1393-1396, (1997)

Chapter 3

Synthesis of Samples

3.1 Combustion Method

In the so-called solid state reaction, most of the perovskite ceramic materials have been traditionally synthesized using a mixture of their constituent oxides. The solid state reaction is a preparative method in which a high temperature (often 1000 to 1500°C) is required in order to accomplish the reaction, result in samples with low homogeneity and large particle size. Manual grinding and ball milling are used to mix the powders which might be contaminated by impurities, creating secondary phases [1].

Alternative routes to the solid state reaction method are wet chemical synthetic methods, including sol-gel process, hydrothermal synthesis, co-precipitation method and combustion synthesis.

Combustion synthesis, called a self-propagating method, is one of the most effective and simplest methods to produce perovskite oxide powders and other various industrially materials. This process involves a highly exothermic self-combustion reaction between the fuel (usually glycine or urea) and the oxidizers (e.g. metal

nitrates) [2, 3]. Compared to the solid state reaction method, this manner of the preparation has benefits such as:

- The liquid media allows mixing of the elements on the molecular level, leading to a uniform and homogeneous formulation of the desired composition.
- The high combustion temperature produces enough heat to achieve the desired phase composition directly, skipping an additional calcination step.
- Rapid combustion process (in seconds) forms the materials in nano-sized particles with high specific surface area.
- The process is usually simple and inexpensive with less contamination.

3.2 Sample Preparation

In this work, a simple precursor method has been adopted to prepare the orthorhombic RCrO_3 from the nitrates of its constituents. Alfa Aesar reactants in high purity were used: cerium nitrate, europium nitrate and chromium nitrate as the oxidizers and glycine as a fuel. Metal nitrates were chosen as the metal precursors due to their great water solubility, allowing a greater homogenization. Glycine is one of the cheapest amino acids whose molecule consists of a carboxylic acid group at one end of the chain and an amino group at the other. The glycine molecule in the solution can behave as a complexing agent for the metal ions, preventing precipitation and forming compositional homogeneity among the constituents. Table 3.1 gives some information of the starting materials used in this experiment.

Table 3.1: Raw materials properties used in the experiment [4].

Compound	Chemical Formula	purity %	Molar Mass (g/mole)	Melting Point (°C)
cerium nitrate	$\text{Ce}(\text{NO}_3)_3 \cdot 6\text{H}_2\text{O}$	99.99	434.23	65
europium nitrate	$\text{Eu}(\text{NO}_3)_3 \cdot 6\text{H}_2\text{O}$	99.9	446.06	85
chromium nitrate	$\text{Cr}(\text{NO}_3)_3 \cdot 9\text{H}_2\text{O}$	99.99	400.14	60
glycine	$\text{NH}_2\text{CH}_2\text{COOH}$	99.5	75.07	233

The raw materials were first weighed according to their stoichiometric formula. In the present case, one mole of each oxidizer and 3.31 mole of fuel were selected. A two-fold stoichiometric excess of glycine was used, in order to obtain the maximum exothermicity. 0.1 mole of $\text{A}(\text{NO}_3)_3 \cdot n\text{H}_2\text{O}$ (where A is Eu or Ce) and 0.1 mole of $\text{Cr}(\text{NO}_3)_3 \cdot 9\text{H}_2\text{O}$ were separately dissolved in 25 ml deionized water, mixed together in 50 ml deionized water and then glycine was added. All the materials are easily dissolvable in water at room temperature, leading to a dark navy solution (Figure 3.1(a)). The solution pH was about 2-3. The solution temperature was checked periodically using a thermometer.

The solution was heated on a hot plate until it boiled and then kept heating at 60-70°C to evaporate water, forming a viscous solution. The solution beaker was covered by an aluminum mesh to prevent losing the materials during the combustion process. By increasing the temperature, the auto-ignition process with the clear flame and brown fume took place in seconds, leaving a fluffy gray ash. As the Eu content increases, the color of the burnt ash changes from gray to green.

Figure 3.1(b) shows the green fluffy ash of EuCrO_3 after the combustion.

The voluminous ash was ground with a mortar and pestle to obtain the homogeneous and soft powder. The ground powder was placed in an alumina crucible boat and then loaded into a horizontal tubal furnace (LINDBERG/ HEVI-DUTY) with an alumina tube to allow calcination at 500°C for 5 h with the heating rate of $4^\circ\text{C}/\text{min}$. Figures 3.1(c) and (d) represent the calcined powders of CeCrO_3 and EuCrO_3 , respectively.

The calcined powders were ground manually and mixed completely with a drop of glycerin as the binder, which decomposed to carbon oxides around 290°C . The ground calcined powders were pressed into the cylindrical pellets using a 13 mm die and a hydraulic press (Model M), under 4 tons pressure. The pressed specimens were then sintered at 950°C for 12 h with the heating rate of $4^\circ\text{C}/\text{min}$ using the same crucible boat and tubal furnace as used in calcination process. Figures 3.1(e) and (f) show the sintered pellets of CeCrO_3 and EuCrO_3 , respectively. The calcining and sintering were done in the air as well as under flowing different gases of oxygen, argon or a mixture of argon and hydrogen in order to achieve the best condition of pure phase $\text{Ce}_{1-x}\text{Eu}_x\text{CrO}_3$ compound. In general, flowing noble gas such as argon is usually used to prevent oxidation to the higher oxidation states while using reducing gases (e.g hydrogen) might form a low oxidation states. For the purpose of an adequate gas input into the furnace, a thin quartz tube open at both ends was passed through a rubber stopper and connected by the rubber tubing to the gas system while the flow-meter was used to ensure the correct gas ratio. The exhausted gases were bubbled in the glass

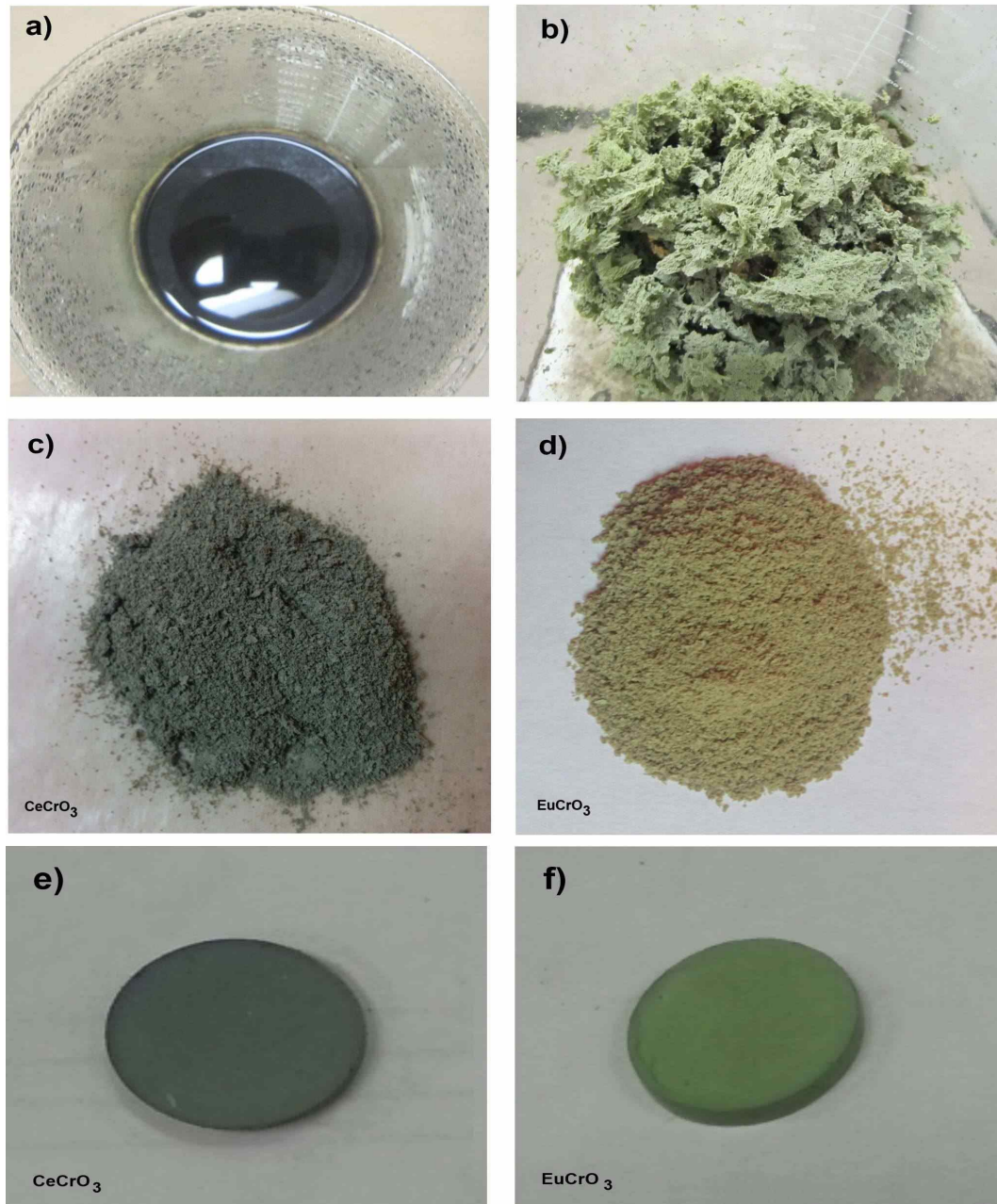


Figure 3.1: The images of (a) starting materials solution, (b) fluffy ash of $EuCrO_3$ after auto-ignition process, (c) $CeCrO_3$ and (d) $EuCrO_3$ calcined powders at $500^\circ C$, (e) $CeCrO_3$ and (f) $EuCrO_3$ sintered pellets at $950^\circ C$.

tube full of oil after passing through the sample in the tube. In order to reduce the heat loss through the tubal furnace, both ends of the tube were covered by the glass fiber. The schematic drawing of sintering set up is observed in Figure 3.2.

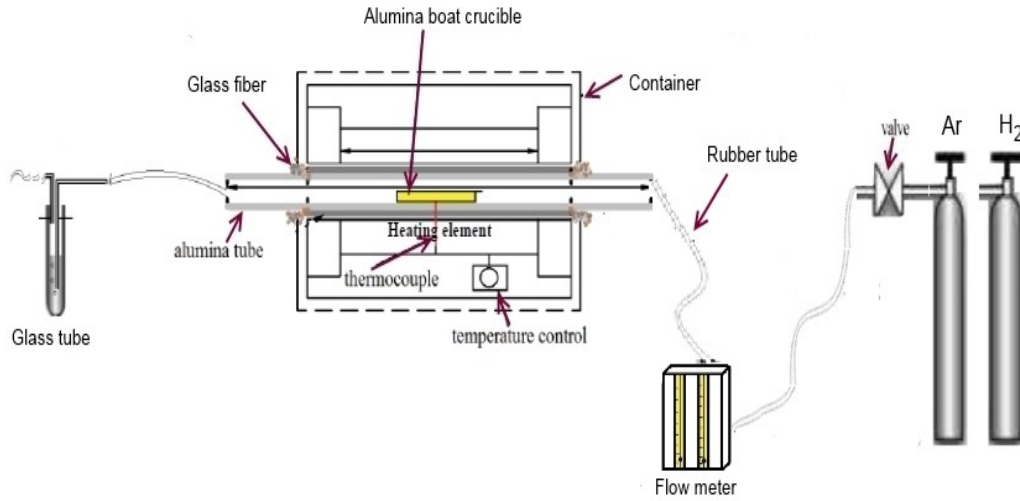
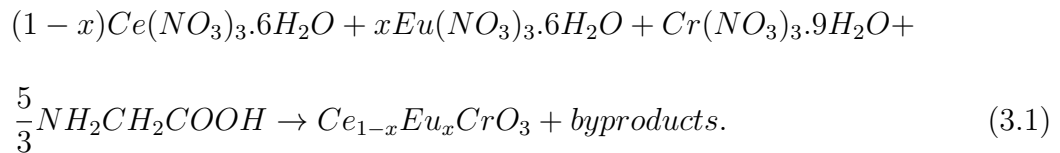


Figure 3.2: Schematic drawing of the horizontal tubular furnace used for preparation of $Ce_{1-x}Eu_xCrO_3$ powders. This was achieved by sintering the samples placed inside an alumina tube in a reducing ambient, namely Ar and H₂.

In this preparation process, first the metal nitrates decompose to cerium oxide, europium oxide and chromium oxide and a large amount of gases such as NO₂, CO₂ and H₂O are released as byproducts. By further heating, the orthorhombic rare earth chromite phase will be formed.

In summary, the stoichiometric chemical reaction equation between the starting materials to obtain one mole $Ce_{1-x}Eu_xCrO_3$ compound can be defined as:



The following flow chart (Figure 3.3) shows the summary of the $Ce_{1-x}Eu_xCrO_3$ powder synthesis using combustion method in this work.

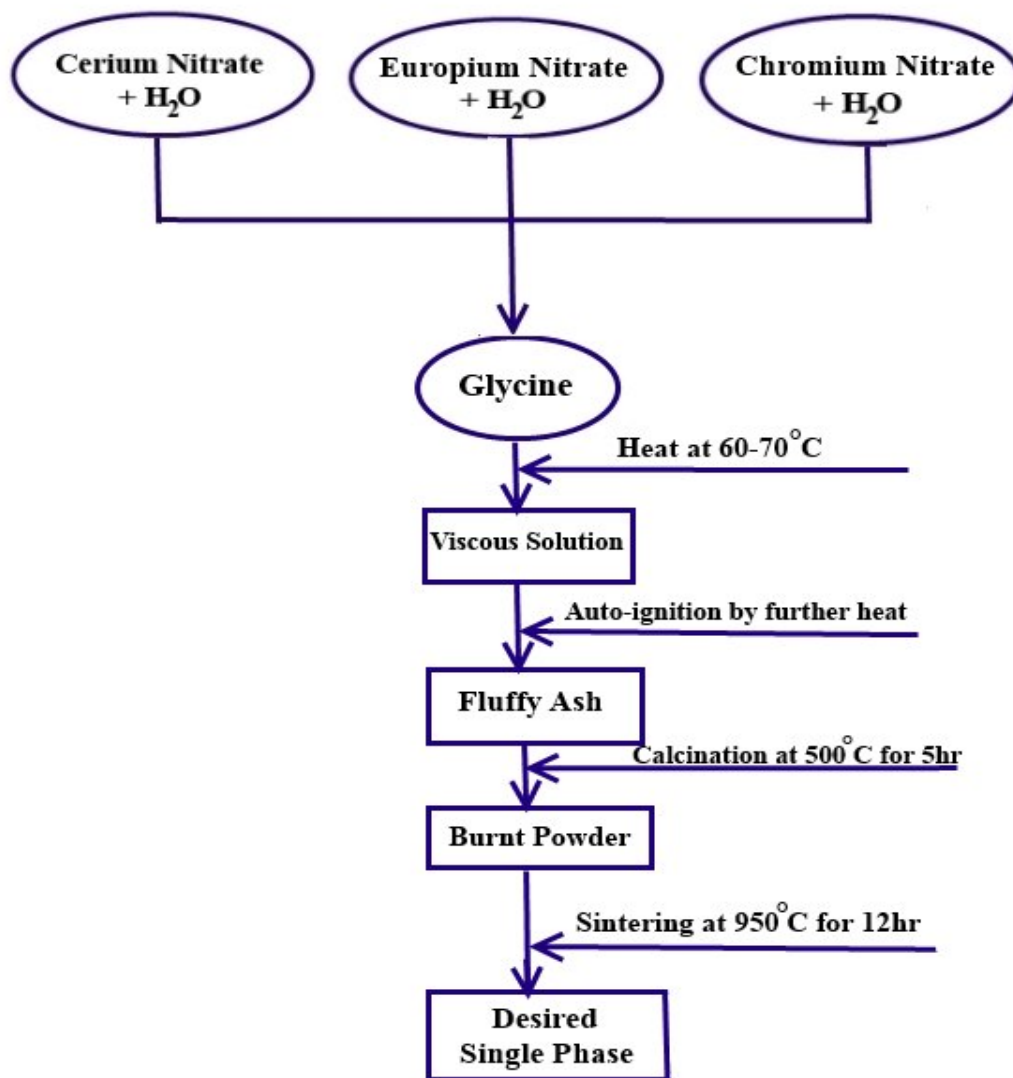


Figure 3.3: The flow chart of the preparation method of $Ce_{1-x}Eu_xCrO_3$ nano-powders, using the combustion method.

Bibliography

- [1] L. E. Smart, E. A. Moore, "Solid State Chemistry: An Introduction", 4th ed., CRC Press, (2012)
- [2] S. T. Aruna, A. S. Mukasyan, *Curr. Opin. Solid State Mater. Sci.*, 12, 4450, (2008)
- [3] A. S. Mukasyan, P. Dinka, *Adv. Eng. Mater.*, 9, (2007)
- [4] www.alfa.com

Chapter 4

Sample Characterization and Morphology

4.1 Crystallography

Crystallography is the science where scientists study the arrangement of the atoms in the solids and symmetry in the crystal structures. X-rays, neutron radiation or electron beams are commonly used in the diffraction patterns of the crystals. Some basic definitions in crystallography are useful to visualize the powder diffraction method.

4.1.1 Direct Lattice

Matter usually exists in one of four states, usually called phases: solid, liquid, gas and plasma. Solids have fixed shape and volume, and are independent of their container. The atoms in the solid phase are tightly bound to each other and cannot easily move away, either in a regular/order arrangement (crystalline solids) or an irregular/disorder distribution (amorphous solids). Therefore, a crystal is

an anisotropic homogeneous solid where its atoms and molecules are formed in the periodic arrangement in all three spatial dimensions, in other words, it has long-range ordering. The periodic structure of the crystal can easily be described in terms of a lattice with a group of atoms (called basis) attached to each lattice point. The primitive unit cell is the smallest volume that can establish the whole crystal by its repetition. In general, the unit cell can be identified by six lattice parameters: a , b , c , α , β , γ . The first three parameters are the lengths of the unit cell and the last three are the angles between the lengths.

Any lattice point in the direct space can be described by a vector which is a linear combination of the three translation direct vectors, \mathbf{a}_1 , \mathbf{a}_2 , \mathbf{a}_3 :

$$\mathbf{r} = \mathbf{a}_1x + \mathbf{a}_2y + \mathbf{a}_3z, \quad (4.1)$$

where x , y , z are integer numbers [1].

The periodic arrangement in the crystal forms planes of atoms which are defined by three integers called Miller Indices (h , k , l). The distance between the neighboring planes are called interplanar distance, d . Figure 4.1 shows the lattice parameters as well as two examples of planes in the crystal lattice.

It is easy to divide all the crystal structures into seven groups or basic systems. These seven basic crystal types are characterized by the lattice parameters and the angles between the three axes. In summary, there are 14 possible Bravais lattices in the three-dimensional space. The lattice is primitive (P) when the lattice points are just located on the corners. It is named body (I) if there is an additional

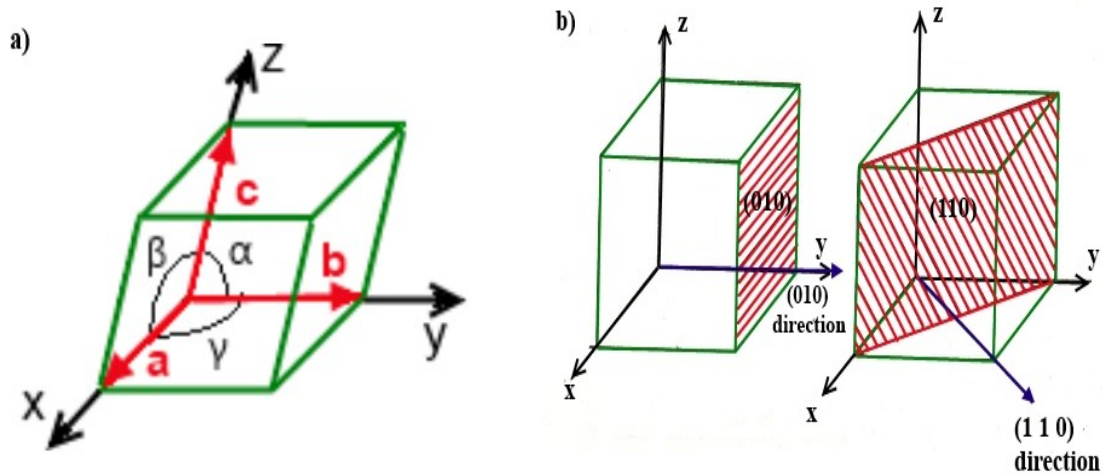


Figure 4.1: (a) Lattice parameters and angles in the cubic crystal structure, (b) planes and directions in the cubic system.

lattice point at the center of the unit cell. The lattice is labeled as face (F) if one additional lattice point is placed at the center of each face of the unit cell. Finally, by adding an additional lattice point at the center of each pair of cell faces, the lattice is called base (C). Figure 4.2 represents all 7 crystal systems and 14 Bravais lattices with the relation between the lattice parameters [2].

In the crystallography, the symmetry of the crystal can be described by the space groups which are made from combinations of the 32 crystallographic point groups with the 14 Bravais lattices in three dimensions, resulting in 230 different space groups. The simple symmetry operations consist of the following, namely, translation, rotation, reflection and inversion [2].

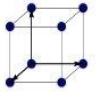

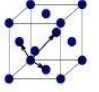
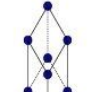
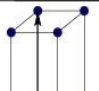
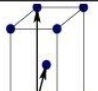
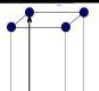
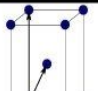
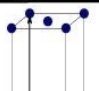
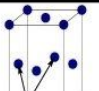
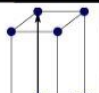
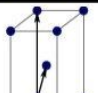
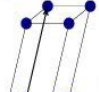
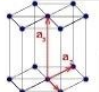
Bravais Lattices	Parameters	P	I	C	F
Cubic	$a=b=c$ $\alpha=\beta=\gamma=90^\circ$				
Trigonal	$a=b=c$ $\alpha=\beta=\gamma < 120^\circ, \neq 90^\circ$				
Tetragonal	$a=b \neq c$ $\alpha=\beta=\gamma=90^\circ$				
Orthorhombic	$a \neq b \neq c$ $\alpha=\beta=\gamma=90^\circ$				
Monoclinic	$a \neq b \neq c$ $\alpha=\gamma=90^\circ \neq \beta$				
Triclinic	$a \neq b \neq c$ $\alpha \neq \beta \neq \gamma$				
Hexagonal	$a=b \neq c$ $\alpha=\beta=90^\circ, \gamma=120^\circ$				

Figure 4.2: Bravais lattice types in the three dimensions. P, I, F and C are referred to as simple, body, face and base centers, respectively [2].

4.1.2 Reciprocal Lattice

The lattice made of the Fourier transform of the direct lattice is named reciprocal lattice which can be determined by three reciprocal primitive vectors of \mathbf{b}_1 , \mathbf{b}_2 and \mathbf{b}_3 through the formula [1]:

$$\begin{aligned}\mathbf{b}_1 &= 2\pi \frac{\mathbf{a}_2 \times \mathbf{a}_3}{\mathbf{a}_1 \cdot \mathbf{a}_2 \times \mathbf{a}_3}; \\ \mathbf{b}_2 &= 2\pi \frac{\mathbf{a}_3 \times \mathbf{a}_1}{\mathbf{a}_1 \cdot \mathbf{a}_2 \times \mathbf{a}_3}; \\ \mathbf{b}_3 &= 2\pi \frac{\mathbf{a}_1 \times \mathbf{a}_2}{\mathbf{a}_1 \cdot \mathbf{a}_2 \times \mathbf{a}_3},\end{aligned}\tag{4.2}$$

where \mathbf{a}_1 , \mathbf{a}_2 and \mathbf{a}_3 are the direct primitive vectors of the crystal lattice. It is worth noting that the reciprocal vectors and the direct lattice vectors are orthogonal, thus:

$$\mathbf{b}_i \cdot \mathbf{a}_j = 2\pi \delta_{ij},\tag{4.3}$$

where $\delta_{ij} = 1$ if $i = j$ and $\delta_{ij} = 0$ when $i \neq j$.

4.1.3 Perovskite Structure

Perovskite oxides, with the ABO_3 chemical formula, have received renewed interest, due to many interesting and intriguing properties from both the theoretical and the application point of view. This structure is named after discovering the mineral perovskite CaTiO_3 by a Russian mineralogist, Count Lev Aleksevich von Perovski. In the ideal cubic perovskite, A cations with 12-fold coordination are

located at the corners; while the B cation with 6-fold coordination, surrounded by 6 oxygen ions, is placed at the middle of the cubic structure. The ideal cubic perovskite structure is not very common. Factors such as ionic size effects, pressure, temperature or composition change, usually cause a distortion from the ideal cubic perovskite structure. The coordination of A cation can be reduced from 12 to as low as 8 due to the tilting of BO_6 octahedra. The low symmetry created by the structure distortion has an important role on the magnetic and electric properties of the perovskite materials, for example, the spontaneous polarization may be achieved by the off-center distortion of the small transition metal cation B at the center of the octahedron of the oxygen atoms [3, 4]. Figure 4.3 shows the ideal perovskite structure. The orthorhombic and tetragonal phases are the most common non-cubic perovskite structures.

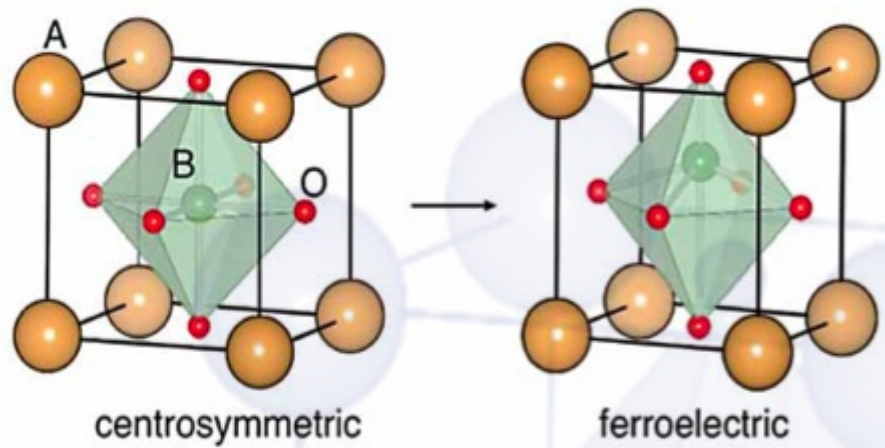


Figure 4.3: The structure of a perovskite, ABO_3 , in the ideal cubic (centrosymmetric) and BO_6 tilted (the ferroelectric phase), reprinted from Ref. [6].

Size Effect

The lattice parameter a in the ideal cubic structure is geometrically related to the ionic radii of A, B and O ions (r_A , r_B , and r_O) as described by:

$$a = \sqrt{2}(r_A + r_O) = 2(r_B + r_O). \quad (4.4)$$

The ratio of the both sides in the Equation (4.4) for the unit cell length is named the Goldschmidt's tolerance factor (t) [5] which is an indicator for the stability and distortion of the crystal structures. The tolerance factor strongly depends on the ionic radii of the ions and is given by:

$$t = \frac{(r_A + r_O)}{\sqrt{2}(r_B + r_O)}. \quad (4.5)$$

Table 4.1 shows the range of the tolerance factor (t) for the different perovskite structures. It is worth noting that the tolerance factor depends on what values are taken for the ionic radii, thus it is only a rough estimate.

4.2 X-Ray Diffraction

4.2.1 X-Rays

The electromagnetic radiation is a fundamental phenomenon of electromagnetism, behaving as the waves as well as the particles called photons. This radiation can be classified as an electromagnetic spectrum in the different wavelengths and frequencies, named radio waves, microwaves, infrared radiation, visible light,

Table 4.1: Tolerance factor (t) in the different perovskite structures with the examples [3].

t factor	Structure	Explanation	Example
>1	Hexagonal	too large A or too small B	BaNiO ₃
0.89-1	Cubic	ideal size of A and B	BaTiO ₃
0.71-0.89	Orthorhombic/Rhombohedral	too small A	($T > 400\text{K}$) CaTiO ₃
<0.71	Different structures	similar ionic radii of A and B	FeTiO ₃

ultraviolet radiation, X-rays and gamma rays. X-rays with short wavelengths (0.1 to 100 Å) are classified as the relative high energy electromagnetic waves ranging from 100 eV to 100 keV, which are located between the gamma radiation and ultraviolet ray. X-radiation, which sometimes is called Röntgen radiation, was discovered in 1895 by Wilhelm Röntgen, an achievement that earned him the first Nobel prize in Physics in 1901.

The wavelengths of X-rays are in the same order of magnitude as the shortest interatomic distances in materials. As a result, some X-rays are able to penetrate through matter, observe the individual atoms and be used for the material characterization and crystallography. Furthermore, an X-ray energy can be adjusted to be suitable in the various penetration depths for the different applications. X-rays can be utilized in cancer treatments to kill diseased cells using radiation therapy. X-radiations with energies above 5 –10 keV can travel through the thick objects without being much absorbed or scattered. For this reason, they are widely used to image the

inside of visually opaque objects. This characteristic makes them special in the medical radiography and airport security scanners [7].

X-ray photons carry enough energy to ionize atoms and disrupt molecular bonds. Exposure to this ionizing radiation can be harmful to living tissues, and a very high radiation dose over a long time causes radiation sickness, cancer, and death. The intensity of X-rays reduces while penetrating, due to the scattering by the electrons around the nucleus of atoms in the sample.

X-rays are usually generated in two methods: X-ray tube and synchrotron.

X-Ray Tube

The first and simplest source of X-ray is the X-ray tube. The electrons released by a hot cathode are accelerated in the vacuum tube with high voltage and collide with a metal target, which create the X-rays. Figure 4.4 represents the schematic of the X-ray tube consisting of a cathode and an anode in the vacuum, generating X-rays.

The X-ray spectrum, produced in the X-ray tube, depends on the target material (anode) and the accelerating voltage. When an electron loses all its kinetic energy in a single collision, the X-ray is produced with the maximum energy and the shortest wavelength. The magnitude of the shortest wavelength limit, λ_{min} , can be given by the accelerating voltage, V , between the electrodes:

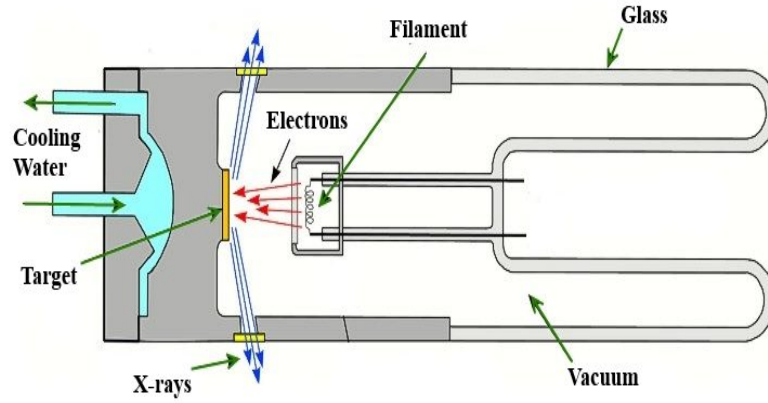


Figure 4.4: The schematic X-ray tube using for X-ray generating, reprinted from Ref [8].

$$eV = h\nu_{max};$$

$$\lambda_{min} = \frac{hc}{eV}, \quad (4.6)$$

where ν , c , e and h are frequency, speed of light, electron charge and Planck constant.

The X-ray tube is the most common X-radiation source used in laboratories. K_{α} and K_{β} are the characteristic X-ray lines wavelengths which are dependent on the target material. When an electron hits an anode atom and ionizes it, the resulting vacancy in the inner shell (K shell) is then filled by an electron from a higher energy level in the outer shells (L or M shells) with the emission of an X-ray photon characterized by the difference in the energy between the two levels. When the transition happens between a K shell with the principal quantum number $n = 1$ and an L shell with $n = 2$, the line is called α , however if a K shell and a M shell

(with $n = 3$) are involved, the line is named β . Since the energy transition for β is larger than for α , then λ_β is smaller than λ_α . A diagram below (Figure 4.5) depicts the atomic levels and the allowed electron transitions of copper. The red circles represent electrons. K_α line is seen to be a doublet with slightly different energies, depending on the $2p_{\frac{1}{2}} \rightarrow 1s$ and $2p_{\frac{3}{2}} \rightarrow 1s$ transitions, which are labeled as $K_{\alpha 1}$ and $K_{\alpha 2}$. In most experimental work, monochromatic radiation is used, thus the K_β intensity is typically suppressed by use of the filtration [9].

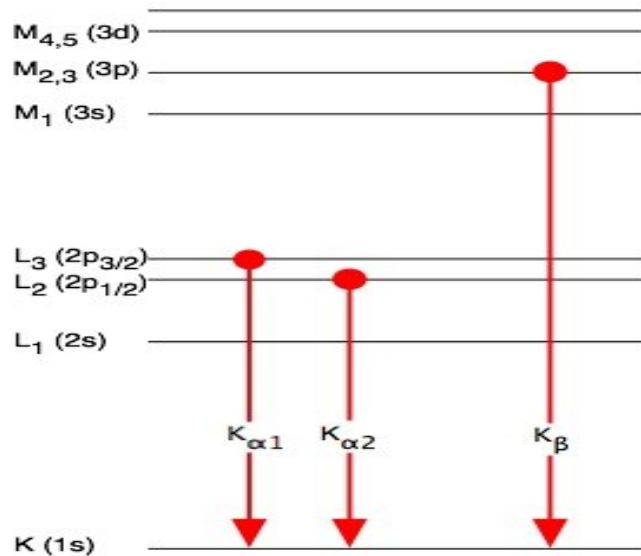


Figure 4.5: The atomic levels and allowed transitions in copper. K_α and K_β are the characteristic X-ray wavelengths.

Table 4.2 shows the summary of common materials with their energy and wavelength used as target materials in the X-ray tubes.

Table 4.2: Characteristic wavelengths and energies of some common target materials used in the X-ray tubes [9].

Target material	Atomic number	Photon energy (keV) K_{α} , K_{β}	Wavelength (nm) K_{α} , K_{β}
W	74	59.3 , 67.2	0.0209 , 0.0184
Mo	42	17.5 , 19.6	0.0709 , 0.0632
Cu	29	8.05 , 8.91	0.157 , 0.139
Ag	47	22.2 , 24.9	0.0559 , 0.0497
Ga	31	9.25 , 10.26	0.134 , 0.121
In	49	24.2 , 27.3	0.0512 , 0.455

The total X-radiation intensity, I , generated in a fixed time interval depends on the atomic number of the target, Z , and the tube current, i . This relation is obtained by [10]:

$$I = AiZV^2, \quad (4.7)$$

where A is the constant. Using tungsten or gold with increasing accelerating voltage and larger current can suggest high intensity of X-rays. It is worth mentioning that most of the kinetic energy of the electrons hitting the target is transformed into the heat and about 1% of the energy is converted into X-rays. Therefore, the anode must be cooled with chilled water to prevent target melting.

Synchrotron

Synchrotron radiation is the electromagnetic radiation emitted by the charged particles moving along a curved trajectory with a large radius of the curvature. Synchrotron radiation was named after its discovery in a General Electric Research Laboratory in New York in 1947 by Frank Elder, Anatole Gurewitsch, Robert Langmuir, and Herb Pollock. Over the past 65 years, synchrotron radiation has become a premier research tool for the study of the matter in the different area and devices, such as spectroscopy, X-ray diffraction, medicine, earth science, chemical, and space industry [11]. The different parts of a synchrotron are shown in Figure 4.6.

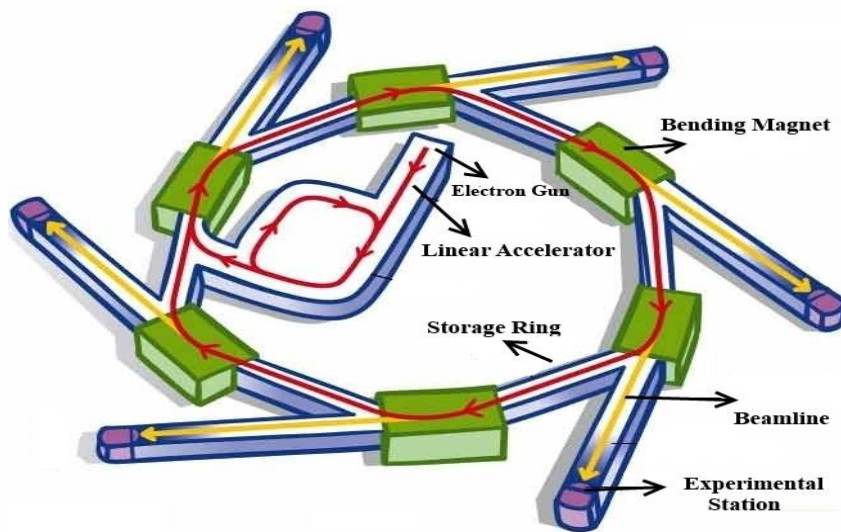


Figure 4.6: The schematic structure of a synchrotron using for X-ray generating, reprinted from Ref. [13].

The storage ring and the beamlines are two main parts of the synchrotron equipment. The storage ring is designed to keep the charged particles circulating

under the vacuum in a closed orbit at the relativistic speed. The Dipole Bending Magnets are used for bending the trajectory of the electrons and forcing them to circulate in the storage ring. The beamlines transfer the produced radiation to the experimental chambers. Also, beamlines help users to select the specific photon energy from the total synchrotron radiation spectrum (according to their applications). The X-ray generated by synchrotron can be widely changeable in the wavelength with much higher intensity than that what obtained by X-ray tubes [10, 12].

4.2.2 X-ray Diffraction

X-ray diffraction is a scientific technique, based on the constructive interference of scattered X-ray beams from a crystalline sample, used for identifying the atomic and molecular structure of a crystal. Scattering can be an elastic or inelastic. In the elastic diffraction, the direction of the beam is changed but the magnitude of the wave vector is fixed. On the contrary, the direction and magnitude of scattered wave vectors will be changed in inelastic scattering. When the interaction of X-rays with the crystal lattices is of concern, the inelastic scattering with high energy is generally neglected. Therefore, only elastic scattering is considered in the X-ray powder diffraction. It is important to remember that X-rays are scattered in the different directions by the electrons in the solid, not the nuclei.

Structure Factor

If the incident X-ray beam with the intensity I_0 traveling along x direction collides with a single electron, the intensity of the scattered X-rays at a distance r from the electron can be defined using the Thomson equation [9]:

$$I = I_0 \left(\frac{K}{r^2} \right) \left(\frac{1 + \cos^2 2\theta}{2} \right), \quad (4.8)$$

where 2θ is the angle between the incident propagation vector and the scattered wave vector and K is the constant ($= 7.94 \times 10^{-30} \text{m}^2$). Calculating the total scattered intensity of the crystal using this equation is challenging. Another way of calculating the scattering amplitude of the X-rays is considering the cloud of electrons around the nucleus. The scattering amplitude of X-rays from an electron density function $\rho(r)$ and the incident wave vector \mathbf{k}_i is given by $\rho(r)e^{i(\mathbf{k}_f - \mathbf{k}_i) \cdot \mathbf{r}}$. The scattering factor per electron, f_e , is found by integrating this scattering amplitude over the occupied volume by the electron:

$$f_e = \int e^{i(\mathbf{k}_f - \mathbf{k}_i) \cdot \mathbf{r}} \rho dV = \int e^{i\mathbf{Q} \cdot \mathbf{r}} \rho dV, \quad (4.9)$$

where \mathbf{k}_f is the scattered X-ray wave vector and \mathbf{Q} is the scattering vector. In elastic scattering $|\mathbf{k}_f| = |\mathbf{k}_i|$, hence:

$$Q = 2k_i \sin\theta = \frac{4\pi}{\lambda} \sin\theta. \quad (4.10)$$

Consider that an atom j is located at \mathbf{r}_j from the origin in a unit cell of a

crystal. Thus, the scattering by atom j is defined by:

$$\mathbf{f}_j = \int e^{i\mathbf{Q}\cdot(\mathbf{r}+\mathbf{r}_j)}\rho(r)dV = f_j e^{i\mathbf{Q}\cdot\mathbf{r}_j}. \quad (4.11)$$

The total scattering power of all atoms in the unit cell, called structure factor, is obtained by the sum of the individual scattering wave:

$$F = \sum_j \mathbf{f}_j = \sum_{j=1}^N f_j e^{i\mathbf{Q}\cdot\mathbf{r}_j}, \quad (4.12)$$

where N is the total number of the atoms in the unit cell. The vector \mathbf{r}_j for the j th atom in the direct lattice can be written as:

$$\mathbf{r}_j = \mathbf{a}_1 x_j + \mathbf{a}_2 y_j + \mathbf{a}_3 z_j, \quad (4.13)$$

and vector \mathbf{Q} in the reciprocal lattice can be expressed as:

$$\mathbf{Q} = \mathbf{b}_1 h + \mathbf{b}_2 k + \mathbf{b}_3 l, \quad (4.14)$$

therefore, the structure factor may be obtained by:

$$F_{hkl} = \sum_j f_j e^{2\pi i(hx_j + ky_j + lz_j)}. \quad (4.15)$$

According to the Equation 4.15, the structure factor can be obtained when the position of the atoms are given [10]. It is noteworthy that the different types of radiations including X-rays, neutrons and electrons can be commonly used in

the powder diffraction experiments, thus all scattering calculations such as the structure factor can be used in the neutron scattering which will be discussed in the Chapter 6.

Bragg's Law

It is known that when the incident radiation is scattered elastically by two or more points in the crystal, spherical waves with the same λ interfere with each other constructively or destructively, depending on their phase difference. If their path difference, Δ , is given by an integer multiple of wavelength λ , the constructive scattered wave can be detected in the powder diffraction. On the other hand, if the path difference is proportional to $\frac{\lambda}{2}$, the waves are completely out of phase and cancel each other, thus no peaks can be detected in the diffraction pattern. This result can be described by the model in the crystallography, named the Bragg's Law.

William Henry Bragg and William Lawrence Bragg described the X-ray diffraction as a reflection of X-rays on the discrete parallel planes separated by a distance d .

In this model, the incident waves with the wavelength λ hit a crystal with parallel planes where all atoms are located in a regular periodic array in each plane. The angle of the incidence beam equals the angle of reflection beam ($\theta_i = \theta_r = \theta$). The constructive difference path of two incident waves in Figure 4.7 is equal to:

$$\Delta = BC + BD = n\lambda, \quad (4.16)$$

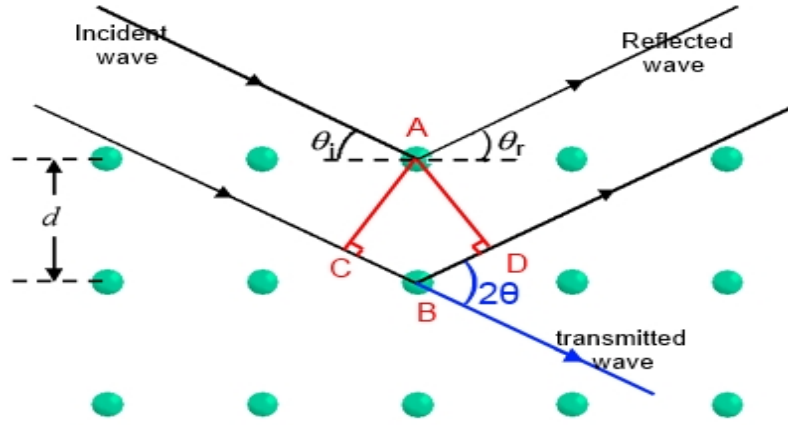


Figure 4.7: The schematic Bragg diffraction. Two beams with an identical wavelength and the same phase approach a crystalline solid and are then scattered off.

where $BC = BD = d \sin \theta$, therefore the constructive interference can be obtained using the Bragg's law [18]:

$$n\lambda = 2d \sin \theta, \quad (4.17)$$

where n is an integer number called an order of the reflection. The angle between the diffracted X-ray beam and the transmitted beam is 2θ , called the diffraction angle, which is seen in Figure 4.7. The maximum value of the wavelength for the diffraction is obtained when $\sin \theta = 1$, therefore X-rays, neutrons and electrons are suitable for the diffraction from crystals with the interatomic distances in the range of 0.1-2 Å, since they have comparable wavelengths. While each set of planes is uniquely identified by its Miller index $(h \ k \ l)$, the Bragg's law may be written in Miller index notation for $n = 1$:

$$\lambda = 2d_{hkl}\sin\theta, \quad (4.18)$$

while $d_{hkl} = \frac{d_{nh\ nk\ nl}}{n}$. The relationship between d and the direct lattice parameters (a, b, c) can be determined geometrically and depends on the crystal structure.

Table 4.3 shows the relation between the lattice spacing, Miller indices and lattice parameters of each crystal structure:

Table 4.3: Geometric relations for the plane spacing (d), Miller indices (h k l) and the lattice parameters (a, b, c) in the different crystal structures [9].

Crystal Structure	d space, lattice parameters and Miller indices
Cubic	$\frac{1}{d^2} = \frac{h^2+k^2+l^2}{a^2}$
Tetragonal	$\frac{1}{d^2} = \frac{h^2+k^2}{a^2} + \frac{l^2}{c^2}$
Hexagonal	$\frac{1}{d^2} = \frac{4}{3} \left(\frac{h^2+hk+k^2}{a^2} \right) + \frac{l^2}{c^2}$
Trigonal	$\frac{1}{d^2} = \frac{(h^2+k^2+l^2)\sin^2\alpha+2(hk+kl+hl)(\cos^2\alpha-\cos\alpha)}{a^2(1-3\cos^2\alpha+2\cos^3\alpha)}$
Orthorhombic	$\frac{1}{d^2} = \frac{h^2}{a^2} + \frac{k^2}{b^2} + \frac{l^2}{c^2}$
Monoclinic	$\frac{1}{d^2} = \frac{1}{\sin^2\beta} \left(\frac{h^2}{a^2} + \frac{k^2\sin^2\beta}{b^2} + \frac{l^2}{c^2} - \frac{2hlc\cos\beta}{ac} \right)$

The intensity of the scattered wave from all atoms in the unit cell is proportional to $\mathbf{F}\mathbf{F}^* = |\mathbf{F}|^2$, thus the diffraction intensity depends on the atomic locations in the specimen. However, additional factors such as the temperature or the multiplicity of Bragg's planes affect the intensity of the diffracted beams [14].

4.2.3 X-ray Powder Diffraction Methods

As mentioned before, the diffraction from the crystal happens while the Bragg's law is satisfied, which requires that an angle θ and wavelength λ are

matched. The experimental diffraction methods are scanning either the angle or the wavelength. The powder diffraction is usually done with two different diffractometers, the Debye-Scherrer powder diffractometer and the Bragg-Brentano diffractometer [9, 10, 14].

Debye-Scherrer Powder Diffractometer

In the Debye-Scherrer powder diffractometer, a monochromatic X-ray beam is used to generate the diffraction pattern. In this technique, the angle is varied by using a powder or a polycrystalline sample with all possible orientations (all possible θ). The sample sealed in a narrow glassy tube is located at the center of the camera, surrounded by a strip of the photographic film. The incident beams are diffracted by the powders according to Bragg's law and produce a set of arcs on the film giving the diffraction lines. The Debye-Scherrer diffraction pattern with the opened film which gives the Debye-Scherrer diffracted lines as shown schematically in Figure 4.8.

Bragg-Brentano Diffractometer Method

The instrumentation for X-ray powder diffractometry has three basic parts: the X-ray source, the detector and the diffractometer. Of the various powder diffractometer designs, the Bragg-Brentano system has become popular. In this design, the mechanical movement can be in two ways: (i) The X-ray tube is fixed. The sample and receiving slit change in the ratio of θ_1 to $2\theta_2$. (ii) The sample is fixed. The tube and receiving slit vary as θ . In both cases, the distance

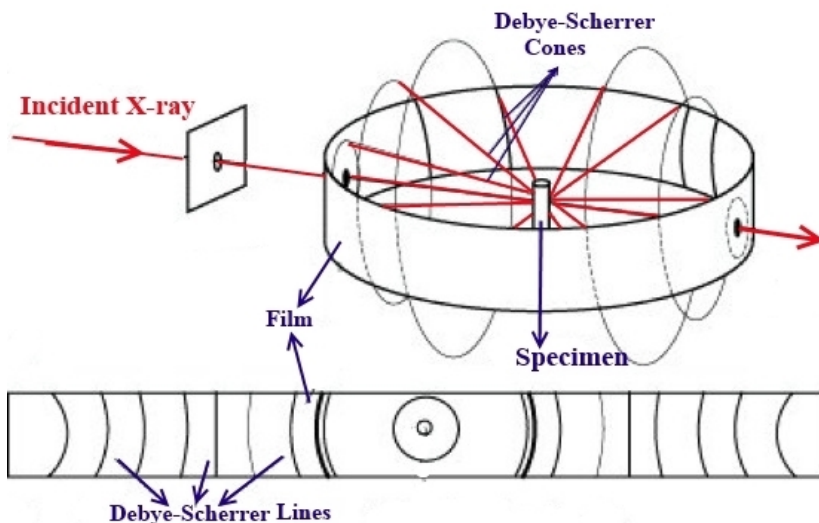


Figure 4.8: The schematic diagram of the Debye-Scherrer powder diffraction method and the opened film represented the diffracted lines [15].

between the tube and the sample, r_1 , is fixed and equal to the distance between the receiving slit and the sample, r_2 . This instrument may have a vertical or horizontal configuration. The incident X-ray beams are reflected by sets of planes in the specimen at the Bragg's angles after passing through a parallel plate set collimator called soller slits and, then, they are focused at the receiving slit and enter a detector. The receiving slit and the detector are coupled and rotate around the sample in order to scan the scattered angles. Figure 4.9 visualizes the vertical geometric Bragg-Brentano diffractometer design including the X-ray source and the detector.

4.2.4 Crystallite Size

Polycrystalline materials or powders are composed of many crystallites which are randomly oriented. The size of crystallites may vary from few nanometers to

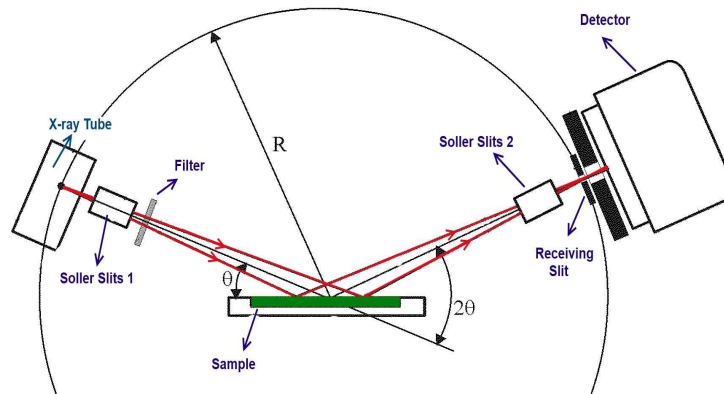


Figure 4.9: The vertical geometric arrangement of the Bragg-Brentano diffractometer, reprinted from Ref [16].

the several millimeters. Crystal size can be measured using the Scherrer equation in the powder diffraction measurement [17]:

$$D = \frac{K\lambda}{\beta \cos\theta}, \quad (4.19)$$

where D , λ and θ are the crystallite size, incident wavelength and the Bragg angle, respectively. β is the line broadening at half the maximum intensity (FWHM), after subtracting the instrumental line broadening (β_{inst}) from the observed line broadening (β_{obs}), in radians, i.e. $\beta^2 = \beta_{obs}^2 - \beta_{inst}^2$. K is a dimensionless shape factor, with a typical value of about 0.9, but varies with the actual shape of the crystallite.

For sufficiently large and strain free particles, the diffraction pattern lines are supposed to be exceedingly sharp. In actual experiments, the completely sharp lines are never observed, due to the factors such as the instrumental effect.

Furthermore, the size of the particles broadens the diffraction pattern [14].

In general, the scattering angle (2θ) in the powder diffraction is inversely proportional to the diameter of the particle while it is considered as a small angle ($\sin\theta \approx \tan\theta \approx \theta$):

$$2\theta = \frac{\lambda}{l}, \quad (4.20)$$

where λ and l are the incident wavelength radiation and particle diameter, respectively.

The FWHM in the diffraction pattern changes as the scattering angle varies, thus:

$$FWHM \propto \frac{\lambda}{l}. \quad (4.21)$$

Therefore, the diffraction peaks become sharper and narrower as crystallites become larger, however, smaller crystals give broader diffraction peaks. Figure 4.10 explains the scattering pattern in a sample with the small particles (l_1) compared to a sample with the large particles (l_2). As $l_1 < l_2$ then $FWHM_1 > FWHM_2$ [18].

4.2.5 Experiment

The X-ray diffraction measurements were carried out at room temperature using the Rigaku Multiflex X-ray diffractometer, using Cu K_α radiation ($\lambda = 1.5405 \text{ \AA}$) at the University of Calgary, Canada and the STOE Stadi P diffractometer, using Mo $K_{\alpha 1}$ radiation ($\lambda = 0.70930 \text{ \AA}$) at the Max Planck Institute for Solid State Research, Germany.

The Rigaku Multiflex X-ray diffractometer consists of 2 kW copper target

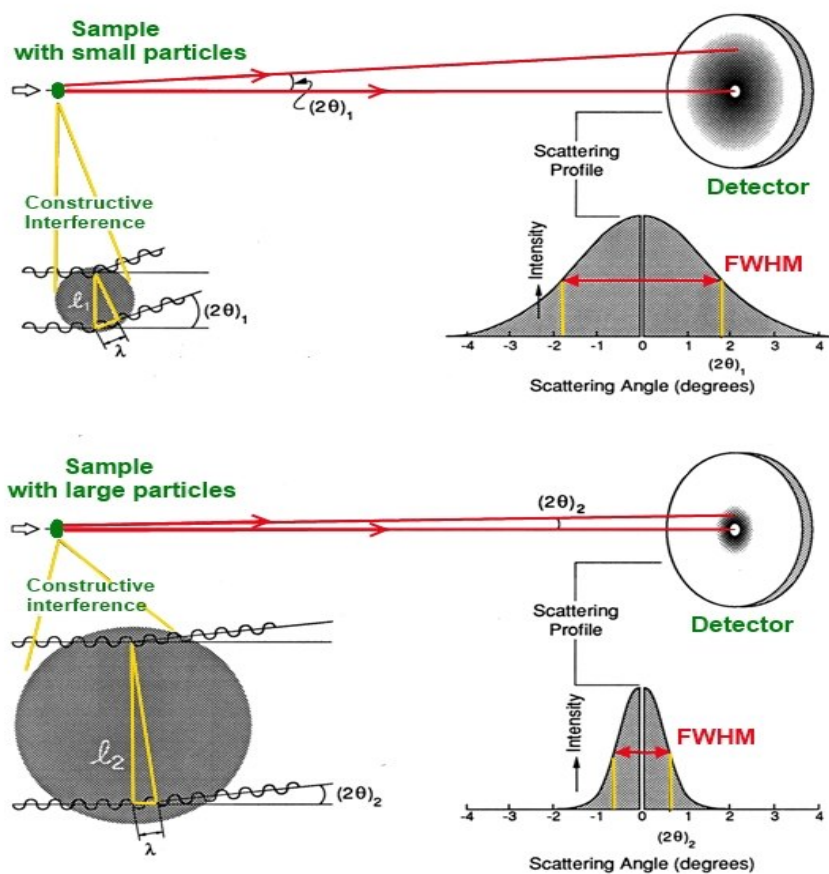


Figure 4.10: Scattering width peaks comparison in the scattering from samples with the small particles and the large particles, reprinted from Ref. [19].

and θ - 2θ goniometer. The sample holder remains horizontal during the scan and therefore, there is no need to use adhesive substances to mount the samples, which is an ideal configuration when dealing with loose powders. Using this instrument, we are able to measure up to six samples in succession automatically. The generator voltage and the tube current used in this work, were set at 40 kV and 20 mA, respectively. The scattered X-rays were counted at the angle range of $2\theta = 20^\circ$ to 90° with 0.02 increments.

First, the sintered pellets were ground manually with a mortar and pestle and a drop of acetone to make a homogeneous and soft powder. Second, they were filled into the aluminum holders. The excess powders were removed with a clean glass slide to make a flat surface, then they were mounted in the diffractometer and the measurements were taken.

The Stoe Stadi P diffractometer is a two-circle goniometer with the Debye-Scherrer geometry which has a pure $K_{\alpha 1}$ radiation using the Mo source. Samples were mounted in a 3 mm vertical quartz capillary sample holder which is about 4 cm in length. The generator voltage and the tube current were set at 50 kV and 40 mA, respectively and the scattered X-rays were counted at the range of $2\theta = 5^\circ$ to 50° with 0.01 increments. The Rietveld refinement of the diffraction patterns was carried out, using the *FullProf* Suite program [23]. Figure 4.11 shows the sample holders and the diffractometers used for the X-ray measurement in this project.

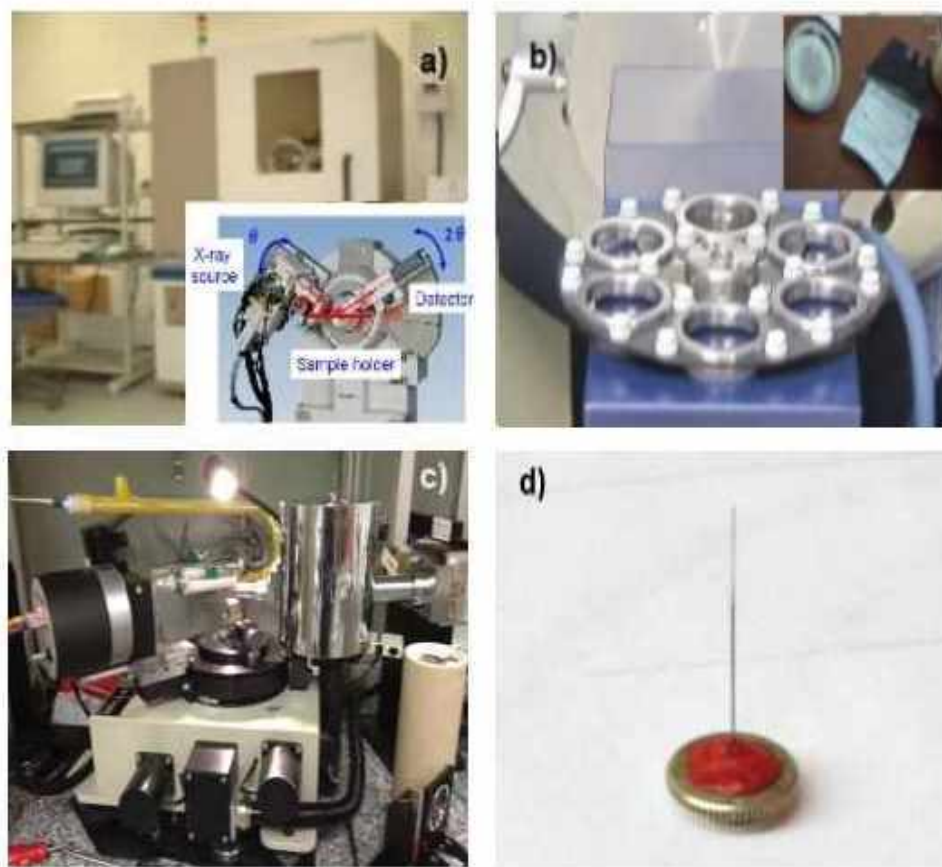


Figure 4.11: (a) The Rigaku Multiflex X-ray diffractometer, (b) a horizontal sample holder, (c) the Stoe Stadi P diffractometer and (d) a vertical capillary sample holder.

X-ray Diffraction Results

The room temperature X-ray diffraction patterns of the sample CeCrO_3 ($x = 0.0$) sintered at 950°C for 12 h in oxygen, argon and air, using Cu K_α radiation, are shown in Figure 4.12. The results confirmed the mixture of Cr_2O_3 and CeO_2 oxides as the major phases.

However, the XRD pattern of the CeCrO_3 sample, sintered at 950°C for 12 h in ($90\% \pm 5\%$) argon and ($10\% \pm 5\%$) hydrogen, shows a different pattern. The pattern in Figure 4.13 confirms the formation of the single orthorhombic phase of CeCrO_3 with no impurity. Therefore, all other samples were prepared in the same sintering condition.

Figure 4.14 represents the database X-ray diffraction patterns of CeO_2 , Cr_2O_3 and CeCrO_3 , using Cu K_α radiation, which are used as the references.

The refined crystal structure of CeCrO_3 done with $\text{Mo K}_{\alpha 1}$ radiation, is shown in Figure 4.15. Apart from the Bragg reflections, which are attributed to CeCrO_3 , no other Bragg reflection could be discerned in the pattern; thus, it confirms the formation of the single phase orthorhombic structure with the space group of $Pbnm$, having no impurity. The (h k l) Miller indices of the Bragg's reflections are given in the XRD pattern. The broad diffracted peaks suggest the formation of the nano-size particles.

The obtained lattice parameters of CeCrO_3 at 300 K, given in the Table 4.4, reveal that a and b parameters are almost identical and different from c parameter, suggesting that this compound is close to the tetragonal structure.

Table 4.5 shows the positions of the atoms in group 62 ($Pbnm$). The point

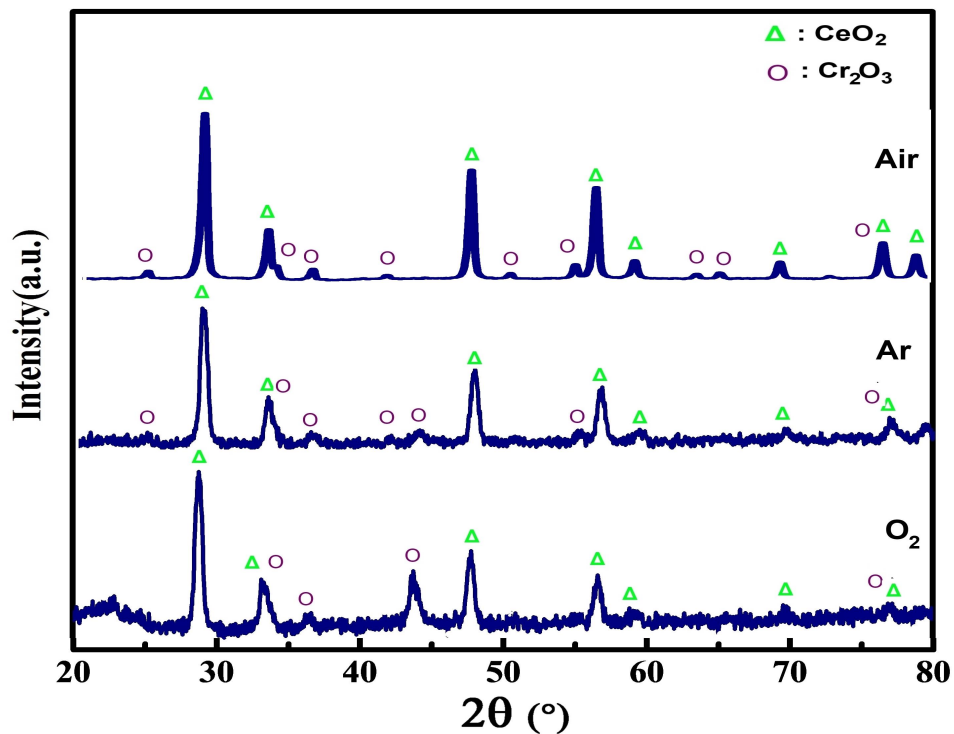


Figure 4.12: XRD patterns of CeCrO₃, sintered at 950°C for 12 h in oxygen, argon and air, using Cu K_α radiation.

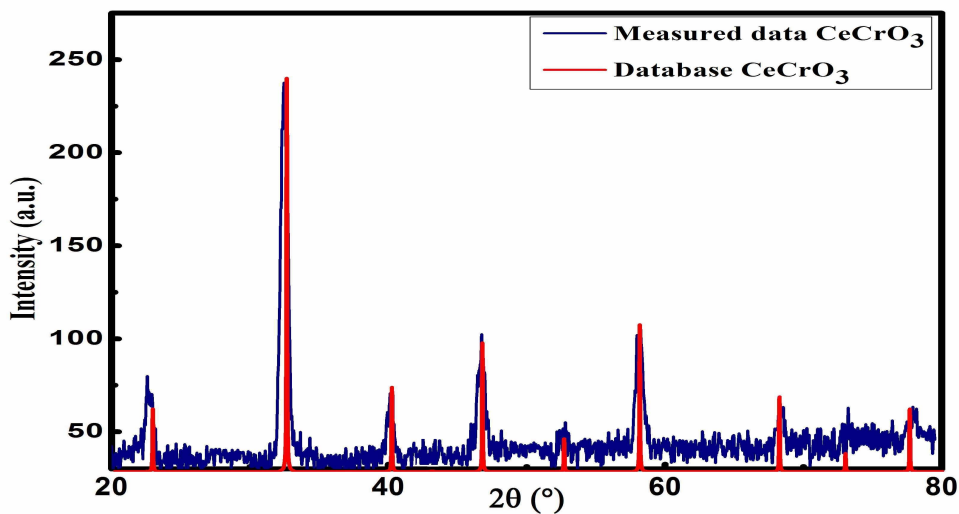


Figure 4.13: XRD pattern of CeCrO₃, sintered at 950°C for 12 h in the mixture of argon and hydrogen, using Cu K_α radiation. The red lines show the CeCrO₃ data base, obtained from Ref. [20].

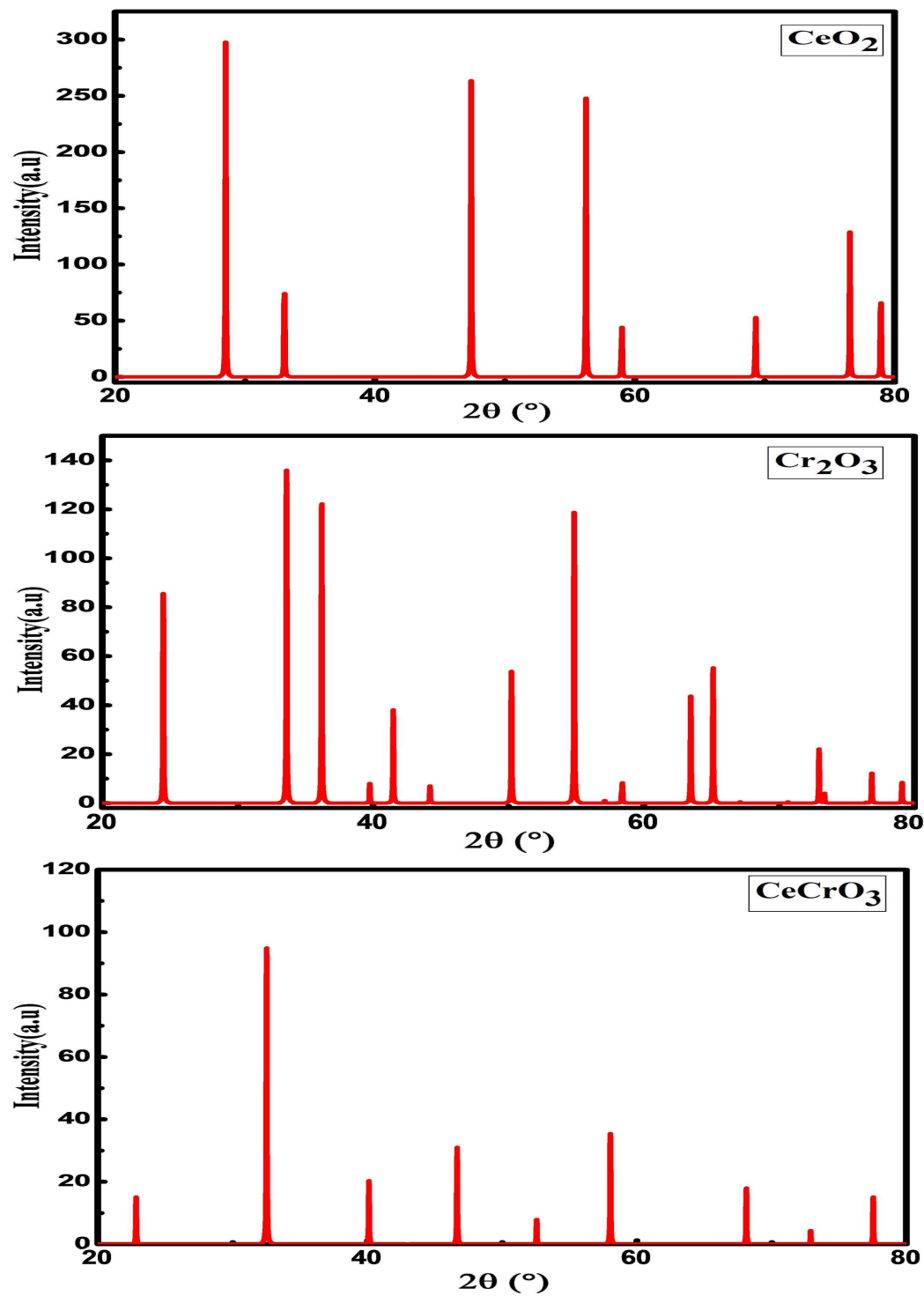


Figure 4.14: The database XRD patterns of CeO_2 , Cr_2O_3 and CeCrO_3 as the references, using $\text{Cu K}\alpha$ wavelength [21, 22, 20].

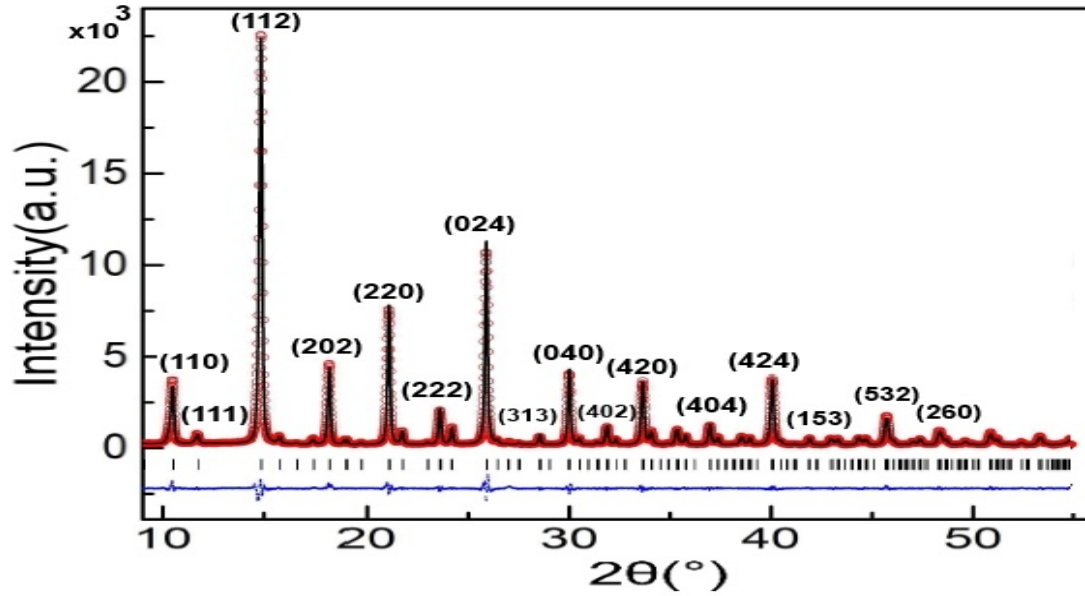


Figure 4.15: Refined XRD pattern of CeCrO₃, sintered at 950 °C for 12 h, using Mo K_{α1} radiation. Red, black and blue lines refer to the observed, fitted and the difference between experimental and fitted X-ray diffraction patterns. The bars show the position of the Bragg's reflections.

Table 4.4: The lattice parameters (a, b, c) and unit cell volume (V) of CeCrO₃ at 300 K.

a (Å)	b (Å)	c (Å)	V (Å ³)
5.47470(13)	5.48911(12)	7.72998(16)	232.2954(41)

group mmm is the centrosymmetric orthorhombic group, which is a shortened form of the full symbol $2/m\ 2/m\ 2/m$. It has three mirrors and three 2-fold rotation axes [25].

Table 4.5: Wyckoff positions of group 62 ($Pbnm$).

Multiplicity	Wyckoff letter	Coordinates
8	d	(x,y,z) $(-x+\frac{1}{2},y+\frac{1}{2},z)$ $(-x,-y,z+\frac{1}{2})$ $(x+\frac{1}{2},-y+\frac{1}{2},z+\frac{1}{2})$ $(-x,-y,-z)$ $(x,y,-z+\frac{1}{2})$ $(x+\frac{1}{2},-y+\frac{1}{2},-z)$ $(-x+\frac{1}{2},y+\frac{1}{2},-z+\frac{1}{2})$
4	c	$(x,y,\frac{1}{4})$ $(-x+\frac{1}{2},y+\frac{1}{2},\frac{1}{4})$ $(-x,-y,\frac{3}{4})$ $(x+\frac{1}{2},-y+\frac{1}{2},\frac{3}{4})$
4	b	$(0,\frac{1}{2},\frac{1}{2})$ $(\frac{1}{2},0,0)$ $(0,\frac{1}{2},0)$ $(\frac{1}{2},0,\frac{1}{2})$

In the perovskite orthorhombic structure of RCrO_3 , each chromium atom is placed at the center of the octahedra which consists of six oxygen atoms. According to the Wyckoff positions of group $Pbnm$, Cr^{3+} ions are located at the 4b Wyckoff position, surrounded by two groups of oxygen: two apical oxygen atoms (4c Wyckoff position) and four equatorial oxygen atoms (8d Wyckoff position). Cerium atoms are placed at a 4c Wyckoff position, surrounded by four apical and eight equatorial oxygen atoms. Figure 4.16 depicts the crystal structure of CeCrO_3 , using VESTA crystallographic software.

Due to the structure distortion, the apical and equatorial bond angles and distances might not be equal. Figure 4.17(a) shows two CrO_6 octahedral, connected

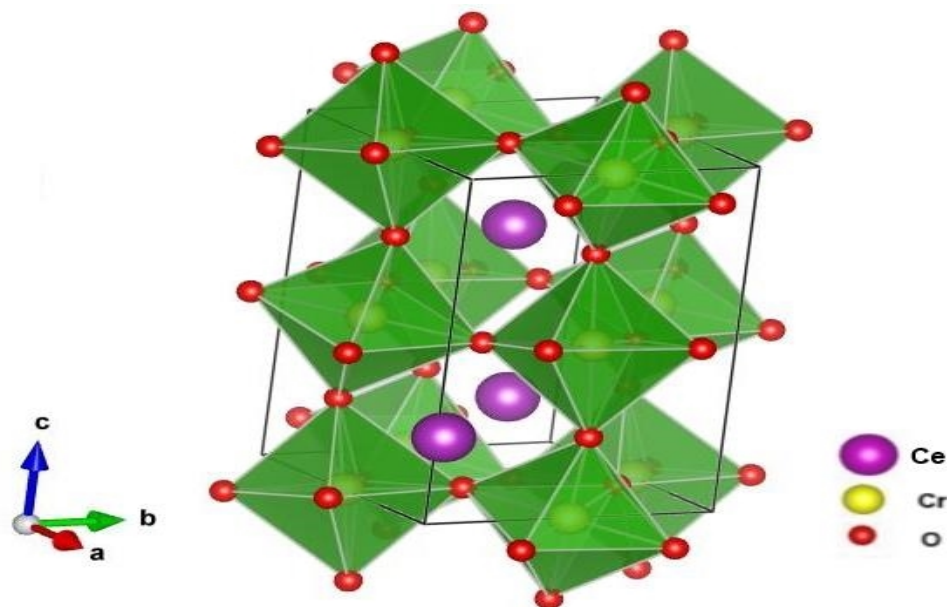


Figure 4.16: The orthorhombic crystal structure of the CeCrO_3 powder. Cr^{3+} (yellow atoms) are located at the center and O^{2-} (red atoms) are at the corners of the octahedral. The purple balls are Ce^{3+} cations.

to each other with an angle smaller than 180° , showing the octahedra distortion in CeCrO_3 . Figure 4.17(b) and (c) represent the cerium ion placed between the apical oxygen atoms (O_1) and equatorial oxygen atoms (O_2) in the CeCrO_3 orthorhombic structure. The calculated unequal bond lengths of Ce-O are the evidence of the cerium off-centering compared to its position in the ideal perovskite structure. The obtained values of all bond lengths and angles are given in Table 4.8.

Substitution of cerium(III) with europium(III) causes the gradual shift in X-ray diffraction patterns, due to the smaller size of the Eu^{3+} ion compared to Ce^{3+} ion. Figure 4.18 illustrates X-ray diffraction patterns of $\text{Ce}_{1-x}\text{Eu}_x\text{CrO}_3$ powders with Cu K_α wavelength at room temperature, where $x = 0.0$ to 0.9 .

The refined crystal structures of $\text{Ce}_{1-x}\text{Eu}_x\text{CrO}_3$ powders where $x = 0.1, 0.3, 0.5, 0.6$, done with Mo $K_{\alpha 1}$ wavelength are observed in Figure 4.19. The refined

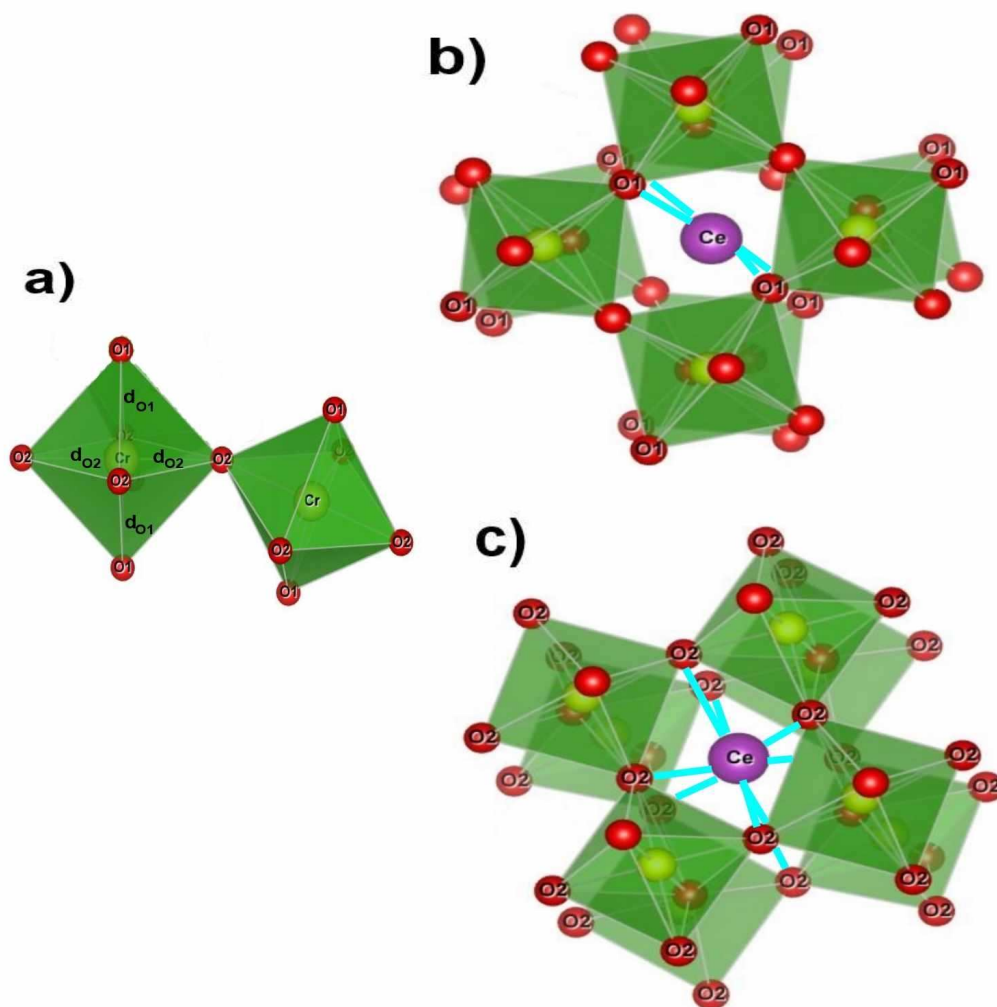


Figure 4.17: (a) Two distorted CrO_6 octahedral that each chromium atom surrounded by two apical oxygen atoms (O_1) and four equatorial oxygen atoms (O_2), (b) and (c) cerium atom placed between four O_1 and eight O_2 with the different Ce-O_1 and Ce-O_2 bond lengths in the CeCrO_3 crystal structure. Ce^{3+} , Cr^{3+} and O^{2-} atoms are shown using purple, yellow and red balls, respectively.

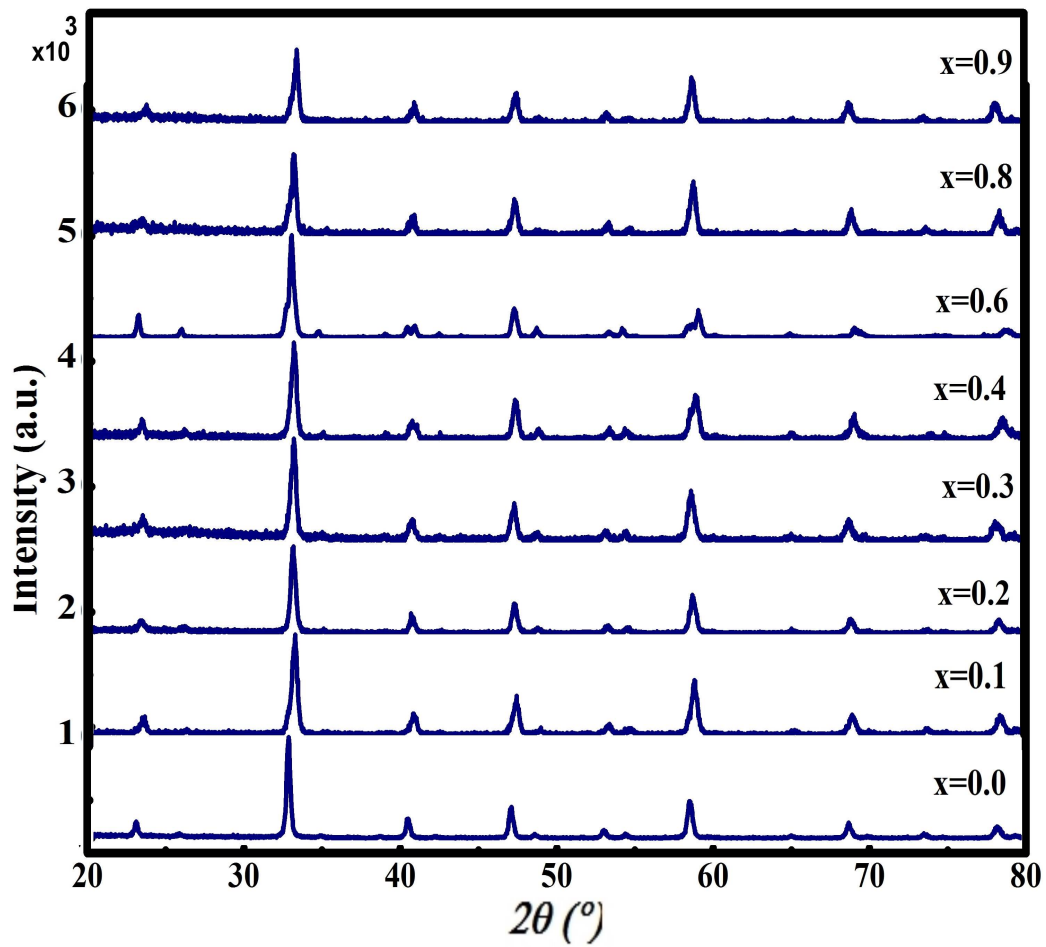


Figure 4.18: XRD patterns of samples $\text{Ce}_{1-x}\text{Eu}_x\text{CrO}_3$, sintered at 950°C for 12 h, using $\text{Cu K}\alpha$ radiation which indicate a small shift in the peaks.

data confirmed the distorted orthorhombic structure in all samples.

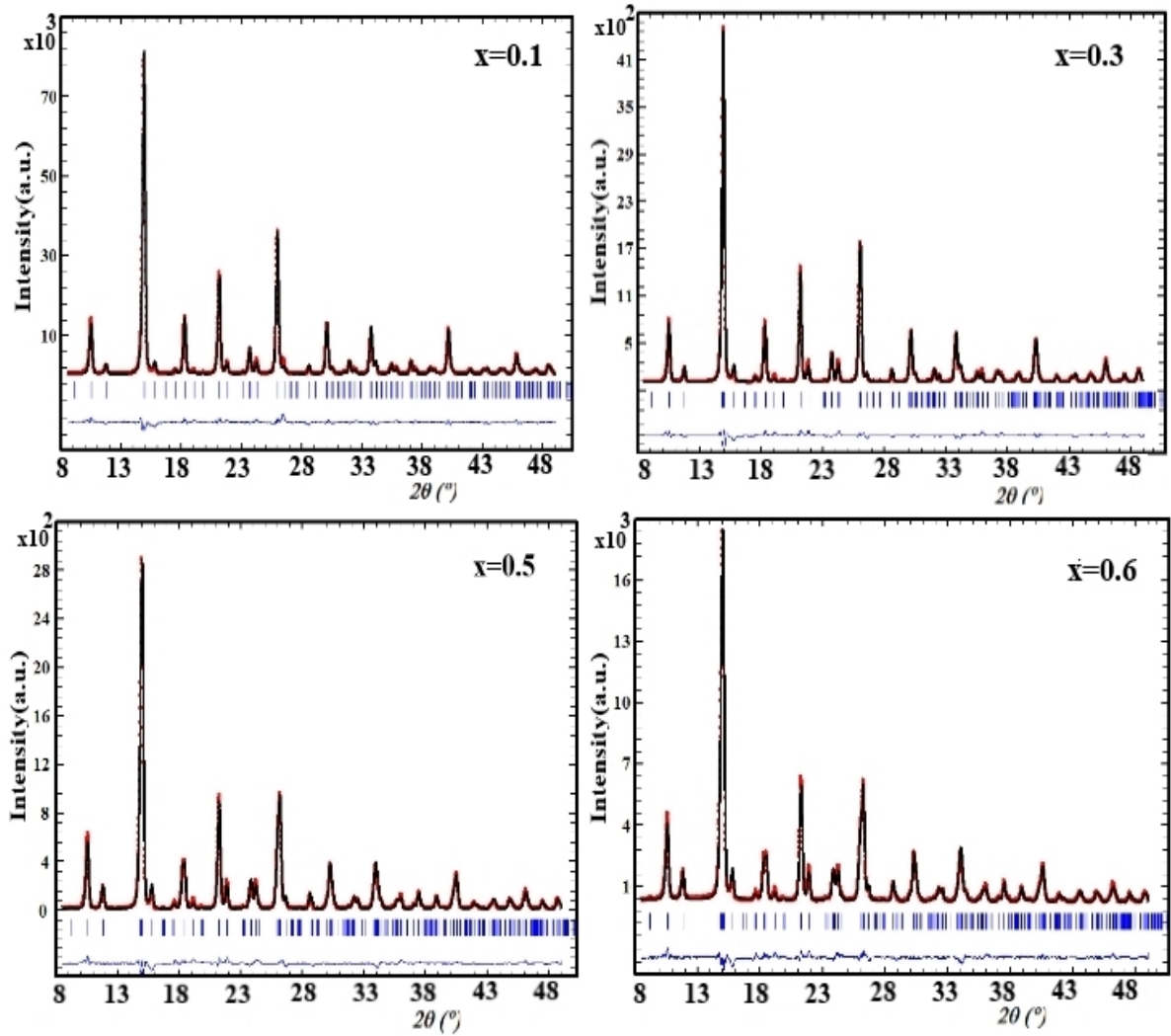


Figure 4.19: Refined XRD patterns of $\text{Ce}_{1-x}\text{Eu}_x\text{CrO}_3$, where $x = 0.1, 0.3, 0.5$ and 0.6 , sintered at $950\text{ }^\circ\text{C}$ for 12 h, using $\text{Mo K}\alpha_1$ wavelength.

The refined crystal structure of EuCrO_3 , using $\text{Mo K}\alpha_1$ radiation, plotted in Figure 4.20, shows the pure single phase of orthorhombic structure. The $(h\ k\ l)$ Miller indices are observed in the X-ray pattern, as well.

The obtained lattice parameters of EuCrO_3 at 300 K are shown in the Table 4.6, confirming the orthorhombic structure in this compound. By comparing the

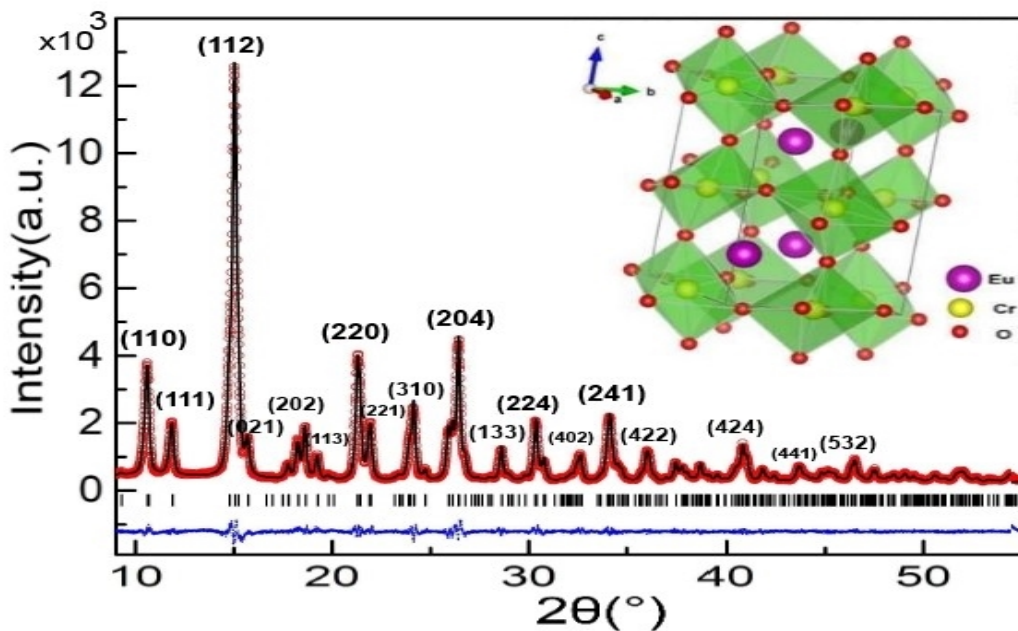


Figure 4.20: Refined XRD pattern of EuCrO_3 , using $\text{Mo K}\alpha_1$ radiation, sintered at 950°C for 12 h. The upper image shows the crystal structure of EuCrO_3 , visualized by VESTA crystallographic program.

lattice parameters of samples CeCrO_3 and EuCrO_3 (Tables 4.4 and 4.6), it is evident that a and b parameters in CeCrO_3 are almost equal, however, they are different from each other in EuCrO_3 .

Table 4.6: The lattice parameters and unit cell volume of EuCrO_3 at 300 K.

a (\AA)	b (\AA)	c (\AA)	V (\AA^3)
5.34622(9)	5.51116(8)	7.62931(13)	224.7890(30)

Apparent broadening of the Bragg reflections of the EuCrO_3 sample was modeled by expanding the particle size and shape into the spherical harmonics,

$c_{mn}Y_{mn}$, with $m = 0, 2, 4$ and even n ; $n \leq m$ appropriate for Laue class mmm (*FullProf* size model no. 18) and fitting the expansion coefficients c_{mn} , (Figure 4.21). A prolate-type particle shape is observed with the waist somewhat bulged. The largest extension of the particle size of about 40 nm is observed along the crystallographic c axis.

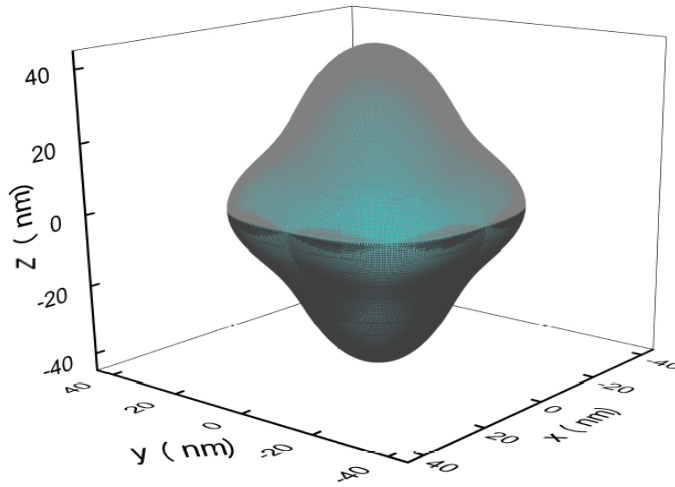


Figure 4.21: Average shape and size of the EuCrO_3 nano-particles, determined from X-ray diffraction by modeling the broadening of the Bragg reflections with spherical harmonics (*FullProf* program, model-size = 18).

The atomic positions and other conventional structural parameters obtained from the X-ray Rietveld refinements of CeCrO_3 and EuCrO_3 samples at $T = 300$ K are given in Table 4.7.

On the other hand, the chromium, cerium and europium atoms are connected to the oxygen atoms with unequal bond lengths. The distortion parameter Δ is an estimation parameter to show the value of the distortion in the polyhedron AO_N , where A is the cation in a given polyhedron. This parameter is defined through the equation [26]:

Table 4.7: Structural parameters and conventional reliability indices obtained from the Rietveld refinement of the X-ray diffraction patterns of CeCrO_3 and EuCrO_3 with the space group of $Pbnm$ at room temperature. An absorption corrections for the XPD of CeCrO_3 and EuCrO_3 were performed assuming $\mu R \sim 0.85$ cm and 1 cm, respectively [24]

Sample	CeCrO_3	EuCrO_3
Ce-Eu (4c)		
x	-0.00290(3)	-0.01313(17)
y	0.02830(15)	0.05413(9)
z	0.250	0.250
B_{iso} (\AA^2)	0.48(28)	0.14(11)
Occ	0.5	0.5
Mult	4	4
Cr (4b)		
x	0.500	0.500
y	0.000	0.000
z	0.000	0.000
B_{iso} (\AA^2)	0.58(2)	0.18(3)
Occ	0.5	0.5
Mult	4	4
O1 (4c)		
x	0.0630(3)	0.0940(2)
y	0.4810(2)	0.4600(1)
z	0.250	0.250
B_{iso} (\AA^2)	0.70(1)	0.70(0)
Occ	0.5	0.5
Mult	4	4
O2 (8d)		
x	-0.2810(2)	-0.2886(13)
y	0.2860(2)	0.2987(12)
z	0.0420(1)	0.0483(10)
B_{iso} (\AA^2)	0.70(1)	0.74(25)
Occ	1.0	1.0
Mult	8	8
Bragg-R-		
factor (%)	1.96	1.72
R_f -fact. (%)	1.43	1.09

$$\Delta = \frac{1}{N} \sum_1^N \left\{ \frac{d_N - \langle d \rangle}{\langle d \rangle} \right\}^2, \quad (4.22)$$

where $\langle d \rangle$ is an average value of bond length. Table 4.8 compares the calculated bond lengths, angles and distortion parameters in CeCrO_3 and EuCrO_3 samples at $T = 300$ K.

The results show that the value of Cr-O-Cr is not the ideal value of 180° , indicating the distortion of the orthorhombic structure which causes the weak ferromagnetism in these perovskite structure. The unequal Ce-O bond lengths in CeCrO_3 and Eu-O bond lengths in EuCrO_3 prove the off-centering displacement of the rare earth ion, which might yield the ferroelectricity in these compounds. In other words, the results reveal the larger symmetry reduction and distortion enhancement in EuCrO_3 compared to CeCrO_3 .

Furthermore, the average Cr-O distance in CeCrO_3 is smaller, thus the Coulomb repulsion energy between Cr^{3+} and O^{2-} ions is larger, indicating the larger overall splitting of the t_{2g} energy levels of chromium, i.e. the splitting of the xy, xz and yz energy levels will be larger for CeCrO_3 than for EuCrO_3 .

The values of average interatomic bond angles and distances of $\text{Ce}_{1-x}\text{Eu}_x\text{CrO}_3$ at 300 K are shown in Table 4.9, where the Cr-O-Cr angle decreases and the average value of the Cr-O bond length slightly increases. According to the literature, the suppression of the Cr-O-Cr super exchange angle leads to a decrease in the $\text{Cr}(t_{2g}^3)\text{-O-Cr}(t_{2g}^3)$ hybridization and an increase in $\text{Cr}(t_{2g}^3)\text{-O-Cr}(e_g^0)$ overlapping, suggesting the distortion improvement and weak ferromagnetism enhancement [27, 28].

Table 4.8: The interatomic distances (d), average distances ($\langle d \rangle$), distortion parameter (Δ) and angles at 300 K obtained from the Rietveld refinement of the XRD patterns of CeCrO_3 and EuCrO_3 .

Sample	CeCrO_3	EuCrO_3
$d_{Cr-O_1} \times 2$ (Å)	1.983(6)	1.986(1)
$d_{Cr-O_2} \times 2$ (Å)	1.954(7)	1.935(6)
$d_{Cr-O_2} \times 2$ (Å)	1.988(0)	2.020(7)
d_{R-O_1} (Å)	3.137(8)	3.236(0)
d_{R-O_1} (Å)	3.000(4)	3.185(1)
d_{R-O_1} (Å)	2.541(0)	2.402(4)
d_{R-O_1} (Å)	2.343(4)	2.223(2)
$d_{R-O_2} \times 2$ (Å)	2.417(0)	2.403(4)
$d_{R-O_2} \times 2$ (Å)	2.759(1)	2.649(4)
$d_{R-O_2} \times 2$ (Å)	2.621(8)	2.582(9)
$d_{R-O_2} \times 2$ (Å)	3.211(6)	3.329(1)
$\langle d_{Cr-O} \rangle$ (Å)	1.9754(3)	1.980(8)
$\langle d_{R-O} \rangle$ (Å)	2.7540(1)	2.7514(4)
Δ_{Cr-O}	5.59055×10^{-5}	3.11208×10^{-4}
Δ_{R-O}	0.01257	0.02175
Cr-O ₁ -Cr (deg)	155.39(16)	147.37(13)
Cr-O ₂ -Cr (deg)	157.12(11)	151.28(9)
R-O ₁ -R (deg)	84.44(7)	82.81(7)
R-O ₂ -R (deg)	98.79(7)	77.09(4)

Table 4.9: Average interatomic distances ($\langle d \rangle$) and angles at 300 K of $\text{Ce}_{1-x}\text{Eu}_x\text{CrO}_3$ obtained from the Rietveld refinement of the XRD patterns.

Value	x = 0.1	x = 0.3	x = 0.5	x = 0.6
$\langle d_{Cr-O} \rangle$ (Å)	1.9689(7)	1.9686(0)	1.9706(3)	1.9764(7)
$\langle d_{R-O} \rangle$ (Å)	2.7504(7)	2.7505(9)	2.7505(0)	2.7520(2)
Cr-O ₂ -Cr (deg)	157.08(5)	157.78(17)	155.54(10)	154.13(9)
Cr-O ₁ -Cr (deg)	155.10(8)	156.19(10)	153.33(16)	150.77(14)
R-O ₂ -R (deg)	83.53(4)	79.93(5)	79.06(5)	78.69(5)
R-O ₁ -R (deg)	101.61(3)	86.18(8)	84.86(8)	83.51(7)

The average crystallite size of $\text{Ce}_{1-x}\text{Eu}_x\text{CrO}_3$ samples were calculated in the range of 22-45 nm. They were obtained from the Rietveld refinement using the Scherrer formula [17].

The stability of perovskite structures can be calculated using Goldschmidt's tolerance factor (Equation 4.5) [5] using $r_{Ce} = 1.34$ Å, $r_{Eu} = 1.12$ Å, $r_{Cr} = 0.615$ Å and $r_O = 1.40$ Å for the ionic radii of cerium and europium (in the coordination 12), chromium (in the coordination 6) and oxygen ions, respectively [29]. The ionic radius size of the A cation for a doped sample is defined by $r_A = (1-x)r_{Ce} + xr_{Eu}$. The calculated tolerance factors for CeCrO_3 and EuCrO_3 are 0.961 ± 0.05 and 0.884 ± 0.04 , respectively, indicating that the tolerance factor will move away from 1 to the smaller values by replacing Ce(III) ion by Eu(III) ion, i.e. by an element with the smaller ionic radius, allowing to explain why EuCrO_3 is orthorhombic whereas CeCrO_3 is almost tetragonal structure. Figure 4.22(a) represents how the tolerance factor decreases and moves away from 1 by increasing

europium substitution in $\text{Ce}_{1-x}\text{Eu}_x\text{CrO}_3$ compounds.

Obviously, the mismatch of the dopant atoms strongly influences the lattice parameters and unit cell of the perovskites. Figure 4.22(b), (c) and (d) show the change of the lattice parameters and unit cell of the $\text{Ce}_{1-x}\text{Eu}_x\text{CrO}_3$ powders while doping. The results show that a and c lattice parameters decrease and b parameter increases. Furthermore, as mentioned before, a and b parameters in CeCrO_3 are close to each other, however, they are split from each other by an increase in dopant in $\text{Ce}_{1-x}\text{Eu}_x\text{CrO}_3$. The unit cell volume decreases by increasing the Eu concentration as well.

In order to study the deformation of the lattice symmetry compared to the ideal cubic structure, other parameters were calculated, i.e. the ratio of $\frac{c}{(a+b)/2}$ versus $\frac{b}{a}$, $\varepsilon = 2\frac{(a-b)}{(a+b)}$ and the atomic positions of Ce/Eu versus europium substitution are plotted in Figure 4.24.

The value of $\frac{b}{a}$ is close to 1 for CeCrO_3 sample ($x = 0.0$) and increases while increasing x. The ratio of the $\frac{c}{(a+b)/2}$ versus $\frac{b}{a}$, which is the square root of 2 for the perovskite type, shown in Figure 4.23(a), represents that the structure becomes orthorhombic when a and b parameters split from each other.

The parameter $\varepsilon = 2\frac{(a-b)}{(a+b)}$ is called the spontaneous orthorhombic strain, where its absolute value increases from 0.0 with increasing Eu content, suggesting the octahedra tilting enhancement (Figure 4.23(b)). Figure 4.23(c) and (d) indicate a decrease in the x atomic position and an increase in the y atomic position of Ce/Eu in $\text{Ce}_{1-x}\text{Eu}_x\text{CrO}_3$ samples.

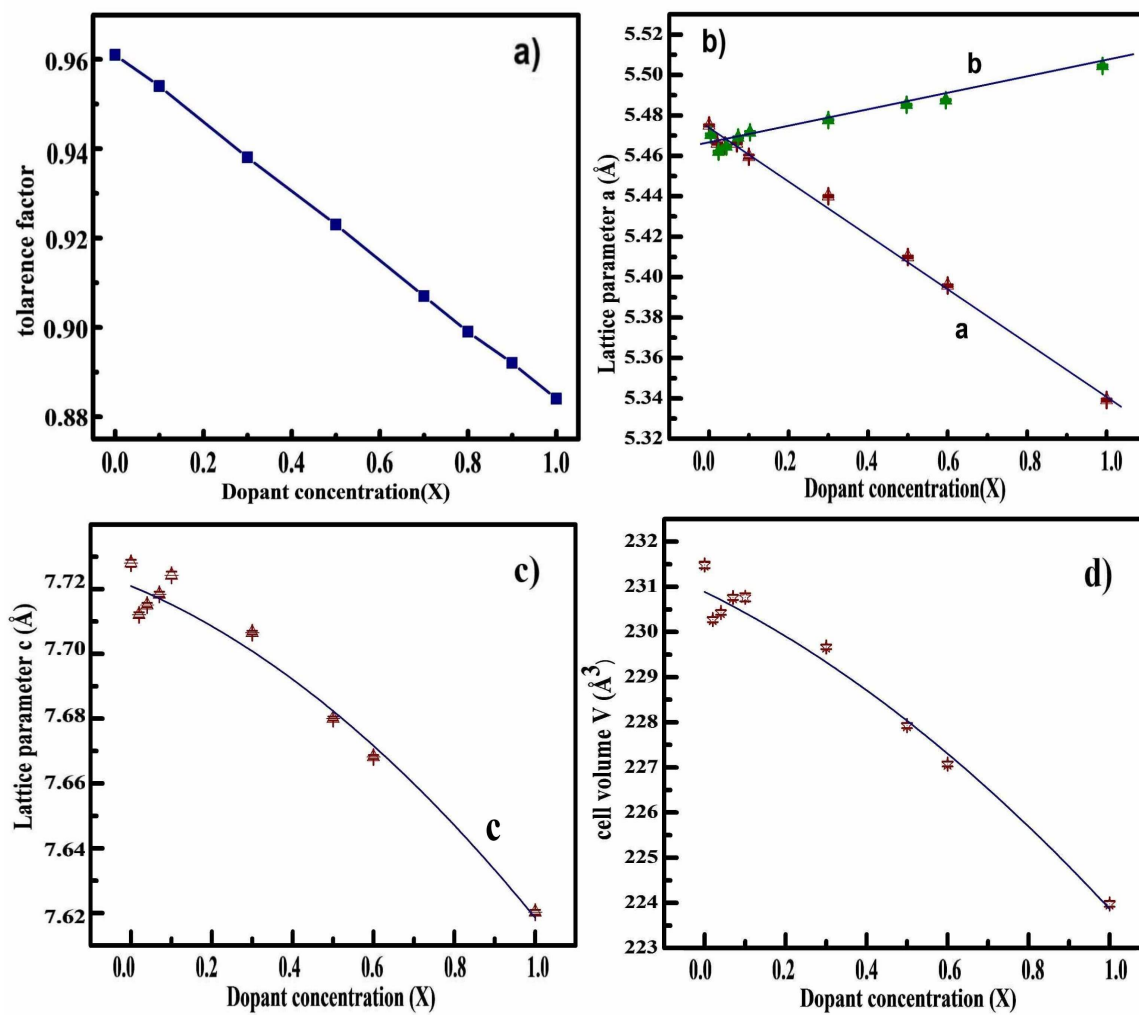


Figure 4.22: (a) Tolerance factor, (b) and (c) lattice parameters and (d) volume unit cell of $\text{Ce}_{1-x}\text{Eu}_x\text{CrO}_3$ versus europium concentration (X).

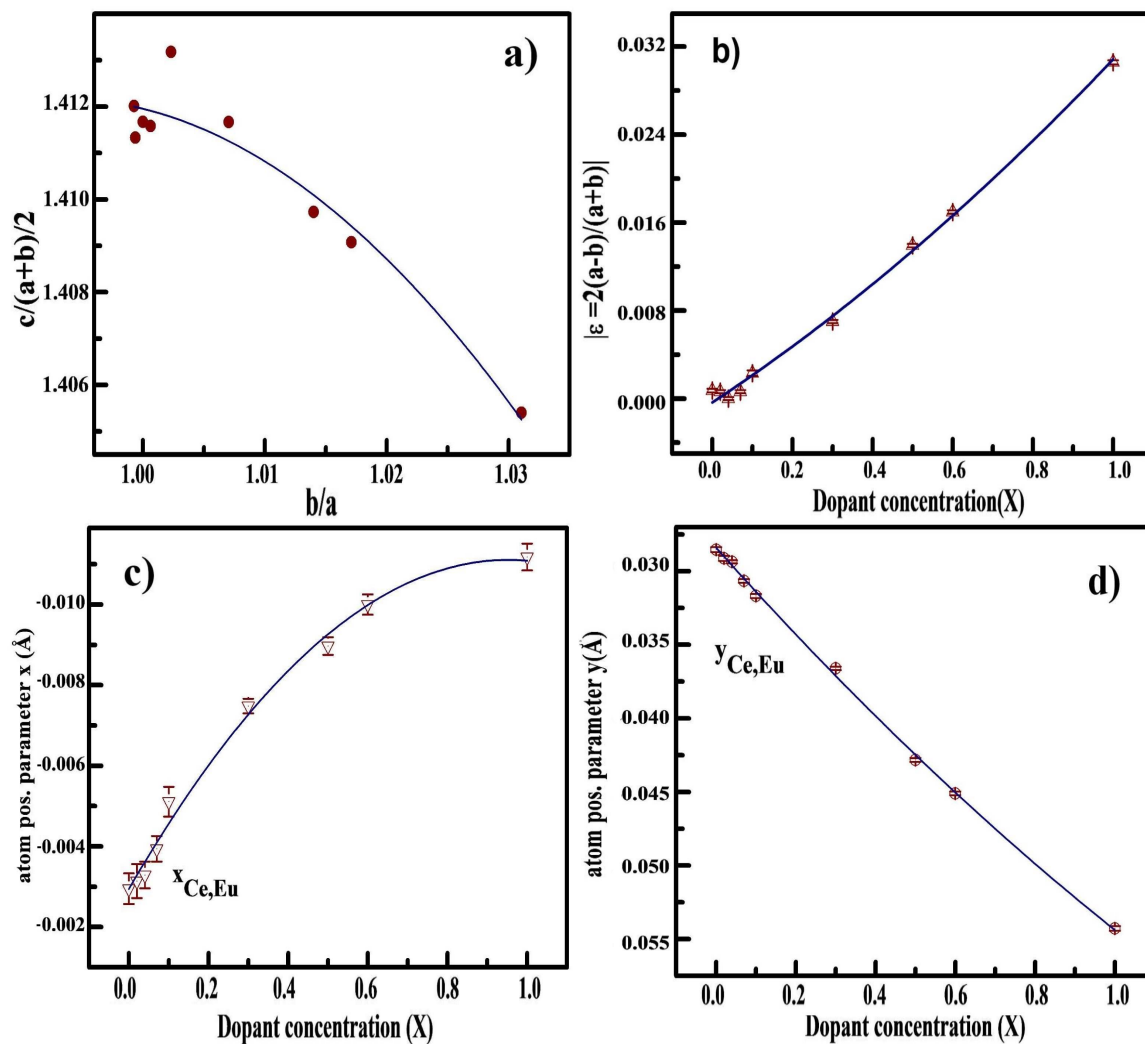


Figure 4.23: (a) Value of $\frac{c}{(a+b)/2}$ versus b/a , (b) the ratio of the $|2(a-b)/(a+b)|$ versus europium concentration, (c) and (d) the x and y atomic positions of Ce/Eu versus europium concentration (X).

4.3 X-Ray Photoelectron Spectroscopy

X-ray Photoelectron Spectroscopy (XPS), also known as the X-ray photoemission spectroscopy, is one of the most sensitive techniques which is able to provide atomic and molecular information of the surface of the material [30].

The XPS spectra are obtained by irradiating the surface of the material (up to 10 nm) with a monochromatic X-ray beam (0.2-2 keV). Thus, the electrons escape from the surface and the kinetic energy and the number of emitted electrons are simultaneously recorded.

In XPS measurement, each core atomic orbital for each element has the specific binding energy which is observed as a characteristic set of peaks in the XPS spectrum. These spectral peaks are related to the electron configuration of the electrons (i.e. 1s, 2s, 2p,...) within the atoms. Hence, XPS is the best method to study the composition and chemical states of the surface of the materials.

The theory of the XPS is based on the photoelectric effect which occurs between tightly bound (inner-shell) electrons and incident low energy X-ray photons (large wavelength). In the photoelectric absorption process, a photon transfers all its energy to the electron of the atom in which the photon completely disappears, ionizes the atom to which the electron was bound and produces a photoelectron. If the energy of the incident X-ray beam is $h\nu$, the maximum kinetic energy (E_K) of the ejected photoelectrons is given by [31]:

$$E_K = h\nu - E_B - E_W, \quad (4.23)$$

where E_B is the electron binding energy. The binding energies of levels in solids are usually considered with respect to the Fermi energy level in that material, thus it needs to add a small correction called the work function (E_W). The basic principles of the photoelectron effect are presented in Figure 4.24.

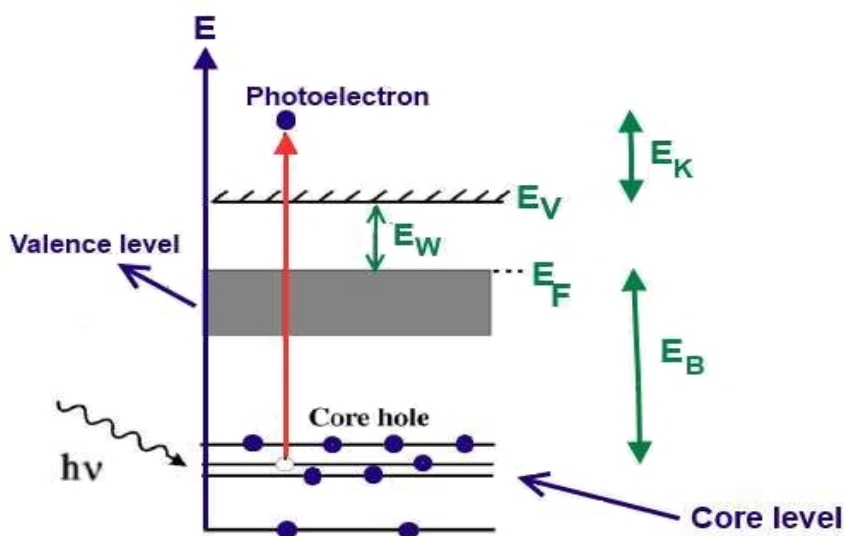


Figure 4.24: The schematic diagram of a core-level-photoelectron emission process, where E_F , E_V , E_K and E_B are the Fermi energy level, vacuum energy level, kinetic energy and binding energy, respectively.

In general, the binding energies of the different levels for any specific element depend on its energy levels, i.e. $E_B(1s) > E_B(2s) > E_B(2p) > E_B(3s)$. Furthermore, the element with the larger atomic number (Z) has the larger binding energy of the particular orbital level, i.e. $E_B(\text{Cr } 1s) < E_B(\text{Mn } 1s) < E_B(\text{Fe } 1s)$.

Another phenomenon in the photoemission effect is the Auger electron spectroscopy which happens when an electron from a higher energy level falls into the hole and creates the energy. This energy can be converted to an emitted photon or transferred to another electron. The second electron, called an Auger electron, escapes from

the atom and creates the broad peaks in XPS spectrum [31, 32, 33]. The basic components of an XPS instrument, shown in Figure 4.25, includes:

- The X-ray source to radiate the monochromatic X-ray beams to the sample.
- Retarding lenses to focus the electrons onto the entrance slit and retard their velocity.
- The concentric hemispherical analyzer to measure and control the energy of the emitted electrons in order to reach the detector.
- A high vacuum environment to keep the surface of the sample clean and keep the rest of the environment safe from gas collisions.
- An electron detector to calculate the binding energy by measuring the kinetic energy of the photoelectrons.

The XPS measurements in this project were performed on AXIS ULTRA spectrometer, equipped with a hemispherical electron energy analyzer and the monochromatic X-ray source of Al K_{α} (1486.58 eV) at 5×10^{-9} mbar at the Max Planck Institute for Solid State Research, Germany. During the photoelectron emission process, insulating samples are usually subjected to charging effects and may shift the peaks in the XPS spectrum. Therefore, charging of the samples was corrected by referring all the spectra to the binding energy of the carbon (C 1s) at 284.8 eV. Furthermore, the important problem in the XPS measurement of the rare earth compounds is the oxygen affinity of the rare earth atoms which causes

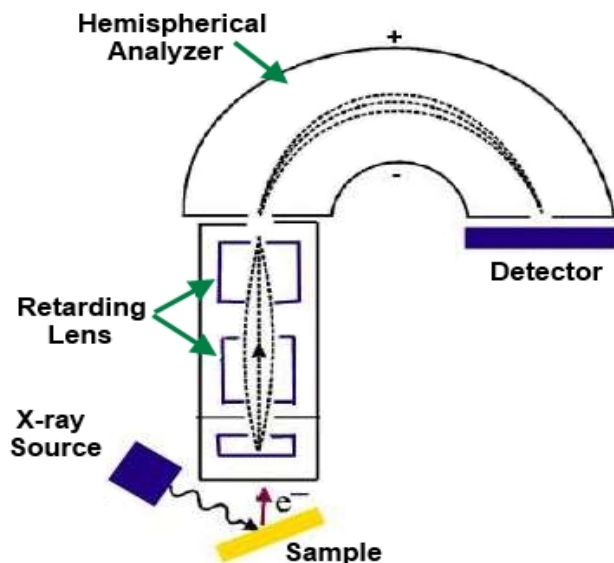


Figure 4.25: The schematic diagram of the basic elements in XPS experiment [34].

a rapid contamination of the surface layer, even in the high vacuum. Therefore, cleaning the surface was done using 4 kV Ar^+ ion sputtering for 10 min.

XPS is a sensitive technique for valence state determination, especially in the rare earth compounds where the valence states fluctuate between $4f^n$ and $4f^{n\pm 1}$ at a rapid rate. In the case of cerium and europium, the internal core levels (3d and 4d) are the main levels to be considered.

4.3.1 XPS Results

The electronic configuration of cerium is $[\text{Xe}] 4f^1 5d^1 6s^2$ which can be ionized to Ce^{3+} ($[\text{Xe}] 4f^1$), and Ce^{4+} ($[\text{Xe}] 4f^0$). As reported in the literature, the XPS spectrum of Ce^{3+} 3d has two pairs of doublets, labeled as u_0/v_0 and u'/v' , due to the mixing of $\text{Ce } 3d^9 4f^1$ and $\text{Ce } 3d^9 4f^2$ states, corresponding to the spin-orbit splitting of $3d_{3/2}$ and $3d_{5/2}$.

On the other hand, the XPS spectrum of Ce^{4+} 3d shows two pairs of doublets with two extra peaks in the range of 905 - 918 eV. The assignment of the multiplet peaks of v_0 , u_0 , u' and v' in Ce 3d spectrum with the shake-down (gaining energy)/shake-up (losing energy) features suggests a different behavior for Ce^{3+} and Ce^{4+} (Figure 4.26) [35, 36, 37].

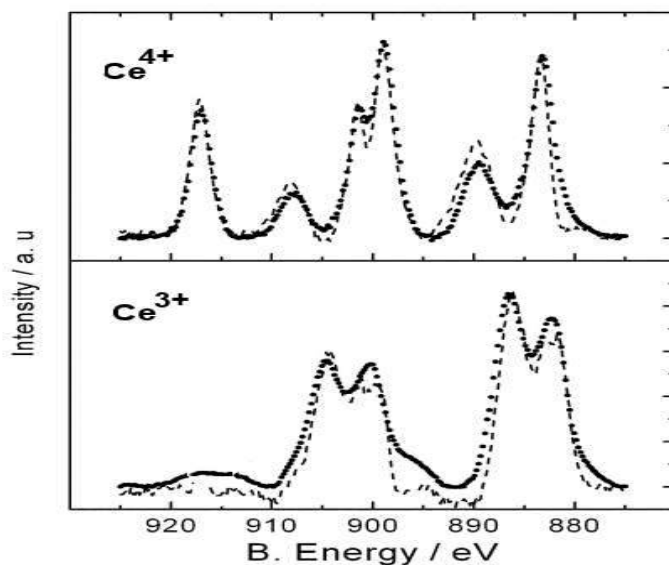


Figure 4.26: The Ce 3d XPS spectra of Ce^{4+} and Ce^{3+} compounds, reprinted from Ref. [36].

Figure 4.27 illustrates the XPS survey spectrum of the CeCrO_3 with the relevant element peaks before cleaning the surface. KLL is the Auger process when an incident electron creates a core hole in the 1s level (K orbital) and an electron from the 2s level (L orbital) falls to the 1s level and fills in the hole, then the electron in 2p level (L orbital) is ejected. The final atomic state thus has two holes, one in the 2s orbital and the other in the 2p orbital. Similarly, MNN is the transitions between M and N orbitals.

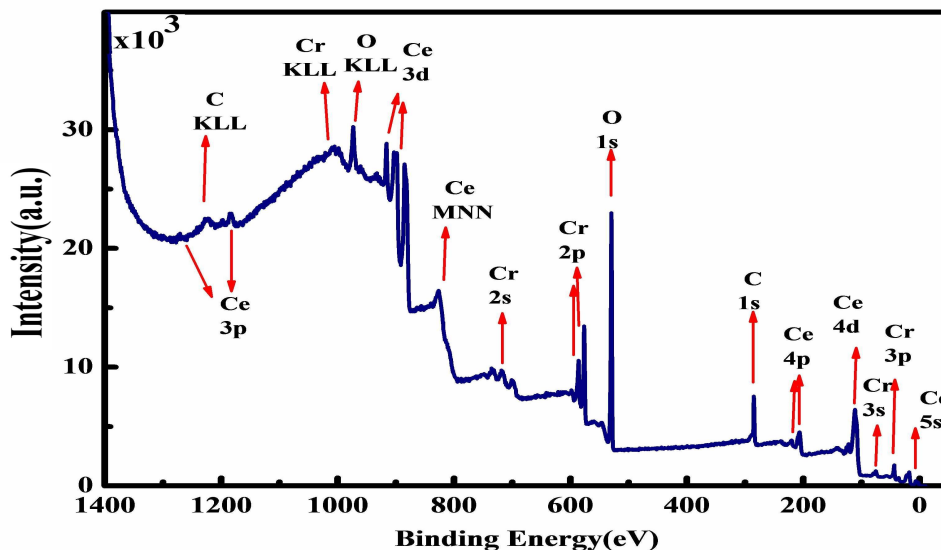


Figure 4.27: The XPS survey spectrum of CeCrO_3 before surface cleaning.

As mentioned before, the Ce 3d and 4d core level XPS are the main levels to be determined. Figure 4.28 shows the Ce 3d XPS spectrum of CeCrO_3 in two conditions of before and after surface sputtering. The presence of the multiplet peaks v_0 , u_0 , u' and v' with binding energies of 882.1, 884.9, 900.5 and 903.3 eV, respectively, in the Ce 3d spectrum of the sample CeCrO_3 before Ar^+ sputtering (Figure 4.28(a)) reveals the existence of Ce^{3+} , although the appearance of two extra peaks at 898.1 and 916.3 eV indicates the formation of Ce^{4+} as a minor valence state at the surface of this sample [38]. After cleaning the surface of CeCrO_3 by Ar^+ bombardment, the peaks attributed to Ce^{4+} disappear and the Ce^{3+} 3d spin-orbit structure is clearly visible (Figure 4.28(b)). The spin-orbit splitting energy of Ce^{3+} 3d ($\Delta_{SO}(\text{Ce}^{3+} 3d)$) calculated before and after surface sputtering are 18.4 and 18.5 eV, respectively, while the $\Delta_{SO}(\text{Ce}^{4+} 3d)$ before sputtering is 18.2 eV, all are in the good agreement with the previous literature [39, 37, 38].

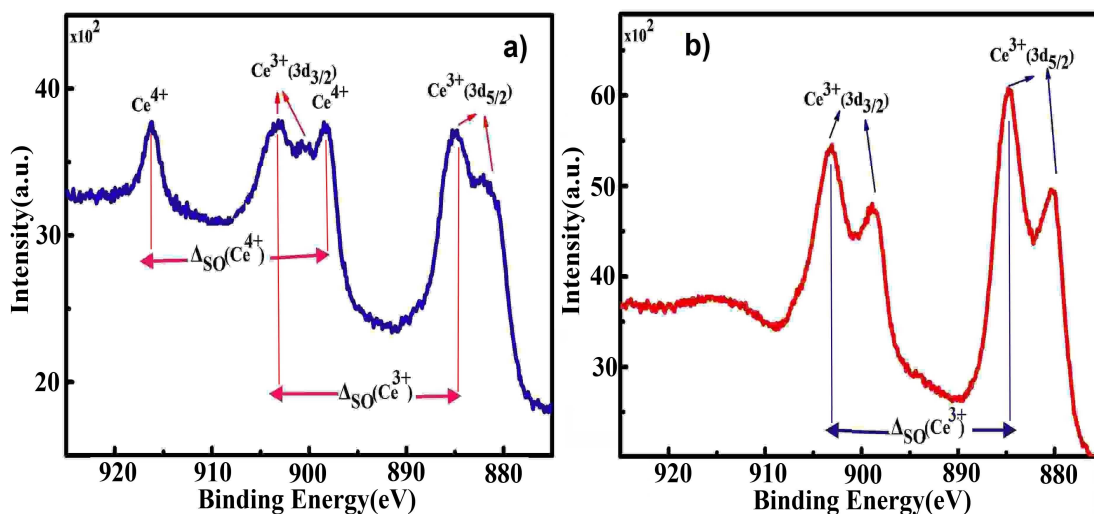


Figure 4.28: Ce 3d core level XPS spectra of CeCrO_3 nano-powders (a) before surface sputtering and (b) after surface sputtering.

The Ce 4d spectra are represented in Figure 4.29, where the peaks at 108.0 and 111.3 eV before sputtering and the peaks at 107.5 and 111.0 eV after sputtering are assigned to the spin-orbit splitting of 4d orbital in Ce^{3+} . The peaks of Ce 4d at binding energies of 122.1 and 125.4 eV confirm the presence of Ce^{4+} before cleaning the surface. The spin-orbit splitting energy $\Delta_{SO}(\text{Ce}^{3+}4d)$ and $\Delta_{SO}(\text{Ce}^{4+}4d)$ before sputtering were obtained 3.3 eV while $\Delta_{SO}(\text{Ce}^{3+}4d)$ after sputtering was calculated 3.5 eV, in the same range as mentioned in the previous reports [39, 37, 38]. The ratio of the peak intensities in the spin-orbit splitting of d level ($\frac{I_{5/2}}{I_{3/2}}$) is usually 3/2, where $I_{5/2}$ and $I_{3/2}$ are the peak intensities of $d_{5/2}$ and $d_{3/2}$, respectively.

Figure 4.30 reports the XPS spectra of Cr 2p region before and after Ar ion sputtering. The spin-orbit splitting of Cr 2p doublets (Cr $2p_{1/2}$ and $2p_{3/2}$) with binding energies of 576.1 and 586.1 eV for sample before Ar sputtering match

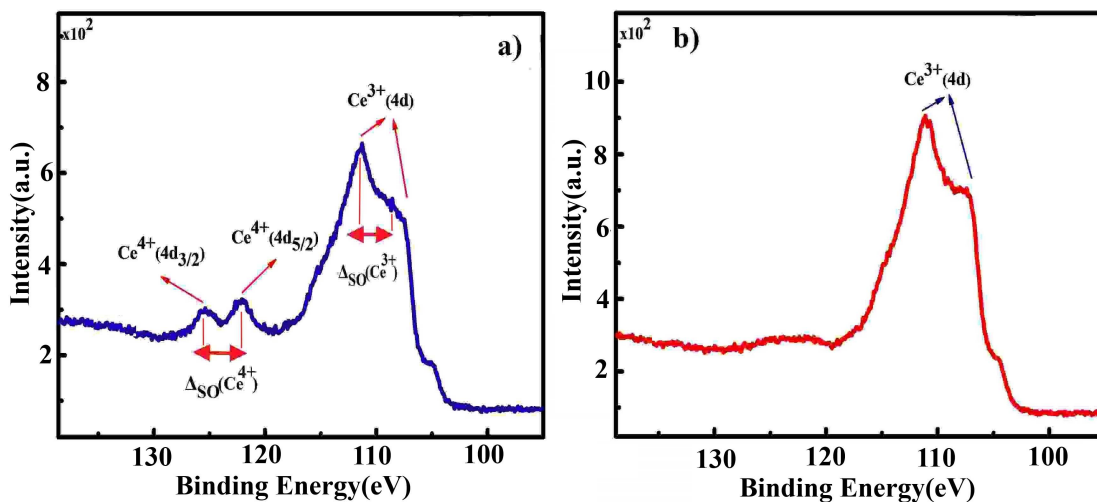


Figure 4.29: Ce 4d core level XPS spectra of CeCrO₃ nano-powders (a) before surface sputtering and (b) after surface sputtering.

satisfactorily other published data for Cr³⁺ compounds [40, 41, 42, 43]. The XPS data done on CeCrO₃ after surface cleaning shows two extra peaks in addition to Cr³⁺ 2p doublets with binding energies of 575.2 and 585.3 eV. According to the 2p binding energies of Cr⁰, Cr³⁺, Cr⁵⁺ and Cr⁶⁺ given in the literature, Ar⁺ ion sputtering creates some Cr⁰ ions on the surface of CeCrO₃ while the majority belongs to Cr³⁺ ion. Furthermore, the observed spin-orbit splitting energy of Cr³⁺ is about 10 eV with the intensity ratio of 2/1, which is in good agreement with the previously published data [40, 41, 42, 43, 44].

The O(1s) spectra illustrate a main peak at 529.7 eV (before surface cleaning (blue line)) and 529.2 eV (after surface cleaning (red line)), assigned to the oxygen atoms in CeCrO₃ structure. The additional broad peak at 531.1 eV (before sputtering) and 531.2 eV (after sputtering) can be attributed to the surface adsorbed oxygen species in the forms of hydroxyl ones (Figure 4.31(a)). The valence band

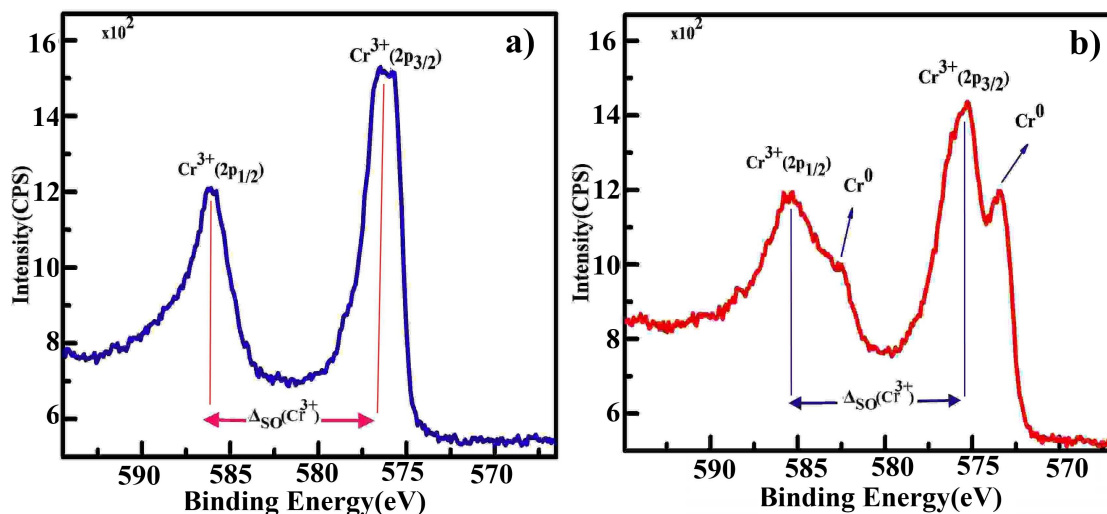


Figure 4.30: Cr 2p core level XPS spectra of CeCrO_3 nano-powders (a) before surface sputtering and (b) after surface sputtering.

(vb) XPS spectrum (Figure 4.31(b)) presents the 1.2-1.5 eV energy gap between Ce 4f level and Fermi energy level while Cr 3d level is located about 2 eV to the Fermi level.

The binding energies of Ce 3d and 4d core-level XPS data of CeCrO_3 before and after surface cleaning are summarized in Table 4.10.

Figure 4.32 shows the XPS spectra of Ce 3d, Eu 3d, Ce/Eu 4d and Cr 2p spectra of samples $\text{Ce}_{1-x}\text{Eu}_x\text{CrO}_3$ ($x = 0.3, 0.5, 0.7$ and 0.8) before Ar ion sputtering. It is obvious that the intensity of the peaks attributed to the Eu^{3+} gradually increases and the intensity of the peaks related to Ce^{3+} ion decreases through Eu doping. Cerium is observed as the Ce^{4+} and Ce^{3+} ions while europium and chromium exists as the 3+ oxidation.

The XPS spectra of Ce 3d, Eu 3d, Ce/Eu 4d and Cr 2p spectra of samples $\text{Ce}_{1-x}\text{Eu}_x\text{CrO}_3$ ($x = 0.3, 0.5, 0.7, 0.8$) after Ar ion sputtering are shown in Figure

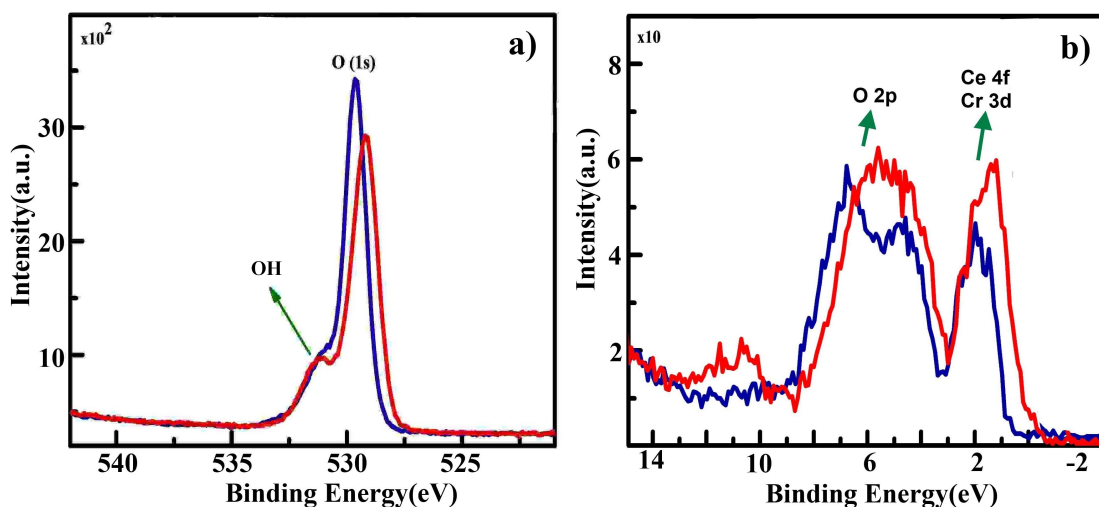


Figure 4.31: (a) O 1s XPS spectra and (b) valence-band level (vb) XPS spectra of the core level for CeCrO_3 nano-powders before surface sputtering (blue line) and after surface sputtering (red line).

Table 4.10: Binding energy values (E_B) of the 3d and 4d level peaks in CeCrO_3 (before Ar ion sputtering) and CeCrO_3 -as (after Ar ion sputtering).

Sample	Ce(3d _{3/2}) (eV)	Ce(3d _{5/2}) (eV)	Ce(4d _{3/2}) (eV)	Ce(4d _{5/2}) (eV)
CeCrO_3	900.5(Ce ³⁺)	882.1(Ce ³⁺)	111.3(Ce ³⁺)	108.0(Ce ³⁺)
	903.3(Ce ³⁺)	884.9(Ce ³⁺)		
	916.3(Ce ⁴⁺)	898.1(Ce ⁴⁺)	125.4(Ce ⁴⁺)	122.1(Ce ⁴⁺)
CeCrO_3 -as	898.8(Ce ³⁺)	880.3(Ce ³⁺)	111.0(Ce ³⁺)	107.5(Ce ³⁺)
	903.1(Ce ³⁺)	884.6(Ce ³⁺)		

4.33. The change in the intensity of the peaks agrees with the data before surface sputtering. Furthermore, Eu 3d and 4d spectra show the existence of Eu^{3+} and Eu^{2+} in the compounds while the Ce^{3+} ion is the only oxidation of the cerium ion. Chromium is observed in the 0 and +3 oxidation, as well.

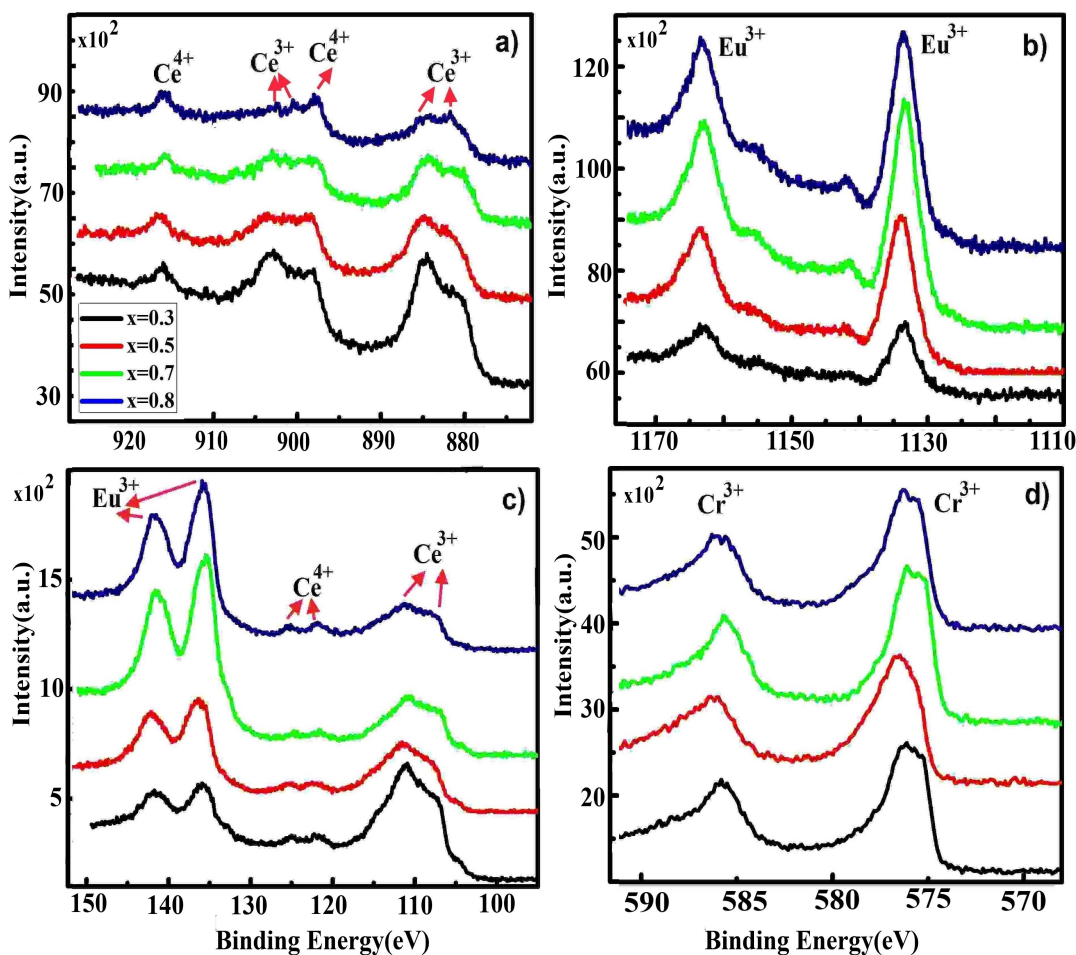


Figure 4.32: (a) Ce 3d, (b) Eu 3d, (c) Ce/Eu 4d and (d) Cr 2p spectra of samples $\text{Ce}_{1-x}\text{Eu}_x\text{CrO}_3$, before Ar ion sputtering.

Europium may exist in a trivalent state with $4d^{10}4f^6$ configuration or divalent state with $4d^{10}4f^7$ configuration in the compounds. For these cases, the Eu 3d core level consists of a doublet, which is labeled $3d_{5/2}$, $d_{3/2}$ doublet, similar to Eu 4d core

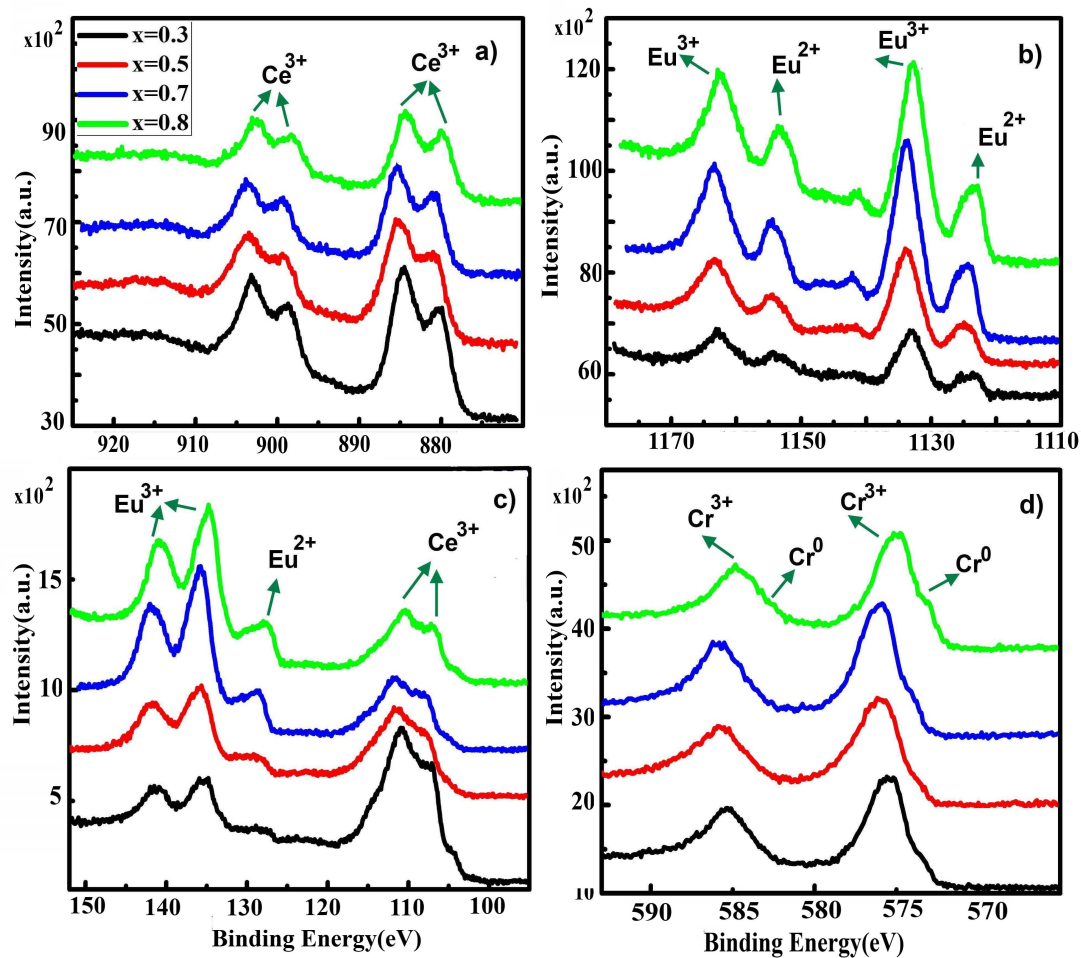


Figure 4.33: (a) Ce 3d, (b) Eu 3d, (c) Ce/Eu 4d and (d) Cr 2p spectra of samples $\text{Ce}_{1-x}\text{Eu}_x\text{CrO}_3$ after Ar ion sputtering.

($4d_{5/2}$, $d_{3/2}$ doublet). In the core-level photoemission spectra of Eu^{3+} compounds, $4f^6$ excites to $4f^7$ as the final state, i.e. the 4f level is filled by an electron from the conduction band level, thus it gains energy and creates a shake-down spectrum, whereas, the Eu^{2+} core-level photoemission loses energy and shows a shake-up process [45].

The XPS survey spectrum of EuCrO_3 with its corresponding element peaks before cleaning the surface is shown in Figure 4.34.

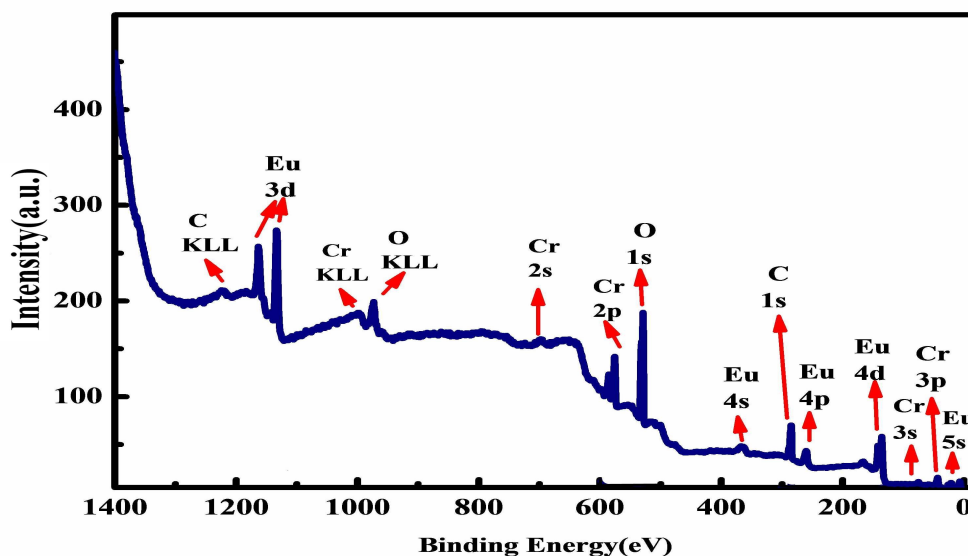


Figure 4.34: The XPS survey spectrum of EuCrO_3 before surface cleaning.

The XPS spectra of the Eu 3d core-level for EuCrO_3 , shown in Figure 4.35, have been done in two conditions of (a) before and (b) after Ar^+ ion sputtering. The data for the sample before sputtering shows the typical two peaks of $3d_{5/2}$ and $3d_{3/2}$ doublet at binding energies of 1133.0 and 1163.1 eV with the spin-orbit splitting energy (Δ_{SO}) of 30.8 eV, close to the values expected for Eu^{3+} ions. After cleaning the surface, the Eu^{3+} $3d_{5/2}$, $d_{3/2}$ doublet are shifted to 1133.2 and 1163.0

eV, respectively, with Δ_{SO} of 29.8 eV as well as an extra doublet with binding energies of 1123.6 and 1153.4 eV and Δ_{SO} of 29.8eV which are in good agreement with Eu^{2+} $3d_{5/2}$, $d_{3/2}$ doublet [43, 46]. The small peak at binding energy of 1141.4 eV (before surface cleaning) and 1141.6 eV (after surface cleaning) can be assigned for the satellite line, with 8.4 eV energy higher than those for $3d_{5/2}$ main peak [47]. Satellite peaks are commonly observed in most XPS spectra with regards to the energy loss attributed to the inelastic electron collisions.

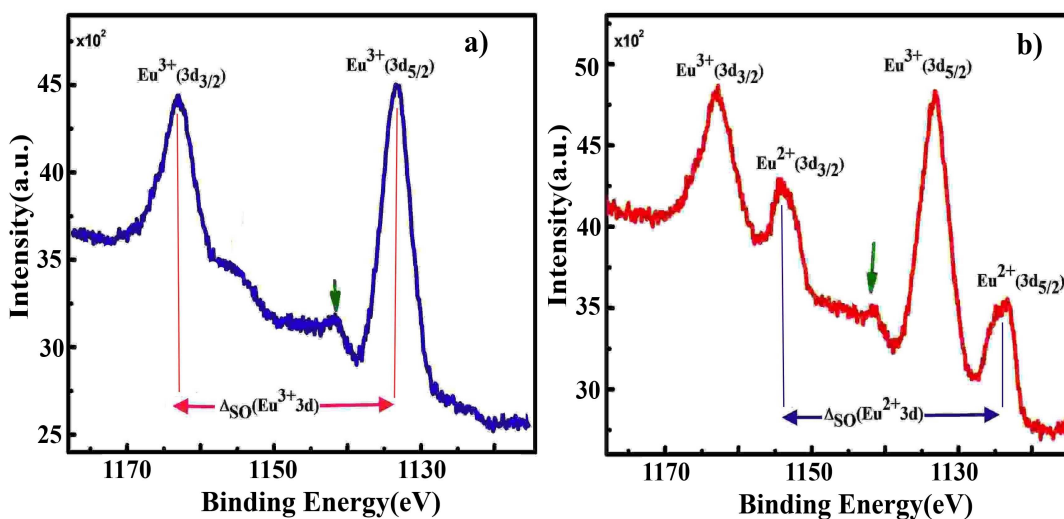


Figure 4.35: Eu 3d core level XPS spectra of EuCrO_3 nano-powders (a) before surface sputtering and (b) after surface sputtering.

Eu 4d core spectra (Figure 4.36) with binding energies of 135.2 and 141.4 eV corresponding to $4d_{5/2}$, $d_{3/2}$ doublet and Δ_{SO} of 6.2 eV in EuCrO_3 confirm the existence of Eu^{3+} valence state at the surface of the sample, although Ar ion sputtering created Eu^{2+} cation with 4d binding energy of 128.3 eV, as well.

Figure 4.37 illustrates the Cr 2p XPS spectra of EuCrO_3 with $2p_{3/2}$, $p_{1/2}$ peaks and binding energies of 575.8 and 585.8 eV (before surface cleaning) and

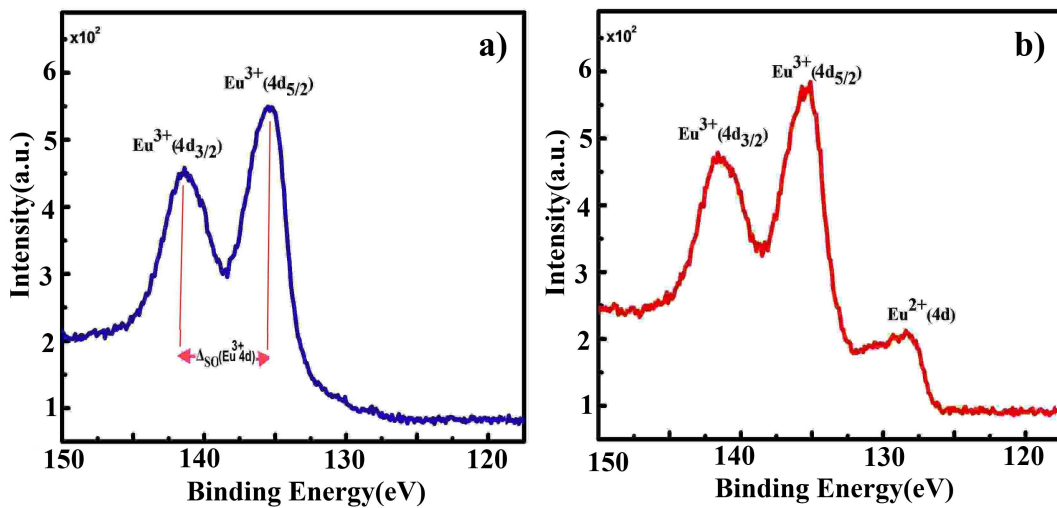


Figure 4.36: Eu 4d core level XPS spectra of EuCrO_3 nano-powders (a) before surface sputtering and (b) after surface sputtering.

575.4 and 585.5 eV (after surface cleaning). The ratio of the spin-orbit intensity of 2p doublet also agrees with the typical ratio of the 2/1 Cr^{3+} 2p doublet [42]. The small shoulder at 573.8 eV after cleaning the surface (Figure 4.37(b)) can be a proof of the small amount of the Cr^0 formation at the surface [44, 43].

The peak of O(1s) in two conditions of before and after surface cleaning is centered at 529.2eV, corresponding to the oxygen atoms in EuCrO_3 compound (shown in Figure 4.38(a)) [40, 42, 46]. The additional broad peak at 529.0 eV for the sample before sputtering can be assigned to the adsorbed OH groups on the surface, which is suppressed in the intensity while Ar ion sputtering. The valence band spectrum of EuCrO_3 (Figure 4.38(b)) shows the larger gap energy of Eu 4f and the Fermi energy level compared to the Ce 4f in CeCrO_3 . The overlapping of the Eu 4f and O 2p orbital is larger than the Ce 4f and O 2p orbitals, as well.

Table 4.11 lists the binding energy (E_B) of XPS spectra of the Eu 3d and Eu

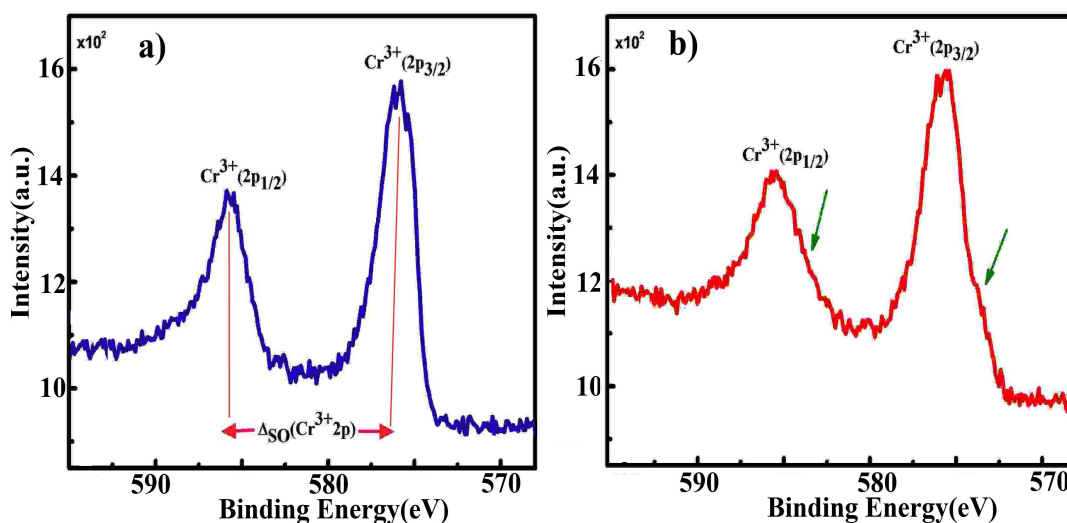


Figure 4.37: Cr 2p core level XPS spectra of EuCrO_3 nano-powders (a) before surface sputtering and (b) after surface sputtering.

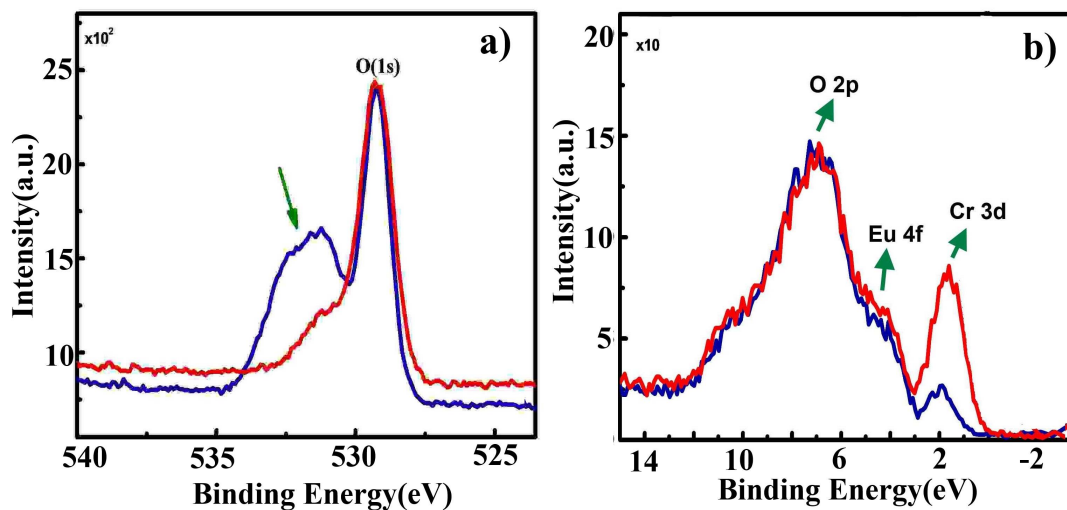


Figure 4.38: (a) O 1s XPS spectra and (b) valence-band level (vb) XPS spectra of EuCrO_3 nano-powders before surface sputtering (blue line) and after surface sputtering (red line).

4d core-levels and the corresponding ions for the samples EuCrO_3 (before Ar ion sputtering) and EuCrO_3 -as (after Ar ion sputtering).

Table 4.11: Binding energy values (E_B) of 3d and 4d level peaks in EuCrO_3 (before Ar ion sputtering) and EuCrO_3 - *as* (after Ar ion sputtering).

Sample	Eu(3d _{3/2}) (eV)	Eu(3d _{5/2}) (eV)	Eu(4d _{3/2}) (eV)	Eu(4d _{5/2}) (eV)
EuCrO_3	1163.1 (Eu ³⁺)	1133.0 (Eu ³⁺)	141.4 (Eu ³⁺)	135.2 (Eu ³⁺)
EuCrO_3 -as	1163.0 (Eu ³⁺)	1133.2 (Eu ³⁺)	141.3 (Eu ³⁺)	135.1 (Eu ³⁺)
	1153.4 (Eu ²⁺)	1123.6 (Eu ²⁺)		128.3 (Eu ²⁺)

Table 4.12 reports the binding energy (E_B) of XPS spectra of the Cr 2p and O 1s core-levels of the samples CeCrO_3 and EuCrO_3 (before Ar ion sputtering) and CeCrO_3 -as and EuCrO_3 -as (after Ar ion sputtering).

The typical binding energies of the Eu 3d, Eu 4d, Ce 3d, Ce 4d and Cr 2p levels for different compounds reported earlier are listed in Table 4.13. It is worth mentioning that the binding energy is not only a property of the atom but also it is dependent on the chemical environment of that atom, i. e. the nature of the compound strongly influences the binding energies of the photoemission peaks, thus, for example, the binding energies of Cr 2p and O 1s in EuCrO_3 and CeCrO_3 may not be equal. Furthermore, ion sputtering may change the surface stoichiometry and structure of the materials, including a reduction in the oxidation state.

Table 4.12: Binding energy values (E_B) of Cr (2p) and O (1s) peaks in CeCrO_3 and EuCrO_3 (before Ar ion sputtering) and CeCrO_3 -as and EuCrO_3 -as (after Ar ion sputtering).

Sample	Cr(2p _{1/2}) (eV)	Cr(2p _{3/2}) (eV)	O(1s) (eV)
CeCrO_3	586.1(Cr ³⁺)	576.1(Cr ³⁺)	529.7
CeCrO_3 -as	585.3(Cr ³⁺) 582.5(Cr ⁰)	575.2(Cr ³⁺) 573.4(Cr ⁰)	529.2
EuCrO_3	585.8 (Cr ³⁺)	575.8 (Cr ³⁺)	529.2
EuCrO_3 -as	585.5 (Cr ³⁺)	575.4 (Cr ³⁺) 573.8 (Cr ⁰)	529.2

Table 4.13: Typical binding energies (E_B) of Eu, Ce, Cr ions in the different compounds, reported in literature.

Level State	E_B (eV)	Valence State	compound
Eu(3d _{5/2})	1128.3	Eu ³⁺	EuCrO ₃ [43]
Eu(3d _{5/2})	1133.7	Eu ³⁺	Eu ₂ O ₃ [46]
Eu(3d _{5/2})	1136.4	Eu ³⁺	Eu(NO ₃) ₃ [46]
Eu(3d _{5/2})	1124.9	Eu ²⁺	EuO [47]
Eu(3d _{3/2})	1154.1	Eu ²⁺	EuO [47]
Eu(4d _{5/2})	131.2	Eu ³⁺	EuCrO ₃ [43]
Eu(4d _{5/2})	134.9	Eu ³⁺	Eu ₂ O ₃ [46]
Eu(4d _{5/2})	137.7	Eu ³⁺	Eu(NO ₃) ₃ [46]
Ce(3d _{5/2})	888.8, 898.0	Ce ⁴⁺	CeO ₂ [39]
Ce(3d _{5/2})	881.8, 885.8	Ce ³⁺	CeNbO ₄ [39]
Ce(3d _{5/2})	881.37, 885.65	Ce ³⁺	CaCe _{0.7} TiNbO _{6.55} [35]
Ce(3d _{3/2})	899.78, 904.06	Ce ³⁺	CaCe _{0.7} TiNbO _{6.55} [35]
Ce(3d)	917.0	Ce ⁴⁺	CeO ₂ [36]
Cr(2p _{3/2})	576.4	Cr ³⁺	EuCrO ₃ [43]
Cr(2p _{3/2})	576.5	Cr ³⁺	LaCrO ₃ [40]
Cr(2p _{3/2})	579.6	Cr ⁵⁺ -Cr ⁶⁺	LaCrO ₃ [40]
Cr(2p _{3/2})	576.2	Cr ³⁺	Cr ₂ O ₃ [41]
Cr(2p _{3/2})	579.1	Cr ⁶⁺	CrO ₃ [41]
Cr(2p _{3/2})	573.8	Cr ⁰	EuCrO ₃ [43]
Cr(2p _{3/2})	574.1	Cr ⁰	Cr metal [44]
Cr(2p _{3/2})	580.3	Cr ⁶⁺	CrO ₃ [42]
Cr(2p _{3/2})	576.6	Cr ³⁺	Cr ₂ O ₃ [42]
Cr(2p _{1/2})	586.4	Cr ³⁺	Cr ₂ O ₃ [42]
Cr(2p _{1/2})	583.5	Cr ³⁺	EuCrO ₃ [43]
Cr(2p _{1/2})	589.4	Cr ⁶⁺	CrO ₃ [42]

4.4 Electron microscopy

The electron microscope is a type of microscope that works with a beam of electrons to create an image of the specimen. The wavelength of an electron is much shorter than that of visible light, thus it is capable of much higher magnifications and resolution than a light microscope, allowing one to see the structure of much smaller objects. Electrons (with the penetration depth of nm) are highly attenuated by matter and can be strongly focused while the focusing of X-rays is not easy.

An electron with the mass of 9.1×10^{-31} kg and an electric charge of -1.6×10^{-19} C interacts with matter both elastically (such as elastic transmitted or scattered beams) and inelastically (such as X-rays, Auger, inelastic scattered or secondary electron beams). These emitted beams can be used to determine the surface morphology and chemical composition of the specimens [48]. In general, two types of electron microscopes, the Scanning Electron Microscope and Transmission Electron Microscope, are used in biological, geological and materials sciences.

4.4.1 Transmission Electron microscopy

Transmission Electron Microscopy (TEM) is a common technique to investigate the particle size, size distribution and morphology. Using this method, a beam of electrons, produced by a high acceleration voltage, is focused by the condenser lenses and then transmitted through a thin sample. The transmitted electrons are focused by the objective lens to form an image which is magnified by a set of electromagnetic lenses. Since electrons that pass through the sample are detected

in TEM, the sample has to be sufficiently thin. Figure 4.39 shows the TEM set up including the electron beam, sample port and viewing screen. The first TEM was built in 1931 by Max Knoll and Ernst Ruska for which Ruska was awarded the Nobel Prize in Physics in 1986. High resolution transmission electron microscopy (HR-TEM) is one mode of TEM, uses both the transmitted and the scattered beams to create an interference image with high resolution [49, 50].

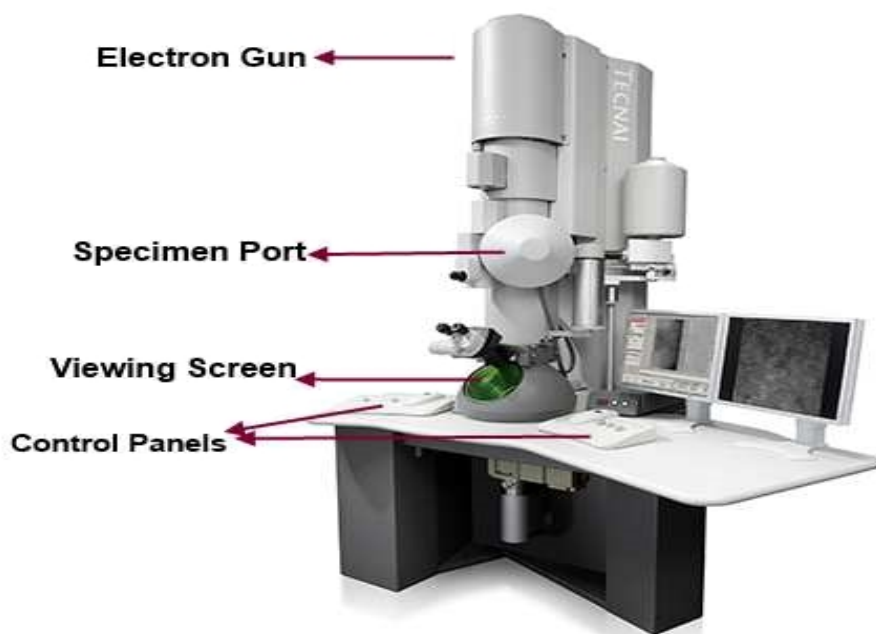


Figure 4.39: Transmission electron microscopy (TEM) system, reprinted from Ref. [51].

All TEM images in this work were carried out on a Hitachi H-7650 TEM (operating at 60 kV acceleration voltage) and high resolution images were taken by the FEI Tecnai F20 TEM (operating at 200 kV acceleration voltage) at room temperature, at the University of Calgary, Canada. For preparing the sample, a drop of ethanol was added to the powder to make a suspended solution. A grid

with a thin carbon film and various holes was dipped into the solution for several seconds and then the grid was allowed to air-dry to be ready for TEM experiment. The particle analysis was performed using ImageJ program.

TEM Results

Figure 4.40 presents the TEM image of the nano-powder CeCrO_3 with the relative frequency distribution of the particle size. A typical method to illustrate the particle size and its distribution is a plot of a frequency histogram. The particle analysis of CeCrO_3 shows that the majority of the particles are in the range of 60-90 nm. The calculated average particle size is 76.5 ± 8.2 nm ($n = 35$), where n is the number of particles. It can be seen that the particles have almost spherical or rounded rectangular shape.

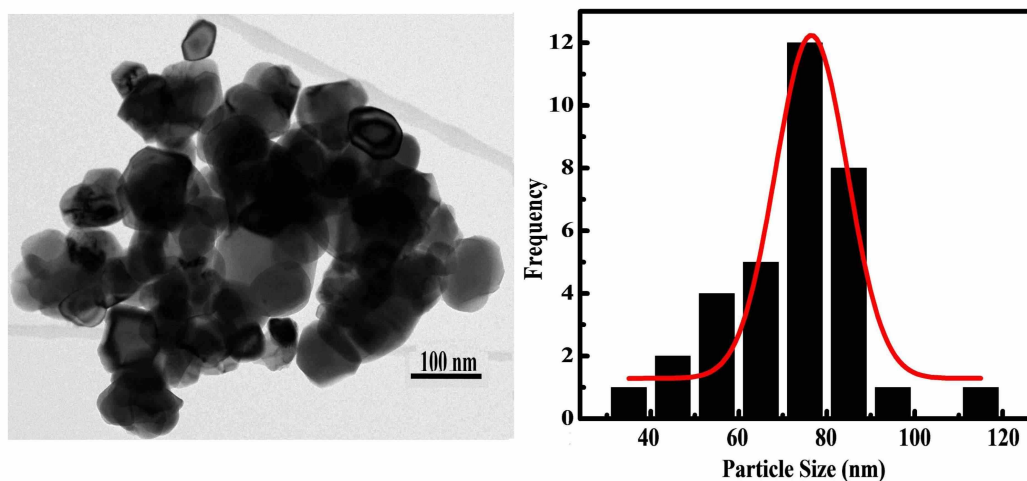


Figure 4.40: TEM image of nano-powder CeCrO_3 with corresponding size distribution histogram.

The overlapping and stacking of the particles with almost rounded rectangular shape are shown in Figures 4.41(a). The Moire effect is shown in Figure 4.41(b),

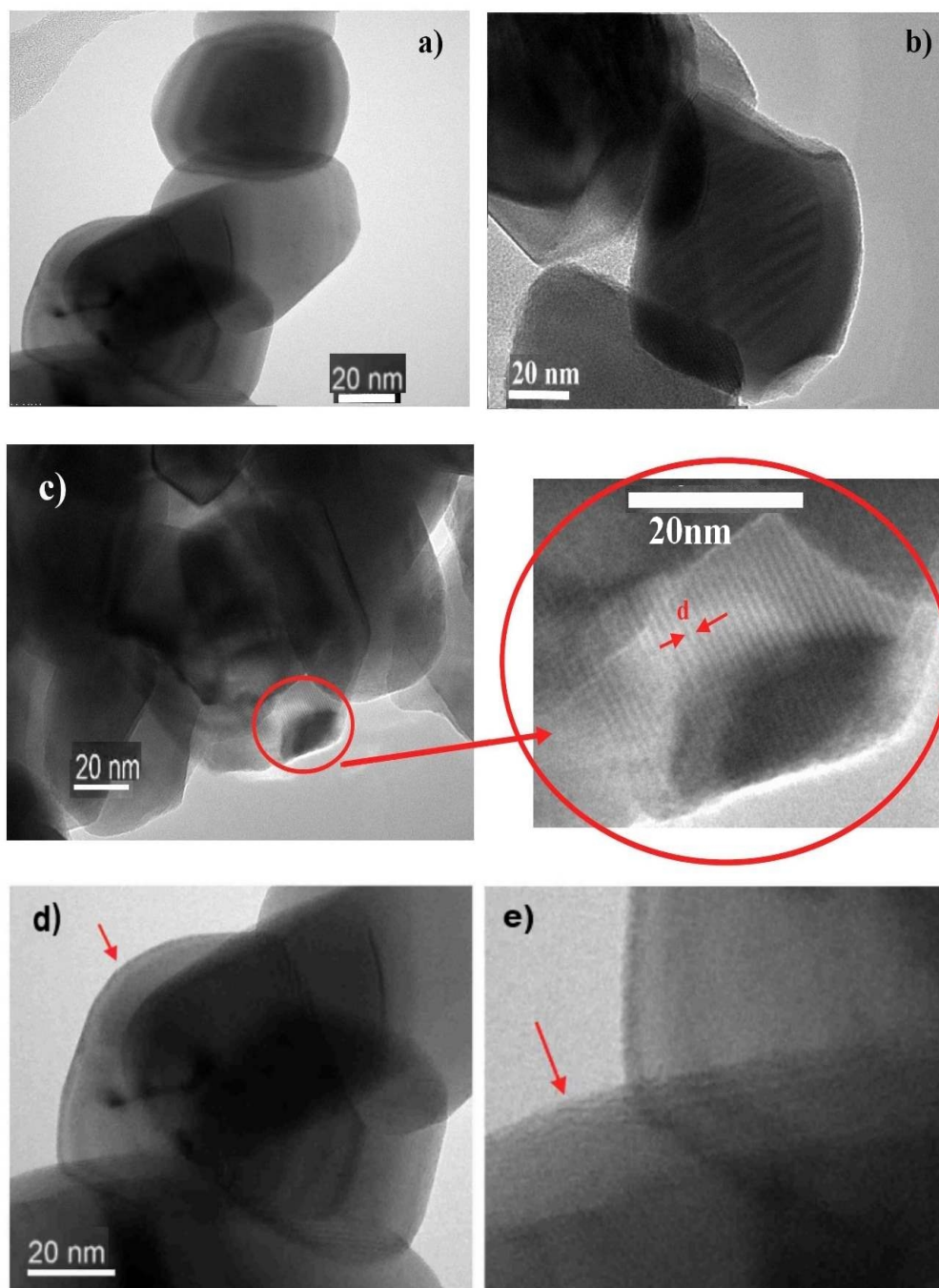


Figure 4.41: HR-TEM micrographs of the nano-powder CeCrO_3 .

where we can see the overlapping of two crystals with the different orientation. Furthermore, the parallel lines in Figure 4.41(c) image clearly confirm the presence of lattice fringes, reflecting good crystallinity with the average fringe spacing (d) of 0.8 nm which is in good agreement with the result obtained from XRD. The red arrow in Figure 4.41(d) indicates the possibility of the core-shell structure for the particle with 65 nm diameter. The zoomed image presented in Figure 4.41(e) serves as an evidence of the surface roughness/defect which can be the reason for core-shell structure in these particles.

The TEM image of the nano-powder $\text{Ce}_{0.9}\text{Eu}_{0.1}\text{CrO}_3$ with the size distribution histogram is shown in Figure 4.42 which indicates an average particle size of 74.4 ± 12.3 nm ($n = 78$).

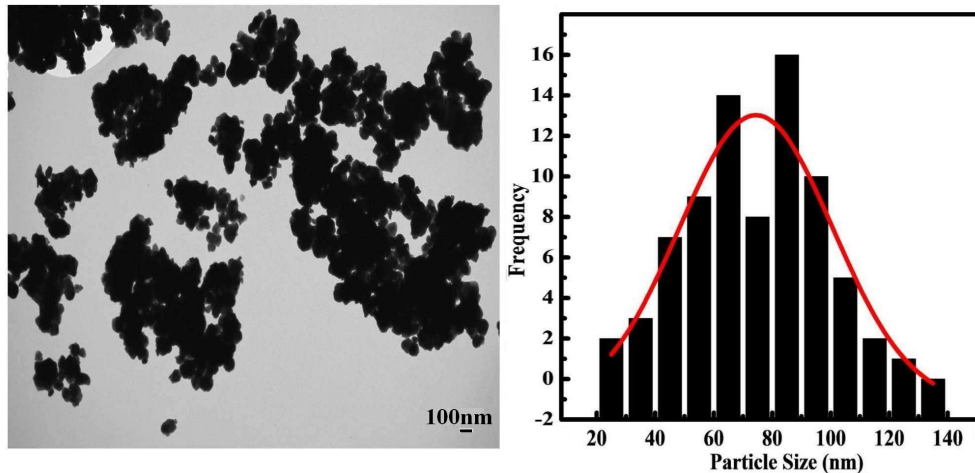


Figure 4.42: TEM image with corresponding size distribution histogram of nano-powders $\text{Ce}_{0.9}\text{Eu}_{0.1}\text{CrO}_3$.

Figure 4.43(a) shows the TEM image of EuCrO_3 with an average particle size of 61.3 ± 9.1 nm ($n = 30$), indicating the particle size reduction compared to CeCrO_3 . The possibility of surface disorder and core-shell structure are seen in

HR-TEM micrographs presented in Figures 4.43(b) and (c).

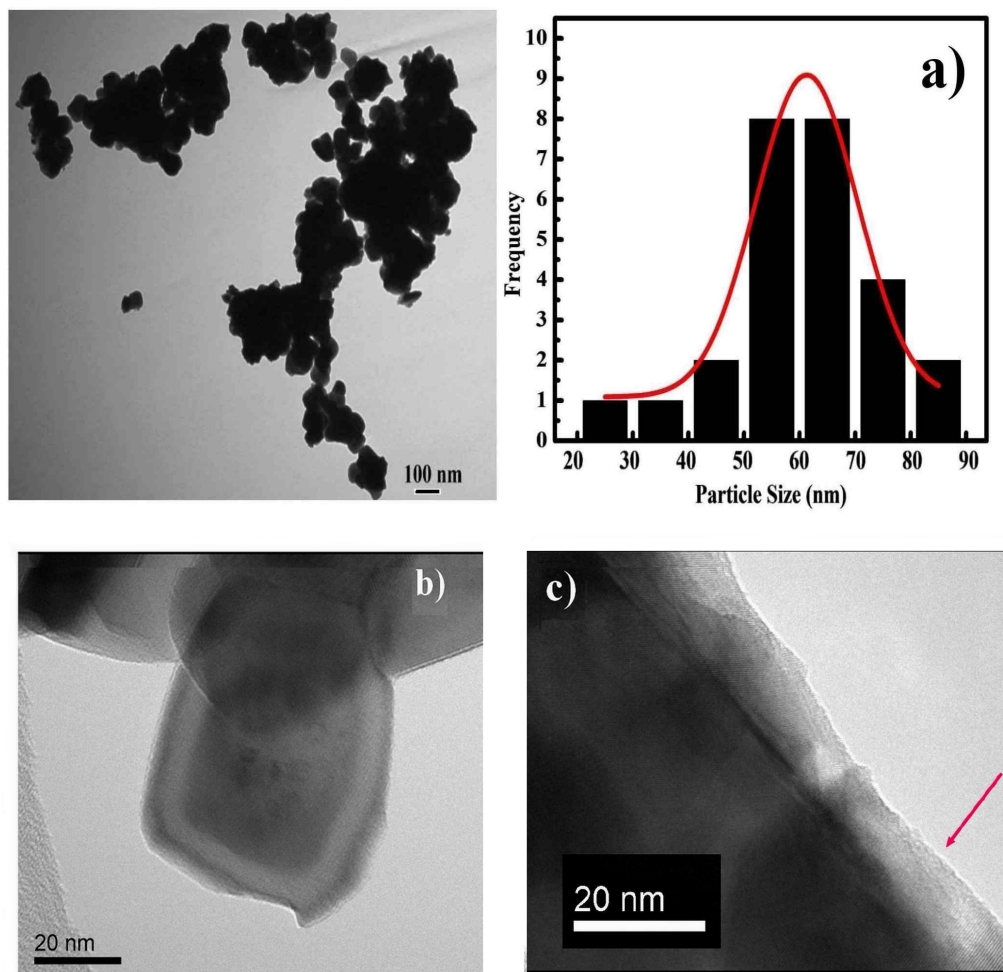


Figure 4.43: (a) TEM image with corresponding size distribution histogram, (b) and (c) HR-TEM images of nano-powder EuCrO_3 .

4.4.2 Scanning Electron Microscopy coupled with Energy Dispersive X-ray Spectroscopy

Scanning Electron Microscopy (SEM) with Energy Dispersive X-ray Spectroscopy (EDX or EDS or EDXS) is one of the most popular techniques for surface analysis.

SEM is a type of electron microscope that creates images of the specimen by scanning it with a focused beam of electrons. The image is produced by detecting secondary electrons which are loosely bound outer shell electrons emitted from the sample. These electrons are created from the inelastic collisions of electron beams with the specimen which have relatively low energy (<50 eV), therefore the accelerating voltage used in SEM is usually lower than that of TEM to prevent beam penetration into the sample. SEM is normally used for bulk specimens and has generally lower resolution compared to TEM.

Another technique for the elemental analysis or chemical characterization of the sample is EDX. This technique is usually employed in the SEM and works similarly to the XPS. The high-energy beam of charged particles hits the sample and may eject an electron in an inner shell and create an electron hole. An electron from an outer shell then fills the hole and generates the X-ray which is the characteristic of that atom. The number and energy of the X-rays emitted from a specimen can be measured by an EDX to identify the elements in the sample material.

It is noteworthy that the EDX spectrum of each sample depends on not only the elements of the specimen, but also the shells of the atom which lost and replaced the electrons. The transition from L-shell to K-shell is named K_{α} and from M-shell to K-shell produces K_{β} [52, 53].

All the SEM micrographs were carried out using the Zeiss Sigma VP SEM under 20 kV operating voltage and high vacuum condition at the university of Calgary, Canada. The SEM was equipped with the Oxford Inca EDX to perform

the elemental analysis of the samples. The samples were placed on a carbon tape which served as a substrate.

SEM/EDX Results

The SEM image of CeCrO_3 with the EDX analysis graph is shown in Figure 4.44. The results represent the agglomeration of the particles with a uniform morphology.

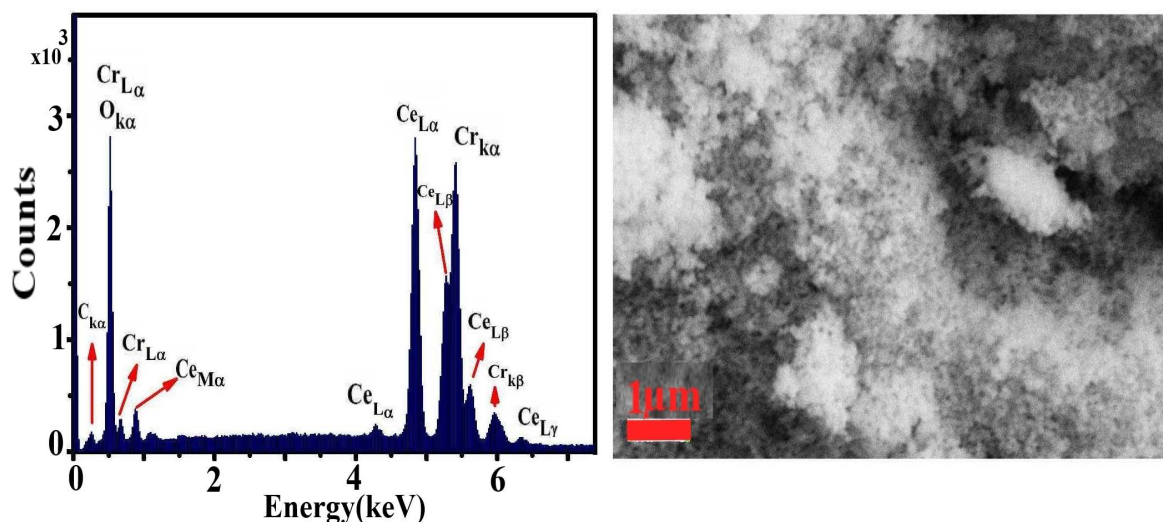


Figure 4.44: SEM micrograph with corresponding EDX spectrum of the nano-powder CeCrO_3 .

The microstructure characterization of $\text{Ce}_{1-x}\text{Eu}_x\text{CrO}_3$ powders ($x = 0.1, 0.3$ and 0.5) are shown in Figure 4.45. The SEM images clearly indicate the rounded homogeneous morphology of the particles in the powders while the EDX data display the increase of the Eu concentration through europium doping. Increasing the Eu content seems to reduce the particle size of samples.

Figure 4.46 shows the SEM micrograph of EuCrO_3 with EDX analysis, displaying its elemental peaks related to Cr, Eu, O.

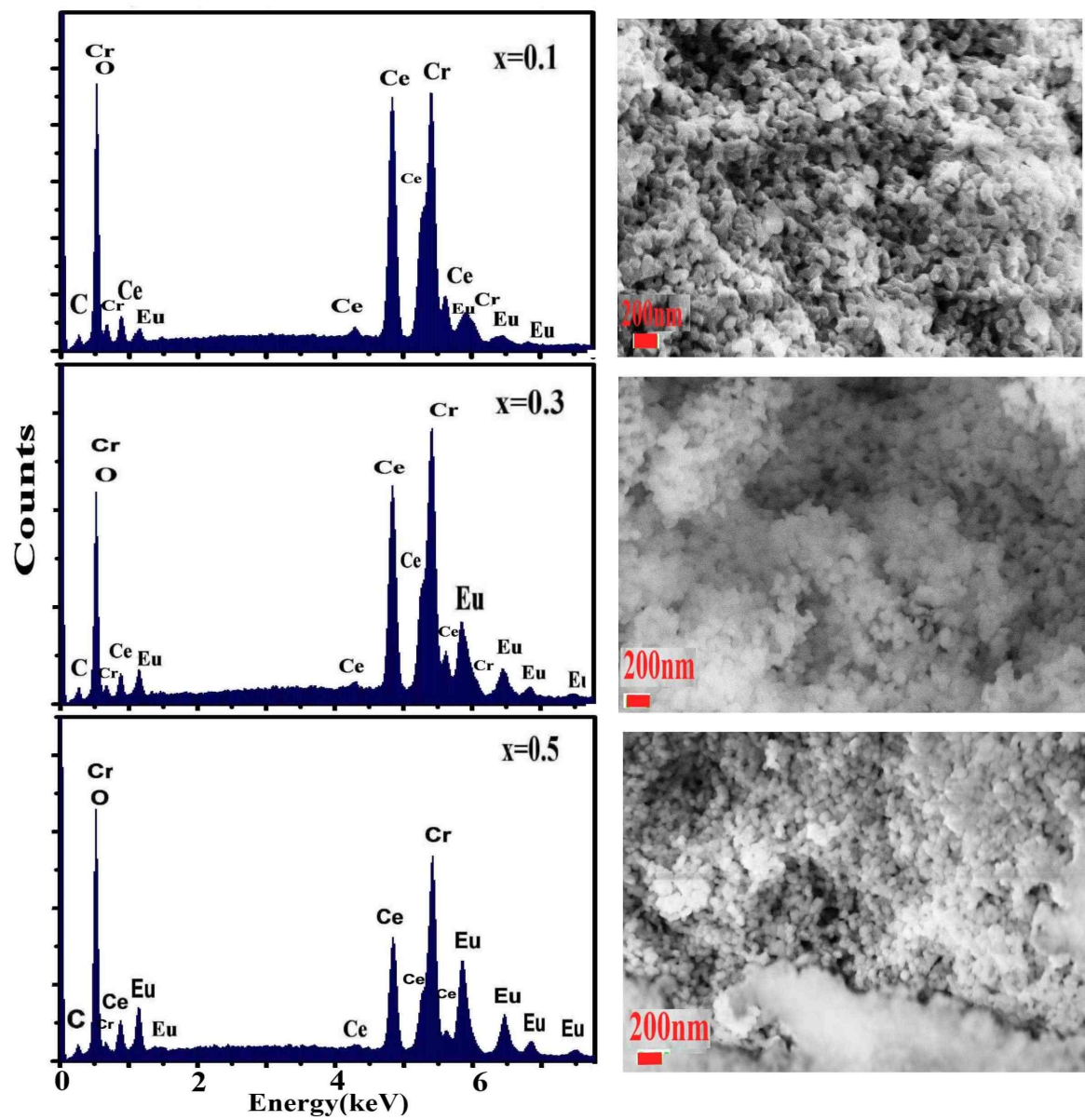


Figure 4.45: SEM images with corresponding EDX results of nano-powders $Ce_{1-x}Eu_xCrO_3$, where $x = 0.1, 0.3$ and 0.5 , respectively.

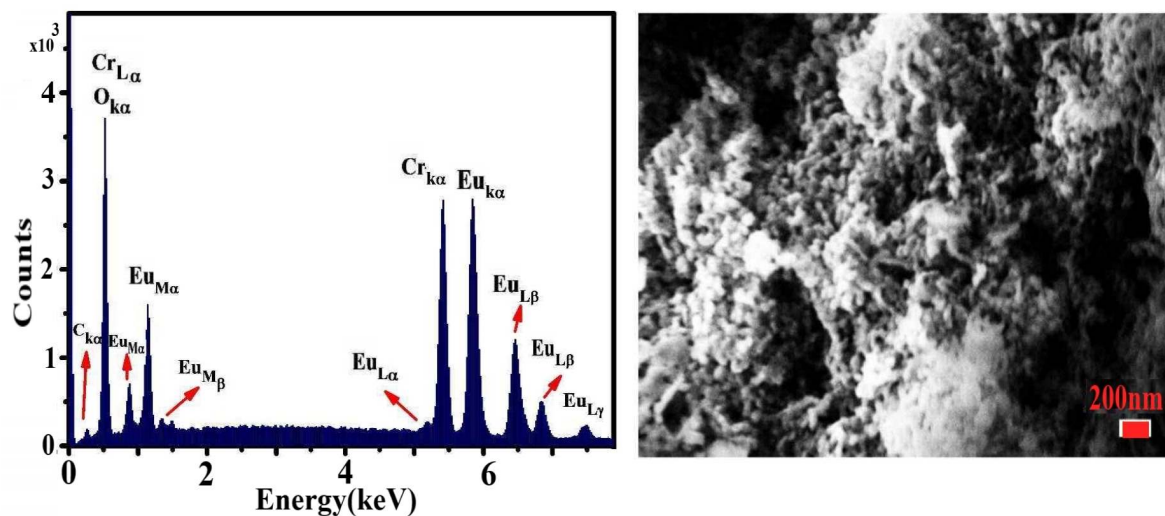


Figure 4.46: SEM micrograph with corresponding EDX result of the nano-powder $EuCrO_3$.

The EDX measurements are usually used to confirm the atomic ratio of components on the surface of the nano-powders. However, it is not expected to get the exact atomic ratio of the metal oxides due to some oxygen contribution on the surface. Table 4.14 presents the atomic percentage of cations in $Ce_{1-x}Eu_xCrO_3$ nano-powders, where $x = 0.0, 0.1, 0.3, 0.5$ and 1.0 .

Table 4.14: Atomic% of $Ce_{1-x}Eu_xCrO_3$, obtained from EDX results.

Element	$x = 0.0$	$x = 0.1$	$x = 0.3$	$x = 0.5$	$x = 1.0$
Ce	50.83	44.74	36.01	25.66	0.00
Eu	0.00	4.03	13.50	23.27	49.37
Cr	49.17	51.23	50.49	51.07	50.63

Bibliography

- [1] J. J. Quinn, K. S. Yi, “Solid State Physics: Principles and Modern Applications”, Springer, (2009)
- [2] C. Kittel, “Introduction to Solid State Physics”, 8th ed., John Wiley & Sons Ltd, (2005)
- [3] M. Johnsson, P. Lemmens, “Handbook of Magnetism and Advanced Magnetic Materials, 4: Novel Materials”, John Wiley & Sons Ltd, Chichester, UK, 2098-2106, (2006)
- [4] M. A. Pen, J. L. G. Fierro, “Chemical Structures and Performance of Perovskite Oxides”, J. Chem. Rev. 2001, 101, 19812017, (2000)
- [5] J. Oliveira, J. A. Moreira, A. Almeida, M. R. Chaves, J. M. M. da Silva, J. B. Oliveira, M. A. Sa, P. B. Tavares, R. Ranjith, W. Prellier, Phys. Rev. B, 84, 094414, (2011)
- [6] www.inside.hlrs.de/_old/htm/Edition.01_11/article.11
- [7] www.en.wikipedia.org/wiki/X-ray
- [8] U. S. Geological Survey website, Open-File Report 01-041.

-
- [9] V. K. Pecharsky, P. Y. Zavalij, “Fundamentals of Powder Diffraction and Structural Characterization of Materials”, Springer, 2nd ed., (2009)
- [10] Y. Waseda, E. Matsubara, K. Shinoda, “X-Ray Diffraction Crystallography”, Springer, (2011)
- [11] S. Mobilio, F. Boscherini, C. Meneghini, “Synchrotron Radiation: Basics, Methods and Applications”, Springer, (2015)
- [12] G. Margaritondo, “Introduction to Synchrotron Radiation”, Oxford University Press, (1988)
- [13] www.tetes-chercheuses.fr/magazines/numero-5/dossier/la-matiere-eclairée-272
- [14] R. Jenkins, R. L. Snyder, “Introduction to X-ray Powder Diffractometer”, John Wiley & Sons Ltd., (1996)
- [15] H. Lipson, H. Steeple, “Interpretation of X-ray powder diffraction patterns”, St. Martin’s Press, (1970)
- [16] B. B. He, U.S. Patent 8548123, B2, (2013)
- [17] www.wikipedia.org/wiki/Scherrer_equation
- [18] C. Hammond, “The basics of Crystallography and Diffraction”, Oxford Science, 3rd ed., (2009)
- [19] www.embl-hamburg.de/biosaxs/courses/embo2012ccmb/slides/03-trewhella-sans-basics1.pdf

-
- [20] A. Wold, R. Ward, *J. Am. Chem. Soc.*, 76, 1029-1030, (1954)
- [21] B. C. Mohanty, J. W. Lee, D. H. Yeon, Y. H. Jo, J. H. Kim, Y. S. Cho, *Mater. Res. Bull.*, 46 (6), 875-883, (2011)
- [22] A. H. Hill, A. Harrison, C. Dickinson, W. Zhou, W. Kockelmann, *Microporous Mesoporous Mater.*, 130, 280-286, (2010)
- [23] J. Rodríguez-Carvajal, *Physica (Amsterdam)*, 192, B, 55, (1993)
- [24] The X-ray absorption has been estimated using the software provided on the webpage: www.11bm.xray.aps.anl.gov/absorb/absorb.php
- [25] W. Borchardt-Ott, "Crystallography An Introduction", 3rd ed., Springer, (2011)
- [26] R. Shukla, A. K. Bera, S. M. Yusuf, S. K. Deshpande, A. K. Tyagi, W. Hermes, M. Eul, R. Pottgen, *J. Phys. Chem. C*, 113, 12663-12668, (2009)
- [27] J. S. Zhou, J. A. Alonso, V. Pomjakushin, J. B. Goodenough, Y. Ren, J. Q. Yan, J.G. Cheng, *Phys. Rev. B* 81, 214115, (2010)
- [28] H. J. Zhao, W. Ren, X. M. Chen, L. Bellaiche, *J. Phys: Condens. Matter*, 25, 385604, (2013)
- [29] R. D. Shannon, *Acta Crystallogr.* A32, 751, (1976)
- [30] H. R. Verma, "Atomic and Nuclear Analytical Methods", Springer Berlin, (2007)

-
- [31] J. F. Moulder, W. F. Stickle, P. E. Sobol, K. D. Bomben, "Handbook of X-ray Photoelectron Spectroscopy", Physical Electronics Inc, US, (1992)
- [32] S. Hüfner, "Photoelectron Spectroscopy: Principles and Applications", 2nd ed., Springer US, (1996)
- [33] T. A. Carlson, "X-ray Photoelectron Spectroscopy", DH & R Inc., 2, (1978)
- [34] www.tut.fi/en/about-tut/departments/optoelectronics-research-centre/research/surface-science/electron-spectroscopy/index.htm
- [35] M. Deepa, P. P. Rao, S. Sumi, A. N. Radhakrishnan, M. R. Chandran, P. Koshy, *J. Mater. Chem. Phys.*, 127, 162-169, (2011)
- [36] J. P. Holgado, R. Alvarez, G. Munuera, *Appl. Surf. Sci.*, 161, 301-315, (2000)
- [37] L. C. Gupta, E. V. Sampathkumaran, R. Vijayaraghavan, M. S. Hegde, C. N. R. Rao, *J. Phys. C: Solid State Phys.*, 13, L455-7, (1980)
- [38] G. Krill, L. Abadli, M. F. Ravet, J. P. Kappler, A. Meyer, *J. Physique*, 41, 1121-1125, (1980)
- [39] Y. A. Teterin, S. V. Stefanovskij, S. V. Yudintsev, G. N. Bek-Uzarov, A. Y. Teterin, K. I. Maslakov, I. O. Utkin, *J. Nucl. Technol. Radiat.*, 19, 1, 31-38, (2004)
- [40] K. Rida, A. Benabbas, F. Bouremmad, M.A. Pena, E. Sastre, A. Martinez-Arias, *Appl. Catal., A*, 327, 173-179, (2007)

-
- [41] B. Wichterlova, L. Krajcikova, Z. Tvaruzkova, S. Beran, *J. Chem. Soc., Faraday Trans.*, 1, 80, 2639-2645, (1984)
- [42] P. G. Harrison, N. C. Lloyd, W. Daniell, *J. Phys. Chem. B.*, 102, 10672-10679, (1998)
- [43] H. M. Widatallah, S. H. Al-Harhi, C. Johnson, Z. Klencsar, A. M. Gismelseed, E. A. Moore, A. D. Al-Rawas, C. I. Wynter, D. E. Brown, *J. Phys. D: Appl. Phys.*, 44, 265403, (2011)
- [44] E. Desimoni, C. Malitesla, P. G. Zambonin, J. C. Riviere, *J. Surf. Interface Anal.*, 13, 173-179, (1988)
- [45] W. D. Schneider, C. Laubschat, I. Nowik, G. Kaindl, *Phys. Rev. B*, 24, 9, 5422, (1981)
- [46] F. Mercier, C. Alliot, L. Bion, N. Thromat, P. Toulhoat, *J. Electron. Spectrosc. Relat. Phenom.*, 150, 1, 2126, (2006)
- [47] C. Caspers, M. Muller, A. X. Gray, A. M. Kaiser, A. Gloskovskii, C. S. Fadley, W. Drube, C. M. Schneider, *Phys. Rev. B*, 84, 205217, (2011)
- [48] T. E. Weirich, J. L. Labar, X. Zou, "Electron Crystallography: Novel Approaches for Structure Determination of Nanosized Materials", Springer, (2006)
- [49] R. F. Egerton, "Physical Principals of Electron Microscopy", Springer US, (2005)

-
- [50] D. B. Williams, C. B. Carter, “Transmission Electron Microscopy”, Springer US, (2009)
- [51] www.fei.com/products/tem/tecna/
- [52] J. Goldstein, D. E. Newbury, D. C. Joy, C. E. Lyman, P. Echlin, E. Lifshin, L. Sawyer, J. R. Michael, “Scanning Electron Microscopy and X-ray Microanalysis”, Springer, 3rd ed., (2003)
- [53] M. T. Postek, K. S. Howard, A. H. Johnson, K. L. McMichael, “Scanning Electron Microscopy”, Ladd Research Industries, Inc., (1980)

Chapter 5

Magnetic and Thermal Measurements

5.1 Magnetic Properties Measurement System

The DC magnetization measurements presented in this thesis were all taken using a Quantum Design Magnetic Properties Measurement System (MPMS) magnetometer, at Brock University, Canada. System is an advanced SQUID (Superconducting Quantum Interference Device) magnetometer for the exact measurements of the magnetic moments of small experimental samples over a broad range of temperatures and magnetic fields. The MPMS allows the researcher to perform the measurements of the magnetization as a function of temperature, magnetic field or time. The main components of this system are:

- Temperature control system for controlling the heat flow into the sample space for a range between 1.8 and 350 K.
- Magnet control system for the magnetic fields from 0 to ± 55 kOe.
- The SQUID detector system, including amplifier control electronics and

pick-up coils, which is the heart of the magnetic moment measurement system.

- Sample handling system for handling the sample automatically through the detection coils.
- Liquid helium dewar mounted in its cabinet, providing temperatures down to 1.8 K.
- Computer operating system.

The schematic drawing of the dewar cabinet and the sample probe in the MPMS are depicted in Figure 5.1, while the principal parts of the SQUID system are shown in Figure 5.2(a).

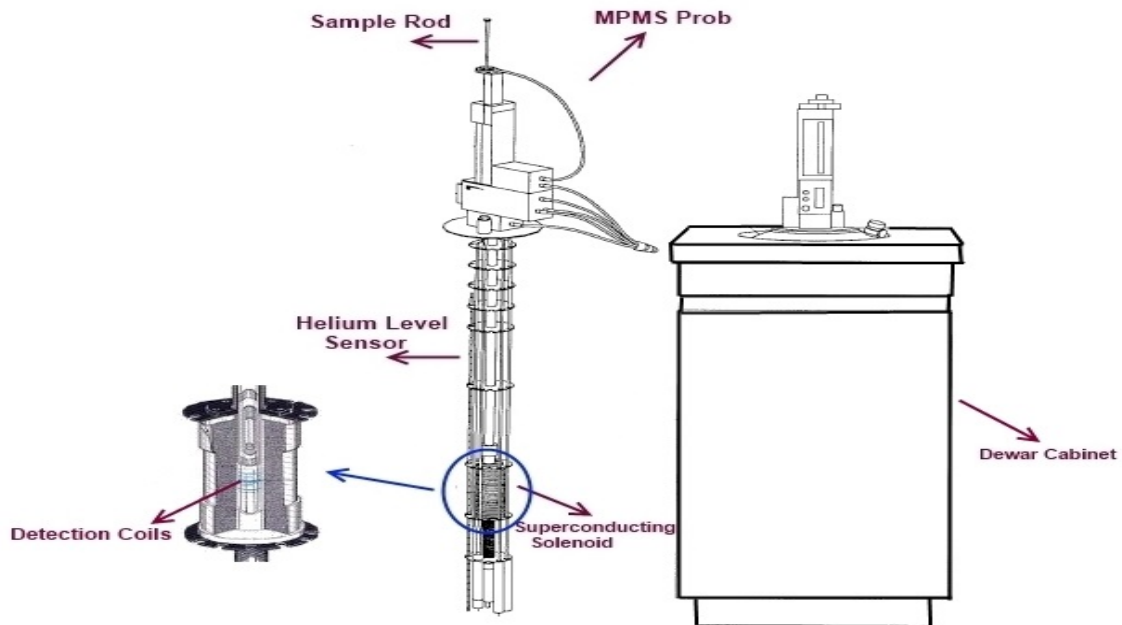


Figure 5.1: Schematic drawing of MPMS probe and dewar cabinet in MPMS system, reprinted from Ref. [1].

In order to detect the sample's magnetization by the SQUID, the sample has to move through the detection coil (pick-up coil) which consists of a set of three coils (Figure 5.2), the upper and the bottom coils are a single turn wound clockwise and the center coil is a two-turn wound counter clockwise. The pick-up coil is connected to the input coil via the superconducting wires, inducing current proportional to the sample magnetization into the SQUID. The SQUID produces the output voltage which is then amplified and read out by the magnetometer's electronics. Monitoring the output voltage of the SQUID as a function of the sample temperature enables us to track changes in the sample magnetization with the temperature [1, 2, 3].

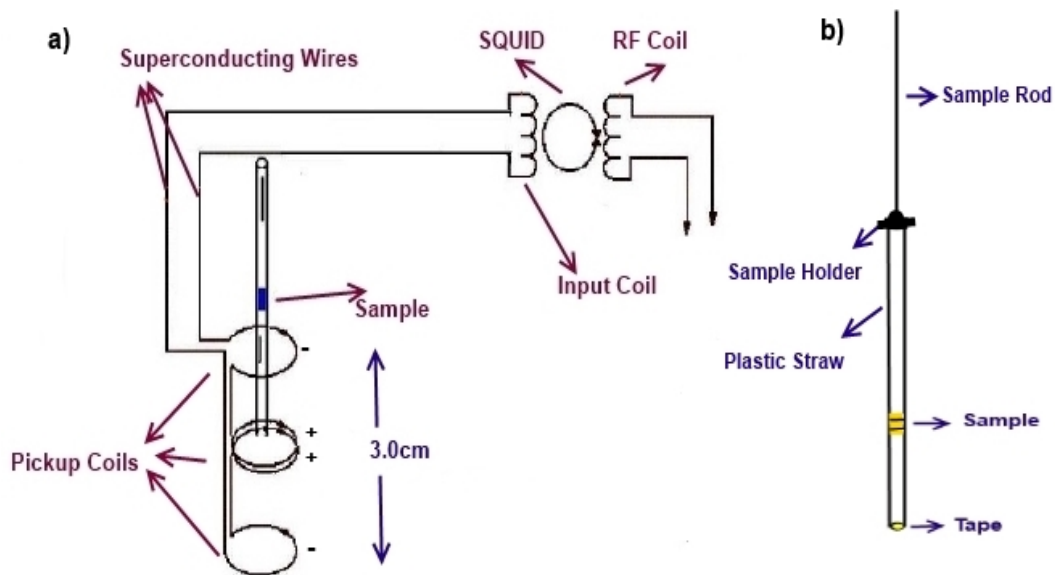


Figure 5.2: Schematic drawings of (a) the SQUID system in the MPMS, (b) a sample mounted in the plastic drinking straw and attached to the sample rod used for the magnetization measurement in the MPMS, reprinted from Ref. [4].

The first step of the magnetic measurement using MPMS is loading the sample. The small piece of a pressed sample was cut, weighed and mounted inside a

plastic drinking straw, where its diamagnetic moment was negligible. For mounting the sample, we made four horizontal cut on the straw and placed the sample inside the segment. Some Kapton tape at the bottom of the straw was used to avoid having the sample drop out of it; and, some holes were made in the straw, allowing air to be pumped out. The plastic straw was then attached to the end of the sample holder, where it was placed about 7 to 10 cm from the end of the sample holder. The plastic straw containing the sample was moved vertically inside the system and the sample was automatically centered in the SQUID pickup coils to ensure that all four coils sensed the magnetic moment of the sample. Now the system is ready to run the sequence.

5.1.1 DC Magnetization Results

The temperature dependence of the DC magnetization for all samples was measured during the warming cycle after cooling the sample from $T = 300$ to 1.8 K in two conditions of zero field-cooled (ZFC) and field-cooled (FC). During the ZFC measurement, a sample was cooled down to 1.8 K in the absence of the magnetic field and then the magnetic field was applied and the magnetization was recorded while warming up to room temperature. On the other hand, in the FC cycle, the sample was cooled down to 1.8 K in the presence of the magnetic field and then the magnetization measurement was done upon warming up.

The ZFC (blue line)/FC (red line) susceptibilities versus temperature of CeCrO_3 with an applied magnetic field of $H = 0.5$ kOe are shown in Figure 5.3(a).

The ZFC and FC magnetic susceptibilities split from each other at the

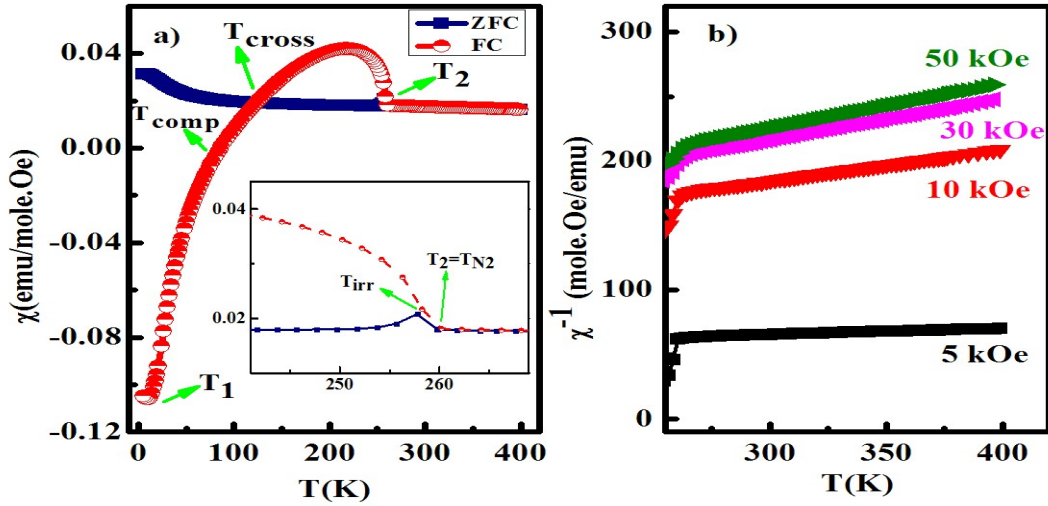


Figure 5.3: (a) ZFC (blue line)/FC (red line) susceptibilities versus temperature measurements of CeCrO₃ under an applied magnetic field of 0.5 kOe. (b) Inverse magnetic susceptibilities of CeCrO₃ under different magnetic field.

irreversible temperature $T_{irr} = 258$ K. They behave differently below this temperature (Figure 5.3 inset). By warming up from 1.8 K to room temperature, the ZFC molar magnetic susceptibility (blue line) decreases gradually until it reaches the transition temperature at $T_2 = 260$ K. According to previous studies on chromites [5, 6, 7], this anomaly can be attributed to the antiferromagnetic Néel temperature of Cr³⁺ moments, denoted by T_{N2} . The χ (ZFC) is positive at all temperatures.

On the other hand, with the FC magnetization measurement, the absolute value of the susceptibility increases up to the transition temperature of $T_1 = 12$ K and then decreases to become zero at the compensation temperature, T_{comp} . Below T_{comp} , the magnetization is negative while with further warming it changes to a positive value. Above T_{comp} , the magnetization increases to reach a maximum at $T_b = 219$ K and then decreases gradually to reach the transition temperature of

260 K. The T_1 anomaly can be attributed to the magnetic ordering of cerium ions which indicates the spin reorientation in different members of RCrO_3 compounds [7, 8, 9].

The ZFC and FC magnetizations cross each other at T_{cross} . Below this temperature, $\chi(\text{FC})$ is lower than $\chi(\text{ZFC})$, contrary most compounds where $\chi(\text{FC})$ usually lies above $\chi(\text{ZFC})$ with a positive value.

To explain this behavior, we can say that in the ZFC magnetization curve, Cr^{3+} and Ce^{3+} moments are uncoupled and independent, so they experience the same external magnetic field. However, in the FC magnetization, the Cr sublattice creates a local field at the Ce sublattice. According to previous studies on RCrO_3 compounds [7, 10], cerium moments align antiparallel with respect to the Cr moments, thus the f-d exchange interaction (J) is negative and the total magnetization can be written as:

$$\begin{aligned} M_{tot} &= M_{\text{Cr}^{3+}} + M_{\text{Ce}^{3+}} = M_{\text{Cr}^{3+}} + J\chi_{\text{Ce}^{3+}}M_{\text{Cr}^{3+}} \\ &= (1 + J\chi_{\text{Ce}^{3+}})M_{\text{Cr}^{3+}}. \end{aligned} \quad (5.1)$$

At high temperatures, $M_{\text{Cr}^{3+}}$ is larger than $M_{\text{Ce}^{3+}}$ and the total magnetization will be positive. However, rare earth ions have a free spin behavior and their magnetic susceptibility satisfies the Curie-Weiss law (Equation (2.4)). Therefore, $\chi_{\text{Ce}^{3+}}$ increases by lowering the temperature and M_{tot} becomes negative and the magnetization reversal happens. In fact, Cr^{3+} starts ordering below $T_{N2} = 260$ K and the Cr^{3+} - Cr^{3+} interaction is dominant until T_b when the R^{3+} - Cr^{3+} interaction appears. The R^{3+} - R^{3+} interaction plays a principal role in the magnetization below

T_1 [11, 12].

The temperature independent diamagnetic susceptibility of CeCrO_3 was estimated $\approx -67 \times 10^{-6}$ emu/mole, where $\chi_D(\text{Ce}^{3+}) \approx -20 \times 10^{-6}$ emu/mole, $\chi_D(\text{Cr}^{3+}) \approx -11 \times 10^{-6}$ emu/mole and $\chi_D(\text{O}^{2-}) \approx -12 \times 10^{-6}$ emu/mole [13]. At sufficiently high temperatures above Néel temperature T_{N2} , the magnetic susceptibility follows a Curie-Weiss law according to Equation (2.12). Figure 5.3(b) displays the inverse magnetic susceptibilities of CeCrO_3 at high temperatures. The data reveal a magnetic field dependence for small magnetic fields which we attribute to a slight trace of ferromagnetic impurities, possibly CrO_2 (≈ 20 ppm), which is saturated with higher fields. The data collected at 30 kOe and 50 kOe fall on top of each other and these were used for the effective magnetic moment analysis. The calculated effective magnetic moment of $\mu_{eff} = 4.88 \pm 0.06 \mu_B/\text{f.u.}$ is in good agreement with the theoretical value of $\mu_{eff} = \sqrt{(\mu_{\text{Cr}^{3+}})^2 + (\mu_{\text{Ce}^{3+}})^2} = 4.63 \mu_B/\text{f.u.}$, where $\mu_{\text{Cr}^{3+}} = 3.87 \mu_B$ and $\mu_{\text{Ce}^{3+}} = 2.54 \mu_B$ [14]. The paramagnetic Curie temperature $\theta_P = -374$ K was determined by the linear extrapolation of χ^{-1} to zero which is about 1.5 times larger than the Néel temperature.

To better characterize the applied magnetic field effect on the magnetic behavior of CeCrO_3 , the temperature dependence of the susceptibility under various magnetic fields were measured. As shown in Figure 5.4(a), the FC susceptibility of CeCrO_3 is negative below 60 K at $H = 2$ kOe while this reversal of magnetization disappears under higher magnetic fields. Furthermore, increasing the magnetic field causes the FC magnetization enhancement at low temperatures. All curves tend to cross at the same temperature (T_{cross}) over the whole range of the applied

magnetic fields. Figure 5.4(b) exhibits the ZFC/FC susceptibilities of CeCrO_3 in the magnetic fields of 5 kOe and 30 kOe. $\chi(\text{ZFC})$ and $\chi(\text{FC})$ have almost similar behavior in $H = 30$ kOe although it shows the existence of irreversibility in ZFC/FC (Fig. 5.4(b) inset). Therefore, by applying the magnetic field higher than the local magnetic field created by Cr sublattice, the magnetization reversal disappears and the ZFC/FC susceptibilities splitting reduces.

The magnetization isotherms of CeCrO_3 over the temperatures of 5 to 300 K were recorded after the sample was cooled in the zero magnetic field. Figure 5.5(a) is the magnetization versus magnetic field of CeCrO_3 at $T = 5$ K which shows a magnetic hysteresis, indicating the existence of the weak ferromagnetism with the remnant magnetization, M_r and the coercivity, H_c of 67.96 emu/mole and 3000 Oe, respectively. However, above 20 K, the magnetic hysteresis disappears and the M-H loops become linear which proves the lack of ferromagnetic ordering (Figure 5.5(b)). In all M-H loops in the region of the high magnetic field, magnetization increases linearly at all temperatures, which can be an evidence of glassy magnetic phases and/or canted spin configuration. All these results suggest the existence of the canted antiferromagnetism/glassy phase with weak ferromagnetism for this compound.

In the $\text{Ce}_{0.8}\text{Eu}_{0.2}\text{CrO}_3$ sample, the ZFC magnetization first decreases to reach 30 K and then increases to create a sharp peak at $T_1 = 47$ K. Above T_1 , the magnetization reduces until $T_{N2} = 242$ K (Figure 4.6(a)). The weak ferromagnetic loop is observed between 30 K to 47 K, while it is antiferromagnetic between T_1 to T_{N2} (Figures 5.6(b), (c) and (d)).

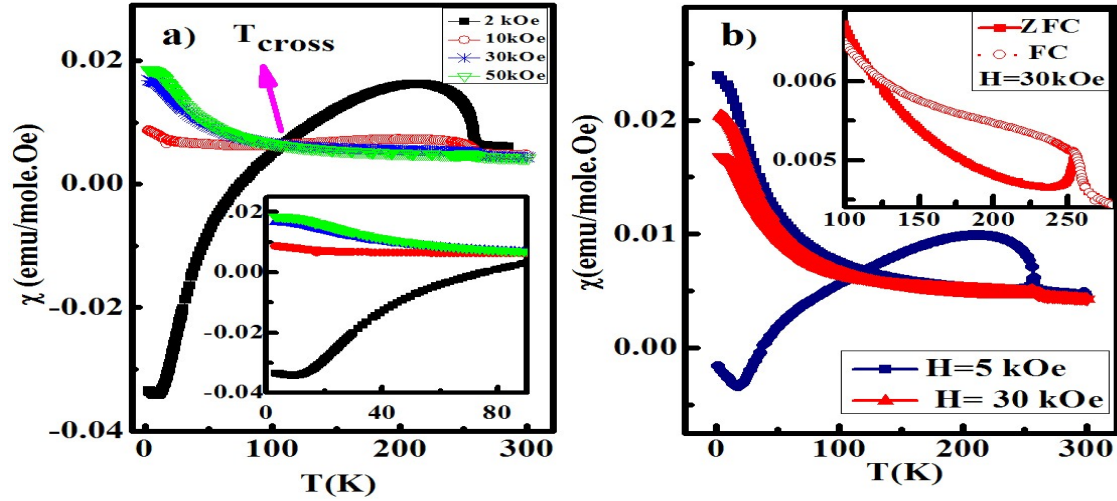


Figure 5.4: (a) FC susceptibility measurements of CeCrO_3 in different magnetic fields, (b) ZFC/FC susceptibility measurements of CeCrO_3 in $H = 5$ kOe (blue line) and $H = 30$ kOe (red line). The inset shows the existence of the divergence in the ZFC and FC susceptibilities even in $H = 30$ kOe.

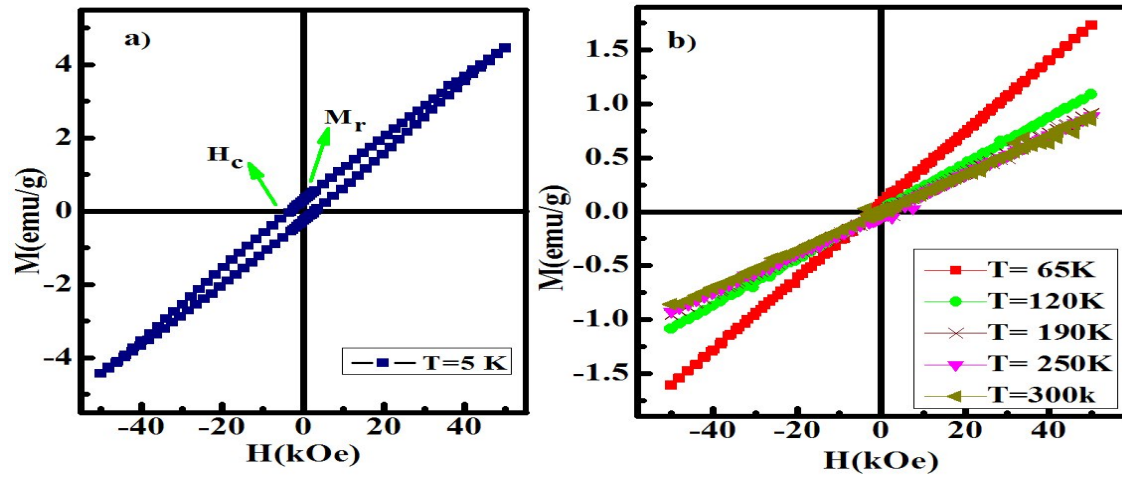


Figure 5.5: The magnetization hysteresis loops of CeCrO_3 at (a) $T = 5$ K, (b) higher temperatures.

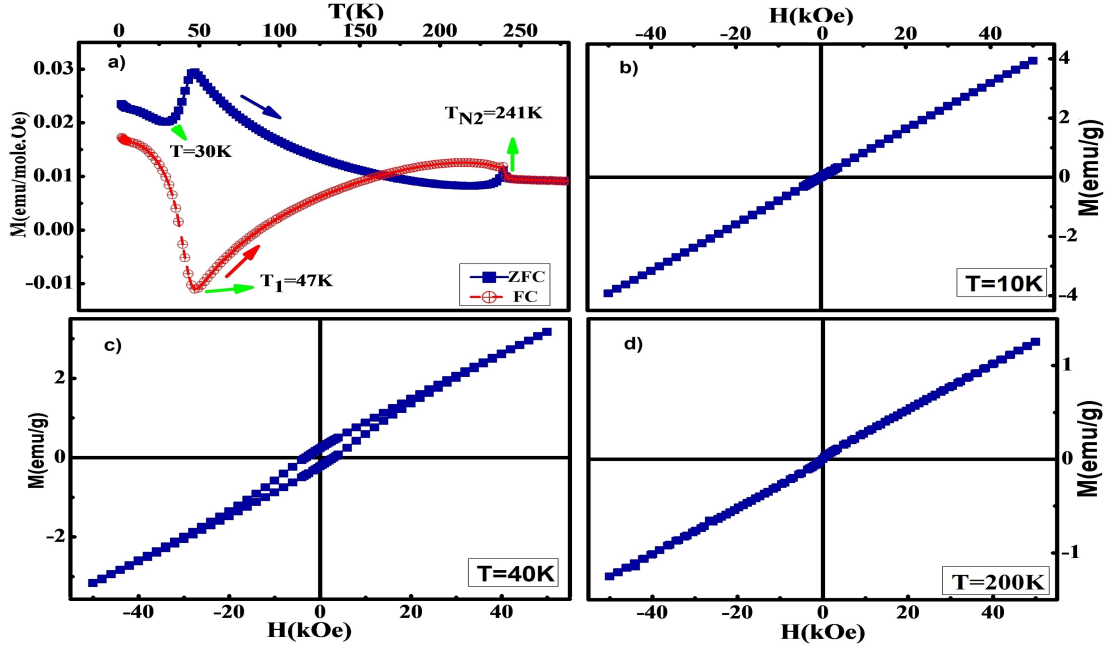


Figure 5.6: (a) ZFC (blue line)/FC (red line) susceptibilities versus temperature measurements under an applied field of 0.5 kOe, (b), (c) and (d) the magnetic hysteresis loops at the different temperatures of the sample $\text{Ce}_{0.8}\text{Eu}_{0.2}\text{CrO}_3$.

Figures 5.7(a) and (b) show the magnetic behaviors of $\text{Ce}_{1-x}\text{Eu}_x\text{CrO}_3$, where $x = 0.1, 0.5, 0.9$ and 0.95 . The transition temperature (T_{N2}) as well as the bifurcation temperature (T_{irr}) move to the lower temperatures and T_1 almost disappears by increasing in Eu substitution. Furthermore, the magnetization reversal vanishes in the samples with the higher Eu^{3+} content.

By increasing the Eu^{3+} substitution to 90 % and 95 %, the magnetization shows a different behavior. As the temperature is lowered from $T_{N2} = 190\text{ K}$, the FC susceptibility in $\text{Ce}_{0.10}\text{Eu}_{0.90}\text{CrO}_3$ increases to reach a broad bump at $T_b = 139\text{ K}$ and then $\chi(\text{FC})$ decreases. $\chi(\text{ZFC})$ is higher than $\chi(\text{FC})$ below 34 K. A weak ferromagnetic ordering was observed between 139 K to 190 K. In $\text{Ce}_{0.05}\text{Eu}_{0.95}\text{CrO}_3$, the $\chi(\text{FC})$ is higher than $\chi(\text{ZFC})$ for all temperatures and the

weak ferromagnetism exists between 122 K and 187 K, which is stronger than that observed in $\text{Ce}_{0.10}\text{Eu}_{0.90}\text{CrO}_3$.

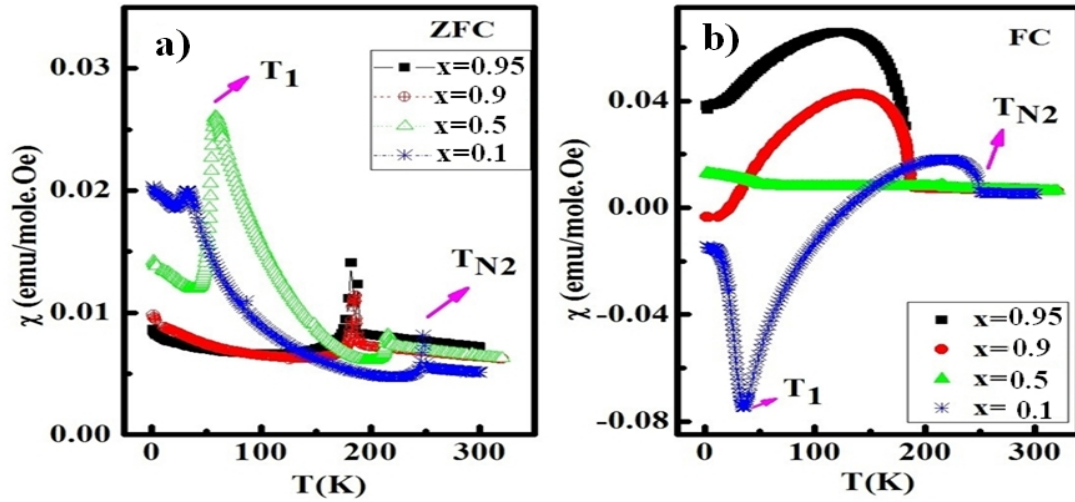


Figure 5.7: (a) ZFC and (b) FC susceptibilities measurements under an applied magnetic field of 0.5 kOe of samples $\text{Ce}_{1-x}\text{Eu}_x\text{CrO}_3$, where $x = 0.1, 0.5, 0.9, 0.95$.

Figure 5.8 represents the magnetic property of the $\text{Ce}_{0.02}\text{Eu}_{0.98}\text{CrO}_3$ which includes a noticeable enhancement in the magnetic susceptibility. The ferromagnetic like hysteresis loops are observed between temperatures T_b and T_{N2} while it is paramagnet below temperature T_1 .

The temperature dependence of the magnetization with an applied magnetic field of $H = 0.5$ kOe for EuCrO_3 with a clear bifurcation of ZFC and FC curves and a transition temperature of 182 K is shown in Figure 5.9. By warming up the temperature above 1.8 K, the FC susceptibility first increases to reach the temperature T_b (lower inset) and then decreases sharply until the Néel transition temperature of 182 K. This behavior at low temperatures resembles the cluster-glass compounds. The upper inset represents the sharp peak in the $\chi(\text{ZFC})$ with the

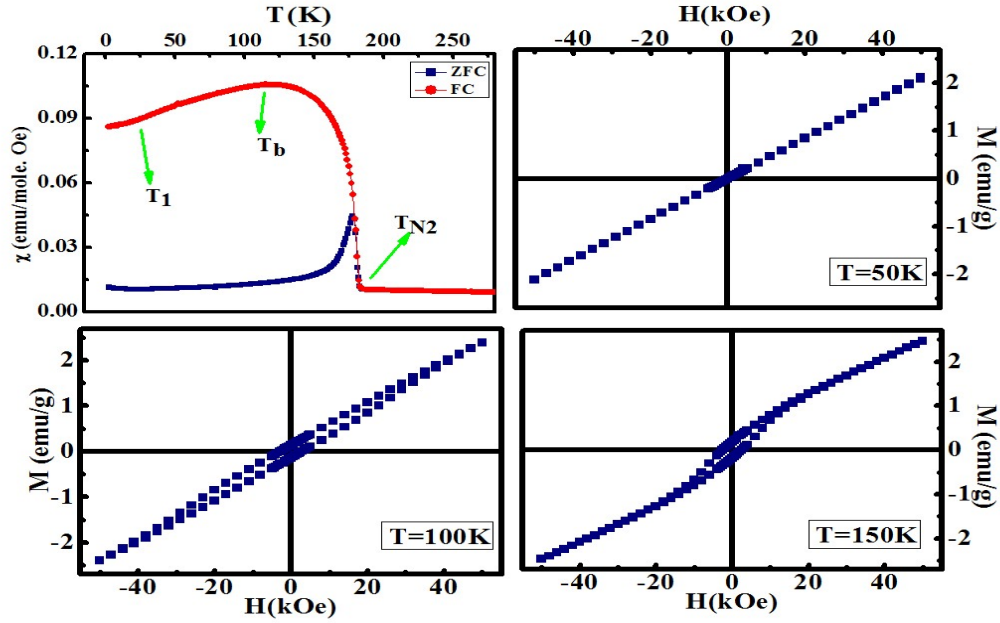


Figure 5.8: (a) ZFC (blue line)/ FC (red line) susceptibilities measurements under an applied magnetic field of 0.5 kOe, (b), (c) and (d) the magnetic hysteresis loops at the different temperatures of $\text{Ce}_{0.02}\text{Eu}_{0.98}\text{CrO}_3$.

maximum transition temperature of $T_m=178$ K, close to the bifurcation temperature (T_{irr} of ZFC and FC graphs). The lack of a real transition temperature at the low temperatures excludes the presence of the long range ordering of europium ions.

The measured magnetic susceptibility of EuCrO_3 can be written as $\chi_{exp} = \chi_{CW} + \chi_D + \chi_{VV}$, where $\chi_{CW} = \frac{C}{T-\theta_c}$, χ_D and χ_{VV} are the Curie-Weiss paramagnetic susceptibility, diamagnetic susceptibility and Van Vleck susceptibility, respectively. χ_D (EuCrO_3) was estimated $\approx -67 \times 10^{-6}$ emu/mole [13].

The inverse magnetic susceptibilities of EuCrO_3 at high temperatures are shown in Figure 5.10(a). The field dependence arises most likely from a trace ferromagnetic impurity (e.g. Eu_2 , CrO_2) which is gradually saturated with higher fields. The data collected at 10 kOe are used for the effective magnetic moment

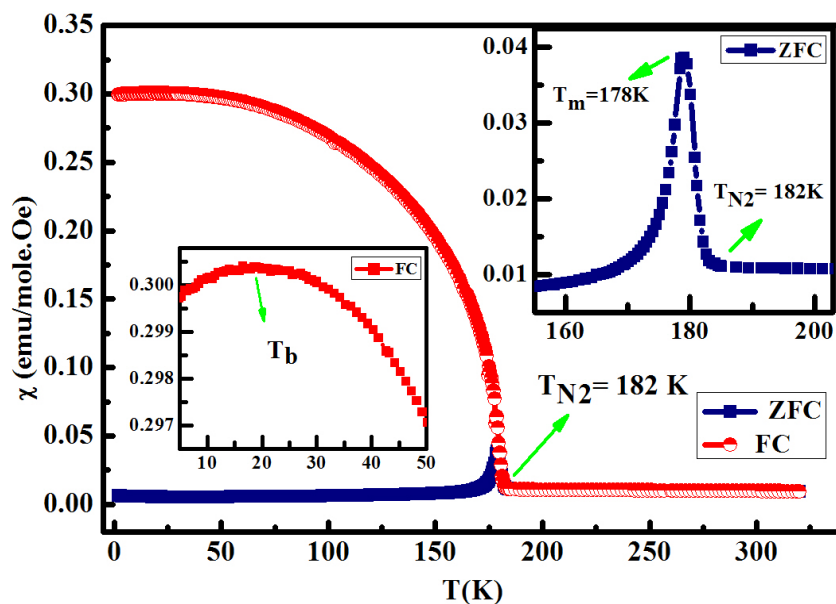


Figure 5.9: ZFC (blue line)/FC (red line) susceptibilities versus temperature of EuCrO_3 under an applied magnetic field of 0.5 kOe, (Lower inset shows the $\chi(\text{FC})$ below 50 K and the upper inset presents $\chi(\text{ZFC})$ around the transition temperature).

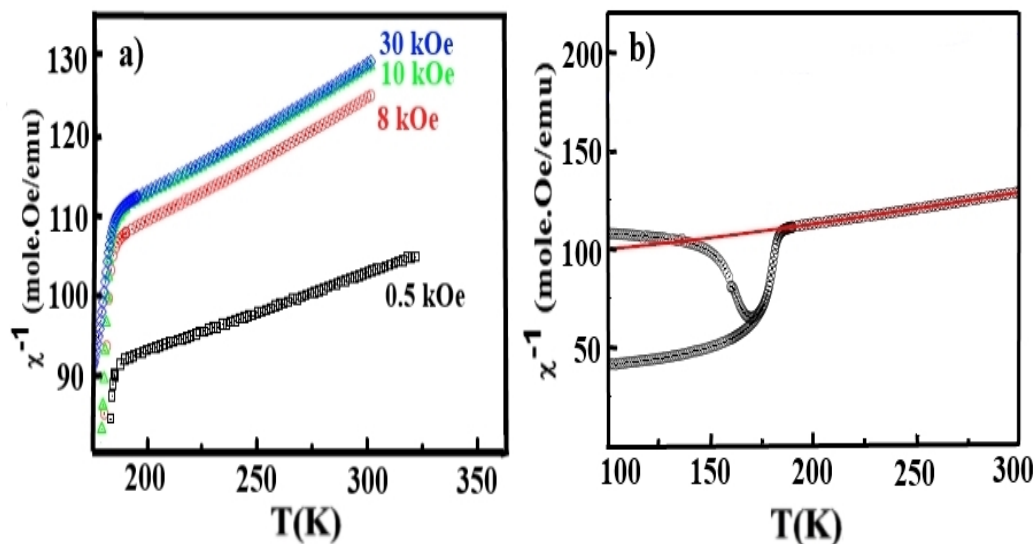


Figure 5.10: Inverse magnetic susceptibility of EuCrO_3 (a) under different magnetic field, (b) measured with a field of 10 kOe. The solid red line represents fit of a Curie-Weiss law.

calculation.

A first analysis of the high temperature susceptibility data in terms of a Curie-Weiss law Equation (2.12) points to a negative Curie-Weiss temperature about three times larger in magnitude than the long range ordering temperature. The negative Curie-Weiss temperature indicates sizable predominant antiferromagnetic spin exchange interaction. The derived Curie-Weiss Constant of $C \approx 6.1 \text{ emu.K/mole.Oe}$ gave an effective magnetic moment of $6.98 \pm 0.11 \mu_B/\text{f.u.}$. If we attribute the difference to the Cr^{3+} moment simply to the magnetism of the Eu^{3+} ion by using $\mu_{eff} = \sqrt{(\mu_{\text{Cr}^{3+}})^2 + (\mu_{\text{Eu}^{3+}})^2}$, one arrives at effective moments for Eu^{3+} of the order of $5.9 \mu_B$, which is by far too large compared to what is expected for Eu^{3+} systems ($\mu_{\text{Eu}^{3+}} = 3.5\mu_B$).

Here we follow an alternative approach: as we explained in Chapter 2, page 34, Eu^{3+} typically shows a weakly temperature dependent Van Vleck like paramagnetism with typical room temperature values of about $4 \times 10^{-6} \text{ emu/mole}$ and increases from liquid He temperatures to room temperature by about 15% [15, 16]. Thus, the measured magnetic susceptibility of EuCrO_3 includes the $\chi_{CW}(\text{Cr}^{3+})$ and $\chi_{VV}(\text{Eu}^{3+})$ after subtracting the diamagnetic contribution. Figure 5.10(b) shows the fit of $\frac{C}{T-\theta_c} + \chi_{VV}(T)$ to the experimental data where $C = 1.873 \text{ emu.K/mole.Oe}$ was used, corresponding to an effective moment of Cr^{3+} of $3.87\mu_B$. In order to fit the data, we multiplied the Eu contribution by a factor of ≈ 1.26 to enlarge the Van Vleck susceptibility. This enhancement can either be due to magnetic polarization of the Eu moments by the Cr moments or due to a slight change of the susceptibility due to crystal field splittings of the excited 7F_J levels

which has not taken into consideration in the calculation of the susceptibility of the free Eu^{3+} moments. As a consequence of the proposed procedure to fit the high temperature magnetic susceptibility of EuCrO_3 , the Curie-Weiss temperature is a factor of two larger than the Néel temperature.

The $\chi(\text{ZFC})$ and $\chi(\text{FC})$ of EuCrO_3 under different magnetic fields have been plotted in Figure 5.11. The higher magnetic field in the ZFC susceptibilities (Figure 5.11(a)) makes the transition temperature broader and reduces its intensity. Furthermore, higher magnetic field lowers the transition temperature. All these results indicate the suppression of the spin disordering by the higher applied magnetic field. The inset shows an increase of ZFC susceptibility at low temperatures in the higher applied magnetic field. Figure 5.11(b) shows the reduction of the FC magnetization at low temperatures with an increase in the applied magnetic field.

Figure 5.12(a) indicates the effect of an applied magnetic fields of 5 kOe and 30 kOe on the divergence between ZFC and FC magnetization for EuCrO_3 . This bifurcation below the irreversible temperature T_{irr} decreases and T_{irr} is shifted to the lower temperatures while increasing an external magnetic field. The field dependence of the temperature T_{irr} fits with the function the $T_{irr} = T_0 + b H_{ext}^n$, where $T_0 = 179$ K, $b = -0.3$ and $n = 1.14$ (Figure 5.12(b)). Consequently, the external magnetic field tries to overcome the magneto-crystalline anisotropy, although a magnetic field as high as 50 kOe was not sufficient to be dominant in EuCrO_3 . Thus, an increase in the applied magnetic field suppresses the ZFC and FC susceptibilities divergence and reduces the spin-glassy behavior in EuCrO_3 . Furthermore, the splitting between ZFC and FC magnetizations can be a property

of the spin disorder systems [17, 18].

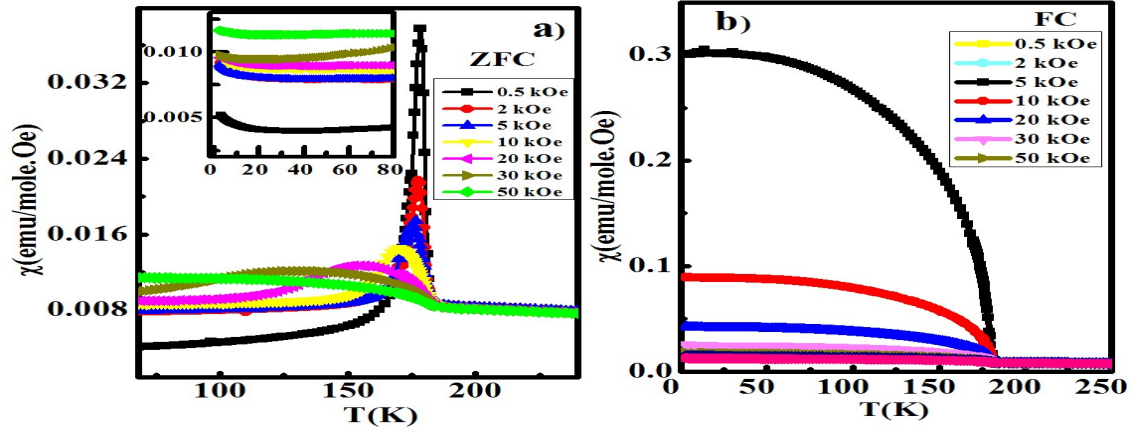


Figure 5.11: (a) ZFC and (b) FC susceptibility measurements of EuCrO_3 in the different magnetic fields.

Magnetic hysteresis measurements in Figure 5.13 show the ferromagnetic like loops below 182 K, however, the shape of M-H graphs is the evidence of existence of two magnetic component. The remnant magnetization, M_r and coercivity, H_c , calculated at 5 K are 112.21 emu/mole and 11000 Oe, respectively, which are higher than those of CeCrO_3 . By increasing the temperature, the area of the magnetic loops reduces until 182 K and then converts to the linear M-H graph which indicates the paramagnetic behavior of the sample at high temperatures.

Figure 5.14(a) shows both FM and AFM component of EuCrO_3 at $T = 100$ K. To show the FM component of the sample (green line), the background (red line) was subtracted from the total magnetization (black line). We measured hysteresis loops from 175 K to 90 K at 10 K intervals. Within the field limit of our magnetometer (55 kOe), all hysteresis loops above 100 K show saturation magnetization. Figure 5.14(b) shows the maximum magnetic field (H_s) which the

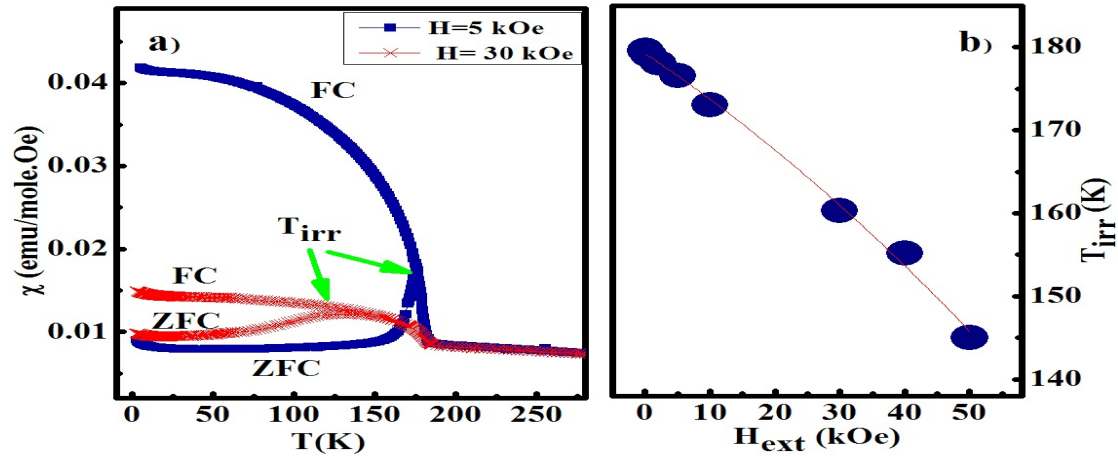


Figure 5.12: (a) ZFC/FC susceptibility measurements of EuCrO_3 in $H=5$ kOe (blue line) and $H=30$ kOe (red line), (b) the irreversible temperature versus an applied magnetic field of EuCrO_3 .

M-H branches converge to each other and start linear increase. The results indicate that for saturating the sample below 100 K, the magnetic field higher than 50 kOe is needed. A linear fit to saturation fields versus temperature indicates a saturation magnetization at about 79.9 ± 1.4 kOe at $T = 5$ K. Figure 5.14(c) illustrates the M-H loops of EuCrO_3 at $T=135$ and 175 K. The saturation magnetization at $T = 135$ K is 38.0 kOe while at $T = 175$ K, it is 17.5 kOe.

The difference between magnetic behavior of EuCrO_3 and CeCrO_3 goes back to the electron configuration of the rare earth ions with the even electrons ($\text{Eu}^{3+}(4f^6)$) and a singlet ground state, compared to the rare earth ions with odd electrons ($\text{Ce}^{3+}(4f^1)$) and the magnetic moment in the ground state. As explained in Chapter 2, a first excited state of Eu^{3+} ($J = 1$) is located slightly above the ground state ($J = 0$) and its paramagnetic susceptibility will be derived from the Van Vleck susceptibility. χ_{CW} disappears when $J = 0$, nevertheless χ_{VV} of Eu^{3+} is not zero

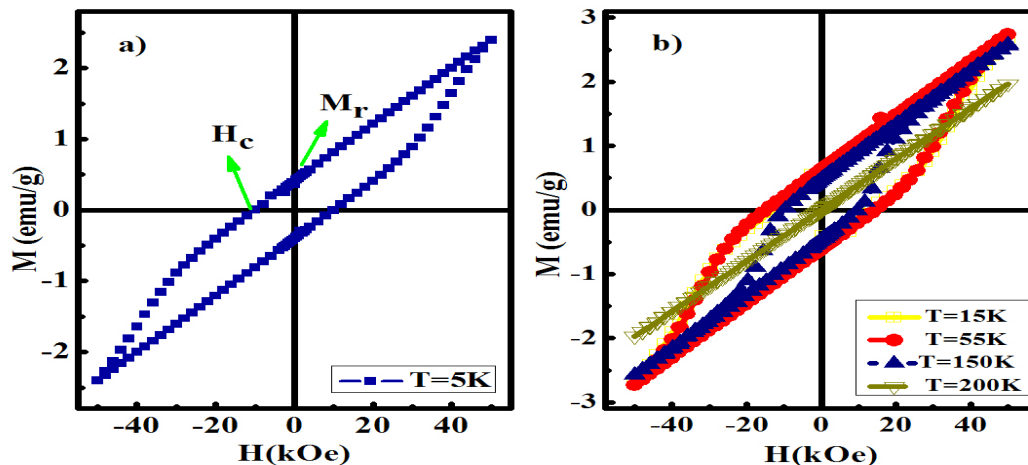


Figure 5.13: The magnetic hysteresis loops of EuCrO_3 at (a) $T = 5\text{ K}$ and (b) $T = 15, 55, 150$ and 200 K .

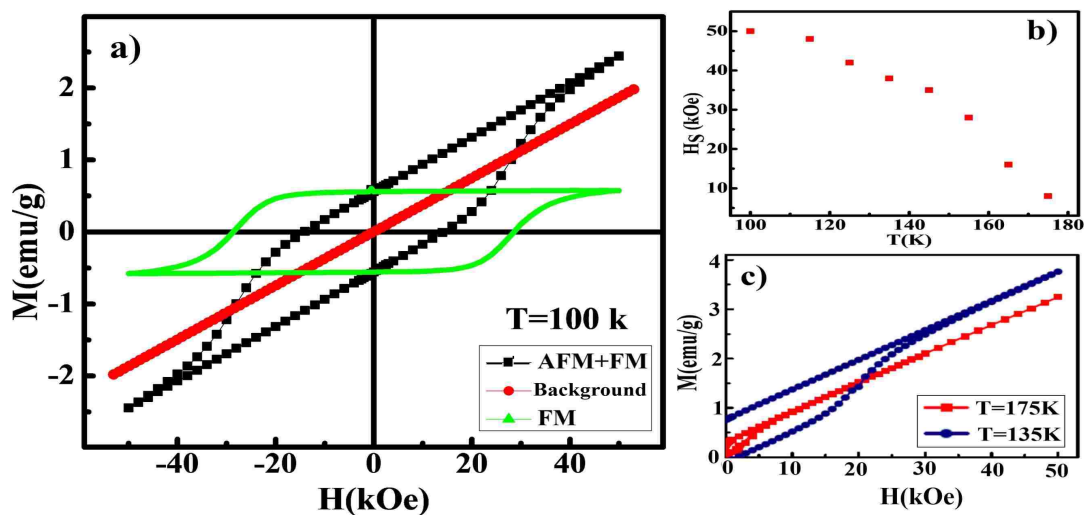


Figure 5.14: (a) Total hysteresis loop (black line), background (red line) and FM component (green line) of EuCrO_3 at 100 K . (b) The temperature dependence of the saturated magnetic field (H_s). (c) Magnetic hysteresis loops of EuCrO_3 at 135 K (blue line) and 175 K (red line).

and mostly temperature independent below ≈ 100 K [15, 16]. Therefore, the total magnetization of EuCrO_3 is positive at all temperatures [19, 20] and calculated using the following equation:

$$M_{tot} = M_{Cr^{3+}} + M_{Eu^{3+}} = (1 + J\chi_{Eu^{3+}})M_{Cr^{3+}}. \quad (5.2)$$

In Table 5.1, there is a summary of the transition temperatures of $\text{Ce}_{1-x}\text{Eu}_x\text{CrO}_3$ while increasing europium dopant x .

Table 5.1: The transition temperatures (T_1 and T_{N2}), the temperature at which $\chi(\text{ZFC})$ and $\chi(\text{FC})$ cross each other (T_{cross}) and temperature at which $\chi(\text{FC})$ is maximum (T_b) in $\text{Ce}_{1-x}\text{Eu}_x\text{CrO}_3$.

x	T_{N2}	T_1	T_b	T_{cross}
0.0	260	12	219	117
0.02	258	14	218	126
0.1	253	34	217	150
0.2	242	47	215	164
0.3	236	54	213	171
0.4	227	57	209	170
0.5	218	58	199	158
0.6	211	56	188	147
0.7	205	52	177	130
0.8	202	50	175	120
0.9	190	13	139	34
0.95	187	9	122	-
0.98	184	18	118	-
1.0	182	-	20	-

The effective magnetic moments (μ_{eff}) of $\text{Ce}_{1-x}\text{Eu}_x\text{CrO}_3$ samples were calculated from the χ^{-1} versus T curve above transition temperature T_{N2} and shown in Figure 5.15, which indicates the magnetic enhancement while increasing the europium

substitution.

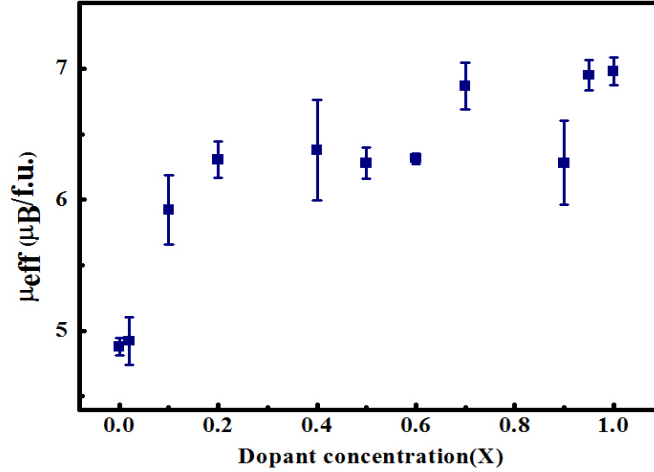


Figure 5.15: The experimental effective magnetic moments of $\text{Ce}_{1-x}\text{Eu}_x\text{CrO}_3$ versus europium dopant (X).

As explained in Chapter 4, Page 108, the physical properties of RCrO_3 compounds strongly depend on the perovskite structure and CrO_6 octahedral distortion. Cr^{3+} has $t_{2g}^3e_g^0$ configuration. When the Cr-O-Cr bond angle is 180° (the ideal CrO_6 octahedral), the super-exchange interaction over $\text{Cr}(t_{2g}^3)\text{-O-Cr}(t_{2g}^3)$ is the only hybridization which leads to an AFM ordering. When Cr-O-Cr is tilted, the super-exchange interaction of $\text{Cr}(t_{2g}^3)\text{-O-Cr}(e_g^0)$ happens as well as creating a FM component. According to the literature [21, 22], the super-exchange coupling (J) in $\text{RCrO}_3 \propto \frac{\cos^4(180^\circ - \theta)/2}{d^7}$, while the Néel temperature $T_N^{\text{Cr}} \propto \frac{\cos^4\theta}{d^7}$. d and θ are the average Cr-O bond length and Cr-O-Cr bond angle, respectively.

Thus, the suppression of the Cr-O-Cr angle and the enhancement of the Cr-O bond length lead to a decrease of the Néel temperature and an increase of the FM property of the compound. The XRD data of $\text{Ce}_{1-x}\text{Eu}_x\text{CrO}_3$ samples (Tables 4.8

and 4.9) show that the Cr-O-Cr bond angle decreases and the $\langle \text{Cr-O} \rangle$ bond length slightly increases through Eu doping due to the smaller radius of the europium ion compared to the cerium ion. Thereby, the Cr^{3+} Néel temperature moves to the lower temperature and the magnetization enhances in $\text{Ce}_{1-x}\text{Eu}_x\text{CrO}_3$ through the Eu substitution which are in good agreement with the obtained magnetic results.

5.1.2 Exchange bias Effect

To further investigate the magnetic properties of CeCrO_3 and EuCrO_3 , the existence of the exchange bias effect was tested. The ZFC and FC magnetic hysteresis loops of these two samples were measured, i.e. in ZFC magnetic loop, the sample was cooled from room temperature in zero magnetic field and then the magnetization was measured at the specific temperature by changing the magnetic field, while in FC measurement, the sample was cooled down under the magnetic field and then the M-H measurement was done.

Figure 5.16 presents the magnetic hysteresis loops of CeCrO_3 measured at 5 K in ZFC (blue line) and FC (red line) conditions. The sample was cooled under 50 kOe applied magnetic field in FC measurement. The results reveal that the magnetic loop is moved to the right and downward, i.e. positive exchange bias. The calculated values of the horizontal shift (H_{EB}) and the vertical shift (M_{EB}) are 3 kOe and 0.25 ± 0.05 emu/g, respectively. The exchange bias observation as well as DC magnetization results suggest the existence of the spin disorder phase in these particles.

To further study the exchange bias effect in CeCrO_3 , the sample was cooled

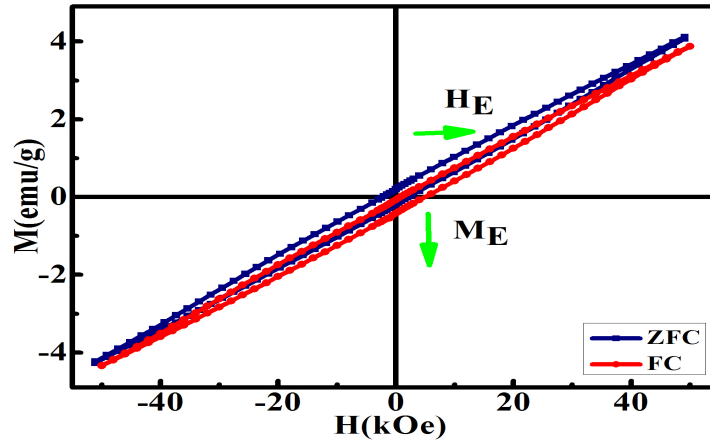


Figure 5.16: ZFC (blue line)/FC (red line) magnetic hysteresis loops of CeCrO_3 after cooling in 50 kOe at 5 K.

down from room temperature to the measuring low temperatures under the cooling magnetic field of 50 kOe and then M-H loops were measured. The temperature dependence of H_{EB} and M_{EB} for CeCrO_3 is shown in Figure 5.17. Interestingly, the exchange bias sign reversal is observed in this sample. Below $T_{cross} = 100$ K, a positive exchange bias effect is observed, i.e. the M-H loop is moved to the right and down while above $T_{cross} = 100$ K, the negative exchange bias effect occurs, i.e. it is shifted to the left and up. The exchange bias effect disappears at $T = 260$ K. At $T_{cross} = 100$ K, the absolute values of H_{EB} and M_{EB} approach zero followed by a minimum in H_{EB} and a maximum in M_{EB} at $T = 220$ K and finally become zero at 260 K. It is noteworthy that a weak ferromagnetic hysteresis loop (non-zero coercivity) in CeCrO_3 was observed below 20 K and the antiferromagnetic M-H loop shifts were recorded above 20 K. The temperature dependence of M_{EB} is similar to the temperature dependence of the CeCrO_3 magnetization plotted in Figure 5.3. The same behavior has been also observed in

$\text{La}_{0.2}\text{Ce}_{0.8}\text{CrO}_3$ nano-particles [23].

Sample CeCrO_3 was cooled down from room temperature under the different cooling magnetic field in order to investigate the effect of cooling field on the exchange bias effect in this compound. Figure 5.18(a) and (b) demonstrate the effect of the cooling magnetic field on the H_{EB} and M_{EB} for CeCrO_3 at $T = 5$ K and $T = 150$ K, respectively. It is noticeable that the absolute values of H_{EB} and M_{EB} increase sharply with the cooling magnetic field and then tend to saturate. No sign reversal of the EB effect was observed while changing the cooling magnetic field.

According to Niebieskikwiat and Salamon's report on the glassy behavior of the surface spin and the EB effect [24], the H_{EB} depends on the cooling magnetic field (H_{ex}) through the following equation:

$$-H_{EB} \propto J_i \left[\frac{J_j \mu_0}{(g \mu_B)^2} L\left(\frac{\mu H_{ex}}{k_B T_f}\right) + H_{ex} \right], \quad (5.3)$$

where $L(x)$, k_B and J_i are the Langevin function, the Boltzmann constant and surface exchange constant, respectively. $\mu = N_v \mu_0$, where μ_0 is the core magnetic moment and N_v is the number of the spins inside the core. The best fit of H_{EB} at $T = 5$ K (Figure 5.18(a)) with this equation gives negative J_i when $\mu_0 \approx 4.5 \mu_B$ and $N_v \approx 392$. The negative exchange constant ($J_i < 0$) indicates the antiferromagnetic interaction between the surface spins of the core and the shell.

On the other hand, the fitted line in Figure 5.18(b) shows the positive exchange constant J_i ($N_v \approx 228$), suggesting the ferromagnetic ordering at the

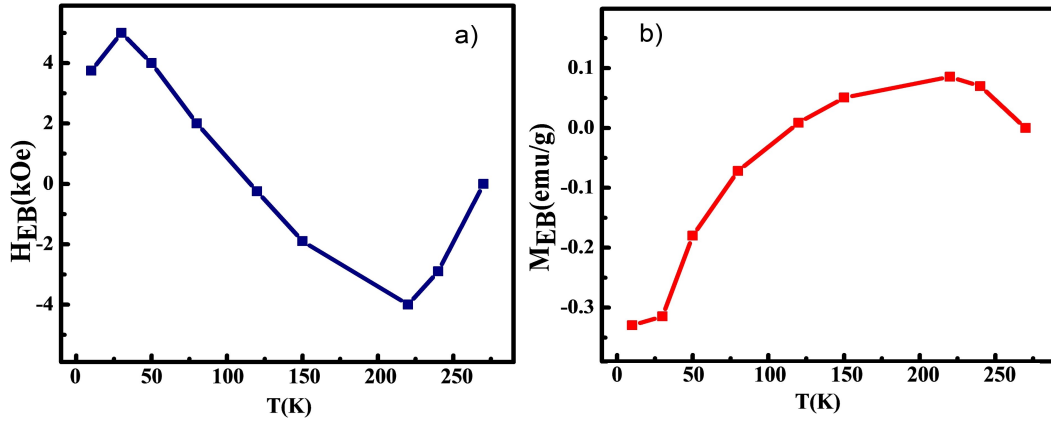


Figure 5.17: The temperature dependence of (a) the exchange bias magnetic field and (b) the exchange bias magnetization of CeCrO₃.

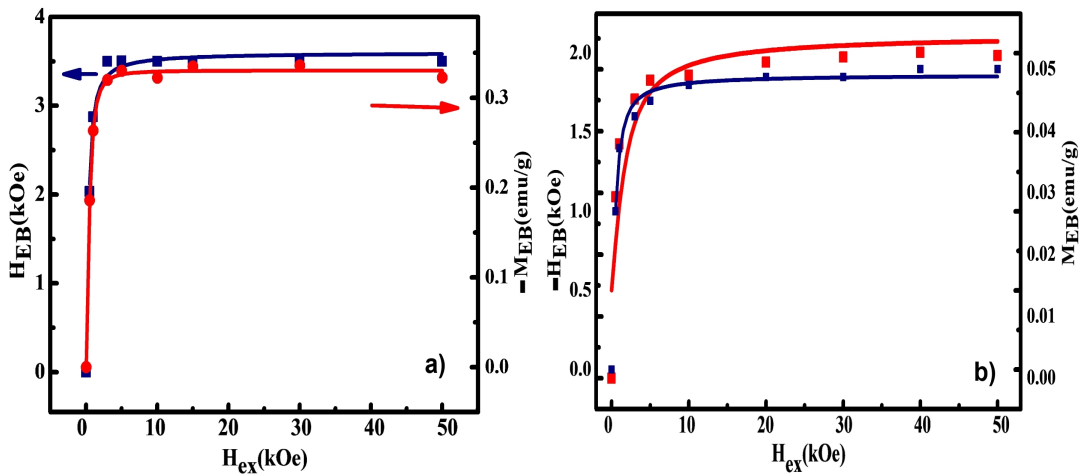


Figure 5.18: The cooling magnetic field dependence of exchange bias magnetic field (blue line) and the exchange bias magnetization (red line) in CeCrO₃ at (a) $T = 5$ K and (b) $T = 150$ K.

interface of the core and the shell of CeCrO_3 at $T = 150$ K. Similarly, the positive exchange bias effect reported in $\text{La}_{0.2}\text{Ce}_{0.8}\text{CrO}_3$ [23] and $\text{La}_{1-x}\text{Pr}_x\text{CrO}_3$ [8] suggested the antiparallel alignment of the spins at the interface.

The ZFC/FC M-H loops of EuCrO_3 done at 5 K under the 50 kOe cooling magnetic field were recorded which indicate the clear horizontal and vertical shifts to the left and upward, i.e. negative exchange bias, as observed in Figure 5.19. This anisotropy interaction in EuCrO_3 is stronger than that in CeCrO_3 , where the obtained values of H_{EB} and M_{EB} of 6 kOe and 0.24 ± 0.04 emu/g, respectively, can prove this theory.

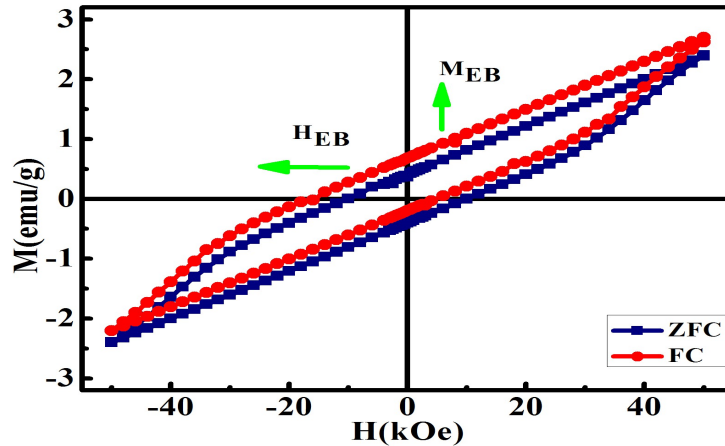


Figure 5.19: ZFC (blue line)/FC (red line) magnetic hysteresis loops of EuCrO_3 after cooling in 50 kOe at 5K.

To study more the exchange bias in EuCrO_3 sample, the sample was cooled down from room temperature to the measuring low temperatures under the cooling magnetic field 50 kOe. The temperature dependence of exchange bias field and magnetization are recorded in Figures 5.20(a) and (b), which lead to the exponential decay. The absolute values of H_{EB} and M_{EB} can be fitted with the function of

$\exp(-\frac{T}{T_0})$, where T_0 is a constant. This behavior has been reported in the spin-glass multilayer systems [25]. These results show the elimination of the exchange bias at the temperature around 150 K, called the blocking temperature.

Figures 5.20(c) and (d) demonstrate the effect of the cooling magnetic field on the exchange bias field (H_{EB}) and magnetization (M_{EB}) at $T = 5$ K. The best fit of H_{EB} in EuCrO_3 with Equation (5.3) gives a positive exchange constant ($J_i > 0$) when $\mu_0 \approx 5\mu_B$ and $N_V \approx 60$, indicating the ferromagnetic interaction between the surface spins of the core and the shell.

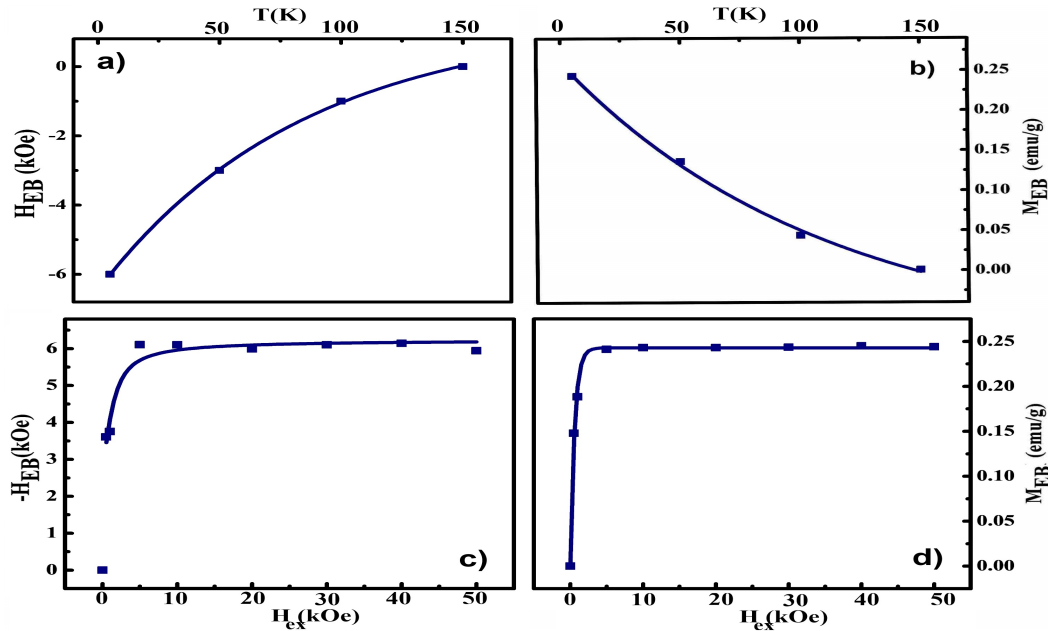


Figure 5.20: (a) and (b) Temperature dependence of the exchange bias magnetic field and exchange bias magnetization under 50 kOe cooling field, (c) and (d) the cooling magnetic field dependence of the exchange bias field and exchange bias magnetization at $T = 5$ K in EuCrO_3 .

To characterize the spin disorder behavior of CeCrO_3 and EuCrO_3 , the thermoremanent magnetization (TRM) and isothermoremanent magnetization (IRM) at 5 K were measured. To measure the TRM, the system was cooled in the specified

magnetic field from room temperature down to 5 K and stayed in the field for 10 min. After that the field was removed and the magnetization was immediately recorded. To measure the IRM, the sample was cooled in zero field down to 5 K, and the field was then applied for 10 min, removed again, and the remanent magnetization recorded.

The IRM and TRM, known as the magnetic fingerprint, show a characteristic difference for different systems, such as spin-glass, 3D diluted AFM (DAFF), an AFM core/2D DAFF shell nano-wires systems and an AFM core/2D DAFF shell nano-powders, as observed in Figure 5.21.

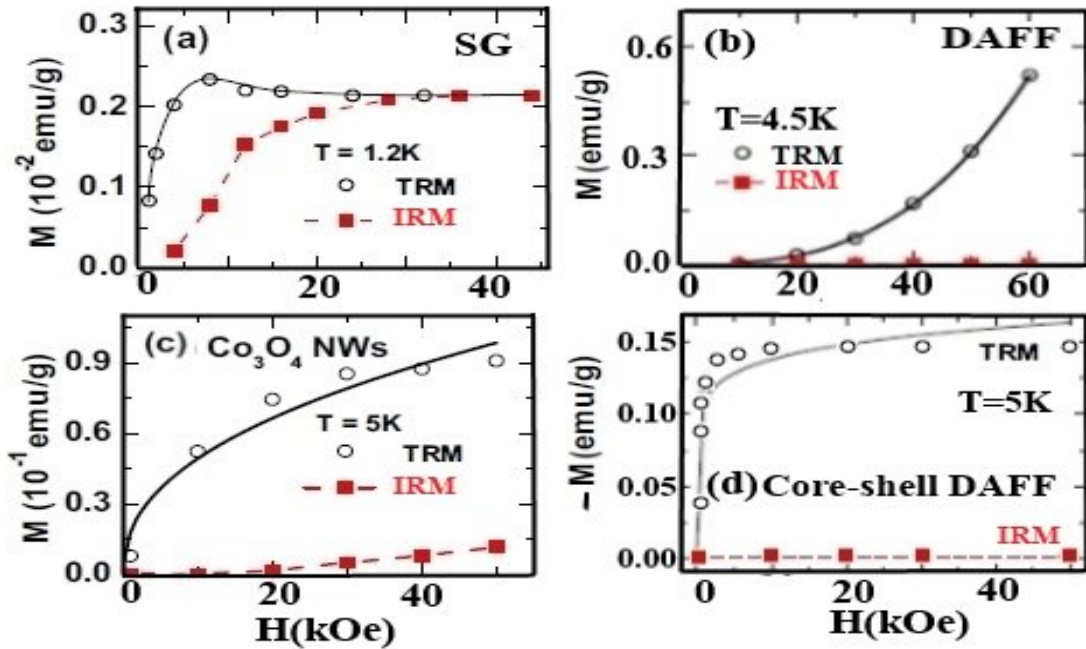


Figure 5.21: IRM and TRM versus magnetic field of the (a) typical spin glass system $\text{AuFe}(0.5\%)$, (b) typical DAFF system $\text{Fe}_{0.48}\text{Zn}_{0.52}\text{Fe}$ and (c) DAFF Co_3O_4 nanowires and (d) core-shell 2D DAFF, reprinted from Ref. [26, 23].

Our result in Figure 5.22(a) shows that the IRM/TRM behavior of CeCrO_3 is similar to the core-shell DAFF systems [23, 27] where the variation of IRM

with the magnetic field is negligible compared to TRM, although the TRM field dependence in our sample does not follow the power law ($\propto H^{\nu_H}$ [28])

Figure 5.22(b) shows the IRM/TRM behavior of EuCrO_3 which is in agreement with the case of a spin glass system. TRM starts from a higher value of magnetization, compared to IRM. It first increases linearly and then saturates with the field. The IRM grows strongly with increasing magnetic field and then converges the TRM curve at high magnetic fields. In some spin glass systems, there is also a characteristic peak at the intermediate fields in TRM before saturation.

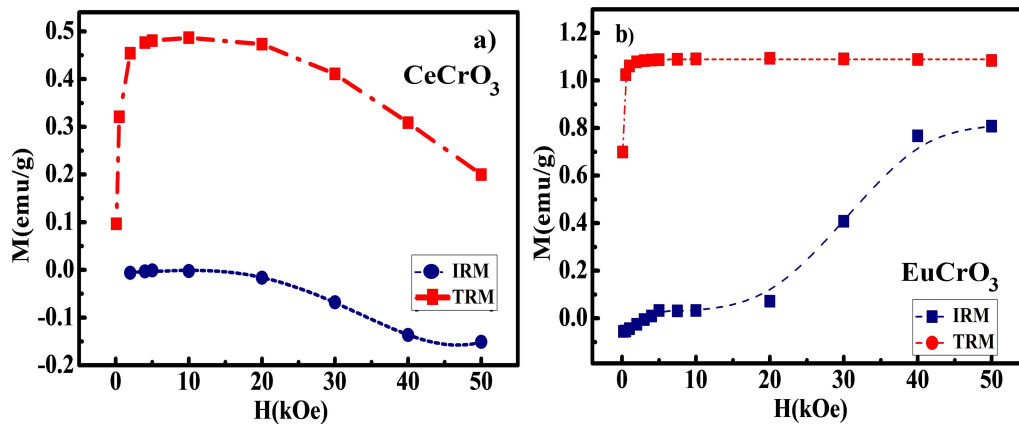


Figure 5.22: IRM (blue line) and TRM (red line) versus magnetic field at $T = 5$ K of the samples (a) CeCrO_3 and (b) EuCrO_3 .

According to all DC magnetic results, we proposed the AFM particles surrounded by a thin spin disorder layer which maybe caused by the broken bounds or oxidation change at the surface (Figure 5.23). The direction of the magnetic spins in the shell and the net magnetic moment of Cr^{3+} are in the same direction of the applied magnetic field. The magnetic moment of Ce^{3+} is small at $T > T_{cross}$, compared to the canted Cr^{3+} magnetic moment. The result is the FM ordering of the shell

and core at the interface which causes the negative EB effect. When $T < T_{cross}$, magnetic moment of cerium increases thus magnetic moments of core and shell order antiparallel and positive EB effect will happen. In EuCrO_3 case, since the magnetic moment of Eu^{3+} does not change by temperature, the magnetic behavior of EuCrO_3 core-shell seems to be similar to that of CeCrO_3 in $T > T_{cross}$ condition.

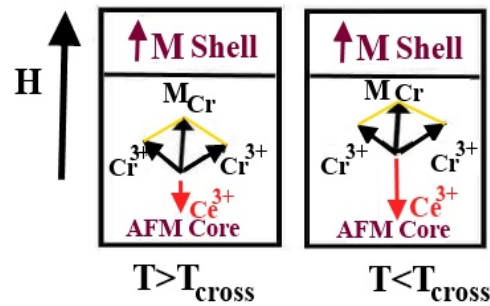


Figure 5.23: The schematic drawing of the core-shell structure of CeCrO_3 in the magnetic field H .

5.2 Physical Property Measurement System

The Quantum Design Physical Properties Measurement System (PPMS) magnetometer is a unique advanced design instrument for the materials characterization with the ability to perform a variety of automated measurements, including AC/DC magnetization, resistivity, heat capacity and thermal transport. This system is capable to be programmed at the temperature range of 1.9 K to 400 K and the magnetic field over 0 to ± 9 T. The following sections give the details of the AC magnetization and heat capacity measurements performed on $\text{Ce}_{1-x}\text{Eu}_x\text{CrO}_3$ compounds in this project, using the PPMS.

5.2.1 AC Measurement System

The Quantum Design AC Measurement System (ACMS) option for PPMS provides the researchers with the capability to perform both AC susceptibility and DC magnetization measurements.

The ACMS contains two coil sets, an AC-drive coil set to provide an alternating excitation field and a detection coil set to respond to the combined sample moment and the excitation field. All these coil sets are situated in the ACMS insert, concentric with the primary superconducting DC magnet of the PPMS. The generated alternating fields by the drive coil can be up to ± 15 Oe in a frequency range of 10 Hz to 10 kHz. Figure 5.24 presents the schematic drawings of the ACMS insert included coil sets.

For AC measurement, the small sample was weighed and mounted inside the bottom of the clear plastic drinking straw, using the Kapton tape. The drinking straw was attached to the sample rod (right picture in Figure 5.24) and mounted to the ACMS insert. The sample was centered automatically to be located at the center of the detection coils. During AC measurements, an alternating field was applied to the sample measurement region and the detection coils recorded the response of the sample when the applied field was changed. In addition to the alternating field applied by the ACMS drive coil, the main magnet in the PPMS can generate a constant DC magnetic field during the measurement. The measurement can be done at the temperature range of 1.9 - 350 K with the AC susceptibility sensitivity of 2×10^{-8} emu.

While the DC susceptibility is obtained using the relation $\chi_{dc} = \frac{M}{H}$, where H

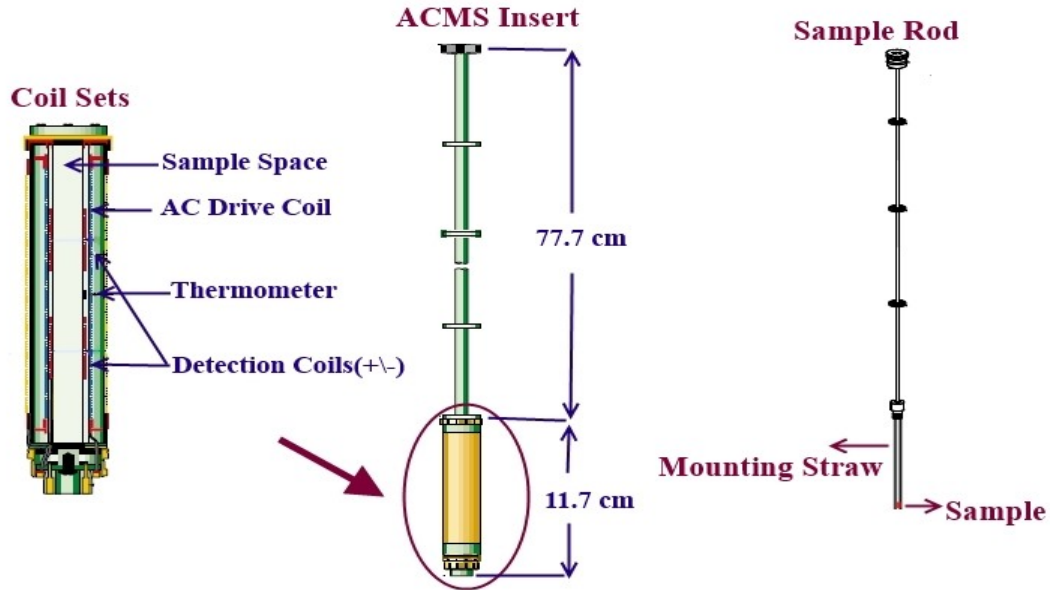


Figure 5.24: The schematic drawings of the ACMS insert and coil sets as well as the sample rod used for the AC magnetization measurement in PPMS, reprinted from Ref. [30].

is an applied DC magnetic field, the AC susceptibility can be defined by the slope of the M-H curve, using the equation $\chi_{ac} = \frac{dM}{dH}$ when an alternating current (AC) is applied. The sample is magnetized by AC magnetic field and produces the flux which is recorded by the detection coil. Thus, there is no need to move the sample, contrary to the DC magnetization measurement [31]. In other words, the magnetic moment of the sample in the DC measurement is constant with time, so it is called the static magnetic susceptibility, while the magnetic moment of the sample in the AC measurement is actually changing in response to an applied AC field, showing the dynamic magnetic property of the sample.

One of the most remarkable properties of the Quantum Design ACMS is its ability to give the complex AC magnetic susceptibility ($\chi_{ac} = \chi' + i\chi''$). The real component χ' is the AC magnetic response that is in phase with the applied

AC field and associated with the dispersive magnetic response, while the imaginary component χ'' represents the out of phase response to the AC field, attributed to the absorptive components which arises from the energy dissipation within the sample. At the end, it is worth mentioning that the AC susceptibility measurement is the important tool in the characterization of the spin glass phase in the compounds.

AC Susceptibility Results

To further study the magnetic behavior of $\text{Ce}_{1-x}\text{Eu}_x\text{CrO}_3$, the temperature dependence of the real part (χ') and the imaginary part (χ'') of AC susceptibility were measured.

The real and imaginary components of AC susceptibility of CeCrO_3 done in the different frequencies and 10 Oe AC and zero DC magnetic fields at high temperatures are plotted in Figure 5.25. It shows the sharp peak near the transition temperature T_{N2} , named magnetic transition temperature T_m . The results reveal the small shift in the magnetic temperature T_m with the clear reduction in its intensity. T_m is the maximum temperature peak in AC susceptibility.

It is well known that the frequency dependency of peak temperature may be used to distinguish the magnetic characteristics of the spin glass phase, cluster glass phase or superparamagnetic phase, which is usually estimated by the quantity of $Q = \frac{\Delta T_m}{T_m \Delta(\log_{10} f)}$, where ΔT_m is the difference between the maximum temperatures (T_m) and f indicates the frequency. The obtained quantity Q is 5.2×10^{-4} where T_{m1} , T_{m2} , f_1 and f_2 are 258.08 K, 258.35 K, 0.1 kHz and 10 kHz, respectively. This value excludes the occurrence of the superparamagnetism in this compound ($Q \sim$

0.3 for superparamagnetism) [29, 25]. The (χ'') data are too noisy and not as clear as (χ').

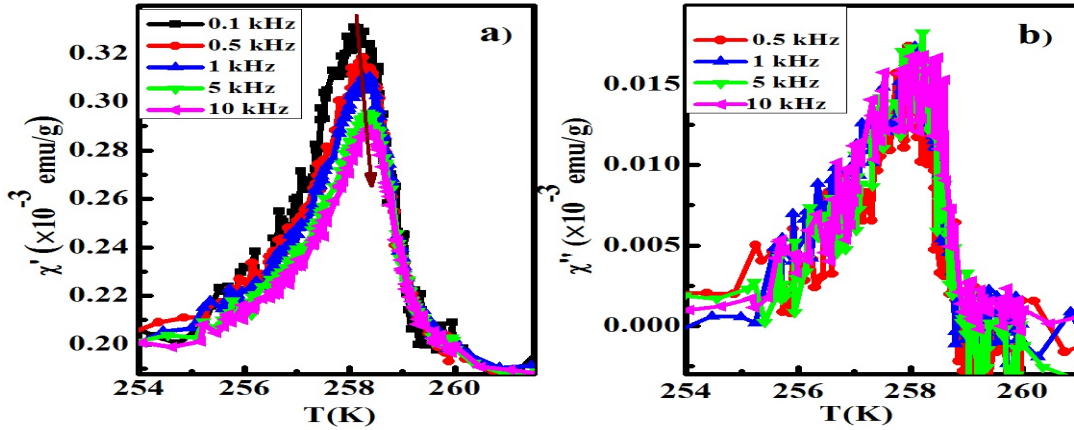


Figure 5.25: (a) Real and (b) imaginary AC susceptibilities versus temperature of CeCrO₃ in different frequencies in 10 Oe AC magnetic field and the zero DC magnetic field.

The effect of AC magnetic field on the real and imaginary components of AC susceptibilities of CeCrO₃ under the fixed frequency of 500 Hz and zero DC magnetic field are presented in Figure 5.26, which shows the intensity enhancement as well as a shift in the magnetic peak while increasing AC magnetic field.

By doping Eu³⁺ in CeCrO₃, the AC susceptibility presents a sharp peaks near T_{N2} and a broader peak near T_1 . Figure 5.27(a) shows the real component of AC susceptibility of Ce_{0.50}Eu_{0.50}CrO₃ under different frequencies and 10 Oe AC and zero DC magnetic fields. We have zoomed in at its two magnetic transition temperatures to check the peak height or position (shown in insets of Figure 5.27(a)). At the peak near T_1 , no change in the peak position is observed, except the slight change in the peak intensity. It can be seen that the peak position near

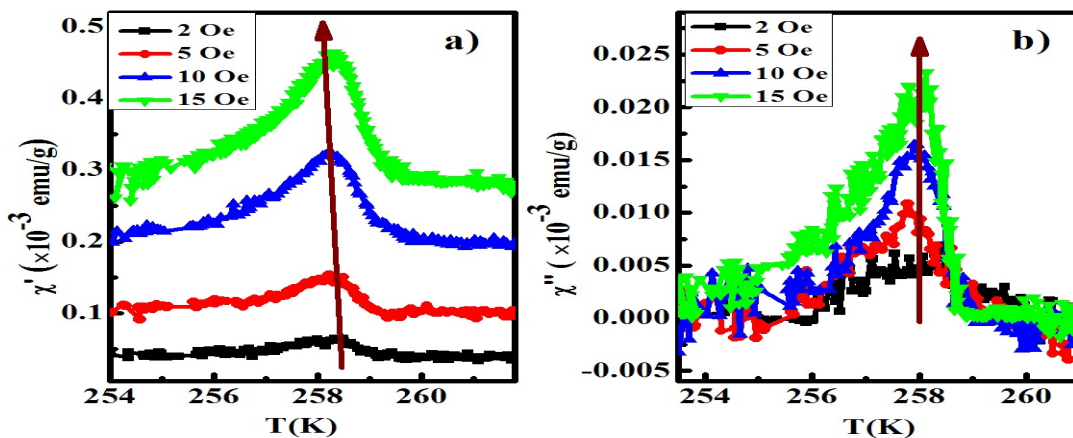


Figure 5.26: (a) Real and (b) imaginary AC susceptibilities versus temperature of CeCrO_3 in different AC magnetic fields under 500 Hz frequency and the zero DC magnetic field.

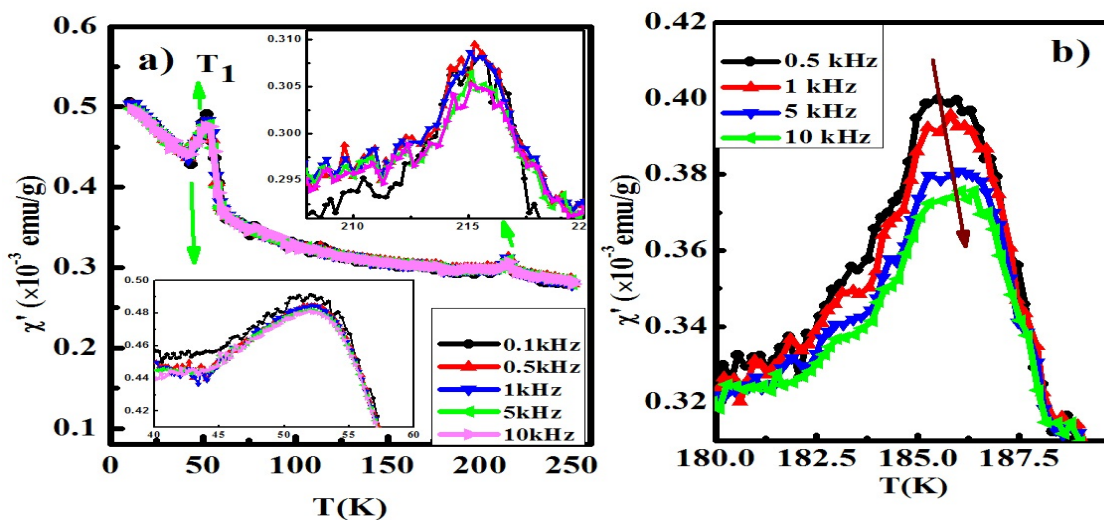


Figure 5.27: Real AC susceptibility versus temperature in different frequencies, 10 Oe AC magnetic field and the zero DC magnetic field of the samples (a) $\text{Ce}_{50}\text{Eu}_{50}\text{CrO}_3$ and (b) $\text{Ce}_{10}\text{Eu}_{90}\text{CrO}_3$.

T_{N2} is shifted slightly as well as its height decreases.

With increasing in europium substitution, the dispersion near T_{N2} in the AC susceptibility enhances (Figure 5.27(b)) where the intensity reduction as well as the peak shift in the χ' for $\text{Ce}_{0.10}\text{Eu}_{0.90}\text{CrO}_3$ is stronger.

The temperature dependence of the real and imaginary components of AC susceptibilities of EuCrO_3 are plotted in Figure 5.28. As expected, the intensities of χ' and χ'' of EuCrO_3 at the transition temperature T_m decrease and T_m has also moved toward higher temperatures. Obviously, the dispersion behavior in EuCrO_3 is much stronger than those in CeCrO_3 , which confirms the possibility of the stronger spin disorder phase in this compound.

The calculated value of Q if T_{m1} , T_{m2} , f_1 and f_2 are 178.43 K, 178.83 K, 10 Hz and 10 kHz respectively, is obtained 7.5×10^{-4} . The calculated Q value is smaller than those reported for the typical spin glass compounds, which suggests the existence of the cluster spin glass-like phase in these compounds [29, 25].

To verify the glassy state of the samples, the temperature dependence of the relaxation time ($\tau = \frac{1}{f}$) can be defined by Vogel-Fulcher and power laws [32], as given in Equations (2.27) and (2.28). To calculate the corresponding parameters, the graph of $\ln\tau$ versus T_m were plotted (Figure 5.29). The best fitted data obtained for CeCrO_3 sample are $\frac{E_a}{k_B} = 22.32$ K, $T_{VF} = 257.1$ K and $\tau_0 = 9.2 \times 10^{-13}$ s. The same way, the values of $\frac{E_a}{k_B} = 31.82$ K, $T_{VF} = 177.1$ K and $\tau_0 = 4.5 \times 10^{-12}$ s are calculated for EuCrO_3 .

On the other hand, the parameters yielded from a power law for CeCrO_3 are $T_g = 257.9$ K, $\tau_0 \approx 10^{-18}$ s, $zv = 5.06$ and for EuCrO_3 are $T_g = 178.2$ K, $\tau_0 \approx$

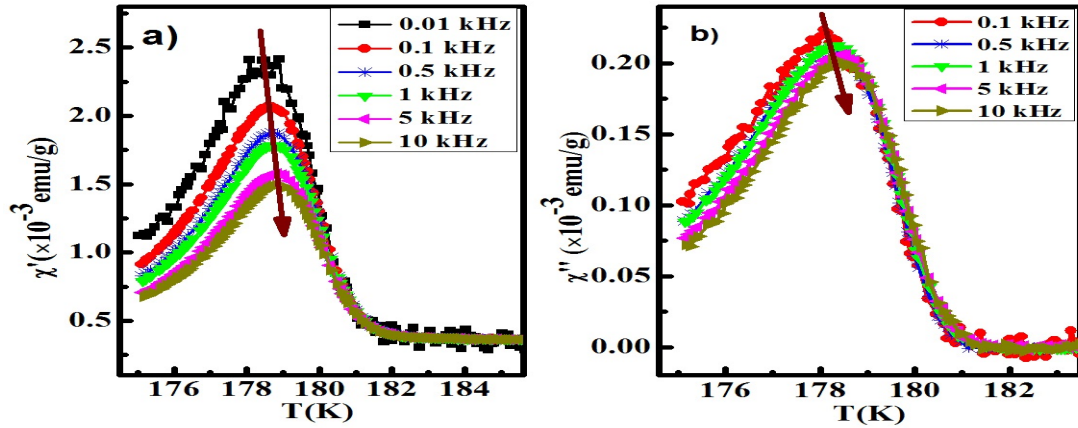


Figure 5.28: (a) Real and (b) imaginary AC susceptibilities versus temperature of EuCrO₃ in different frequencies in 10 Oe AC magnetic field and the zero DC magnetic field.

10^{-17} s and $zv = 5.56$. According to the τ_0 and zv values reported in the literature [29, 25, 32], our obtained values are much closer to those with cluster spin glass behavior.

Interestingly, the temperature dependence of the real AC susceptibilities in different AC magnetic fields and a fixed frequency of 500 Hz for EuCrO₃ are illustrated in Figure 5.30 which depict an enhancement of χ' magnitude at the magnetic peak as well as a small shift toward lower temperatures while the AC magnetic field increases. The same behavior has been reported in the RuSr₂Eu_{1.4}Ce_{0.6}Cu₂O_{10- δ} glassy system [29].

5.2.2 Heat Capacity Measurement

The heat capacity of a system equals to the ratio of the heat (dQ) enters (or exits) a system to the temperature change (dT), either at the constant pressure

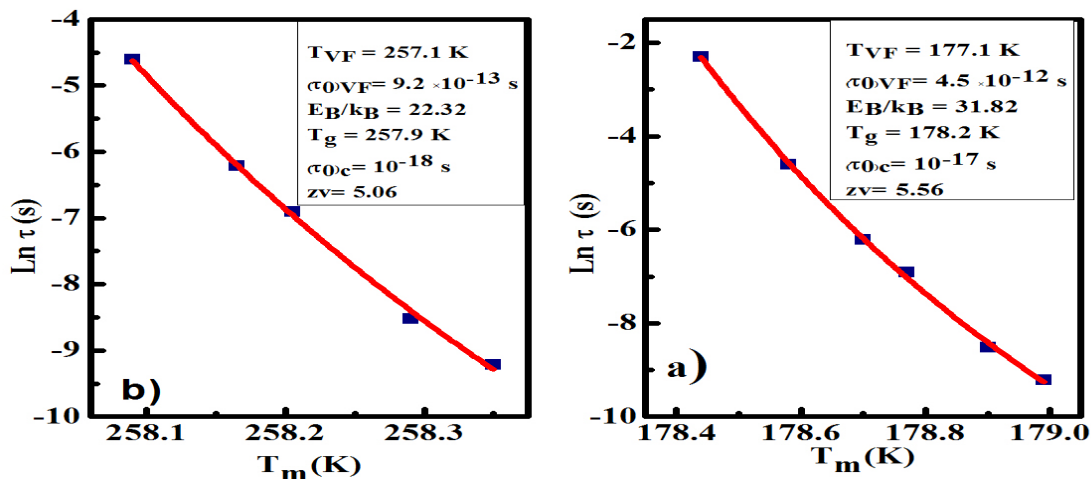


Figure 5.29: $\ln \tau$ versus freezing temperature T_m for (a) CeCrO_3 and (b) EuCrO_3 . The figure shows the best fitting data corresponding to the Vogel-Fulcher and power laws.

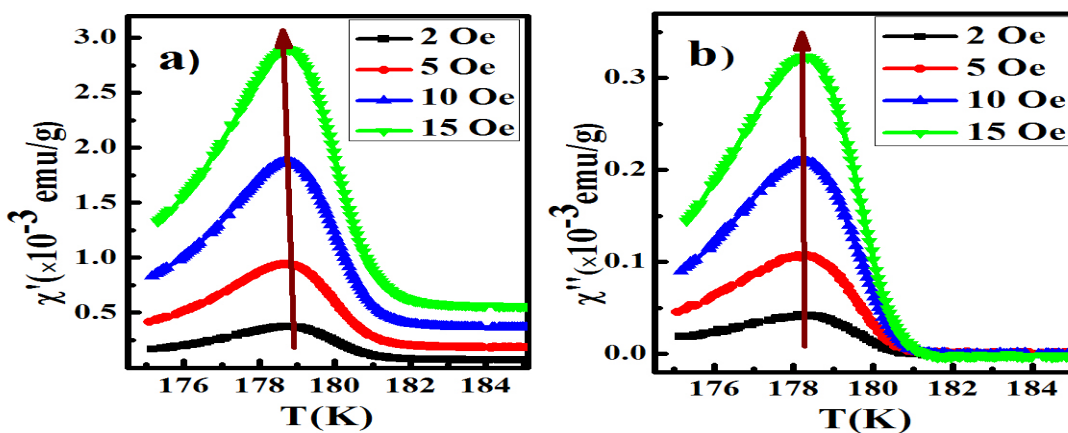


Figure 5.30: (a) Real and (b) imaginary AC susceptibilities versus temperature of EuCrO_3 in different AC magnetic fields, the zero DC magnetic field and the frequency of 500 Hz.

(P) or constant volume (V), written mathematically as:

$$C_i = \left(\frac{\partial Q}{\partial T}\right)_i, \quad \text{where } i = P, V \quad (5.4)$$

Heat capacity is an extensive property of matter, i.e. it is proportional to the size of the system. In order to make the heat capacity independent of the size, it can be divided by the mass, denoted by the specific heat capacity.

According to the first law of thermodynamics, the applied heat (dQ) to the system will increase the internal energy (dU) as well as be employed as an external work (dW), using the equation:

$$dQ = dU + dW. \quad (5.5)$$

When an external work is done by the system in order to increase its volume V with an external pressure P , $dW = PdV$ and Equation (5.5) changes to:

$$dQ = dU + PdV, \quad (5.6)$$

taking Equations (5.4) and (5.6) in the volume constant condition:

$$C_V = \left(\frac{\partial U}{\partial T}\right)_V. \quad (5.7)$$

On the other hand, the second law of thermodynamics shows the relation between entropy of the system (S) and the heat exchange in the reversible condition:

$$dQ = TdS, \quad (5.8)$$

hence, heat capacity can be obtained using the following equation during the temperature change, either the constant P or V:

$$C_i = T\left(\frac{\partial S}{\partial T}\right)_{i.}, \quad \text{where } i = P, V \quad (5.9)$$

The difference between C_P and C_V can be calculated using the following equation:

$$C_P - C_V = \frac{TV\beta^2}{k_T}, \quad (5.10)$$

where V is the molar volume, $\beta = V^{-1}\left(\frac{\partial V}{\partial T}\right)_P$ is the cubical expansion coefficient and $k_T = -V^{-1}\left(\frac{\partial V}{\partial P}\right)_T$ is the isothermal compressibility. It is worth noting that for solids at the temperature and the pressure under which we perform our experiments, there is very little difference between C_P and C_V [33, 34].

Lattice Heat Capacity

A simple solid consists of N atoms which are free to vibrate about their equilibrium positions. Such vibrations are defined by the quantum lattice vibration called phonons. The molar heat capacity of the solids near room temperature should be classically independent of the temperature, approximately equal to $3Nk_B = 3R$, where $R = 8.314 \text{ J/mol K}$ is the ideal gas constant. This statement was first proposed using the Dulong-Petit law in 1819. However, experiments at low temperatures showed that the heat capacity decreases by lowering the temperature and the heat capacity goes up when temperature increases until it approaches the

Dulong-Petit law at the high temperature.

Einstein proposed his model in 1907, suggesting the independent vibration of the N atoms in a system with a common frequency ν_E in three dimensions. The thermal energy of this system is defined using the Bose statistics:

$$U = 3N \langle n \rangle h\nu_E, \quad (5.11)$$

where $\langle n \rangle = \frac{1}{e^{\frac{h\nu_E}{k_B T}} - 1}$. h and k_B are the Planck's constant and Boltzmann constant, respectively. Thus, the heat capacity of the system is:

$$C_{lat} = \left(\frac{\partial U}{\partial T}\right)_V = 3Nk_B \left(\frac{h\nu}{k_B T}\right)^2 \frac{e^{\frac{h\nu_E}{k_B T}}}{\left(e^{\frac{h\nu_E}{k_B T}} - 1\right)^2}. \quad (5.12)$$

At the high temperature limit, the molar specific heat reduces to the $3Nk_B = 3R$ limit and at low temperatures, it approaches zero at a rapid rate. Although this model works well for the high energy phonons in a system, it fails to quantitatively explain the low temperature behavior due to having one common frequency. With the help of the Debye model, we can understand the behavior as it proposes the total thermal energy of a system using the equation:

$$U = \int d\omega D(\omega) \langle n \rangle \hbar\omega, \quad (5.13)$$

where $D(\omega) = \frac{V\omega^2}{2\pi^2v^3}$ is the density of phonon states. ω , v and V are the angular frequency, velocity and volume, respectively. Hence, the Equation (5.13) for each polarization can be written as:

$$U = \int_0^{\omega_D} d\omega \left(\frac{V\omega^2}{2\pi^2v^3} \right) \left(\frac{\hbar\omega}{e^{\frac{\hbar\omega}{k_B T}} - 1} \right). \quad (5.14)$$

Specific heat capacity can be obtained by the appropriate derivative of the Equation (5.14) and be multiplied by the factor 3 when it is assumed that the phonon velocity is independent of the polarization:

$$C_{lat} = 9Nk_B \left(\frac{T}{\theta_D} \right)^3 \int_0^{x_D} dx \frac{x^4 e^x}{(e^x - 1)^2}, \quad (5.15)$$

where $x = \frac{\hbar\omega}{k_B T}$, $x_D = \frac{\hbar\omega_D}{k_B T} = \frac{\theta_D}{T}$ and $\omega_D^3 = \frac{6\pi^2 v^3 N}{V}$. ω_D and θ_D are called the cut-off Debye frequency and the Debye temperature, respectively.

At high temperatures ($T \gg \theta_D$), the heat capacity goes to the classical value of $3Nk_B$ while at very low temperatures ($T \ll \theta_D$), the upper limit of the integral can be taken to be infinity and the heat capacity will be proportional to the T^3 which is defined as [14]:

$$C_{lat} \simeq 234Nk_B \left(\frac{T}{\theta_D} \right)^3 = \beta T^3. \quad (5.16)$$

Electronic Heat Capacity

In metals, the free conduction electrons make the significant contribution to the heat capacity, considered as a non-interacting gas obeying the Fermi-Dirac statistics. If N is the total numbers of electrons in a metal, only the electrons near the Fermi surface are excited by thermal energy $k_B T$, i.e. a fraction of the order

of $\frac{T}{T_F}$, where T_F is the Fermi temperature. Hence, the electronic specific heat in the $T \ll T_F$ region is given by [14]:

$$C_{el} \simeq \frac{\partial}{\partial T} \left(\frac{NT}{T_F} k_B T \right) \simeq N k_B \left(\frac{T}{T_F} \right) \simeq \gamma T, \quad (5.17)$$

where $\gamma = \left(\frac{\pi^2 N k_B}{2 T_F} \right)$ is the Sommerfield constant. The linear dependence of the electronic heat capacity in metals at sufficiently low temperatures, is in good agreement with experimental results.

Magnetic Heat Capacity

The basic thermodynamic relation for a magnetic system with the magnetization M under the magnetic field of H , using Equations (5.6) and (5.8) can be written:

$$T dS = dU + H dM + M dH, \quad (5.18)$$

where the mechanical work PdV is neglected. The HdM term is the energy required to increase the magnetization of the sample from M to $M+dM$, while MdH is the work done in order to increase the magnetic field over the sample. Hence, the principal magnetic heat capacity at the constant magnetization (C_M) and the magnetic heat capacity at the constant magnetic field (C_H) are given by [34]:

$$C_M = T \left(\frac{\partial S}{\partial T} \right)_M; \quad (5.19a)$$

$$C_H = T \left(\frac{\partial S}{\partial T} \right)_H. \quad (5.19b)$$

In our experiment, C_H is measured which is labeled by C_{mag} .

Most of the ferrimagnets and antiferromagnets are insulators, thus the electronic heat capacity is neglected and the total heat capacity is given by:

$$C_{tot} = C_{lat} + C_{mag}. \quad (5.20)$$

To extract the magnetic contribution of the heat capacity, the lattice heat capacity has to be subtracted from the total heat capacity. Furthermore, by integrating the magnetic heat capacity, the magnetic entropy can be calculated using the equation:

$$S_{mag}(T) = \int_0^T \frac{C_{mag}(T')}{T'} dT'. \quad (5.21)$$

The obtained magnetic entropy (S_{mag}) near the phase transition can be estimated theoretically by:

$$\Delta S_{mag} = R \ln(2S + 1), \quad (5.22)$$

where S is the magnetic spin of the system [34].

Schottky anomalous heat capacity

Heat capacity usually reduces when temperature decreases, thus most substances have very small heat capacities at low temperatures. However, the heat capacity of some materials shows a peak at low temperatures, called Schottky anomaly. An increase in the heat capacity of these materials by temperature reduction can

be explained in terms of a two-level system with the energy apart, Δ , proposed by Walter H. Schottky. At temperatures comparable to Δ/k_B , transitions from one level to another take place, which is observed by a bump in the heat capacity measurement. The heat capacity coming from the Schottky anomaly is given using [34]:

$$C_{Sch} = R \left(\frac{\Delta}{T} \right)^2 \frac{e^{\Delta/T}}{[1 + e^{\Delta/T}]^2}. \quad (5.23)$$

Measurement Set-Up

The Quantum Design Heat Capacity option measures the heat capacity of the solid at constant pressure, using the relaxation time technique, by applying a known amount of heat for a fixed time.

The heat capacity holder used in PPMS includes a copper puck frame, a sample platform and a copper cap to cover the sample platform with the sample on it. The eight platinum wires connect the sample platform to the frame. There are a platform heater and a platform thermometer, attached to the bottom side of the sample platform. The small sample is weighed and located on the platform by using a thin layer of GE varnish thermal grease, providing the required thermal contact to the platform. Heat capacity measurements are performed in the high vacuum to ensure that the heat flow between the sample platform and the thermal bath (puck) takes place only through the wires. Figure 5.31 presents the schematic drawing of the PPMS heat capacity puck including thermal connections to the sample and the sample platform.

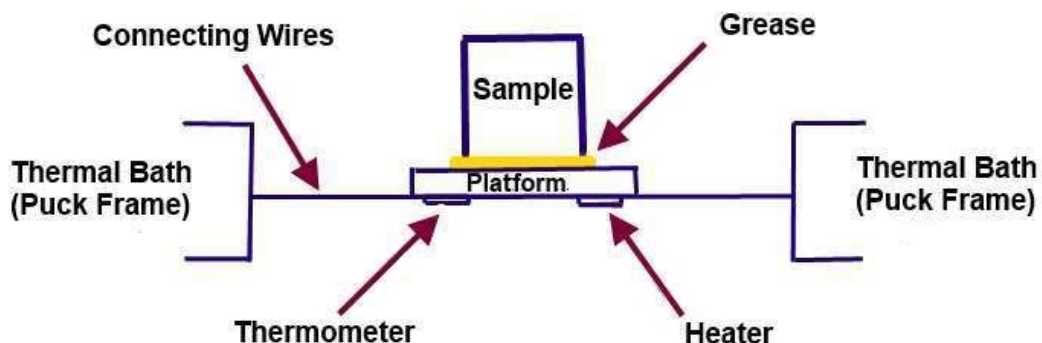


Figure 5.31: The schematic drawing of thermal connections to the sample and the sample platform in the PPMS heat capacity measurements, reprinted from Ref. [35].

In order to do the heat capacity measurement of each sample, first the heat capacity of the addenda, i.e., the sample holder with the small amount of the thermal grease on it, is measured and second the sample is mounted and the heat capacity of the sample plus the addenda (total heat capacity) is carried out. The heat capacity of the sample is calculated by subtracting the heat capacity of the addenda from the total heat capacity.

Heat Capacity Measurement Results

The heat capacities of rather complete set of rare earth chromites, RCrO_3 ($\text{R} = \text{La, Pr, Nd, Sm, Gd, Dy, Ho, Er}$ and Y), has been measured by Satoh et al. down to liquid nitrogen temperature and the anomalies associated with the long-range magnetic ordering of Cr have been well documented [36]. Recently, Bartolomé et al. and Su et al. have extended the heat capacity measurements down to liquid helium temperatures on the systems NdCrO_3 , YbCrO_3 and HoCrO_3 [6, 37, 38]. In

this work, we present the heat capacity of CeCrO_3 and EuCrO_3 1.8 - 300 K which all were measured at Department of Physics, Brock University.

The heat capacity of CeCrO_3 was performed in the warming cycle. The temperature dependence of the heat capacity of the sample CeCrO_3 in the zero magnetic field is shown in Figure 5.32(a), which shows two significant features: (i) the second order phase transition λ -shaped anomaly at 256 K where the Cr^{3+} moments order canted antiferromagnetically and (ii) the clear spin reorientation phase transition at low temperatures (Figure 5.32(a) inset), which is considered as the Schottky anomaly and will be discussed later. This anomaly confirms the existence of the short range magnetic contribution of cerium ions in CeCrO_3 .

Rare earth chromites are almost good insulators, thus the electronic heat capacity can be neglected. Total heat capacity of these compounds consists of the phonon and magnetic terms. In order to study the magnetic contribution of the heat capacity for CeCrO_3 , the non-magnetic isostructural compound LaGaO_3 was made and its heat capacity was measured as a function of temperature (red line in Figure 5.32(b)). The LaGaO_3 heat capacity is considered as the lattice heat capacity. It is noteworthy that the molar masses of CeCrO_3 and LaGaO_3 are different; thus, the temperatures of the LaGaO_3 data must be scaled by multiplying them by the ratio of the effective Debye temperatures (θ_D) of these two compounds, using the method proposed by Bouvier [39]:

$$\frac{\theta_D(\text{CeCrO}_3)}{\theta_D(\text{LaGaO}_3)} = \left[\frac{(M_{\text{La}})^{3/2} + (M_{\text{Ga}})^{3/2} + 3(M_{\text{O}})^{3/2}}{(M_{\text{Ce}})^{3/2} + (M_{\text{Cr}})^{3/2} + 3(M_{\text{O}})^{3/2}} \right]^{1/3}, \quad (5.24)$$

where M is the molar mass of each element. Thus, a correction factor of 1.027 was applied to the LaGaO_3 temperature data.

Figure 5.32(b) presents the total heat capacity of CeCrO_3 (blue line) and LaGaO_3 (red line). The magnetic contribution of the heat capacity is obtained by subtracting the lattice heat capacity from the total heat capacity (green line).

Between the temperatures 25-45 K, the heat capacity versus temperature was well fitted by the Debye T^3 law (Equation (5.16)) and the Debye temperature of 440 K was calculated, using $\theta_D = [234NN_A k_B / \beta]^{1/3}$ where N , N_A and k_B are the number of atoms per formula unit, the Avogadro number and the Boltzmann constant, respectively.

The magnetic entropy (S_{mag}) is calculated by the numerical integration of $\frac{C_{mag}}{T}$ with respect to the temperature (Equation 5.21). Both $\frac{C_{mag}}{T}$ and S_{mag} are presented in Figure 5.33(a) and (b), respectively. The entropy enhances as the temperature increases, an evidence of the disordering of the spins. The magnetic entropy at $T = 256$ K is 11.89 J/mol.K., which is in good agreement with the theoretical value of $R \ln(2S+1) = R \ln 4 = 11.526$ J/mol.K., where $R = 8.314$ J/mol.K. and $S = 3/2$ for Cr^{3+} . Furthermore, the magnetic entropy at $T = 60$ K reaches to 0.8% $R \ln 2$, indicating the doublet ground state of Ce^{3+} with $S = 1/2$ at low temperatures.

It is worthy of note that Ce^{3+} is a Kramer's ion with $J = 5/2$. In the orthorhombic symmetry and under the effect of the crystalline electric field, 4f levels of Ce(III) are split into three doublets ($\pm\frac{1}{2}$, $\pm\frac{3}{2}$, $\pm\frac{5}{2}$). The energy splitting of these Kramer's ions can be calculated by studying the Schottky heat capacity

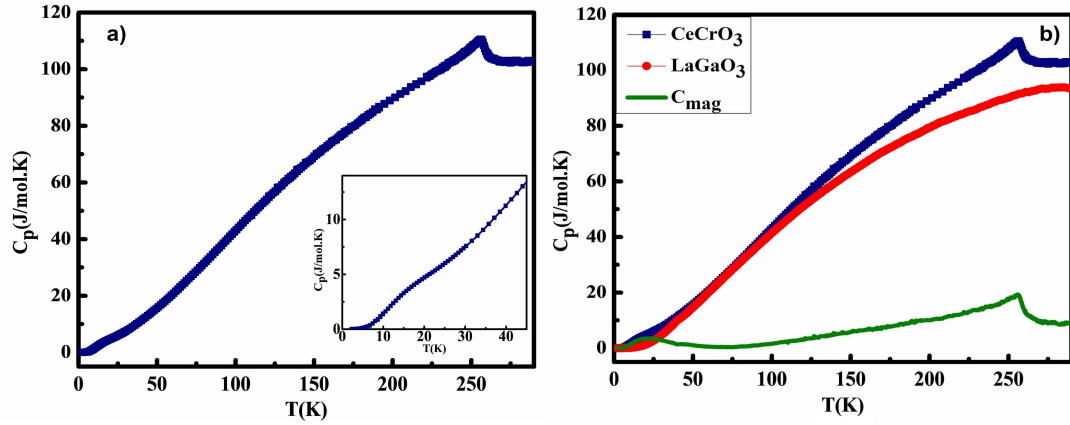


Figure 5.32: (a) Total heat capacity of CeCrO_3 which shows λ -like transition at $T = 256$ K and Schottky anomaly at low temperatures (inset), (b) total heat capacity of CeCrO_3 (blue line) with the heat capacity of LaGaO_3 (red line) and the magnetic heat capacity of CeCrO_3 (green line) at the zero magnetic field.

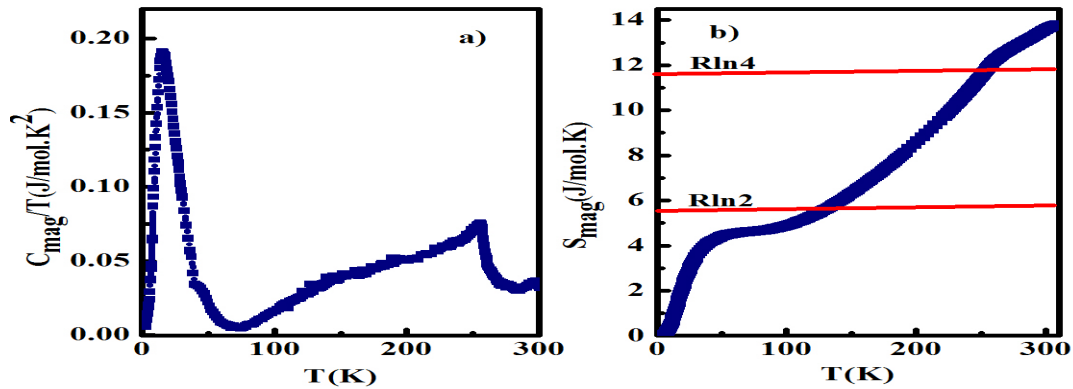


Figure 5.33: (a) Temperature dependence of the magnetic heat capacity and (b) temperature dependence of the magnetic entropy of CeCrO_3 at the zero magnetic field.

anomaly. The largest contribution to the Schottky heat capacity occurs at the temperature where $k_B T$ is comparable to the energy between the levels.

Figure 5.34(a) (blue line) shows the Schottky anomaly of CeCrO_3 with a maximum at $T = 20$ K. In order to determine the low temperature Schottky anomaly, the cubic background and Schottky heat capacity model were considered. At this range of temperature, the two-level Schottky model seemed to be the best fit without considering the cubic background as well. Thus, the magnetic heat capacity was fitted with the two-level Schottky function (Equation 5.24) which is shown in Figure 5.34(a) (red line). The first splitting energy levels was 4.41 ± 0.03 meV (51.34 ± 0.32 K) at zero external magnetic field which is increased to 4.64 ± 0.03 meV (53.96 ± 0.31 K) at 9 T (Figure 5.34(b)). The field dependence of this energy splitting of Ce^{3+} in CeCrO_3 is shown in the Figure 5.34(c) with the slope of 0.0259 ± 0.001 meV/T. Landé-g factor in the direction of the magnetic field can be calculated using $\Delta = \mu_B g H$, which gives the value of 0.449 where μ_B is the Bohr magneton. Δ and H are the energy splitting of first doublet ($\pm \frac{1}{2}$ states) and an applied magnetic field, respectively.

The effect of an applied magnetic field at the ordering temperature of Cr^{3+} as well as the magnetic entropy are presented in Figures 5.35(a) and (b). Data shows that the magnetic field makes the transition temperature broader and moves to the lower temperatures. Furthermore, increasing the magnetic field reduces the rate of disordering in the system which decreases the entropy.

Similarly, the heat capacity of sample EuCrO_3 versus temperature in the zero magnetic field was measured in the warming cycle which was observed in Figure

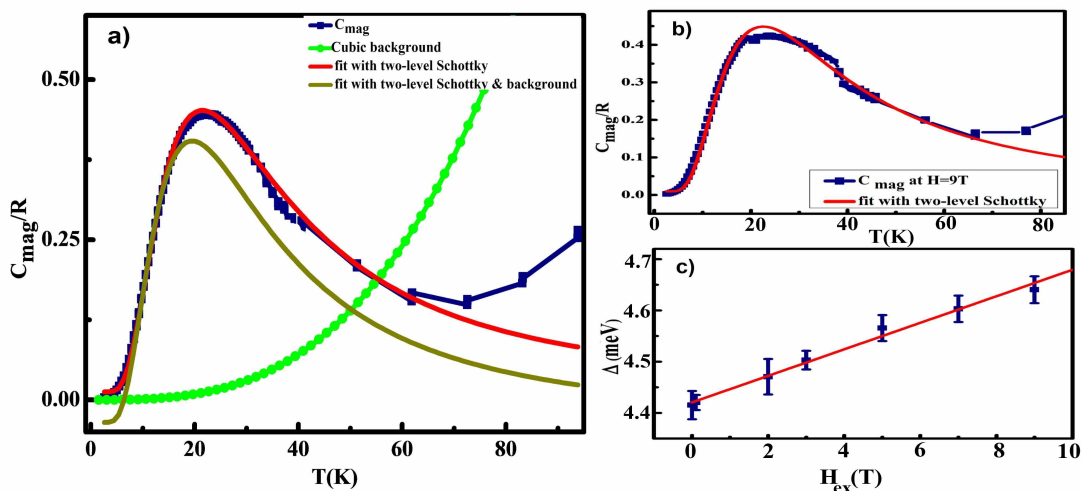


Figure 5.34: (a) Schottky heat capacity anomaly of CeCrO_3 (blue line) with the cubic back ground (green) and fitting with two-level Schottky model at the zero magnetic field, (b) Schottky heat capacity anomaly of CeCrO_3 with two-level model fitting at $H=9$ T, (c) the energy splitting versus an applied magnetic field obtained using the two-level Schottky model.

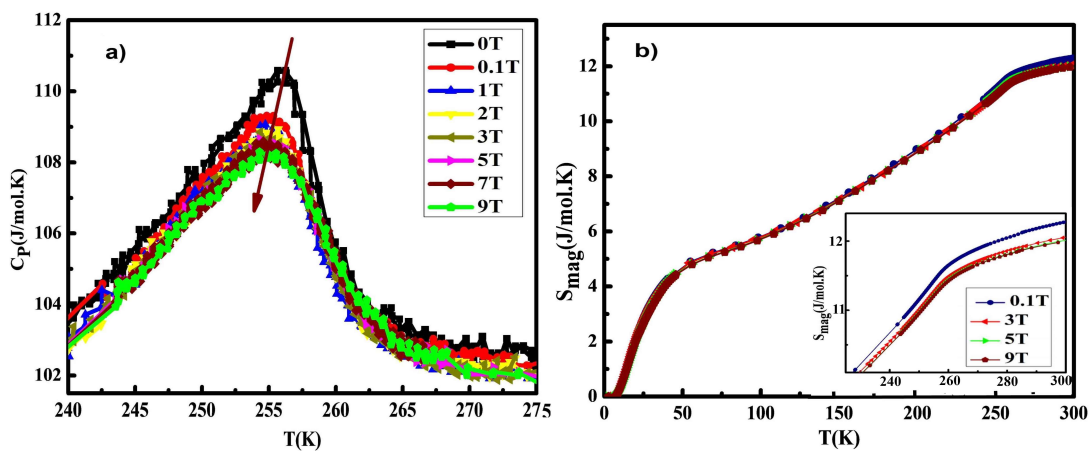


Figure 5.35: Magnetic field dependence of (a) the magnetic ordering transition temperature and (b) the magnetic entropy in CeCrO_3 .

5.36(a). The total heat capacity (blue line) shows the magnetic transition λ -shaped anomaly at 177 K which indicates the long-range magnetic ordering of Cr^{3+} ion. There is no anomaly at low temperatures. To calibrate the LaGaO_3 heat capacity data used as the lattice heat capacity contribution, the 0.996 correction factor was applied (red line) and the magnetic heat capacity (green line) was obtained after subtracting the total heat capacity and the lattice heat capacity. The Debye temperature of 260 K was obtained using the Debye T^3 law. Eu^{3+} is a non-Kramers ion thus a Schottky anomaly was not seen in EuCrO_3 heat capacity.

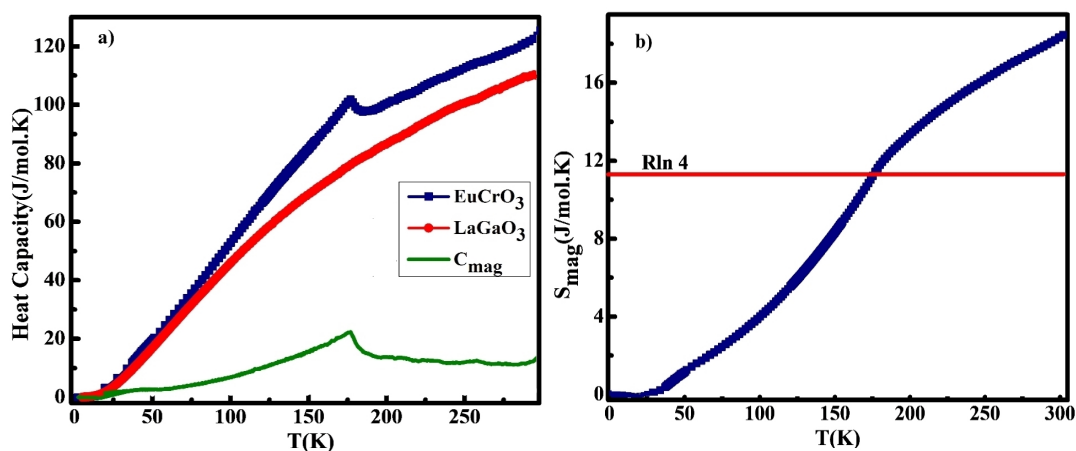


Figure 5.36: (a) Total heat capacity of EuCrO_3 (blue line) with the heat capacity of LaGaO_3 (red line) and the magnetic heat capacity of EuCrO_3 (green line) at the zero magnetic field, (b) the magnetic entropy of EuCrO_3 .

By the numerical integration of $\frac{C_{\text{mag}}}{T}$ with respect to temperature, the magnetic entropy (S_{mag}) was plotted in Figure 5.36(b) which shows the increase in entropy by temperature, similar to what we observed in CeCrO_3 . The obtained magnetic entropy of 11.48 J/mol.K. at $T = 177$ K shows the Cr^{3+} magnetic contribution at this temperature which is close to the theoretical value of $R \ln 4 = 11.526$ J/mol.K.

5.3 Thermal Expansion

Thermal expansion is the tendency of matter to change in the length, the area or the volume while the temperature increases. The dimension of most solids expands when temperature increases, although the negative change with increasing temperature has also been reported (e.g. Si, Ge, ZnS and CdTe) [40, 41].

The linear coefficient of thermal expansion (α_L) describes how the length of an object changes with a change in the temperature, using an equation:

$$\alpha_L \approx \frac{1}{L} \left(\frac{\Delta L}{\Delta T} \right), \quad (5.25)$$

where L is a particular length measurement and $\frac{\Delta L}{\Delta T}$ is the rate of the linear dimension change in the temperature change under a constant pressure. In this work, the relative length change ($\frac{\Delta L}{L}$) is used where L is the room temperature length of the sample and $\Delta T \ll T$ [40, 41].

The linear thermal expansions of samples CeCrO_3 and EuCrO_3 were measured at the Max Plank Institute, Germany, using a high resolution miniature dilatometer. This dilatometer has been designed by Rotter et al. [42] which it was fitted into the PPMS chamber. This special type of dilatometer was designed to measure samples with the small thickness ($\approx 0.1 - 3$ mm). The dilatometer cell is included two silver plates separated by a gap width d where the plates are insulated from sample holders by sapphire washers. The schematic drawing of the dilatometer cell is represented in Figure 5.37(a) where the dilatometer cell mounted in PPMS prob is shown in Figure 5.37(b).

For mounting the sample, it must be placed on the sapphire disk. The dielectric capacitance (C) of the two electrodes of the dilatometer is measured with Andeen-Hagerling ultra-precision capacitance bridge (AH2700A) (with high accuracy $\approx 10^{-7}$ pF). Temperature or magnetic field may change the length of the sample which changes the gap between the two electrodes (d). The change in the gap distance (Δd) will be directly calculated using the corresponding change in the capacitance of the electrodes (ΔC):

$$C = \epsilon_r \epsilon_0 \frac{A}{d}; \quad (5.26a)$$

$$\Delta C \approx \epsilon_0 \frac{\Delta d}{d^2} \quad \text{with} \quad \epsilon_r = 1, \quad (5.26b)$$

where A is the area of two electrodes, ϵ_r is the relative permittivity of helium used in the measurement and ϵ_0 ($\approx 8.854 \times 10^{-12}$ F/m) is the permittivity of free space. Small changes in the capacitance of the dilatometer can be observed with a resolution of 10^{-12} m.

The length change of the sample as a function of the temperature is calculated using the written program after applying corrections for the length change of the dilatometer body and the spacer. More details about the dilatometer cell and the thermal expansion measurement are in Ref. [43, 44].

5.3.1 Thermal Expansion Results

Thermal expansion measurements were performed by starting at 300 K and cooling down to 5 K. Figure 5.38(a) and (b) illustrate the relative length change

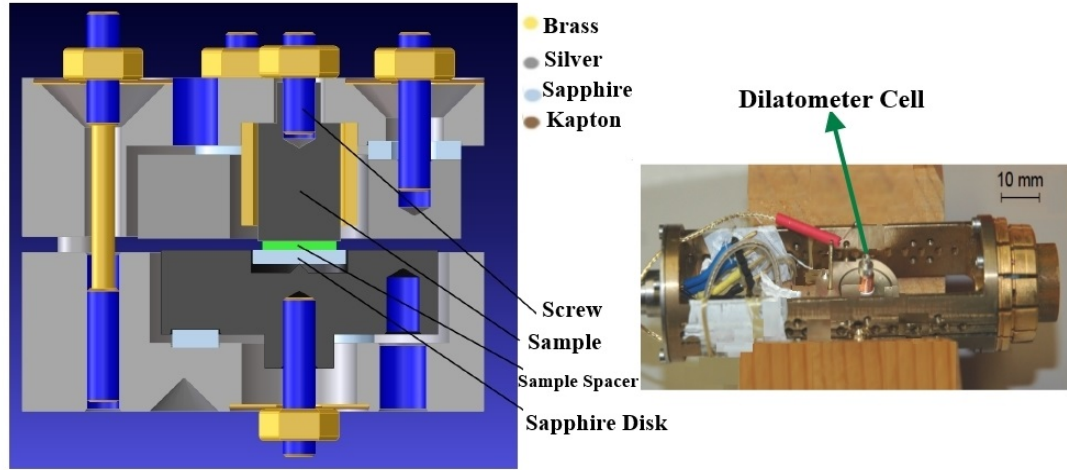


Figure 5.37: (a) The schematic drawing of the thermal expansion dilatometer cell and (b) the dilatometer cell which was mounted in PPMS probe, reprinted from Ref. [43, 44].

and the coefficient of the linear thermal expansion of the polycrystalline CeCrO_3 with the length of ≈ 1.035 mm at the zero magnetic field, respectively. The results confirm the positive thermal expansion with the anomaly temperature of $T \approx 256$ K which is in good agreement with the magnetic transition temperature. No other anomaly was observed in low temperatures.

The temperature dependence of the linear thermal expansion of the sample EuCrO_3 with the length of $\approx 0.801(1)$ mm at the zero magnetic field is shown in Figure 5.39.

Raising the temperature from lowest temperatures in Figure 5.39(a), the thermal expansion is characterized by an extended plateau whereas above $T \approx 70$ K the sample starts to contract, i.e. between $T \approx 70$ K and $T \approx 100$ K, EuCrO_3 shows the negative thermal expansion. Above $T \approx 100$ K, the length change grows monotonically with a slight change of the slope at $T \approx 175$ K, in the range of

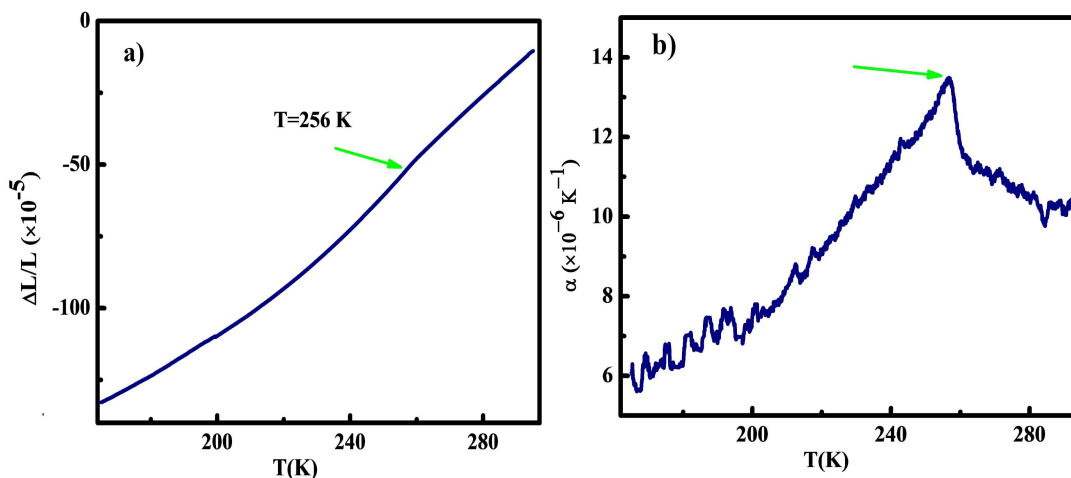


Figure 5.38: The temperature dependence of (a) the length change ($\frac{\Delta L}{L}$) relative to 300 K and (b) the coefficient of the linear thermal expansion (α) for sample CeCrO₃. (α) derived from the length change displayed in (a)

the Néel transition temperature. These anomalies are clearly revealed in the the coefficient of linear thermal expansion, (Figure 5.39(b)) which is negative between $T \approx 70$ K and 100 K. This anomaly is even stronger than the magnetic ordering induced peak centered at 175 K.

To further study of the low temperature anomaly ($T \approx 70$ K) of EuCrO₃, the Raman modes and dielectric property of this sample were measured as the results are given in the following sections.

5.4 Raman Spectroscopy

Raman spectroscopy is an inelastic scattering of the monochromatic light (10^2 - 10^4 cm^{-1}) which is used to study the vibrational characteristics of a material. When a laser beam with a frequency ν_0 radiates on a sample, an elastic scattering (named Rayleigh) and an inelastic scattering (named Raman) can occur. Raman

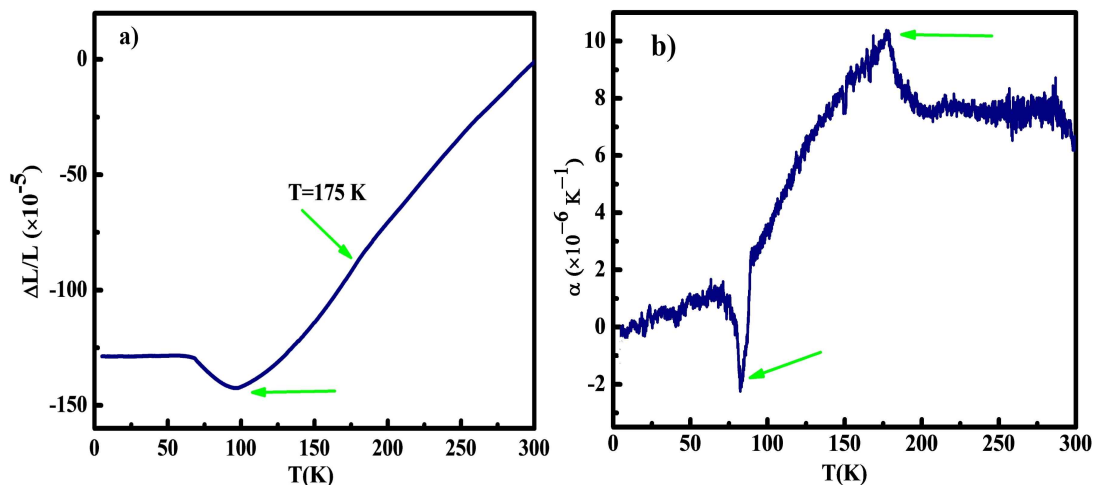


Figure 5.39: The temperature dependence of (a) the length change ($\frac{\Delta L}{L}$) relative to 300 K and (b) the coefficient of the linear thermal expansion (α) for sample EuCrO₃.

beam usually scatters weaker ($\approx 10^{-5}$) than the incident beam, with the frequency of $\nu_0 \pm \nu_m$ where ν_m is the vibrational frequency of a molecule [45]. Raman spectroscopy is a proper technique to study phase transitions as well as structural distortions in perovskites. According to the group theory, there are 24 Raman active modes for the orthorhombic structure with four formula per unit cell (group 62): $7 A_g + 5 B_{1g} + 7 B_{2g} + 5 B_{3g}$ [46].

Raman scattering investigations on the compounds RCrO₃ (R = Y, La, Nd, Pr, Sm, Gd, Dy, Ho, Er, Yb, Lu) have been rather extensively carried out at room temperature and also to temperature of $T \approx 100$ K in order to assign the modes and study the lattice response to the magnetic ordering either of the Cr or the rare earth moments [46, 47, 48]. At present, only one Raman study on EuCrO₃ down to $T \approx 90$ K is available, reporting some anomalies near the Néel temperature in the Raman shift of some modes as well as in their linewidth [49]. Here, we have

extended the Raman scattering investigation down to 10 K and studied in detail the Raman shift of the modes and their linewidth versus temperature.

The Raman spectra of EuCrO_3 were measured using a Jobin Yvon Typ V 010 LabRAM single grating spectrometer with $\approx 1 \text{ cm}^{-1}$ spectral resolution, at the Max Plank Institute, Germany. The spectrometer setup was equipped with a double super razor edge filter, Peltier cooled CCD camera and a Mikrocryo cryostat with a copper cold finger. Measurements were performed with linearly polarized He/Ne gas laser light of 632.817 nm with the power less than 1 mW. The light beam was focused to a 10 μm spot on the top surface of the sample using a microscope. Measurements were taken in temperatures ranging between 4 K and 325 K.

Raman Spectroscopy Results

Figure 5.40 shows the Raman spectra of EuCrO_3 between 10 K and room temperature with the assignments according to Weber et al. [46]. The spectra are similar to what has been observed for other rare earth orthochromites. According to literature [46], there are four common spectral regions in RCrO_3 which are summarized as:

- A region below 200 cm^{-1} , characterized by two sharp and intense bands. They are attributed to rare earth cation vibrations.
- A region between 200 to 380 cm^{-1} , characterized by four partly overlapping bands, where they depend on changes in the orthorhombic distortion.

- A region between 380 to 500 cm^{-1} with two bands of similar intensity.
- A region between 500 to 600 cm^{-1} with two features, each characterized by overlapping bands which are mainly assigned to the stretching vibrations of the CrO_6 octahedra

As Figure 5.40 shows, 11 Raman modes are labeled, thus the other predicted modes have either too low intensity to be observed or are located below our experimental region.

The $A_g - B_{1g}$ doublet near 375 cm^{-1} is split whereas the mode at 470 cm^{-1} is still degenerate but clearly broadened as compared to modes in its neighborhood. Above 600 cm^{-1} , a broad band is seen centered at 650 cm^{-1} which corresponds to the analogous broad band at 720 cm^{-1} in LaCrO_3 which has been assigned to lattice imperfections possibly involving Cr^{4+} centers [47].

At first glance, all Raman modes appear to show hardening with decreasing temperature. A closer inspection of the shift and the linewidth of the Raman modes was carried out by fitting Lorentzian line shapes to the modes. This discloses especially a weak but noticeable mode softening for all analyzed modes below $T \approx 75$ K. Some modes show additional magnetoelastic anomalies below $T \approx 175$ K. Generally, the linewidths decrease and pass through a minimum at $T \approx 75$ K and grow again towards lowest temperatures. Magnetoelastic effects could not be detected in mode linewidths.

Generally, the temperature dependent change of the phonon frequency of an insulator ($\omega(T)$) has contributions from the change of the lattice volume ($\Delta\omega_{latt}$),

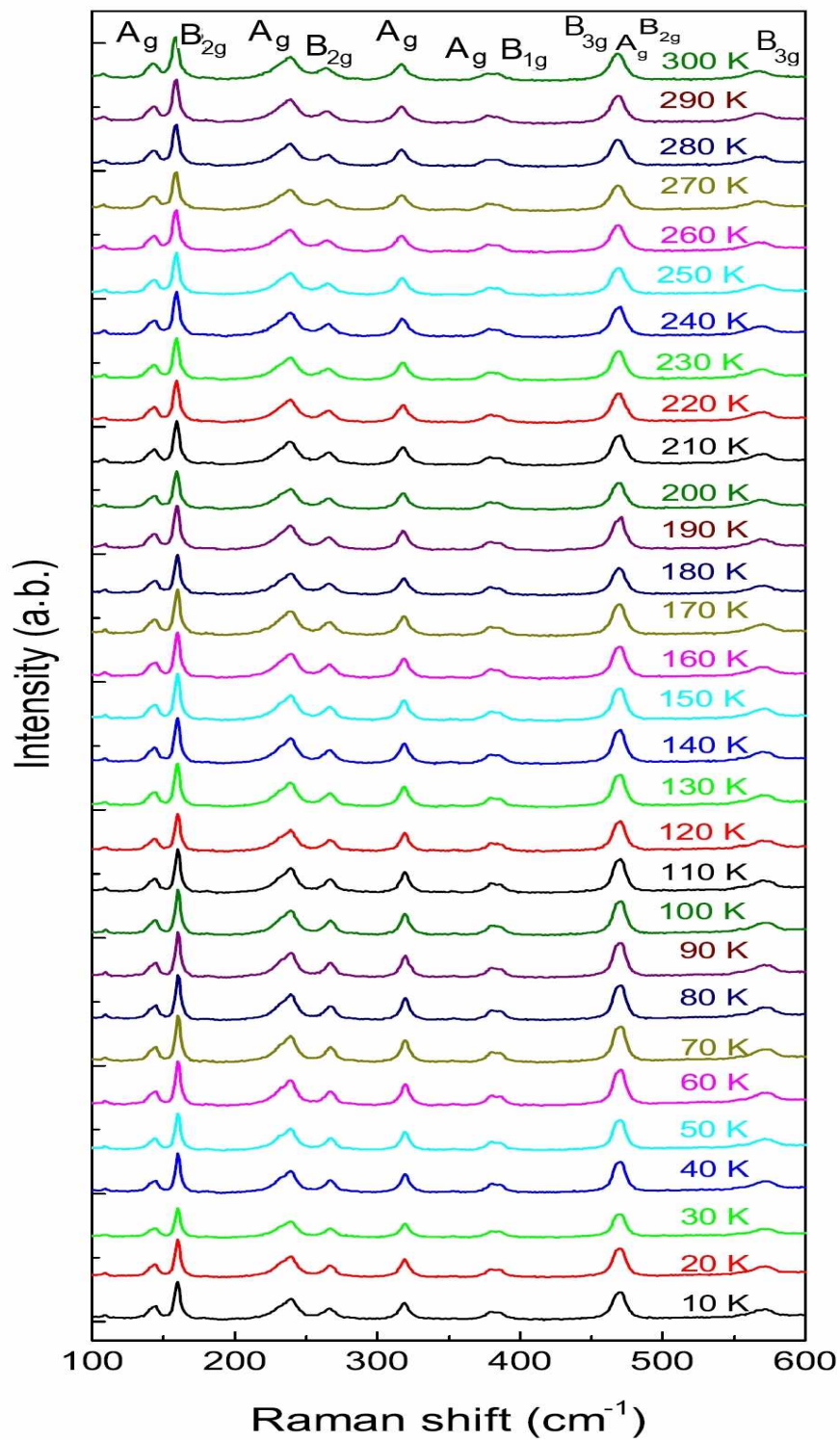


Figure 5.40: Raman spectra of EuCrO₃ at different temperatures. The mode assignment is given above the topmost (300 K) spectrum.

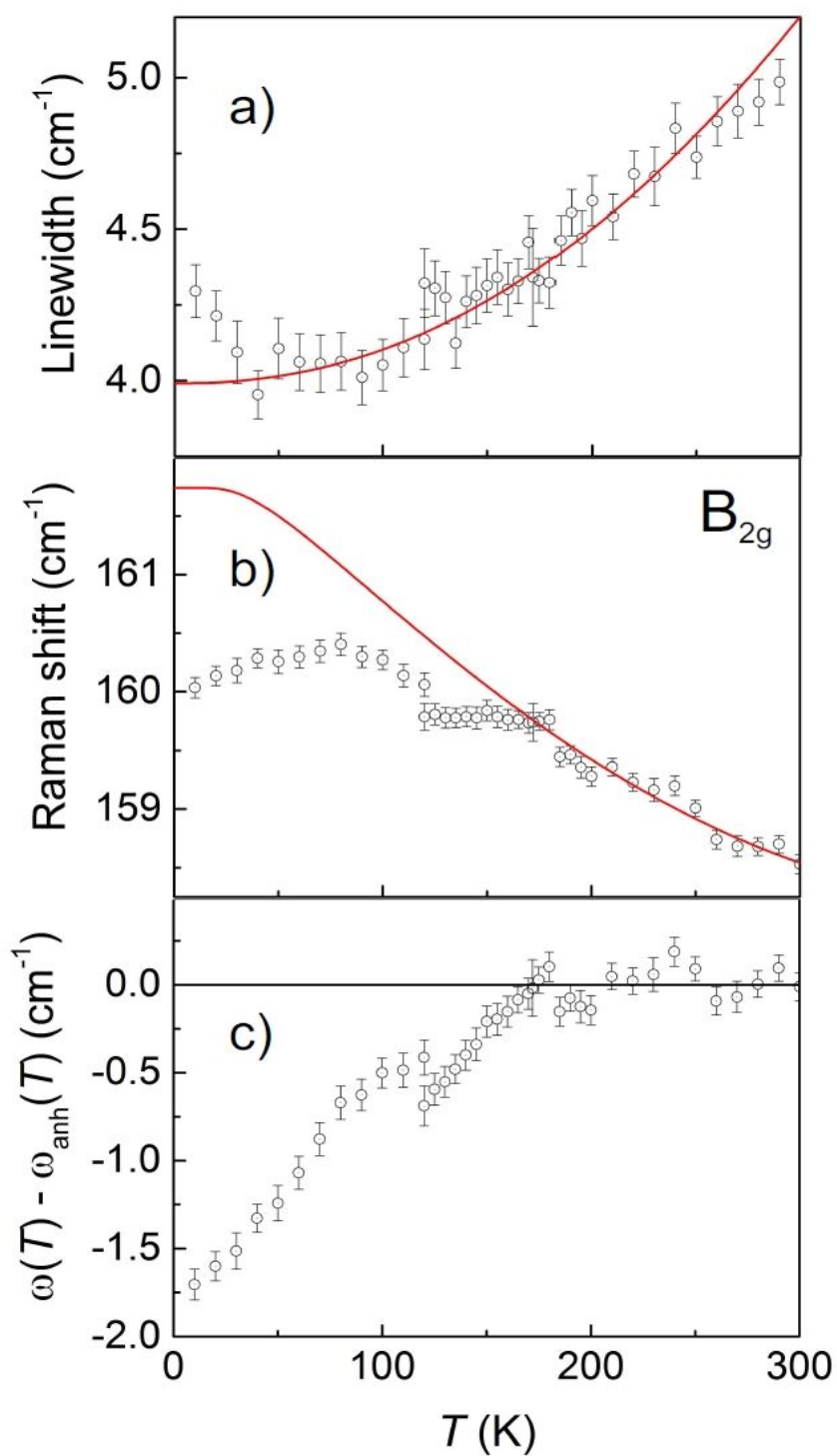


Figure 5.41: (a) linewidth, (b) Raman shift and (c) the difference $\omega(T) - \omega_{anh}$ of B_{2g} at $\approx 160 \text{ cm}^{-1}$. The red line is the Lorentzian fitting.

intrinsic anharmonic contributions ($\Delta\omega_{anh}$), and contributions from magnetoelastic coupling effects ($\Delta\omega_{mag}$), which add according to:

$$\omega(T) = \omega_0 + \Delta\omega_{latt}(T) + \Delta\omega_{anh}(T) + \Delta\omega_{mag}(T). \quad (5.27)$$

Based on the work of Klemens assuming that three and four-fold phonon decay processes, Balkanski has given the following relationship for the temperature dependence of the line shift [50, 51]:

$$\Delta\omega_{anh}(T) = C_2(1 + 2n_{BE}(x)) + C_3(1 + 3n_{BE}(y) + 3n_{BE}^2(y)), \quad (5.28)$$

where $n_{BE}(x) = \frac{1}{(\exp(x)-1)}$ and $n_{BE}(y) = \frac{1}{(\exp(y)-1)}$ are Bose-Einstein statistical factors with $x = \frac{\hbar\omega_0}{2k_B T}$ and $y = \frac{\hbar\omega_0}{3k_B T}$ appropriate for the decay of an optical phonon into two and three acoustic phonons of the identical energy [50]. For the lattice term in a first approximation, one can assume that it is proportional to the volume thermal expansion ($\Delta\omega_{latt} \propto \frac{\Delta V(T)}{V_0}$) [52].

Figure 5.41 displays the linewidth, the Raman shift and the residual $\omega(T) - \omega_{anh}$ of the B_{2g} at 160 cm^{-1} . Above $T \approx 175 \text{ K}$, Raman shift and linewidth follow well a temperature dependence expected for anharmonic phonon decay processes according to the Equation (5.28). Between $T \approx 175$ and 125 K , the Raman shift levels off, apparently due to magnetoelastic effects. After a step-like increase below 125 K , the Raman shift passes through a maximum centered at $T \approx 75 \text{ K}$ and decreases again to lowest temperatures. In contrast to the Raman shift, the linewidth shows no apparent magnetoelastic anomalies. Analogous to the Raman

shift, the linewidth attains a minimum at $T \approx 75$ K and grows again by about $\approx 10\%$ to lowest temperatures.

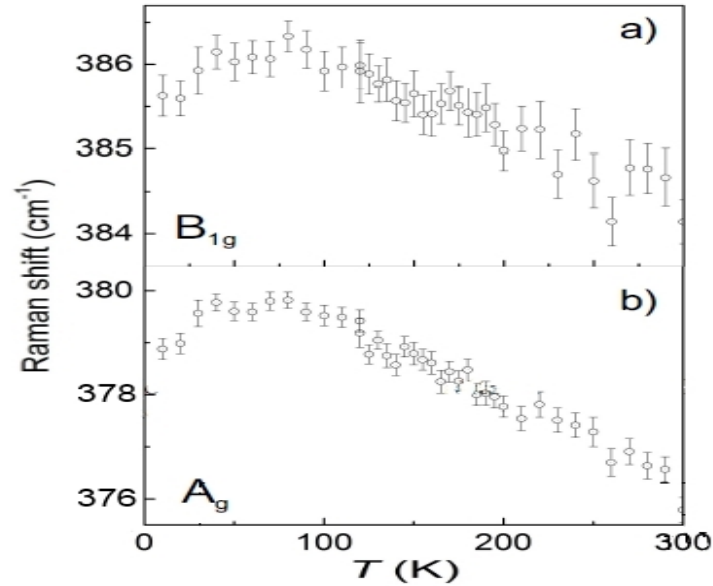


Figure 5.42: Raman shifts of $A_g - B_{1g}$ doublet observed near 380 cm^{-1} .

Figure 5.42 displays the Raman shift of the $A_g - B_{1g}$ doublet near 380 cm^{-1} . In contrast to the $160 \text{ cm}^{-1} B_{2g}$ mode, magnetoelastic effects in Raman modes at higher frequencies are either weaker or cannot be verified due to an increased linewidth of these modes. Figure 5.43 shows the Lorentzian linewidth of these two modes. However, the Raman shifts as well as the linewidth show maxima and a minimum centered at $T \approx 75$ K similar to the behavior of the $160 \text{ cm}^{-1} B_{2g}$ mode.

The anomalies in the Raman shift at $T \approx 75$ and 175 K, observed in the shift of the $160 \text{ cm}^{-1} B_{2g}$ mode, correspond well to anomalies seen in the thermal expansion and are attributed to lattice effects.

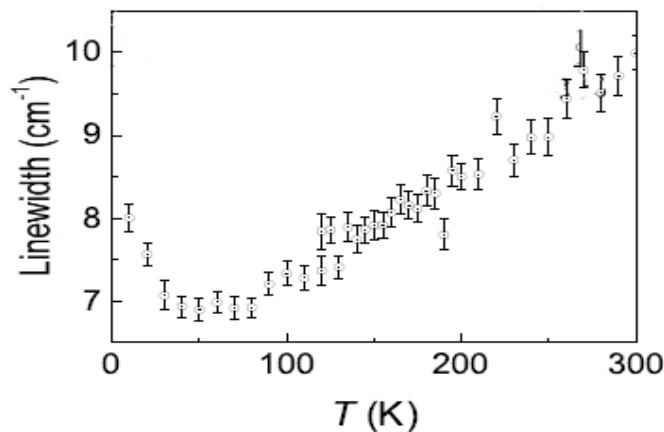


Figure 5.43: The common Lorentzian linewidth of $A_g - B_{1g}$ doublet observed near 380 cm^{-1} .

5.5 Dielectric Properties

The dielectric constant describes the response of a material to an electric field which is sometimes called relative permittivity (ϵ_r), i.e. the ratio of the permittivity of a substance (ϵ_s) to the permittivity of free space (ϵ_0). The dielectric constant can be obtained by locating the dielectric material between two parallel conducting plates and measuring the capacitance of the system (C), through the Equation (5.26(a)) [53].

In dielectrics, the permittivity can be expressed as a complex value of $\epsilon(\omega) = \epsilon'(\omega) + i\epsilon''(\omega)$, where the real part (ϵ') is the dielectric constant and the imaginary part (ϵ'') is the dielectric loss. Conductance with the nanosiemens unit is directly proportional to the amount of loss in the capacitor [54].

Dielectric properties of the rectangular shaped EuCrO_3 sample ($6.4 \times 1.6 \text{ mm}^2$, thickness $\approx 0.88 \text{ mm}$) were measured versus temperature at discrete frequencies using an AH2700A capacitance bridge (Andeen-Hagerling, Inc.) at Department

of Physics, Brock University. The AH2700A capacitance bridge is an accurate and stable instrument used for capacitance and loss measurement over a range of frequencies (50 to 20000 Hz). It is able to measure the small conductance as low as 3×10^{-7} nanosiemens [55]. The bridge was connected to MPMS in order to do the measurement from room temperature down to 1.8 K.

5.5.1 Dielectric Results

Figure 5.44(a) and (b) show the relative permittivity and the two-terminal conductance of EuCrO_3 measured at frequencies of 100, 1000 and 10000 Hz. On cooling cycle, the relative permittivity (Figure 5.44(a)) exhibits a step-like feature which for 100 Hz starts at $T \approx 100$ K and leads to a decrease of the permittivity by a factor of 2.5. With increasing frequency, the step-like feature moves to higher temperatures. The relative permittivity at $T = 300$ K is about 80 at $f = 100$ Hz which decreases to ≈ 70 at $f = 10000$ Hz. The permittivity step and its frequency dependence are accompanied by a broad resonance-like feature in the conductance displayed in Figure 5.44(b). The anomaly at $T \approx 100$ K observed in the relative permittivity and the conductance is in good agreement with the thermal expansion and Raman spectroscopy results. The temperature of the conductance maximum, T_m follows the Arrhenius law (Equation (2.26)) which was plotted in Figure 5.44(c). The activation energy of 170(10) meV ($\approx 1370 \text{ cm}^{-1}$) was obtained with $f_0 \approx 1.3(8)$ Hz. The characteristic relaxation frequency at infinite temperature is f_0 while the required energy switching the direction of the polar regions is the activation energy. The activation energy of $\approx 1300 \text{ cm}^{-1}$ corresponds to typical phonon frequencies

of oxygen related vibrations.

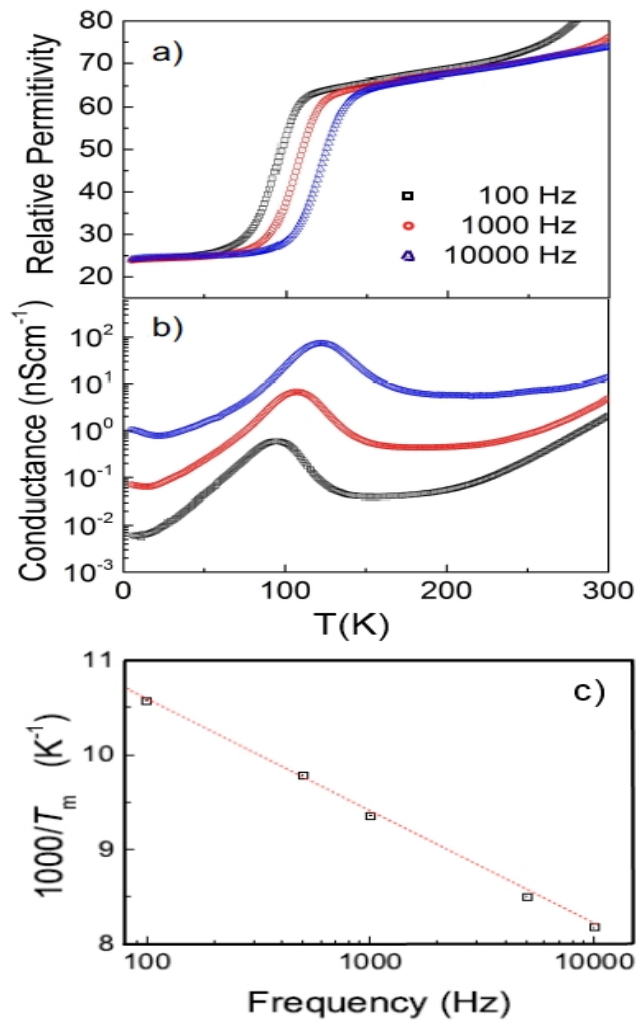


Figure 5.44: Temperature dependence of (a) the relative permittivity and (b) the conductance of EuCrO_3 at different frequencies, (c) Arrhenius Plot of the maximum peak versus frequency. The best fit line is shown in red.

Bibliography

- [1] M. Mcelfresh, “Fundamentals of Magnetism and Magnetic Measurements”, Quantum Design Support, 15-25, (1994)
- [2] SQUID Application Note, 1052-202, Quantum Design, (2001)
- [3] J. Clarke, A.I. Braginski, “The SQUID Handbook: Application of SQUIDs and SQUID Systems”, Wiley-VCH, Chapter 13, (2006)
- [4] www.icmmo.u-psud.fr/Labos/LCI/Service_SQUID/squid.php
- [5] A. Jaiswal, R. Das, S. Adyanthaya, P. Poddar, J. Nanopart. Res., 13, 1019-1027, (2011)
- [6] Y. Su, J. Zhang, Z. Feng, Z. Li, Y. Shen. S. Cao, J. Rare Earths., 29, 1060, (2011)
- [7] R. Shukla, A. K. Bera, S. M. Yusuf, S. K. Deshpande. A. K. Tyagi, W. Hermes, M. Eul, R. Pottgen, J. Phys. Chem. C, 113, 12663-12668, (2009)
- [8] K. Yoshii, Appl. Phys. Lett., 99, 142501, (2011)
- [9] B. Tiwari, M. K. Surendra, M. S. R. Rao, Mater. Res. Express, (2014)

-
- [10] K. Sardar, M. R. Lees, R. J. Kashtiban, J. Sloan, R. I. Walton, *J. Chem. Mater.*, 23, 4856, (2011)
- [11] S. Picozzi, C. Ederer, *J. Phys. Condens. Matter.*, 21, 303201, (2009)
- [12] J. R. Sahu, C. R. Serrao, N. Ray, U. V. Waghmare, C. N. R. Rao, *J. Mater. Chem.*, 17, 42-44, (2007)
- [13] G. A. Bain, J. F. Berry, *J. Chem. Educ.* 85, 532, (2008)
- [14] C. Kittel, "Introduction to Solid State Physics", 8th ed., John Wiley & Sons Ltd, (2005)
- [15] J. H. Van Vleck, "Theory of Electric and Magnetic Susceptibilities", Oxford University Press, (1932)
- [16] H. Lueken, "Course of Lectures on Magnetism of Lanthanide Ions under Varying Ligand and Magnetic Fields", Institute of Inorganic Chemistry, RWTH Aachen, (2008)
- [17] S. Bedanta, W. Kleemann, *J. Phys. D: Appl. Phys.* 42, (2009)
- [18] B. Issa, I. M. Obaidat, B. A. Albiss, Y. Haik, *Int. J. Mol. Sci.*, 14, 21266-21305, (2013)
- [19] K. Umemoto, Y. Seto, Y. Masuda, *Thermochimica Acta*, 431, 117-122, (2005)
- [20] Y. Takikawa, S. Ebisu, S. Nagata, *J. Phys. Chem. Solids.*, 71(11), 1592-1598, (2010)

-
- [21] J. S. Zhou, J. A. Alonso, V. Pomjakushin, J. B. Goodenough, Y. Ren, J. Q. Yan, J. G. Cheng, *Phys. Rev. B*, 81, 214115, (2010)
- [22] H. J. Zhao, W. Ren, X. M. Chen, L. Bellaiche, *J. Phys: Condens. Matter*, 25, 385604, (2013)
- [23] P. K. Manna, S. M. Yusuf, R. Shukla, A. K. Tyagi, *Appl. Phys. Lett.*, 96, 242508, (2010)
- [24] D. Niebieskikwiat, M. B. Salamon, *Phys. Rev. B*, 72, 174422, (2005)
- [25] S. Karmakar, S. Taran, E. Bose, B. K. Chaudhuri, C. P. Sun, C. L. Huang, H. D. Yang, *Phys. Rev. B*, 77, 144409, (2008)
- [26] M. J. Benitez, O. Petravic, H. Tüysüz, F. Schüth, H. Zabel, *Phys. Rev. B*, 83, 134424, (2011)
- [27] V. Markovich, R. Puzniak, Y. Skourski, A. Wisniewski, D. Mogilyanski, G. Jung, G. Gorodetsky, *J. Phys. Condens Matter*, 24, 266001, (2012)
- [28] J. Villain, *Phys. Rev. Lett.*, 52, 1543, (1984)
- [29] A. Kumar, R. P. Tandon, V. P. S. Awana, *Eur. Phys. J. B*, 85, 238-247, (2012)
- [30] www.qdusa.com/sitedocs/productBrochures/mag3-07.pdf
- [31] Quantum Design Physical Property Measurement System AC Measurement System (ACMS) Option Users Manual, (2003)

-
- [32] K. Vijayanandhini, Ch. Simon, V. Pralong, V. Caignaert, B. Raveau, *Phys. Rev. B*, 79, 224407, (2009)
- [33] D. L. Anderson, "Theory of the Earth", Blackwell Scientific Publications, Boston, (1989)
- [34] E. S. R. Gopal, "Specific Heats at Low Temperatures", Springer, (1966)
- [35] Quantum Design Physical Property Measurement System Heat Capacity Option Users Manual, (2004)
- [36] H. Satoh, S. Koseki, M. Takagi, W. Y. Chung, N. Kamegashira, *J. Alloys. Compd.*, 259, 176, (1997)
- [37] F. Bartolomé, J. Bartolomé, M. Castro, J. J. Melero, *Phys. Rev. B*, 62,1058, (2000)
- [38] Y. Su, J. Zhang, Z. Feng, L. Li, B. Li, Y. Zhou, Z. Chen, S. Cao, *J. Appl. Phys.*, 108, 013905, (2010)
- [39] M. Bouvier, P. Lethuillier, D. Schmitt, *Phys. Rev. B*, 43, (1991)
- [40] Y. Touloukian, "Thermal Expansion: Metallic Elements and Alloys of Thermophysical Properties of Matter", 12, New York, Plenum Press, (1977)
- [41] R. S. Krishnan, R. Srinivasan, S. Devanarayanan, "Thermal Expansion of Crystals", Pergamon Press, (1979)
- [42] M. Rotter, H. Müller, E. Gratz, M. Doerr, M. Loewenhaupt, *Rev. Sci. Instrum.*, 69, 2742, (1998)

-
- [43] H. Müller, M. Rotter, Capacitance Dilatometer DIL20-11 User Manual, Institute of Solid State Physics, Vienna University of Technology, Austria, (2011)
- [44] P. G. Reuvekamp, “Investigation into the magnetic and the structural properties of two low dimensional antiferromagnets TiPO_4 and CrOCl ”. Ph.D thesis, Stuttgart University, (2014)
- [45] D. R. Vij, “Handbook of Applied Solid State Spectroscopy”, Springer US, (2006)
- [46] M.C. Weber, J. Kreisel, P. A. Thomas, M. Newton, K. Sardar, R. I. Walton, Phys. Rev. B, 85, 054303, (2012)
- [47] M.N. Iliev, A. P. Litvinchuk, V. G. Hadjiev, Y. Q. Wang, J. Cmaidalka, R. L. Meng, Y. Y. Sun, N. Kolev, M. V. Abrashev, Phys. Rev. B, 74, 214301, (2006)
- [48] M. El. Amrani, M. Zaghrioui, V. TaPhuoc, F. Gervais, N. E. Massa, J. Mag. Mater., 361, 1, (2014)
- [49] V. S. Bhadram, B. Rajeswaran, A. Sundaresan, C. Narayana, Eur. Phys. Lett., 101, 17008, (2013)
- [50] P. G. Klemens, Phys. Rev. 148, 845, (1966).
- [51] M. Balkanski, R. F. Wallis, E. Haro, Phys. Rev. 28, 1928, (1983)
- [52] M. Cardona, Solid State Commun. 133, 3, (2005)

- [53] www.en.wikipedia.org/wiki/Relative-permittivity
- [54] L. Chen, V. K. Varadan, "Microwave electronics: measurement and materials characterization", John Wiley & Sons, (2004)
- [55] AH2700A 50Hz-20 kHz Ultra-Precision Capacitance Bridge
ANDEEN-HAGERLING, Operation and Maintenance Manual, (2003)

Chapter 6

Neutron Scattering

6.1 Why Neutrons?

A neutron, a subatomic particle consists of two down quarks with charge ($-\frac{1}{3}e$) and one up quark with charge ($+\frac{2}{3}e$), has mass of 1.674×10^{-27} kg (1.008 u), an electric dipole moment less than 2.9×10^{-26} e.cm, spin $\frac{1}{2}$ and magnetic moment of $-1.913 \mu_N$, where $\mu_N = \frac{e\hbar}{2m_n}$, \hbar and m_n are the nuclear magneton, the Planck's constant and neutron mass, respectively [1]. Neutrons are the essential constituent within an atomic nucleus which bind with protons and stabilize the electromagnetic repulsion and the nuclear interaction. The zero net electric charge allows thermal neutrons to penetrate many materials in depth without being scattered or absorbed. For example, the attenuation of neutrons by Al is about 1% per mm compared to more than 99% per mm for X-rays [2]. Neutrons interact with the nucleus of atoms as well as magnetic fields of unpaired electrons in matter. Free neutrons are unstable and undergo β decay with a mean life time of less than 15 minutes. Free neutrons have wave-like properties with a wavelength given by the de Broglie relation ($\lambda_n = \frac{h}{m_n v_n}$) and the energy $E_n =$

$\frac{h^2}{2m_n\lambda_n^2} = k_B T$, where k_B , T and v_n are Boltzmann constant, temperature and speed of a neutron, respectively. Neutrons' wavelength is dependent on the speed and hence their energy. The wavelengths are comparable to the atomic spacing, hence neutrons are strongly diffracted by the atoms in the crystals, consequently they can be used in crystallography to determine the crystal structure [3]. All physical properties of neutrons, especially the zero net electric charge and half magnetic spin, make them the unique tool for the identification of material structures, phase transitions and magnetic structures. Neutron scattering offers potential advantages compared to the X-ray scattering, such as:

- i) Neutron scattering is isotopic specific due to the different scattering lengths.
- ii) Adjacent elements in the periodic table with the very similar X-ray form factors, such as Fe and Co, are often distinguishable.
- iii) Neutrons are sensitive to the light atoms (such as hydrogen); therefore, their light element visibility is good.
- iii) Neutrons have high sample penetration compared to X-rays.

Neutrons are classified in three groups of cold ($T \sim 20$ K), thermal ($T \sim 300$ K) and hot neutrons ($T \sim 1200$ K). Energies of thermal neutrons are similar to energies of elementary excitations in the crystals; thus, they can be a proper tool to study the lattice and molecular dynamics [3, 4].

6.2 Neutron Scattering Sources

Neutrons can be produced by the fission of uranium in nuclear reactors (Figure 6.1(a)) or by the spallation due to the collision of high energy particles such as protons with a heavy metal target (Figure 6.1(b)).

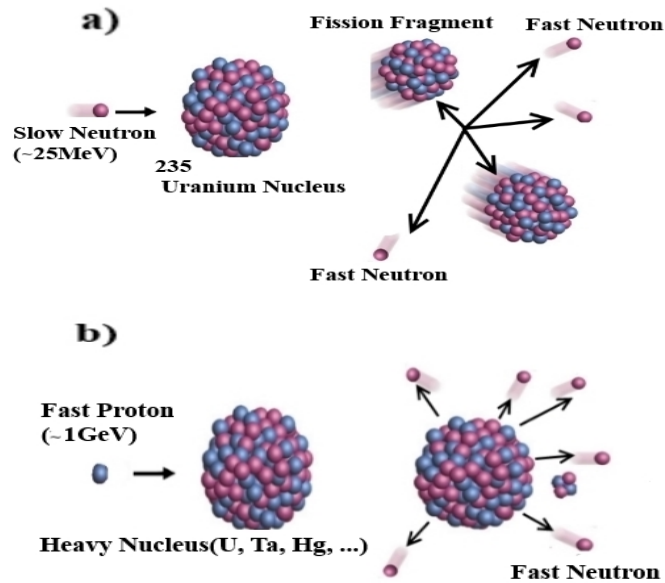


Figure 6.1: Producing neutrons by (a) fission process and (b) spallation reaction, printed from Ref. [5].

In fission process, fast neutrons are produced in the core of the nuclear reactor. These fast neutrons are required to be slowed down by a moderator. Liquid H₂, H₂O and CH₄ are the examples of common moderators used for the neutron production process in the spallation as well as reactors. The reflectors are usually used to reduce neutron loss from the core [4, 6].

The National Research Universal (NRU) reactor is the neutron source for the NRC Canadian Neutron Beam Center, located in Chalk River Laboratories, Ontario, Canada, where all the neutron experiments in this research were done.

The moderator used in the NRU reactor is heavy water. Most neutrons emitted from NRU are in a thermalized spectrum of energies ($T \sim 300$ K), hence their wavelengths were in the range of 0.8 - 8.0 Å and the energies of 1 meV - 130 meV. Several beam tubes through the reactor wall allow the neutrons to exit as a neutron beam and before selecting neutrons of the desired energy for the specific experiment. Figure 6.2 shows the reactor and six available neutron beam instruments at NRU. The spectrometer mounted at each beam port was referred by a letter-number such as C2 or L3. The spectrometers C2 and N5 were used in our experiments.

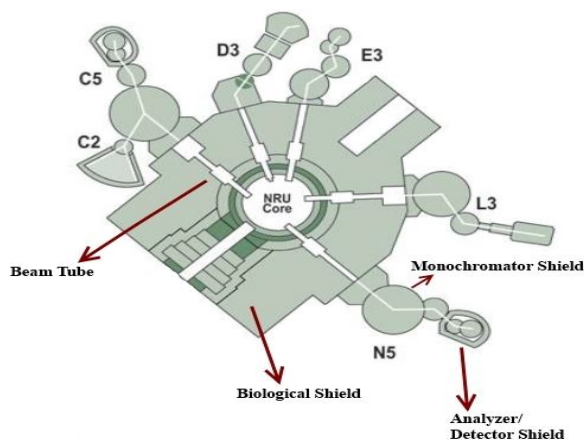


Figure 6.2: National Research Universal (NRU) Reactor (Plan View), printed from Ref. [5]

The interaction between a neutron and matter can be elastic or inelastic. The elastic neutron scattering (neutron diffraction) is usually used to determine the atomic as well as magnetic structure of solids, making the neutron diffraction an important tool of the crystallography. Inelastic neutron scattering is an experimental technique commonly used to study the atomic and molecular vibrations as well as

magnetic crystal field excitations [4, 6] .

6.3 Theory of Neutron Scattering

Neutrons interact elastically or inelastically with the atomic nuclei and magnetic fields from unpaired electrons. There are two types of scattering: coherent scattering describes roughly the scattering of a neutron from all the nuclei in the sample while in incoherent scattering, the scattered waves can not produce the constructive interference and intensities of each scattered wave are added up independently, commonly contributing as a background in the scattering pattern [7].

6.3.1 Elastic Neutron Scattering

Nuclear dimensions are about 10^{-15} m, a small point compared to the common neutron wavelength 10^{-10} m; therefore, neutrons mostly see materials as an empty space. Suppose the incident neutron moves as a plane wave with the wave function ψ_i and wave vector \mathbf{k}_i in the x direction. The nucleus isotropically scatters the incident beam. The scattered neutron behaves as a spherical wave (ψ_f) with the scattered wave vector of \mathbf{k}_f :

$$\psi_i \sim \exp ik_i x; \quad (6.1a)$$

$$\psi_f \sim -\frac{b}{r} \exp i\mathbf{k}_f \cdot \mathbf{r}, \quad (6.1b)$$

where b is the scattering length of the nucleus which measures the strength of the neutron-nucleus interaction. Figure 6.3 shows the incident plane waves and

circular scattered waves produced by a nucleus at $r = 0$.

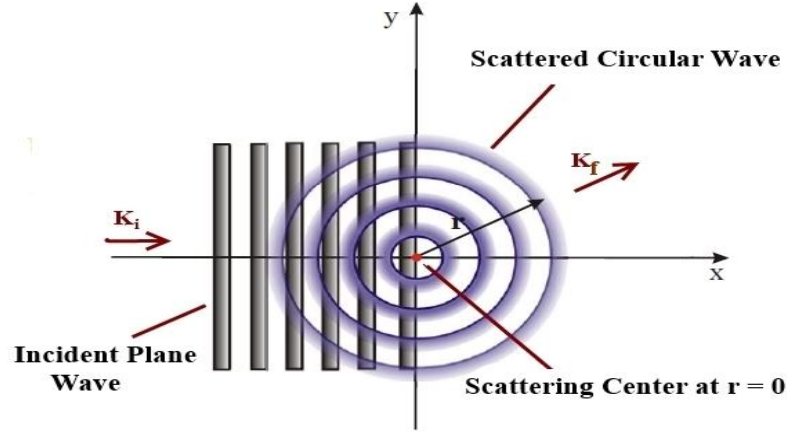


Figure 6.3: Incident plane waves are scattered by a nucleus at $r = 0$ and produced circular scattered waves [8].

Elastic scattering happens when only the direction of scattered neutrons changes after a collision with atoms in the sample but the energy is conserved. According to the momentum conservation of incident and scattered neutrons at the scattering object, scattering vector (\mathbf{Q}), is obtained as:

$$\mathbf{Q} = \mathbf{k}_i - \mathbf{k}_f, \quad (6.2)$$

\mathbf{Q} is the momentum transfer, which in the case of elastic scattering ($|k_i| = |k_f|$) will be given by:

$$Q = \frac{4\pi \sin \theta}{\lambda}. \quad (6.3)$$

The probability of finding a neutron at a given point in the space is $|\psi^2| = \psi \times \psi^*$. The scattering probability can be described in terms of a cross section. Scattering function, $S(\mathbf{Q})$, which is the number of scattered neutrons as a function

of Q , only depends on the properties of the sample. Scattering diagram from one nucleus in three-dimensions is shown in Figure 6.5(b), in which the incident neutron beam is directed along the z -direction and scattered beam is in the (θ, ϕ) direction. Detectors record the directions of the scattered neutrons, in other words, they measure all neutrons which are scattered from a nucleus into the solid angle $d\Omega$.

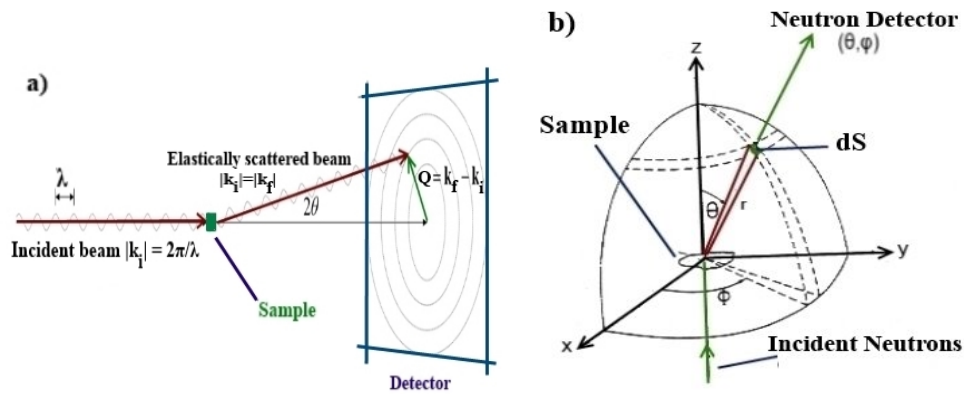


Figure 6.4: (a) Incident and scattered beams produce the scattering vector, Q . (b) Incident neutrons along z -direction are scattered into a scattering angle θ with the azimuthal angle ϕ in a solid angle $d\Omega$. dS is an scattering area on a detector [8].

The differential cross section, $\frac{d\sigma}{d\Omega}$, and the total cross section, σ , for a fixed single nucleus are defined by the following formulas:

$$\frac{d\sigma}{d\Omega} = \frac{\text{number of neutrons scattered per second into } d\Omega}{\Phi d\Omega}; \quad (6.4a)$$

$$\sigma = \int_0^{4\pi} \frac{d\sigma}{d\Omega} d\Omega = \frac{\text{total number of neutrons scattered per second}}{\Phi}, \quad (6.4b)$$

where Φ is the incident flux which defined by the number of the incident neutrons with a velocity v passing through a unit area in the unit of $\frac{n}{cm^2 s}$. Hence, it can be obtained using:

$$\Phi = v |\psi_i|^2 = v, \quad (6.5)$$

and similarly, the number of scattered neutrons with a velocity v passing through an area dS will be defined using:

$$vdS |\psi_s|^2 = vdS \frac{b^2}{r^2} = vb^2 d\Omega, \quad (6.6)$$

by substitution of equations (6.5) and (6.6) in (6.4), total cross section for a single fixed nucleus will be given by:

$$\sigma_{total} = 4\pi b^2. \quad (6.7)$$

For considering the scattering by many fixed nuclei, it is convenient to use an effective potential (Fermi pseudo-potential) which is much weaker than the actual interaction. The Fermi potential for an interaction between a neutron and a nucleus can be defined in the term of $\frac{2\pi\hbar^2}{m_n} b\delta(\mathbf{r} - \mathbf{R})$, where \mathbf{r} , \mathbf{R} , m_n and δ are the instantaneous positions of a neutron and a nucleus, mass of a neutron and delta Dirac function, respectively. Thus, the total interaction potential between a neutron and a specimen may be calculated by sum over all atoms in the sample:

$$V(\mathbf{r}) = \frac{2\pi\hbar^2}{m_n} \sum_j b_j \delta(\mathbf{r} - \mathbf{R}_j). \quad (6.8)$$

According to the Born approximation, the probability of a transition of a neutron wave vector from \mathbf{k}_i to \mathbf{k}_f by a potential $V(\mathbf{r})$ through scattering can be

defined using:

$$\int | e^{i\mathbf{k}_i \cdot \mathbf{r}} V(\mathbf{r}) e^{-i\mathbf{k}_f \cdot \mathbf{r}} |^2 d\mathbf{r} = \int | V(\mathbf{r}) e^{i\mathbf{Q} \cdot \mathbf{r}} |^2 d\mathbf{r}, \quad (6.9)$$

thus:

$$\frac{d\sigma}{d\Omega} = \left[\frac{m}{2\pi\hbar^2} \right]^2 \left| \int V(\mathbf{r}') e^{i\mathbf{r}' \cdot \mathbf{Q}} d\mathbf{r}' \right|^2 = \left| \sum_j b_j e^{i\mathbf{R}_j \cdot \mathbf{Q}} \right|^2 = \sum_{j,k} b_j b_k e^{-i(\mathbf{R}_k - \mathbf{R}_j) \cdot \mathbf{Q}}. \quad (6.10)$$

By using delta Dirac function, $f(x) = \int \delta(x-\alpha) f(\alpha) d\alpha$, when $x = (\mathbf{R}_k - \mathbf{R}_j)$ and $\alpha = \mathbf{r}$, the equation (6.10) can be written as:

$$\frac{d\sigma}{d\Omega} = \sum_{j,k} b_j b_k \int_{-\infty}^{\infty} \delta(\mathbf{r} - (\mathbf{R}_j - \mathbf{R}_k)) e^{-i\mathbf{r} \cdot \mathbf{Q}} d\mathbf{r}. \quad (6.11)$$

If we supposed that the scattering lengths for all atoms in the sample are the same ($b_j = b_k = b$), what we expect in the coherent scattering, then we have:

$$\frac{d\sigma}{d\Omega} = N b^2 \int_{-\infty}^{\infty} G(\mathbf{r}) e^{-i\mathbf{r} \cdot \mathbf{Q}} d\mathbf{r}, \quad (6.12)$$

where $G(\mathbf{r}) = \frac{1}{N} \sum_{j,k} \delta(\mathbf{r} - (\mathbf{R}_j - \mathbf{R}_k))$ is called the pair-correlation function because it shows the correlation between two particles with the different positions. N is the number of the atoms in the sample [7, 8, 9].

Similar to the Equation (4.12), the nuclear structure factor function can be given using:

$$F(\mathbf{Q}) = \sum_{\text{all nuclei}} b_j e^{i\mathbf{R}_j \cdot \mathbf{Q}}. \quad (6.13)$$

Each atom consists of a lattice and basis attached to the lattice points. The position of nucleus j is given by $\mathbf{R}_j = \mathbf{T} + \mathbf{r}_j$ where \mathbf{T} and \mathbf{r}_j are the lattice translation vector and the position of nucleus relative to the origin of the unit cell. Therefore, the structure factor can be written as:

$$F(\mathbf{Q}) = \sum_{lattice} e^{i\mathbf{T}\cdot\mathbf{Q}} \sum_{basis} b_j e^{i\mathbf{r}_j\cdot\mathbf{Q}}. \quad (6.14)$$

The first term is equal to the total number of the atoms and the second term is the structure factor. For direct vector $\mathbf{r}_j = \mathbf{a}_1x_j + \mathbf{a}_2y_j + \mathbf{a}_3z_j$ and the reciprocal vector $\mathbf{Q} = \mathbf{b}_1h + \mathbf{b}_2k + \mathbf{b}_3l$, the structure factor can be expressed as which we found in the X-ray diffraction:

$$F_{hkl} = \sum_{basis} b_j e^{2\pi i(hx_j + ky_j + lz_j)}. \quad (6.15)$$

C2 High Resolution Powder Diffractometer

All the powder diffraction patterns were collected using the DUALSPEC C2 powder neutron diffractometer at NRC Canadian Neutron Beam Center, Chalk River, Canada. The C2 diffractometer was equipped with a curved 800-wire BF_3 position sensitive detector. The detector could be positioned in low and high angle settings to collect data from the complete 120° range of scattering angles. It could be moved in steps as small as 0.01° within each setting. A hot squeezed single crystal silicon flat plate was used as the monochromator. We used 2.37 Å (the silicon 311 reflection) and 1.33 Å (the silicon 531 reflection) wavelengths

to obtain the diffraction patterns. The short wavelength was employed to obtain Bragg's reflections at high scattering angles to assist with refinement of nuclear structure while the long wavelength was used to better separate low angle peaks where the magnetic signal was expected to be stronger. Changing the wavelength was computer automated and performed by rotating the monochromator crystal, without changing the take-off angle. A pre-sample graphite filter was placed in the neutron beam to eliminate contamination from higher order neutron wavelengths by the silicon monochromator at 2.37 Å. There was an additional sensor at the bottom of the powder specimen to check the precise of the whole powder temperature.

The powders were grounded as finely as possible for the neutron powder diffraction. Neutron powder containers for samples CeCrO_3 and 10% Eu^{3+} dopant were the cylindrical thin wall vanadium metal. Cd metal sheet was used to cover areas of the mount that did not include the sample to reduce the background because Cd is a very good neutron absorbing material. A flat plate aluminum holder with narrower sample space was used for samples with the higher europium concentration since Eu has a large neutron absorption cross section. Aluminum is almost neutron transparent while vanadium has high incoherent scattering. Figures 6.5(a) and 6.5(b) represent the vanadium and aluminum sample holders used in the experiments, respectively.

6.3.2 Inelastic Neutron Scattering

In reality, atoms are not fixed in their positions inside a crystal. Their thermal energy makes them vibrate in the vicinity of their equilibrium positions. The

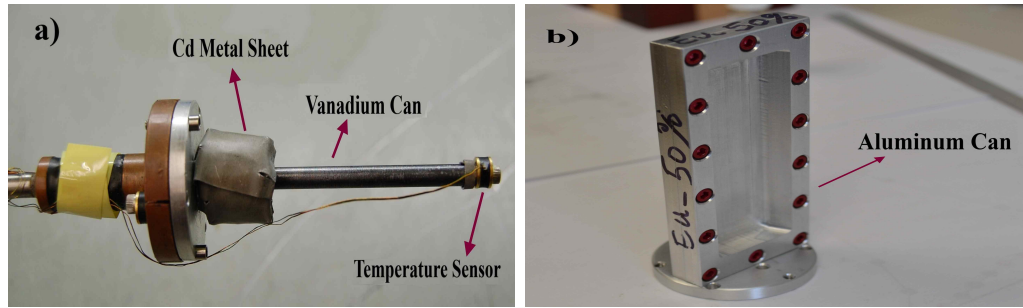


Figure 6.5: (a) The vanadium cylindrical sample holder and (b) an aluminum flat sample holder.

dynamical behavior of atoms in the crystal lattice can be explained by coupling atoms via spring-like forces. The displacement of one atom causes the neighboring atoms to move, creating a wave-like motion propagating through the lattice. These lattice waves are known as phonons with the quantized energy $h\nu$, where ν is the frequency of the atomic motion.

When neutrons penetrate in the sample in an inelastic coherent scattering, they create or annihilate an excitation inside the atom. This excitation can be either a phonon or a magnon. A collective excitation of the electrons' spin structure in a crystal lattice is called a magnon which can be viewed as a quantized spin wave. If neutrons create phonons or magnons, they themselves lose their energy, thus we will have:

$$E_n = \hbar\omega = \frac{\hbar^2 k_i^2}{2m_n} - \frac{\hbar^2 k_f^2}{2m_n} = E_i - E_f, \quad (6.16)$$

here E_i , E_f and ω are the incident neutron energy, the scattered neutron energy and the excitation angular frequency, respectively. Energies of thermal neutrons

are in the same range of the elementary excitation's energies in solids. Hence, they can be proper to be used in the inelastic scattering in order to study the lattice and molecular dynamics as well as magnetic excitations.

For inelastic scattering, Equation (6.9) can be written as:

$$\left| \int V(\mathbf{r}, t) e^{i\mathbf{Q}\cdot\mathbf{r}} d\mathbf{r} \right|^2 \delta(\Delta E - \hbar\omega), \quad (6.17)$$

where ΔE is the change in the energy due to the scattering. This equation shows the probability of a neutron with the wave vector \mathbf{k}_i and energy E_i scattered by the potential $V(\mathbf{r}, t)$ and converted to a neutron with the wave vector \mathbf{k}_f and energy E_f . The neutron flux into $d\Omega$ with the final energy between $E_f + dE_f$, named the double differential cross-section, will be:

$$\frac{d^2\sigma}{d\Omega dE_f} = \frac{\text{number of neutrons scattered per second into } d\Omega \text{ and } dE_f}{\phi d\Omega dE_f}, \quad (6.18)$$

thus, the double differential cross-section can be written as:

$$\begin{aligned} \frac{d^2\sigma}{d\Omega dE_f} &= \frac{k_f}{k_i} \frac{1}{2\pi\hbar} \left(\frac{m}{2\pi\hbar^2}\right)^2 \int_{-\infty}^{\infty} |V(\mathbf{r}', t) e^{-i\mathbf{Q}\cdot\mathbf{r}'} d\mathbf{r}'|^2 e^{i\Delta Et} e^{-i\omega t} dt \\ &= \frac{k_f}{k_i} \frac{1}{2\pi\hbar} \sum_{jj'} b_j b_{j'} \int_{-\infty}^{\infty} dt e^{-i\omega t} [e^{i\mathbf{Q}\cdot\mathbf{R}_j(t)} e^{i\mathbf{Q}\cdot\mathbf{R}_j(0)}] \\ &= \frac{k_f}{k_i} \frac{1}{2\pi\hbar} \sum_{jj'} b_j b_{j'} \int_{-\infty}^{\infty} dt e^{-i\omega t} \int_{-\infty}^{\infty} \delta[\mathbf{r} - (\mathbf{R}_{j'}(0) - \mathbf{R}_j(t))] e^{-i\mathbf{Q}\cdot\mathbf{r}} d\mathbf{r}. \end{aligned} \quad (6.19)$$

Supposed $b_j = b_{j'}$, which is true in the coherent scattering; therefore, we can simplify the Equation (6.18):

$$\frac{d^2\sigma}{d\Omega dE_f} = \frac{Nb^2}{2\pi\hbar} \frac{k_f}{k_i} \int_{-\infty}^{\infty} \mathbf{G}(\mathbf{r}, t) e^{-i\omega t} e^{-i\mathbf{Q}\cdot\mathbf{r}} d\mathbf{r} dt = N \frac{k_f}{k_i} b^2 S(\mathbf{Q}, \omega), \quad (6.20)$$

where $\mathbf{G}(\mathbf{r}, t) = \frac{1}{N} \sum_{j,j'} \delta(\mathbf{r} - (\mathbf{R}_{j'}(0) - \mathbf{R}_j(t)))$ is the time-dependent pair correlation function which shows the probability of finding two atoms being in a certain distance at a certain time. Function $S(\mathbf{Q}, \omega)$ is the dynamic structure factor [7, 8, 10, 11].

N5 Three-axis Spectrometer

All inelastic scattering measurements in this research were done using N5 three-axis spectrometer which is schematically shown in Figure 6.6. Initial and final neutron energies were chosen by the monochromator and the analyzer, respectively. Pyrolytic graphite was the material which used in both the monochromator and the analyzer in this experiment. The monochromator produced a monochromatic beam and then the parallel plates of neutron absorbing materials named collimators reduced the beam divergence. The gaseous 3He was used as a detector.

6.3.3 Magnetic Neutron Scattering

A neutron has a magnetic moment, $\boldsymbol{\mu}_n$, which can be defined by the Pauli spin operator $\boldsymbol{\sigma}$:

$$\boldsymbol{\mu}_n = -\gamma\mu_N\boldsymbol{\sigma}, \quad (6.21)$$

where μ_N and γ are the nuclear magneton and a numerical constant of 1.913,

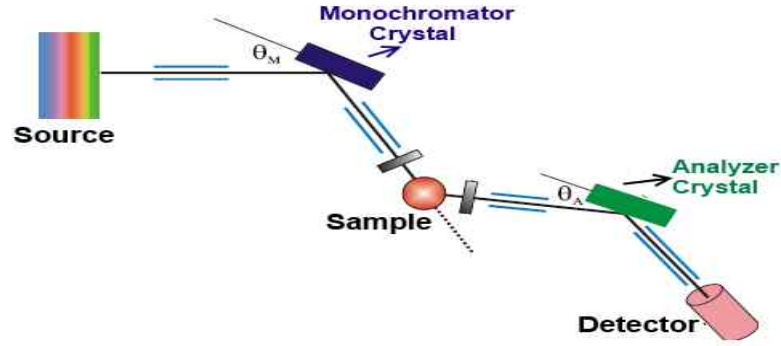


Figure 6.6: The schematic diagram of three-axis spectrometer using in the inelastic scattering, reprinted from Ref. [11].

respectively. Each neutron can interact with the magnetic field of unpaired electrons, $\mathbf{B}(\mathbf{r})$, using the equation:

$$V_M(\mathbf{r}) = -\boldsymbol{\mu}_n \cdot \mathbf{B}(\mathbf{r}). \quad (6.22)$$

Only the perpendicular component of the sample's magnetization with respect to the scattering vector is effective in the magnetic scattering; thus, the interaction potential can be obtained in the wave vector space by using the relation $\mathbf{B} = \mu_0 \mathbf{M}$ (SI units):

$$V_M(\mathbf{Q}) = -\mu_0 \boldsymbol{\mu}_n \cdot \mathbf{M}_\perp(\mathbf{Q}), \quad (6.23)$$

where $\mathbf{M}_\perp(\mathbf{Q})$ is the perpendicular component of the electron magnetic moment which is calculated using:

$$\mathbf{M}_\perp(\mathbf{Q}) = \hat{\mathbf{Q}} \times \{\mathbf{M}(\mathbf{Q}) \times \hat{\mathbf{Q}}\}. \quad (6.24)$$

The magnetic field of an unpaired electron created by the magnetic moment

of an electron spin in the specimen is given using:

$$\mathbf{B} = \frac{\mu_0}{4\pi} (\nabla \times \left\{ \frac{\boldsymbol{\mu}_e \times \mathbf{R}}{|\mathbf{R}|^3} \right\}), \quad (6.25)$$

where $\boldsymbol{\mu}_e = -g_e \mu_B \mathbf{S}$ is the magnetic moment of the electron with the spin operator \mathbf{S} . If the orbital magnetic field of an electron is neglected, the interaction potential can be rewritten by:

$$V_M = -\frac{\mu_0 \mu_B \mu_N}{4\pi} g_e \gamma \boldsymbol{\sigma} \cdot \left\{ \nabla \times \left(\frac{\mathbf{S} \times \hat{\mathbf{R}}}{R^2} \right) \right\}. \quad (6.26)$$

The value of $(\frac{\mu_0 \mu_B \mu_N}{4\pi}) g_e \gamma$ is equal to $\frac{\gamma}{4\pi} r_0$, where $r_0 = 2.82 \times 10^{-15}$ m is known as the classical radius of an electron. According to the curl definition, the equation can be simplified:

$$\nabla \times \left(\frac{\mathbf{S} \times \hat{\mathbf{R}}}{R^2} \right) = \frac{1}{2\pi^2} \int \hat{\mathbf{k}} \times (\mathbf{S} \times \hat{\mathbf{k}}) e^{ikR} dk. \quad (6.27)$$

The differential cross section through the transition from initial state with wave vector \mathbf{k}_i , spin state $\boldsymbol{\sigma}_i$ and wavelength λ_i to the scattered state of \mathbf{k}_f , $\boldsymbol{\sigma}_f$ and λ_f is obtained by:

$$\frac{d\sigma}{d\Omega} = \frac{m}{2\pi\hbar^2} \langle k_f \boldsymbol{\sigma}_f \lambda_f | V_m | k_i \boldsymbol{\sigma}_i \lambda_i \rangle. \quad (6.28)$$

When the sample is magnetically ordered, the magnetic Bragg's peaks can be observed in the elastic scattering. By substituting of Equations (6.26) and (6.27)

into (6.28), the time-independent structure of the differential cross section in the unpolarized scattering can be given by:

$$\frac{d\sigma}{d\Omega} = (\gamma r_0)^2 \left[\frac{1}{2} g F(\mathbf{Q}) \right]^2 e^{-2W} \sum_{\alpha, \beta} (\delta_{\alpha\beta} - \hat{Q}_\alpha \hat{Q}_\beta) \cdot \sum_{l, l'} e^{i\mathbf{Q} \cdot (\mathbf{r}_l - \mathbf{r}_{l'})} \langle S_l^\alpha \rangle \langle S_{l'}^\beta \rangle. \quad (6.29)$$

In this equation :

- $F(\mathbf{Q}) = \int \mathbf{M}(\mathbf{r}) e^{i\mathbf{Q} \cdot \mathbf{r}} d\mathbf{r}$ is the magnetic form factor.
- e^{-2W} is the Debye-Waller factor due to the thermal motions of atoms which shows a decrease in peak intensity by temperature.
- $\sum_{\alpha, \beta} (\delta_{\alpha\beta} - \hat{Q}_\alpha \hat{Q}_\beta)$, called the polarization factor, refers to the perpendicular component of the electron spins. There is no magnetic scattering if the spins are parallel to the scattering wave vector \mathbf{Q} .
- $\delta_{\alpha\beta}$ is the Kronecker delta.
- $\langle \dots \rangle$ term is called the spin correlation functions [12].

Neutron Powder Diffraction Results

Neutron diffraction data for sample CeCrO₃, recorded at T = 3.5 K and T = 280 K with 2.37 Å wavelength, are shown in Figures 6.7(a) and (b). Our Rietveld analysis confirms the formation of the pure single orthorhombic structure with the space group of *Pbnm* at both temperatures.

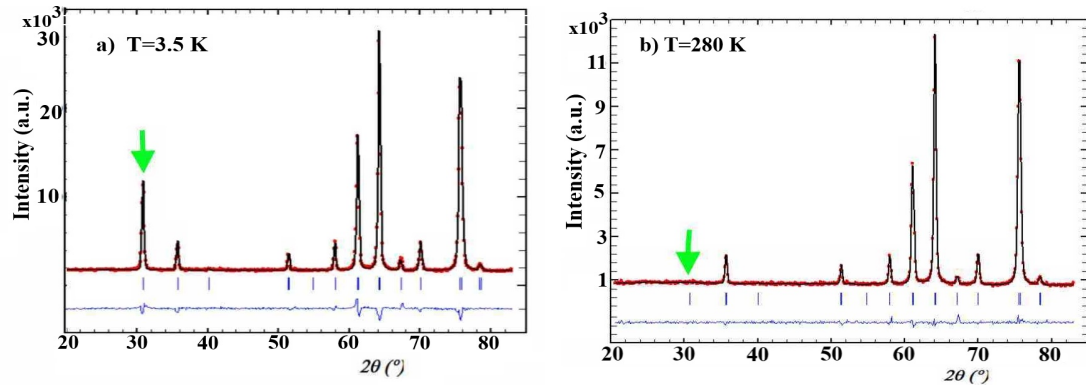


Figure 6.7: Neutron diffraction patterns of CeCrO_3 with 2.37 \AA wavelength at (a) $T = 3.5 \text{ K}$ and (b) $T = 280 \text{ K}$.

The lattice parameters and other conventional structural data obtained from the Rietveld refinement of the neutron diffraction patterns of CeCrO_3 at $T = 3.5 \text{ K}$ and $T = 280 \text{ K}$ are in Table 6.1. Lattice parameters at $T = 280 \text{ K}$ are larger than those at $T = 3.5 \text{ K}$ consistent with the thermal expansion of the nuclear unit cell by temperature.

Furthermore, the neutron diffraction pattern at $T = 3.5 \text{ K}$ indicates an extra Bragg peak at the scattering angle of $2\theta = 30.87^\circ$ (green arrow) which disappears at $T = 280 \text{ K}$, indicating the existence of the magnetic ordering in this compound at low temperatures. To determine the magnetic transition temperature of CeCrO_3 , diffraction patterns as a function of temperature from room temperature down to 3.5 K were recorded. The intensity of the magnetic peak at $2\theta = 30.87^\circ$ at different temperatures is plotted in Figure 6.8(a). As seen, the peak intensity reduces with increasing temperature, indicating the development of a magnetic order at low temperatures. The data is fitted with a Gaussian function. The intensity versus temperature is shown in Figure 6.8(b) which confirms the magnetic phase transition

Table 6.1: Structural parameters and conventional reliability indices obtained from the Rietveld refinement of the neutron diffraction patterns of CeCrO₃ with the space group of *Pbnm* at T = 3.5 K and T = 280 K.

	T = 3.5 K	T = 280 K
a (Å)	5.4615(5)	5.4661(5)
b (Å)	5.4697(5)	5.4775(6)
c (Å)	7.7060(6)	7.7224(7)
Ce (4c)		
x	-0.01370(2)	-0.00642(2)
y	-0.02886(1)	-0.02789(9)
z	0.250	0.250
B _{iso} (Å ²)	0.082(1)	0.009(7)
Occ	0.5	0.5
Mult	4	4
Cr (4b)		
x	0.500	0.500
y	0.000	0.000
z	0.000	0.000
B _{iso} (Å ²)	0.347(2)	0.100(0)
Occ	0.5	0.5
Mult	4	4
O1 (4c)		
x	0.08506(1)	0.07313(1)
y	0.48492(1)	0.51160(9)
z	0.250	0.250
B _{iso} (Å ²)	0.145(1)	0.084(7)
Occ	0.5	0.5
Mult	4	4
O2 (8d)		
x	0.28585(8)	0.28397(6)
y	0.27867(9)	0.28258(6)
z	-0.04073(5)	-0.03771(4)
B _{iso} (Å ²)	0.660(1)	0.213(1)
Occ	1.0	1.0
Mult	8	8

of 260 K for sample CeCrO_3 (green arrow). This is consistent with the transition temperature determined from DC magnetization (Chapter 5) as well as previous literature [14], this peak is attributed to the magnetic ordering of Cr^{3+} ions.

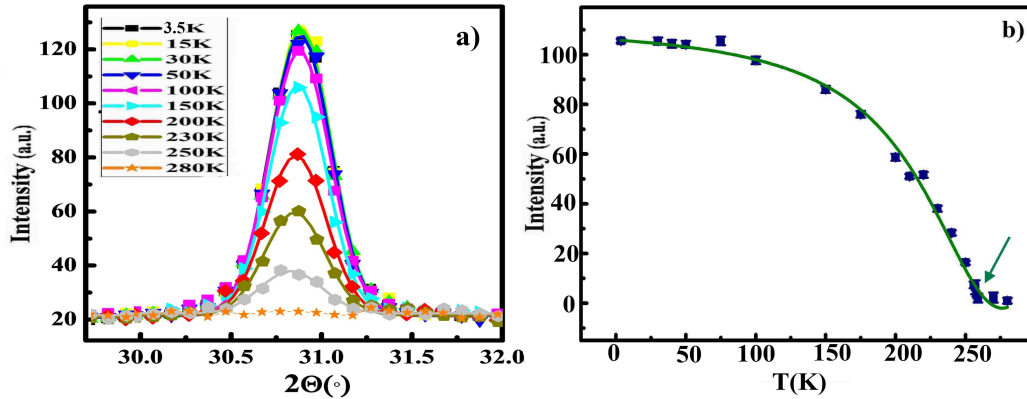


Figure 6.8: (a) Neutron diffraction patterns of CeCrO_3 with $\lambda = 2.37 \text{ \AA}$ at different temperatures and (b) the magnetic phase transition diagram of CeCrO_3 .

Figure 6.9(a) presents the neutron diffraction pattern measured with 2.37051 \AA in very high statistics focused on the magnetic Bragg's peak at $T = 3 \text{ K}$ and 290 K , showing the peak at $T = 3 \text{ K}$ centered at $30.83^\circ \pm 0.003^\circ$ with the maximum half width (FWHM) of $0.782^\circ \pm 0.007^\circ$.

On the other hand, according to the Shukla et al. [14], one expects a peak around $2\theta \approx 44.18^\circ$ in neutron patterns of CeCrO_3 with $\lambda = 2.37 \text{ \AA}$ that is assumed to be related to the magnetic ordering of Ce^{3+} ion. Figure 6.9(b) shows neutron diffraction patterns of CeCrO_3 focused on $2\theta = 44^\circ$ with very high statistics at $T = 3 \text{ K}$ and 290 K . Our results show that the intensity of this peak does not change; thus, this peak is mainly structural. None of the diffraction patterns collected at different temperatures down to $T = 3 \text{ K}$ revealed the magnetic peak at the expected position. Thus, we could not detect the magnetic ordering of the cerium

ion in this sample.

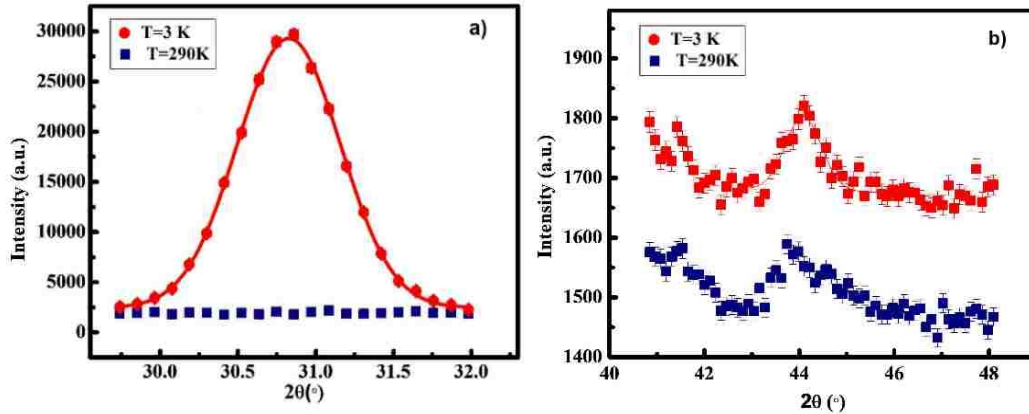
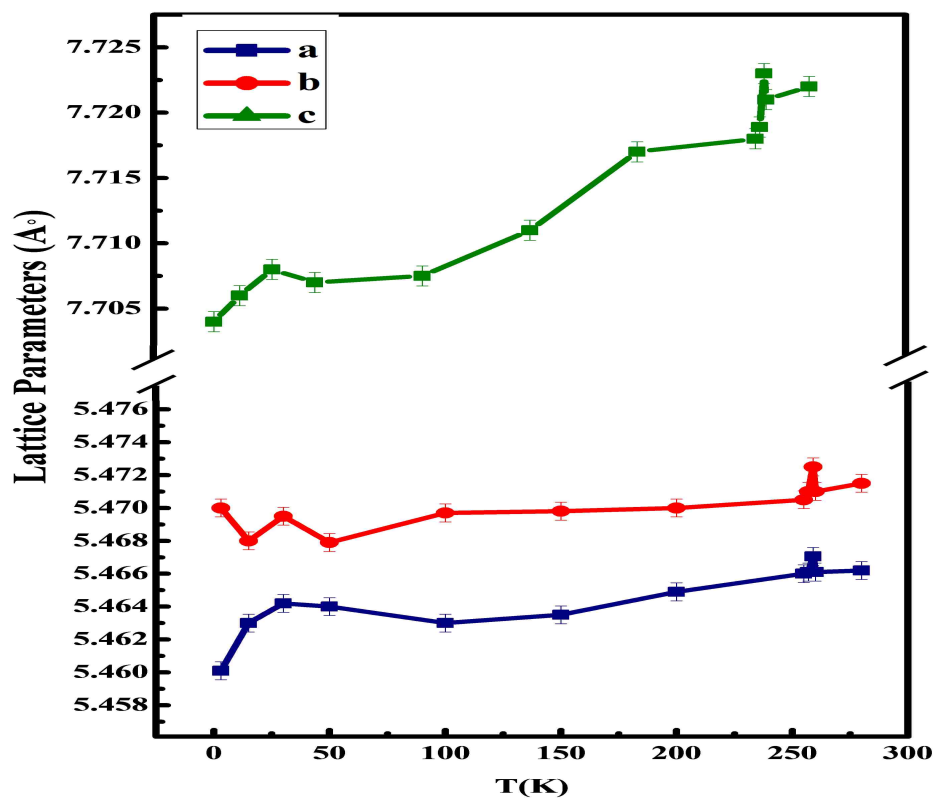


Figure 6.9: Neutron diffraction patterns of CeCrO_3 with $\lambda = 2.37 \text{ \AA}$ zoomed around (a) $2\theta = 31^\circ$ and (b) $2\theta = 44^\circ$ with high statistics.

The low temperature refinement of neutron diffraction patterns of CeCrO_3 shows that Cr^{3+} ions order in $\Gamma_4(G_x, A_y, F_z)$ magnetic configuration with the magnetic moment of $2.42 \pm 0.01 \mu_B$, which is in good agreement with previous results [14]. Furthermore, the refinement of the diffraction patterns at different temperatures indicates that the nuclear structure of CeCrO_3 remains orthorhombic with no additional structural phase transitions down to 3.5 K. Figure 6.10 shows that nuclear lattice parameters of CeCrO_3 expand while temperature increases.

In order to determine the effect of the Eu substitution on the nuclear and magnetic structures of $\text{Ce}_{1-x}\text{Eu}_x\text{CrO}_3$, we performed neutron powder diffraction measurements on doped samples where $x = 0.1, 0.5, 0.9$. Figure 6.11(a), (b) and (c) present elastic neutron scattering patterns of $\text{Ce}_{1-x}\text{Eu}_x\text{CrO}_3$ at $T = 3.5 \text{ K}$ (red line) and $T = 280 \text{ K}$ (blue line) with $\lambda = 2.37 \text{ \AA}$. The nuclear structural refinement of all samples confirmed the orthorhombic structure with the $Pbnm$ space group.

Figure 6.10: Temperature dependence of nuclear lattice parameters of CeCrO_3 .

Furthermore, the magnetic ordering peak of Cr^{3+} ion is obviously seen at $T = 3.5$ K while it is disappeared at $T = 280$ K for all samples.

The magnetic peak intensity versus temperature for samples $\text{Ce}_{1-x}\text{Eu}_x\text{CrO}_3$ are plotted in Figures 6.12(a), (b) and (c) where $x = 0.1, 0.5$ and 0.9 , respectively. The green arrow in each graph indicates the magnetic transition temperature of that compound which it moves to the lower temperature while Eu^{3+} concentration increases.

The refined neutron diffraction patterns of EuCrO_3 at temperatures 3.5 K and 280 K with $\lambda = 1.3282$ Å are shown in Figure 6.13(a) and (b). Similar to other samples, the crystal structure is orthorhombic with the space group of $Pbnm$. The refined nuclear unit cell parameters and other structural parameters for both temperatures are given in the Table 6.2. The sharp peaks in diffraction patterns at $2\theta \approx 32.87^\circ$ and 38.17° are attributed to the Al sample holder. Similar to CeCrO_3 , the appearance of an extra Bragg's peak around the scattering angle of $2\theta \approx 16.94^\circ$ at $T = 3.5$ K compared to 280 K (shown with a green arrow) proves the presence of a long-range antiferromagnetic ordering of Cr^{3+} ions in EuCrO_3 . The magnetic refinement of neutron diffraction pattern with the peak at (110) at low temperature confirmed the Γ_4 configuration with the magnetic moment of $2.55 \pm 0.06 \mu_B$.

Figure 6.14(a) illustrates the intensity of the magnetic peak corresponded to the magnetic ordering of Cr^{3+} ion located around 31° with $\lambda = 2.37$ Å at different temperatures which shows the intensity reduction by temperature. The temperature dependence of this intensity create the magnetic phase diagram of

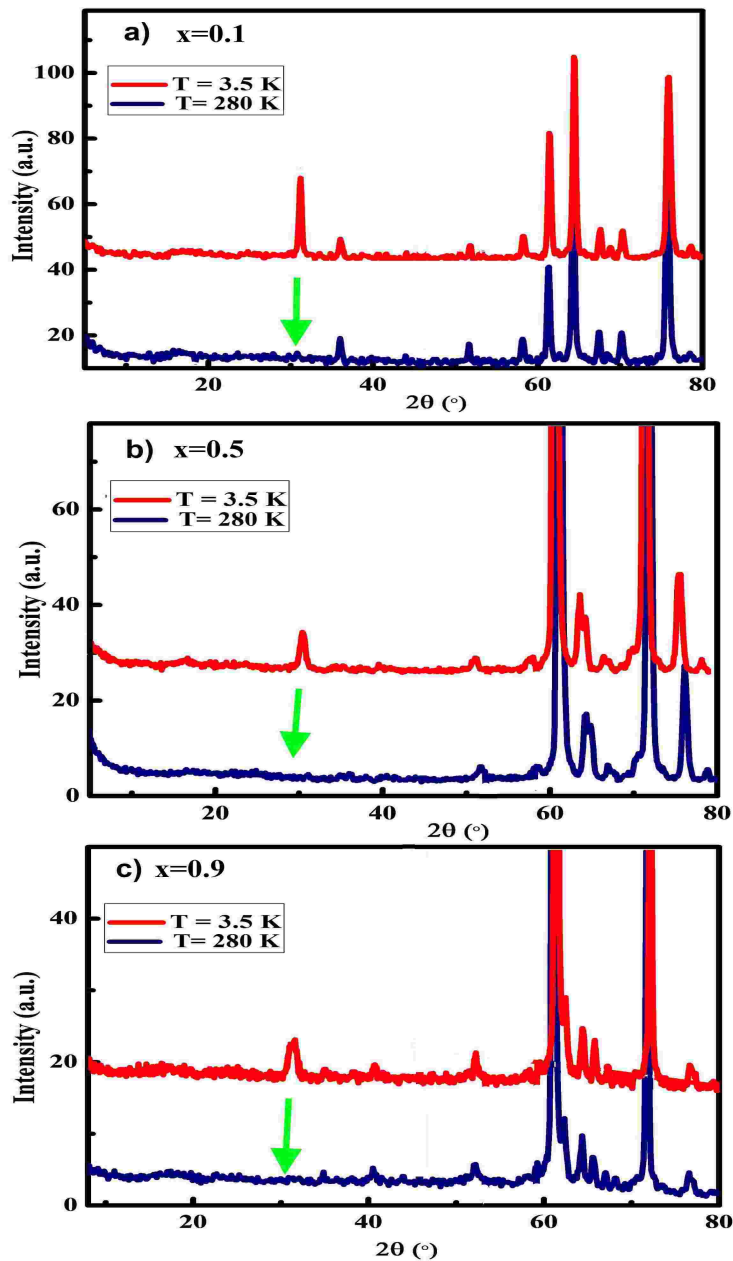


Figure 6.11: Neutron diffraction patterns of $\text{Ce}_{1-x}\text{Eu}_x\text{CrO}_3$ at $T = 3.5 \text{ K}$ (red line) and 280 K (blue line) with $\lambda = 2.37 \text{ \AA}$ where (a) $x = 0.1$, (b) $x = 0.5$ and (c) $x = 0.9$.

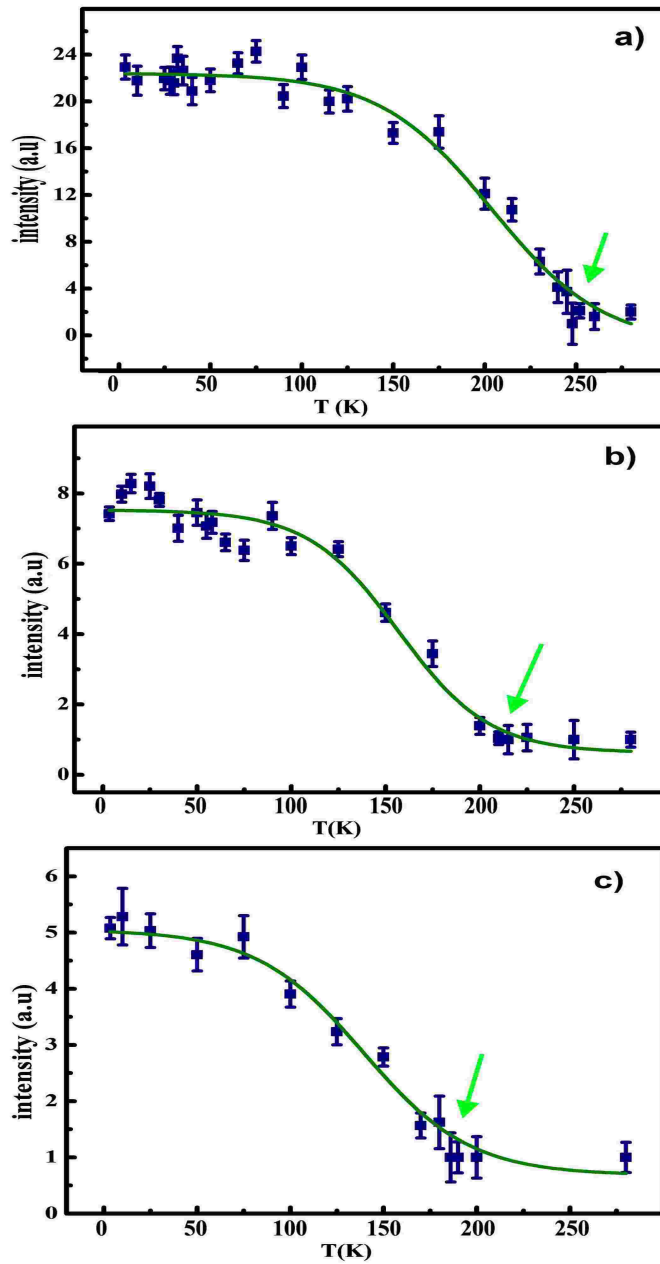


Figure 6.12: Temperature dependence of the magnetic peak, indicating the magnetic phase transition temperature of $\text{Ce}_{1-x}\text{Eu}_x\text{CrO}_3$ where (a) $x = 0.1$, (b) $x = 0.5$ and (c) $x = 0.9$.

Table 6.2: Structural parameters and conventional reliability indices obtained from the Rietveld refinement of the neutron diffraction patterns of EuCrO_3 with the space group of $Pbnm$ at $T = 3.5$ K and $T = 280$ K.

	T = 3.5 K	T = 280 K
a (\AA)	5.3194(8)	5.3364(9)
b (\AA)	5.4924(7)	5.4988(9)
c (\AA)	7.5935(12)	7.6122(13)
Eu (4c)		
x	-0.0098(39)	-0.0094(39)
y	0.0544(22)	0.00400(26)
z	0.250	0.250
B_{iso} (\AA^2)	0.48(28)	0.54(27)
Occ	0.5	0.5
Mult	4	4
Cr (4b)		
x	0.500	0.500
y	0.000	0.000
z	0.000	0.000
B_{iso} (\AA^2)	0.37(32)	0.63(37)
Occ	0.5	0.5
Mult	4	4
O1 (4c)		
x	0.0996	0.1053(37)
y	0.4786(32)	0.4746(38)
z	0.250	0.250
B_{iso} (\AA^2)	0.94(28)	1.01(32)
Occ	0.5	0.5
Mult	4	4
O2 (8d)		
x	-0.2944(25)	-0.2884(28)
y	0.2855(23)	0.2863(26)
z	0.0507	0.0448
B_{iso} (\AA^2)	0.94(28)	0.74(25)
Occ	1.0	1.0
Mult	8	8

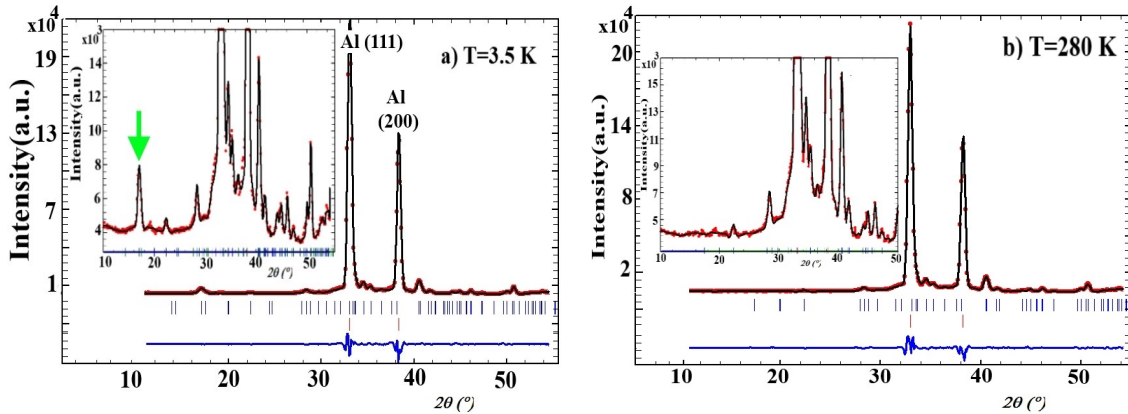


Figure 6.13: Neutron diffraction patterns of EuCrO_3 with 1.3282 \AA wavelength at (a) $T = 3.5 \text{ K}$ and (b) $T = 280 \text{ K}$.

EuCrO_3 shown in Figure 6.14(b), indicating the temperature 180 K as the Néel temperature.

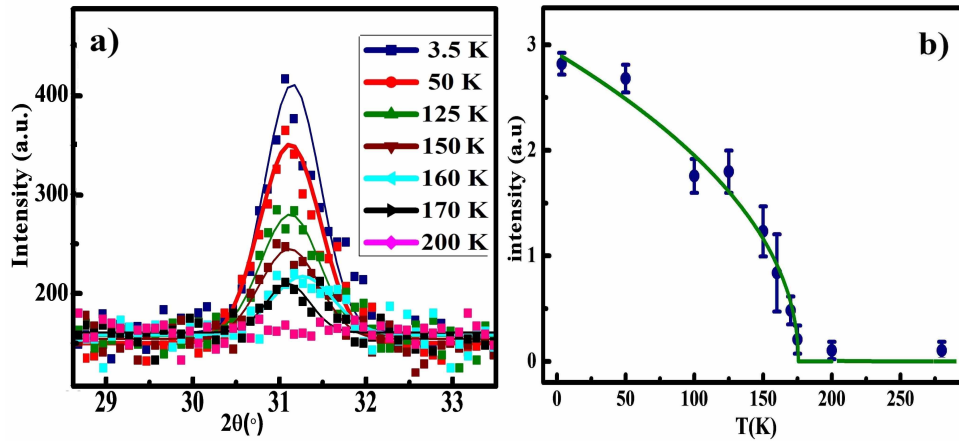


Figure 6.14: (a) Neutron diffraction patterns of EuCrO_3 with 2.37 \AA wavelength at different temperatures and (b) magnetic phase transition diagram of EuCrO_3 .

The diffraction patterns of EuCrO_3 in the range of the observed magnetic peak attributed to the Cr^{3+} ions in the high statistics at $T = 3 \text{ K}$ (red line) and 290 K (blue line) measured with $E_f = 30 \text{ meV}$ are plotted in Figure 6.15(a) which

clearly shows the peak at $T = 3$ K centered at $2\theta = 21.32^\circ \pm 0.01^\circ$ and the maximum half width (FWHM) of $0.83^\circ \pm 0.03^\circ$. The inset shows this magnetic peak at $T = 3$ K with $E_f = 14.5$ meV which is centered at $2\theta = 30.95^\circ \pm 0.05^\circ$ and FWHM = $0.89^\circ \pm 0.12^\circ$.

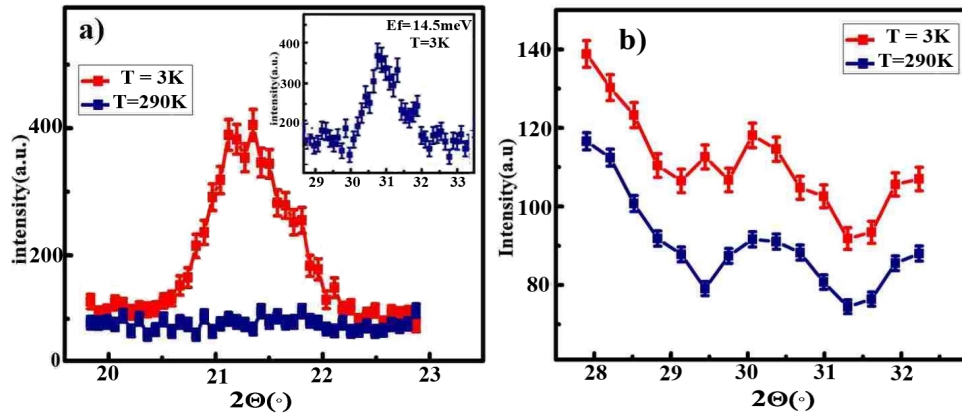


Figure 6.15: (a) Neutron diffraction patterns of EuCrO_3 at $T = 3$ K (red line) and 290 K (blue line) with $E_f = 30$ meV. (Inset is the neutron diffraction pattern with $E_f = 14.5$ meV at 3 K) and (b) neutron diffraction patterns of EuCrO_3 with very high statistics at $T = 3$ K (red line) and 290 K (blue line) with $\lambda = 1.638$ Å zoomed in expected rare earth magnetic peak region.

Figure 6.15(b) shows the neutron diffraction intensities of the expected angle attributed to the magnetic ordering of the rare earth ion in this compound ($\lambda = 1.638$ Å) with very high statistics at $T = 3$ K (red line) and 290 K (blue line). No magnetic peak attributed to Eu^{3+} ions were observed.

Figure 6.16 shows the temperature dependence of the nuclear volume cell of EuCrO_3 as derived from neutron diffraction patterns collected with $\lambda = 2.37$ Å. The cell volume exhibits a decrease starting at the Néel temperature with a minimum at $T \approx 70$ K and then an increase towards lowest temperatures. The limited number of data points does not allow to reveal further details. The observed

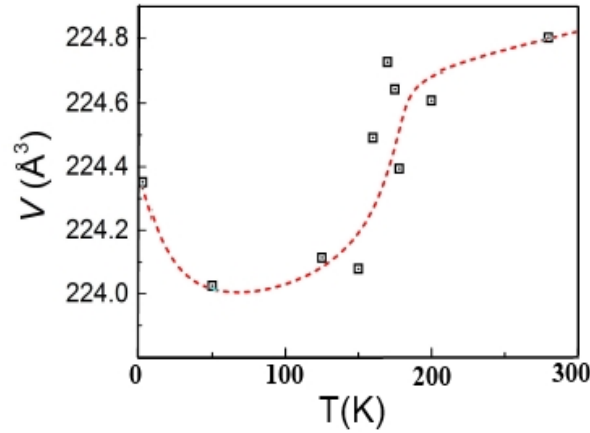


Figure 6.16: Temperature dependence of the nuclear volume cell of EuCrO_3 with 2.37 \AA wavelength. The dash red line is a guide to the eye.

anomaly in the nuclear cell volume is in good agreement with those obtained in the thermal expansion, Raman data and dielectric measurements in Chapter 5.

Inelastic Neutron Scattering Results

In order to study the energy level transitions by the crystalline electric field in CeCrO_3 , the inelastic neutron scattering was performed. The measurements were done with momentum transfer $Q = 1 \text{ \AA}^{-1}$ at $T = 3$ and 290 K , shown in Figure 6.17(a). The peak obtained during the constant Q scan reveals the energy of the crystal field excitation. An excitation appears at $T = 3 \text{ K}$ (red line) at the peak position of $E = 4.57 \pm 0.02 \text{ meV}$ and the peak width of $\text{FWHM} = 1.22 \pm 0.03 \text{ meV}$. The transition energy value is in the good agreement with the value obtained by the heat capacity measurement (Chapter 5) which satisfies the transition between ground state and first excited state. The measurement was done at $T = 3 \text{ K}$ with the momentum transfer of $Q = 1.4 \text{ \AA}^{-1}$ and compared with

the previous measurement, as illustrated in Figure 6.17(b). The result shows that the excitation peak is Q -independent and it stays at $E = 4.57$ meV at both $Q = 1$ and 1.4 \AA^{-1} , indicating that it is the crystal field excitation energy level.

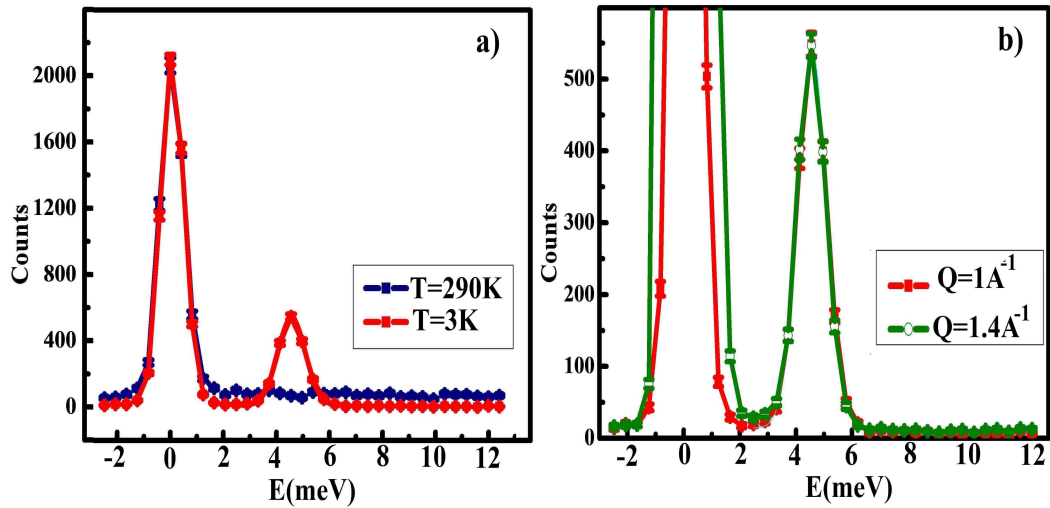


Figure 6.17: Inelastic neutron scattering of CeCrO_3 at (a) $T = 3$ K (red line) and 290 K (blue line) with $Q = 1 \text{ \AA}^{-1}$, (b) $T = 3$ K with $Q = 1 \text{ \AA}^{-1}$ (red line) and $Q = 1.4 \text{ \AA}^{-1}$ (green line).

Next, we examined the magnetic excitation of CeCrO_3 by plotting the energy transfer versus the momentum transfer color map at $T = 3$ K, shown in Figure 6.18. It is observed that there is a band of scattering exactly at $E = 4.57$ meV where the intensity of this band does not increase with Q . This is a confirmation that $E = 4.57$ meV indeed is the crystalline electric field energy level because crystalline electric field interaction is a local interaction and should not show any Q -dependence as a result. There are several high intensity regions at the zero energy transfer (elastic) at different Q values which are just simply either the nuclear or magnetic Bragg peaks.

It is essential to determine the difference between the excitation caused by

magnetism of nuclear scattering or phonons in a material. In general, the intensity of phonons tend to grow with Q^2 , while magnetic excitations tend to decrease in the intensity as Q increases. Figure 6.19(a) presents the Q -dependence of the form factor at 4.57 meV with $E_f = 14.5$ meV (blue line) and 30 meV (green line). The graph was fitted nicely with Ce^{3+} magnetic form factor Q -dependence ($f = \langle j_0 \rangle + c_2 \langle j_2 \rangle$, where $c_2 = 1.33$ is the cerium free ion coefficient and $j_k = \int dr u(r) J_k(qr)$ is the spatial average of the spherical Bessel function $J_k(qr)$ [15]). Results show that the intensity decreases while Q increases which confirm that the peak at 4.57 meV is the magnetic crystal field excitation.

Furthermore, the intensity of the magnetic excitation peak usually decreases with the temperature unlike the phonon. Temperature dependence of the excitation peak at 4.57 meV and the fixed momentum transfer $Q = 1 \text{ \AA}^{-1}$ in Figure 6.19(b) is another indication that this is the crystal field excitation.

Inelastic neutron scattering measurement to the higher energies with the fixed momentum transfer of 2.8 \AA^{-1} at both temperatures of 3 and 290 K were shown in Figure 6.20(a). The results do not show any other magnetic excitation peaks up to 30 meV. The same measurement was done with the higher momentum transfer ($Q = 1.4 \text{ \AA}^{-1}$) at $T = 3$ and 290 K where no other apparent peaks show up all the way to 20 meV (Figure 6.20(b)). It seems that the second excitation level is located above our measurement range.

In order to determine the exact value of magnetic phase transition, the temperature dependence of the magnetic peak intensity at $2\theta = 30.86^\circ$ and the fixed momentum transfer of $Q = 1.4104 \text{ \AA}^{-1}$ was plotted in Figure 6.21(a). The

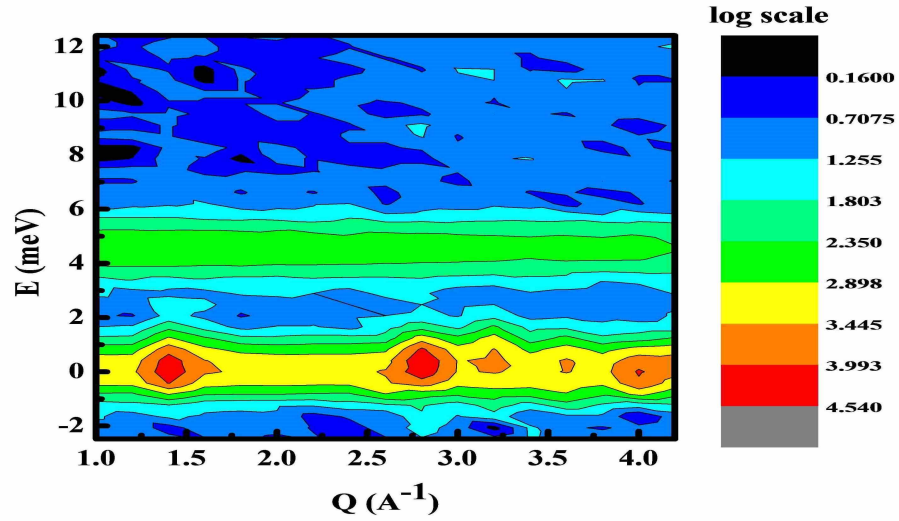


Figure 6.18: Q-E color map of CeCrO_3 at $T = 3$ K.

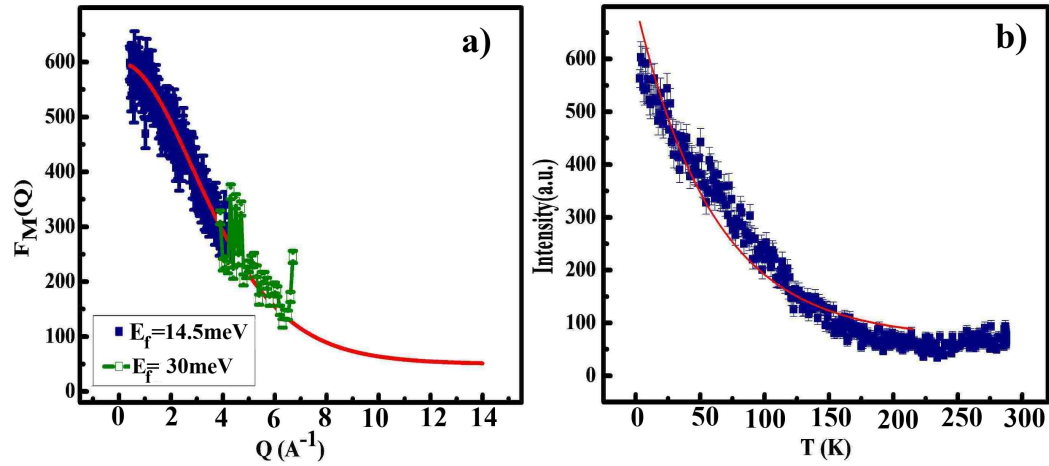


Figure 6.19: (a) Momentum transfer dependence of the magnetic form factor of CeCrO_3 with the energy transfer of 4.57 meV, $E_f = 14.5$ meV (blue line) and $E_f = 30$ meV (green line), (b) T-dependence of the peak at 4.57 meV.

measurement was done on the cooling cycle. The graph was fitted with $(T_N - T)^\beta$ and the values of $T_N = 258.57 \pm 0.57$ K and $\beta = 0.46 \pm 0.01$ were obtained. While by fitting the graph by $(1 - (\frac{T}{T_N})^\alpha)^\beta$, the values of $T_N = 262 \pm 0.2$ K, $\alpha = 2.26 \pm 0.03$ and $\beta = 0.72 \pm 0.01$ were calculated. The intensity of the magnetic peak above 260 K is the temperature independent which indicated that this temperature is the magnetic transition temperature (Figure 6.21(b)).

Inelastic neutron scattering measurements of $\text{Ce}_{0.9}\text{Eu}_{0.1}\text{CrO}_3$ at the fixed momentum transfer of $Q=1.4104 \text{ \AA}^{-1}$ at $T= 3$ K (red line) and 290 K (blue line) are plotted in Figure 6.22(a). The first excitation energy level at $T = 3$ K is located at the $E = 4.99 \pm 0.03$ meV with the half width of $\text{FWHM} = 1.44 \pm 0.07$ meV.

The energy dependence of the intensity in the inelastic neutron scattering of the $\text{Ce}_{0.5}\text{Eu}_{0.5}\text{CrO}_3$ with $E_f = 14.5$ meV at $T = 3$ K and 290 K (Figure 6.22(b)) gives better resolution than the energy scan with the higher energy (inset) which clearly shows that there is a peak at 6.51 ± 0.10 and half width of 1.86 ± 0.26 meV. The same scan with $E_f = 30$ meV shows no clear excitation peak which is not surprising since it has a worse resolution than the smaller E_f .

Inelastic neutron scattering measurements of $\text{Ce}_{0.1}\text{Eu}_{0.9}\text{CrO}_3$ at $T = 3$ and 290 K with $E_f = 14.5$ meV and 30 meV were plotted in Figure 6.22(c). At this high Eu-doping and within this energy range, no inelastic peak is observed. It seems that the crystalline electric field levels of $\text{Ce}_{0.1}\text{Eu}_{0.9}\text{CrO}_3$ are located at the higher energy than that of measured or the measurable signal can not be detected due to the high absorption of Eu at this high concentration of 90 %.

Figure 6.22(d) presents the magnetic phase transition of $\text{Ce}_{1-x}\text{Eu}_x\text{CrO}_3$ measured

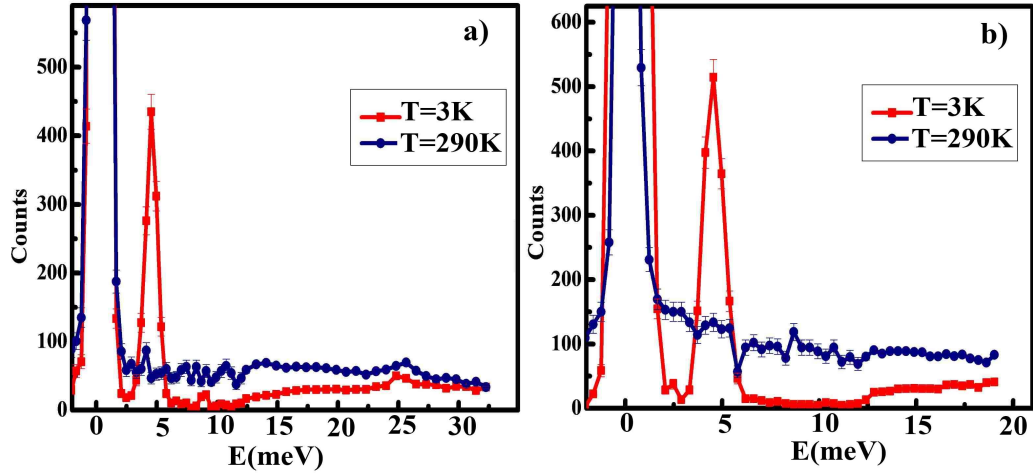


Figure 6.20: Energy scan of CeCrO_3 to the higher energies at $T = 3 \text{ K}$ (red line) and 290 K (blue line) with (a) $Q = 2.8 \text{ \AA}^{-1}$ and (b) $Q = 1.4 \text{ \AA}^{-1}$.

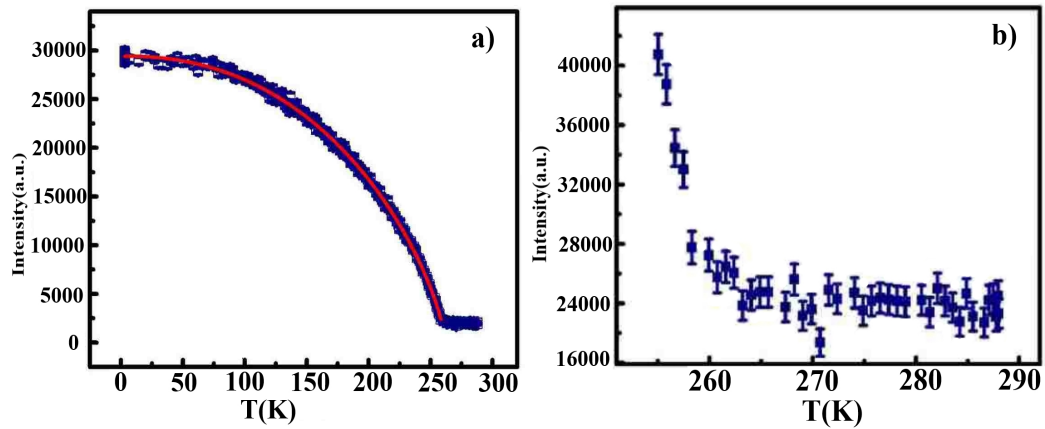


Figure 6.21: (a) Temperature dependence of the magnetic peak intensity of CeCrO_3 with 1.4104 \AA^{-1} . (b) Zoomed in temperature dependence of the magnetic peak around the transition temperature.

at $Q = 1.4104 \text{ \AA}^{-1}$ in the cooling cycle which gives the $T_N = 249.09 \pm 1.28 \text{ K}$ for $x = 0.1$, $T_N = 215.35 \pm 0.48 \text{ K}$ for $x = 0.5$ and $T_N = 187.04 \pm 0.72 \text{ K}$ for $x = 0.9$. The magnetic transition temperature shifts to the lower temperature while Eu content increases which is in good agreement with our DC magnetization measurement.

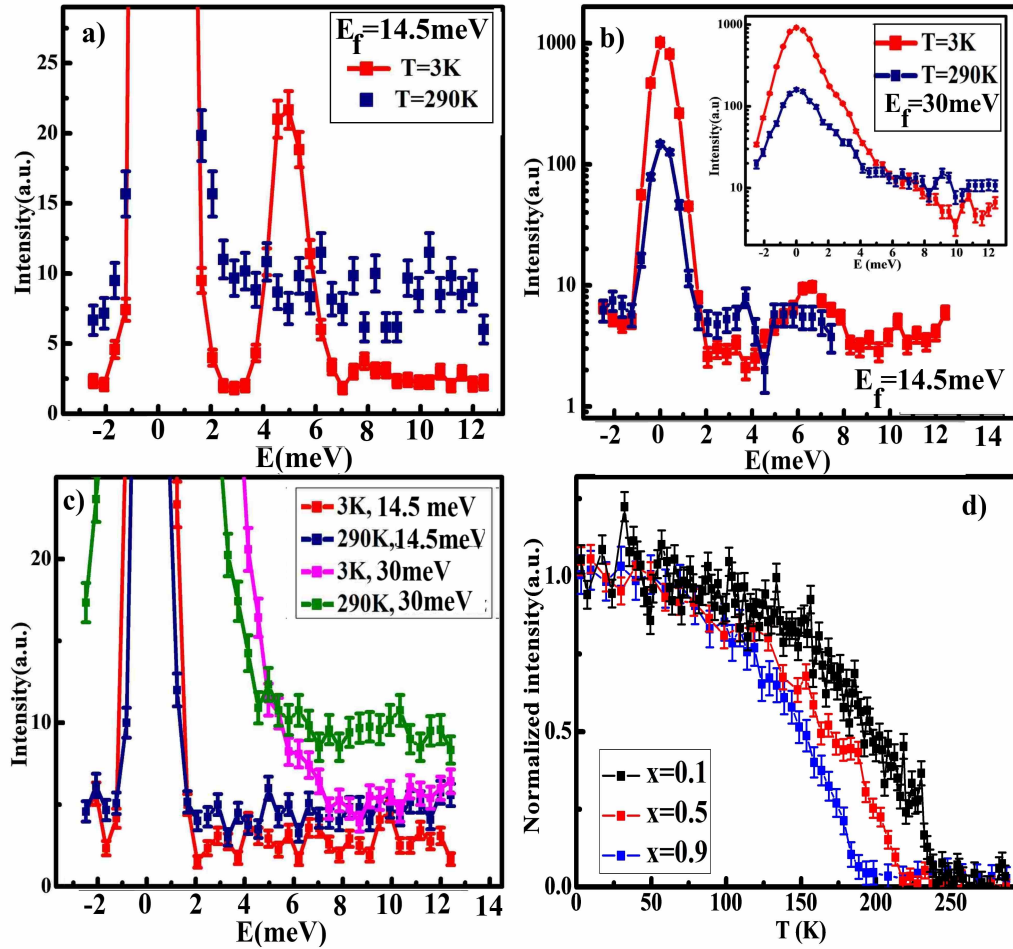


Figure 6.22: Inelastic neutron scattering of $\text{Ce}_{1-x}\text{Eu}_x\text{CrO}_3$ at $T = 3 \text{ K}$ (red line) and $T = 290 \text{ K}$ (blue line) (a) $x = 0.1$, (b) $x = 0.5$, (c) $x = 0.9$ and (d) the magnetic phase transition of $\text{Ce}_{1-x}\text{Eu}_x\text{CrO}_3$.

In order to determine the exact value of the magnetic phase transition of EuCrO_3 , the temperature dependence of the Cr^{3+} magnetic peak intensity with

the final energy of $E_f = 30$ meV and the fixed momentum transfer $Q = 1.4164 \text{ \AA}^{-1}$ were plotted in Figure 6.23(a). The transition temperature obtained from this graph is 177.50 ± 0.78 K with $\beta = 0.26 \pm 0.02$. The inset represents the temperature dependence of the peak attributed to the magnetic ordering of Eu^{3+} which does not show any significant change in the intensity.

The inelastic scattering of EuCrO_3 was performed at $T = 3$ K (blue and green lines) and 290 K (red line) with the final energy of $E_f = 30$ and 14.5 meV, which are shown in Figure 6.23(b). No inelastic peak is observed within this energy range. It seems that crystalline electric field levels of EuCrO_3 are located at the higher energy than those we measured or the high absorption of Eu prevents a measurable signal. In general, the ground state 7F_0 level is a singlet and not affected by the crystal field, thus its excited energy levels can be affected by the crystal field. For example, in orthorhombic EuAlO_3 , the excited levels of 7F_1 and 7F_2 are located about 45 and 124 meV above the ground state, respectively [16].

Figure 6.23 presents Néel transition temperature of $\text{Ce}_{1-x}\text{Eu}_x\text{CrO}_3$ versus europium concentration which were obtained from all measurements done in this work. The consistency of results shows a reduction in the magnetic ordering temperature of Cr^{3+} through Eu^{3+} doping in these compounds.

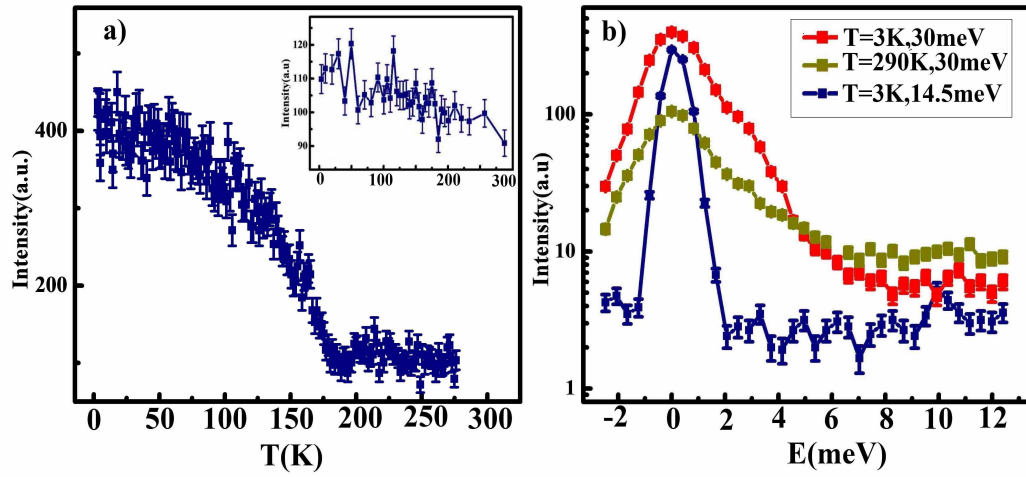


Figure 6.23: (a) Temperature dependence of the Cr^{3+} magnetic peak with the fixed momentum transfer $Q = 1.4164 \text{ \AA}$ (Inset shows the T -dependence of the Eu^{3+} magnetic peak). (b) Inelastic neutron scattering of EuCrO_3 at $T = 3 \text{ K}$ (blue and red lines) and 290 K (green line) with final energy of $E_f = 30 \text{ meV}$ and 14.5 meV .

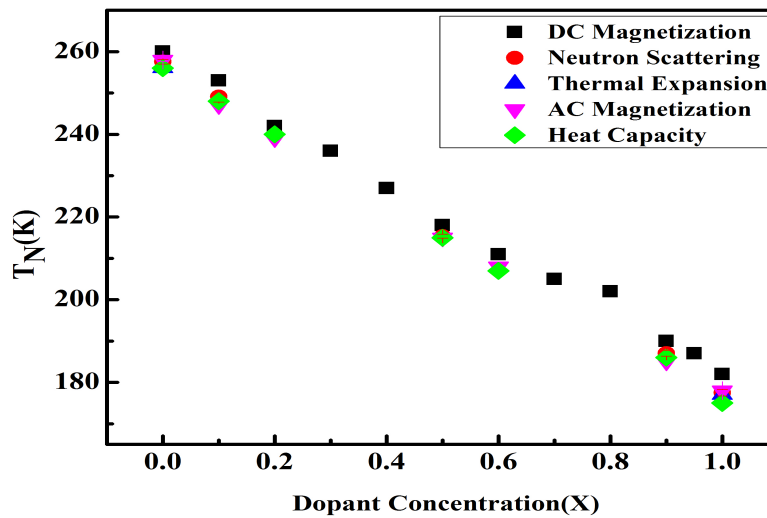


Figure 6.24: Néel transition temperature (T_N) versus europium concentration (x) in $\text{Ce}_{1-x}\text{Eu}_x\text{CrO}_3$, obtained from different experiments in this work.

Bibliography

- [1] www.cins.ca/ss2011/lectures/Holden.pdf
- [2] S. Chen, M. Bourham, A. Rabiei, *Radiat. Phys. Chem.*, 117, 12-22, (2015)
- [3] G. Eckold, H. Schober, S. E. Nagler, “Studying Kinetics with Neutrons”, Springer Berlin Heidelberg, (2010)
- [4] F. Fernandez-Alonso, D. L. Price, “Neutron Scattering: Fundamentals”, Academic Press, (2013)
- [5] www.cins.ca/ss2013/lectures/Root.pdf
- [6] B. T. M. Willis, C. J. Carlile, “Experimental Neutron Scattering”, Oxford University Press, (2009)
- [7] www.neutrons.ornl.gov/sites/default/files/intro_to_neutron_scattering.pdf
- [8] www.cins.ca/docs/SS09/basic_theory1_yamani.pdf
- [9] G. L. Squires, “Introduction to the Theory of Thermal Neutron Scattering”, Cambridge University Press, Cambridge, UK., (1978)
- [10] S. W. Lovesey, “Theory of Neutron Scattering from Condensed Matter”, Clarendon Press, Oxford, (1984)

-
- [11] www.cins.ca/docs/SS09/basic_theory2.pdf
- [12] www.cins.ca/ss2013/lectures/Broholm.pdf
- [13] E. Balcar, S. W. Lovesey, “Theory of Magnetic Neutron and Photon Scattering”, Clarendon Press, Oxford, (1989)
- [14] R. Shukla, A. K. Bera, S. M. Yusuf, S. K. Deshpande, A. K. Tyagi, W. Hermes, M. Eul, R. Pottgen, *J. Phys. Chem. C*, 113, 12663-12668, (2009)
- [15] B. Chakrabarti, M. E. Pezzoli, G. Sordi, K. Haule, G. Kotliar, *Phys. Rev. B.*, 89,125113, (2014)
- [16] D. Petrov, B. Angelov, V. Lovchinov, *J. Alloy. Compd.*, 509, 50385041 (2011)

Chapter 7

Conclusion and Future Work

7.1 Conclusion

- Nano-sized $\text{Ce}_{1-x}\text{Eu}_x\text{CrO}_3$ powders were synthesized using the solution combustion method. The optimum condition for the single phase formation was sintering at 950°C for 12 h in the mixture of argon and hydrogen.
- The refined X-ray and neutron diffraction patterns of $\text{Ce}_{1-x}\text{Eu}_x\text{CrO}_3$ polycrystalline confirmed the distorted orthorhombic structure with $Pbnm$ space group in samples. No structural phase transition by temperature was observed.
- a and c lattice parameters were decreased and b parameter was increased through increasing the europium content in $\text{Ce}_{1-x}\text{Eu}_x\text{CrO}_3$, leading to a general decrease in the unit cell volume of samples.
- The smaller size of Eu^{3+} in comparison with Ce^{3+} caused a distortion enhancement in $\text{Ce}_{1-x}\text{Eu}_x\text{CrO}_3$. a and b lattice parameters in CeCrO_3 ($x = 0$) were almost equal, thus the crystal structure was close to tetragonal, however they were

more different from each other by increasing europium content, converting the crystal structure to more orthorhombic.

- The average Cr-O distance was increased through europium doping which indicates a smaller Coulomb repulsion energy and thus, the smaller overall splitting of the t_{2g} energy levels of chromium.
- The temperature dependence of the volume unit cell of EuCrO_3 obtained from neutron diffraction patterns showed an anomaly at $T \approx 100$ K due to the lattice effects which was in good agreement with the anomaly observed in the thermal expansion, Raman spectroscopy and dielectric data.
- The average particle size of $\text{Ce}_{1-x}\text{Eu}_x\text{CrO}_3$ was decreased by an increase in Eu^{3+} concentration, due to the different diffusion rate in the ions with different radius size. Morphology of samples showed almost homogeneous rounded rectangular shape particles with an average particle size of 60-80 nm.
- The smaller size of Eu^{3+} caused a reduction in the super-exchange Cr-O-Cr angle and increase in an average Cr-O distance which were increased the structural distortion. Consequently, the Néel transition temperature of $\text{Ce}_{1-x}\text{Eu}_x\text{CrO}_3$ was decreased from $T \approx 260$ K for $x = 0.0$ to $T \approx 182$ K in $x = 1.0$ and the effective magnetic moment of samples was increased from $4.88 \pm 0.06 \mu_B/\text{f.u.}$ for $x = 0.0$ to $6.98 \pm 0.11 \mu_B/\text{f.u.}$ in $x = 1.0$.
- The magnetic susceptibility of CeCrO_3 consisted of χ_D , $\chi_{CW}(\text{Cr}^{3+})$ and

$\chi_{CW}(\text{Ce}^{3+})$ while the magnetic susceptibility of EuCrO_3 was composed of χ_D , $\chi_{CW}(\text{Cr}^{3+})$ and $\chi_{VV}(\text{Eu}^{3+})$ where χ_D , χ_{CW} and χ_{VV} are the diamagnetic, Curie-Weiss and Van Vleck susceptibility, respectively.

- An exchange bias effect, magnetization irreversibility and AC susceptibility dispersion in these samples provided evidence of the presence of the spin disorder magnetic phase at the surface of the particles. XPS results confirmed the oxidation change at the surface of compounds.
- The exchange bias sign reversal and magnetization reversal in CeCrO_3 indicated that exchange interaction between Cr^{3+} and Ce^{3+} was changed by temperature. The exchange bias effect was positive at low temperatures, indicating the antiferromagnetic exchange interaction at the interface of the core and the shell while the exchange bias effect converted to negative at high temperatures. Conversely, the negative exchange bias was observed in EuCrO_3 at all temperatures, confirming the ferromagnetic arrangement at the interface in this sample.
- Neutron diffraction patterns confirmed the long range magnetic ordering of Cr^{3+} ion in Γ_4 configuration although no magnetic contribution attributed to the rare earth ions was detected.
- Inelastic neutron scattering of CeCrO_3 detected a magnetic excitation peak which was in good agreement with the data obtained from heat capacity measurement. This crystal field excitation peak moved to the higher energies through Eu^{3+} doping although it was not able to detect in the samples with high europium concentration in our energy measurement range.

7.2 Recommendation for Future Work

Although the results presented in this work have demonstrated structural, magnetic and thermal properties of CeCrO_3 through Eu^{3+} doping, it could be further developed in other physical properties of these compounds especially their electric properties. $\text{Ce}_{1-x}\text{Eu}_x\text{CrO}_3$ nano-powders are canted antiferromagnetic with the Néel transition temperature between 180 - 260 K. Furthermore, they have showed weak ferromagnetism and relaxor-like dielectric behavior, which empower them with the multifunctional applications. My particular interest on these compounds would be the study of ferroelectricity and the possibility of its coupling with the magnetization, as a means of the multiferroic devices. On the other hand, it would be interesting to work on the preparation and physical investigation of $\text{Ce}_{1-x}\text{Eu}_x\text{CrO}_3$ thin films. The possibility of the exchange bias and magnetoelectric effects in their thin films makes them good candidates in the modern magnetoelectronic devices such as tunnel magnetoresistance sensors and spin valves.